

LASER SPECTROSCOPIC ANALYSIS  
OF ATMOSPHERIC GASES  
IN SCATTERING MEDIA

Mikael Sjöholm

Doctoral Thesis  
2006



LUND UNIVERSITY

LASER SPECTROSCOPIC ANALYSIS OF ATMOSPHERIC GASES  
IN SCATTERING MEDIA

Copyright © 2006 Mikael Sjöholm  
All rights reserved  
Printed in Sweden by KFS AB, Lund, 2006

Atomic Physics Division  
Department of Physics  
Faculty of Engineering (LTH)  
Lund University  
P.O. Box 118  
SE-221 00 Lund  
Sweden

ISSN 0281-2762  
Lund Reports on Atomic Physics, LRAP-367

ISBN 13: 978-91-628-6962-5  
ISBN 10: 91-628-6962-0

TILL MIN FAMILJ



# ABSTRACT

---

---

Laser spectroscopic techniques for gas analysis under various influences of light scattering are explored in a wide spectral range from the ultraviolet to the infrared. The techniques rely on spectrally narrow-band light sources that are used in differential optical absorption measurements.

A **differential absorption light detection and ranging (DIAL)** application for the monitoring of atomic gaseous mercury, utilizing ultraviolet light from an **optical parametric oscillator (OPO)**, is introduced. Results from six two-week field campaigns at chlor-alkali plants in Sweden, Italy, and Poland, performed within a cross-disciplinary European Union funded project concerning **European mercury emissions from chlor-alkali plants (EMECAP)** are presented. The resulting time series of the mercury flux and the animations showing the spatial concentration distributions constitute important input for the environmental community. In addition, by employing a multiple-wavelength DIAL technique in the infrared spectral region, simultaneous remote measurement of mixtures of gaseous substances with overlapping spectra is achieved.

A diode-laser-based spectrometer comprising nonlinear frequency mixing for the detection of sulfur dioxide in the ultraviolet region is presented, as well as a temporal gas correlation procedure that does not require any knowledge of the exact spectrum of either the gas or the light.

Finally, a novel concept of non-intrusive, real-time tunable-laser-based **gas in scattering media absorption spectroscopy (GASMAS)** measurements is introduced. Sensitive detection of absorption is obtained by utilizing wavelength modulation spectroscopy. Combined with time-resolved measurements employing **time-correlated single-photon counting (TCSPC)**, the gas concentration in various porous materials is estimated. Applications related to the food packaging industry, e.g., **modified atmosphere packaging (MAP)**, are explored by studies of gas exchange in horticultural produce. Furthermore, applications related to the building industry are explored in studies on gas transport and drying processes in wood by the detection of molecular oxygen and water vapor in the near-infrared spectral region.



# SAMMANFATTNING

---

---

Doften av blommor och mat förnimmer vi med näsan, vilken är en finurlig gassensor som även känner av mindre trevliga lukter från exempelvis rök och avgaser. Våra ögon ser färger och former hos föremål genom att detektera ljus som har reflekterats, brutits, spridits eller delvis absorberats i vår omgivning.

Denna avhandling beskriver i någon mening en sorts konstgjorda ögon som fungerar som känsliga näsor, det vill säga optiska tekniker som utnyttjar ljus för att förnimma gaser. Den underliggande principen består i att gaser absorberar ljus, vilket betyder att mängden ljus som har passerat genom en gas är lägre än mängden som sänts in. Selektiv gasförnimmelse uppnås genom att varje gas har sitt eget karaktäristiska fingeravtryck i termer av vilka färger, det vill säga våglängder, av ljuset som den absorberar. Uppsättningen våglängder som absorberas kallas för spektrum och följaktligen kallas vetenskapen att studera sådana spektra för spektroskopi.

En speciell sorts ljus som endast består av en färg åt gången, det vill säga ljus i ett smalt intervall centrerat kring en våglängd, har använts i alla de tekniker som presenteras i denna avhandling. Ljuskällan som avger sådant ljus känner vi under namnet laser, vilket är en förkortning av det engelska uttrycket för ljusförstärkning genom stimulerad utsändning av strålning. Följaktligen kallas denna sorts teknik för laserspektroskopi.

De laserspektroskopiska tekniker för analys av gas under olika inflytande av ljusspridning som här utforskats i det breda spektralområdet från ultraviolett till infrarött delar alla principen för differentiell absorption. Det betyder att man jämför ljus vid en våglängd som påverkas av den eftersökta gasen med ljus vid en närliggande våglängd som inte påverkas av gasen ifråga. Fördelen med denna metod är att man eliminerar inverkan från svagt våglängdsberoende absorption och spridning hos värdmaterialet i vilket den intressanta gasen finns.

Trots att de använda teknikerna är generella till sin natur har de här tillämpats på några specifika gaser såsom syre, vattenånga, svaveldioxid, kvicksilver, metan och andra kolväten, som alla finns i atmosfären. Syre

och vattenånga har exempelvis betydelse för livets processer och vid bevarande av mat. Svaveldioxid och kvicksilver är miljömässigt problematiska gaser och kolväten och vattenånga är industriellt viktiga gaser. Således spänner studierna i de 13 inkluderade artiklarna, som utgör grunden för avhandlingen, över ett brett område av gaser, som är av miljömässig, biologisk och industriell betydelse.

En tillämpning som introduceras är övervakning av kvicksilveratomer i luften med ett laserradarsystem baserat på en ljuskälla i det ultravioletta spektralområdet i form av en så kallad optisk parametrisk oscillator. Laserradarsystemet sänder ut korta pulser av ljus som ute i luften studsar mot molekyler och partiklar. En bråkdel av ljuset studsar tillbaka från olika avstånd och genom att tidsupplöst mäta mängden ljus som reflekterats kan man få information om hur långt bort ljuset varit. Hur mycket absorberande gas det finns på olika avstånd längs med den riktning som ljuspulsen färdats i kan man klura ut på ett finurligt sätt genom att mäta differentiellt. Genom att sedan lysa i olika riktningar kan man skapa hela kartor över hur hög gaskoncentrationen är på olika ställen i luften kring exempelvis en fabrik. Om man dessutom mäter hur snabbt det blåser vinkelrätt mot det plan där man har mätt upp koncentrationen, kan man räkna ut hur stort flöde av gas som släpps ut från fabriken.

Resultat presenteras från sex tvåveckorlånga fältkampanjer vid kloralkalifabriker i Sverige, Italien och Polen utförda inom ramen för ett tvärdisciplinärt EU-finansierat projekt (EMECAP) om kvicksilverutsläpp från kloralkalifabriker. De erhållna tidsserierna av kvicksilverflöde och filmer med rumsliga koncentrationsfördelningar är viktiga inparametrar för miljösamfundet. Dessutom presenteras en differentiell laserradartechnik som utnyttjar flera våglängder för samtidig fjärrmätning av substanser med överlappande spektra såsom exempelvis kolväten i det infraröda spektralområdet.

Ett mindre, diodlaserbaserat system för detektion av svaveldioxid i det ultravioletta området presenteras. Det ultravioletta ljuset fås genom att blanda blåviolett ljus med närinfrarött ljus (som är rödare än rött) i en speciell så kallad icke-linjär kristall. Dessutom presenteras en metod som bygger på att man samtidigt mäter på en känd mängd av en viss gas för att avslöja hur mycket av samma gas det finns på ett annat ställe. Det är helt enkelt gasen själv som känner sitt eget spektrum bäst och tekniken kan benämnas gaskorrelation i tiden.

Avslutningsvis introduceras ett nytt koncept (GASMAS) med icke-förstörande, absorptionsspektroskopiska mätningar av gas i spridande porösa material med laserljus vars våglängd kan svepas över en smal gasabsorptionsprofil. Genom utnyttjande av en speciell teknik som kallas våglängdsmodulationsspektroskopi åstadkoms särskilt känslig absorptionsdetektion. Det görs genom att man märker ljuset på ett speciellt sätt så att man kan känna igen det även om det är insvept i störande

brus. Det är ungefär som att man lättare kan uppfatta vad en viss person i ett sorlande folkhav säger om personen är ensam om att tala på en säregen dialekt eller ett speciellt språk, givet att man förstår dialekten eller språket. Att ett material är spridande betyder att ljuspartiklarna inte går raka vägen igenom materialet utan att de istället studsar runt och går en mycket längre väg än den kortaste raka vägen. Detta kan liknas med den väg en berusad tar när den raglar hem från krogen. För att uppskatta gaskoncentrationen i ett spridande, poröst material behövs tidsupplösta mätningar där man tar reda på hur lång sträcka ljuspartiklarna studsar runt innan de detekteras. Tillämpningar relaterade till förpackningsindustrin, till exempel förpackningar med modifierad atmosfär, utforskas genom studier av gasutbyte i trädgårdsprodukter såsom exempelvis äpplen efter skörd. Dessutom utforskas tillämpningar relaterade till byggbranschen genom studier av exempelvis gastransport och torkprocesser i trä genom detektion av syrgas och vattenånga i det nära infraröda spektrala området.



# CONTENTS

---

---

<b>List of publications</b>	<b>xv</b>
<b>1 Introduction</b>	<b>1</b>
<b>2 Tunable light sources</b>	<b>3</b>
2.1 The nature of light . . . . .	3
2.2 Lasers . . . . .	4
2.2.1 Historical introduction . . . . .	4
2.2.2 Operating principles of lasers . . . . .	5
2.3 Diode lasers . . . . .	7
2.3.1 Operating principles of diode lasers . . . . .	8
2.3.2 Wavelength tunability . . . . .	9
2.4 Nonlinear optical frequency conversion . . . . .	10
2.4.1 Nonlinear optical media . . . . .	11
2.4.2 Phase matching . . . . .	12
2.4.3 Optical frequency conversion applications . . . . .	13
2.5 Optical parametric oscillators . . . . .	13
2.5.1 Operating principles of OPO . . . . .	14
2.5.2 The implementation used . . . . .	15
<b>3 Light propagation</b>	<b>17</b>
3.1 Light absorption . . . . .	17
3.1.1 Optical transitions . . . . .	18
3.1.2 Line shapes . . . . .	18
3.1.3 Beer-Lambert's law . . . . .	21
3.2 Light scattering . . . . .	22
3.2.1 Rayleigh and Raman scattering . . . . .	23
3.2.2 Mie scattering . . . . .	24
3.2.3 Scattering phase function . . . . .	24
3.2.4 Reduced scattering . . . . .	25
3.3 Light absorption and scattering . . . . .	26
3.3.1 Spatial dependent attenuation . . . . .	26
3.3.2 Range-resolved absorption . . . . .	26
3.3.3 Differential absorption . . . . .	27
3.4 Light transport in multiple scattering media . . . . .	28
3.4.1 Radiative-transport theory . . . . .	28
3.4.2 The diffusion approximation . . . . .	29
3.4.3 Time-dependent solutions . . . . .	30
3.4.4 Steady-state solutions . . . . .	33
3.4.5 Absorption path length . . . . .	35

<b>4</b>	<b>Spectroscopic techniques</b>	<b>39</b>
4.1	Tunable diode laser spectroscopy . . . . .	39
4.1.1	Modulation techniques . . . . .	40
4.1.2	Phase modulation . . . . .	40
4.1.3	Wavelength modulation . . . . .	41
4.2	Light detection and ranging (lidar) . . . . .	45
4.2.1	The lidar system . . . . .	47
4.2.2	Flux measurements . . . . .	48
4.3	Calibration techniques . . . . .	49
4.3.1	Wavelength calibration . . . . .	49
4.3.2	Concentration calibration . . . . .	50
4.4	Optical techniques for scattering media . . . . .	51
4.4.1	Temporal domain techniques . . . . .	51
4.4.2	Frequency domain techniques . . . . .	52
4.4.3	Spatial domain techniques . . . . .	53
4.5	Gas in scattering media absorption spectroscopy (GASMAS) . . . . .	53
4.5.1	General aspects . . . . .	53
4.5.2	The small case . . . . .	54
4.5.3	The large case . . . . .	54
<b>5</b>	<b>Gas in nature and industry</b>	<b>57</b>
5.1	Atmospheric pollution . . . . .	57
5.1.1	Climate change . . . . .	57
5.1.2	Acidification . . . . .	58
5.1.3	Heavy metals . . . . .	59
5.2	Gases of life . . . . .	60
5.2.1	Gas in porous plants . . . . .	60
5.2.2	Gas of human health . . . . .	62
5.3	Prospectives of performed porous projects . . . . .	62
5.3.1	Pharmaceutical physics . . . . .	63
5.3.2	Drying diagnostics . . . . .	64
5.3.3	Packaging processes . . . . .	64
5.3.4	Developing devices . . . . .	65
	<b>Summary of Papers</b>	<b>67</b>
	<b>Acknowledgements</b>	<b>75</b>
	<b>References</b>	<b>79</b>

## Papers

---

<b>I</b>	<b>Atmospheric mercury near a chlor-alkali plant in Sweden</b>	<b>91</b>
<b>II</b>	<b>Atomic mercury flux monitoring using an optical parametric oscillator based lidar system</b>	<b>107</b>
<b>III</b>	<b>Elemental mercury emission from chlor-alkali plants measured by lidar techniques</b>	<b>115</b>
<b>IV</b>	<b>Multi-component chemical analysis of gas mixtures using a continuously tuneable lidar system</b>	<b>125</b>

V	All-diode-laser ultraviolet absorption spectroscopy for sulfur dioxide detection	133
VI	Temporal correlation scheme for spectroscopic gas analysis using multimode diode lasers	141
VII	Analysis of gas dispersed in scattering media	147
VIII	Concentration measurement of gas embedded in scattering media by employing absorption and time-resolved laser spectroscopy	153
IX	Laser spectroscopy of free molecular oxygen dispersed in wood materials	163
X	Diode laser absorption spectroscopy for studies of gas exchange in fruits	171
XI	Studies of gas exchange in fruits using laser spectroscopic techniques	185
XII	Spectroscopic studies of wood-drying processes	197
XIII	Gas diffusion measurements in porous media by the use of a laser spectroscopic technique	213



# LIST OF PUBLICATIONS

---

---

The thesis is based on the following original scientific papers:

**Paper I. Atmospheric mercury near a chlor-alkali plant in Sweden**

I. Wängberg, H. Edner, R. Ferrara, E. Lanzillotta, J. Munthe, J. Sommar, M. Sjöholm, S. Svanberg, and P. Weibring  
The Science of the Total Environment **304**, 29–41 (2003).

**Paper II. Atomic mercury flux monitoring using an optical parametric oscillator based lidar system**

M. Sjöholm, P. Weibring, H. Edner, and S. Svanberg  
Optics Express **12**, 551–556 (2004).

**Paper III. Elemental mercury emission from chlor-alkali plants measured by lidar techniques**

R. Grönlund, M. Sjöholm, P. Weibring, H. Edner, and S. Svanberg  
Atmospheric Environment **39**, 7474–7480 (2005).

**Paper IV. Multi-component chemical analysis of gas mixtures using a continuously tuneable lidar system**

P. Weibring, Ch. Abrahamsson, M. Sjöholm, J. N. Smith, H. Edner, and S. Svanberg  
Applied Physics B **79**, 525–530 (2004).

**Paper V. All-diode-laser ultraviolet absorption spectroscopy for sulfur dioxide detection**

G. Somesfalean, Z. G. Zhang, M. Sjöholm, and S. Svanberg  
Applied Physics B **80**, 1021–1025 (2005).

**Paper VI. Temporal correlation scheme for spectroscopic gas analysis using multimode diode lasers**

G. Somesfalean, M. Sjöholm, L. Persson, H. Gao, T. Svensson, and S. Svanberg  
Applied Physics Letters **86**, 184102 (2005).

- 
- Paper VII. Analysis of gas dispersed in scattering media**  
M. Sjöholm, G. Somesfalean, J. Alnis, S. Andersson-Engels, and S. Svanberg  
Optics Letters **26**, 16–18 (2001).
- Paper VIII. Concentration measurement of gas embedded in scattering media by employing absorption and time-resolved laser spectroscopy**  
G. Somesfalean, M. Sjöholm, J. Alnis, C. af Klinteberg, S. Andersson-Engels, and S. Svanberg  
Applied Optics **41**, 3538–3544 (2002).
- Paper IX. Laser spectroscopy of free molecular oxygen dispersed in wood materials**  
J. Alnis, B. Anderson, M. Sjöholm, G. Somesfalean, and S. Svanberg  
Applied Physics B **77**, 691–695 (2003).
- Paper X. Diode laser absorption spectroscopy for studies of gas exchange in fruits**  
L. Persson, H. Gao, M. Sjöholm, and S. Svanberg  
Optics and Lasers in Engineering **44**, 687–698 (2006).
- Paper XI. Studies of gas exchange in fruits using laser spectroscopic techniques**  
L. Persson, B. Anderson, M. Andersson, M. Sjöholm, and S. Svanberg  
Proceedings of FRUTIC 05, Information and Technology for Sustainable Fruit and Vegetable Production, 543–552, Montpellier (September 2005).
- Paper XII. Spectroscopic studies of wood-drying processes**  
M. Andersson, L. Persson, M. Sjöholm, and S. Svanberg  
Optics Express **14**, 3641–3653 (2006).
- Paper XIII. Gas diffusion measurements in porous media by the use of a laser spectroscopic technique**  
M. Sjöholm, L. Persson, and S. Svanberg,  
Manuscript in preparation.

# INTRODUCTION

---

---

We sense the pleasant scent of flowers and food by our nose; a gas sensor that also detects the usually unpleasant smells from other substances such as smoke and exhaust fumes. Our eyes can see the colors and the shapes of objects in the world around us by detecting light that has been reflected, refracted, scattered or partially absorbed by those same objects.

This thesis explores optical techniques that utilize light for gas sensing which, in some sense, can be seen as a kind of artificial eyes acting as very sensitive noses. The underlying principle for gas sensing is light absorption, which means that the amount of light after passage through a gas is lower than the amount of light sent into the gas. Selective sensing can be achieved since each gas has its own characteristic fingerprint in terms of which colors, i.e, wavelengths, of the light that it absorbs. The set of wavelengths absorbed is called a spectrum and thus the art of studying such spectra is called spectroscopy.

A special kind of light that has only one color at a time, i.e., light that is narrowly centered around one wavelength, has been used in all the techniques presented in this thesis. A light source that generate this type of light is known as a laser (light amplification by stimulated emission of radiation). Consequently, the kind of spectroscopy described here is known as laser spectroscopy.

All the laser spectroscopic techniques explored share the common principle of differential absorption in that the gas absorption signatures are measured relative to the light level just outside the narrow absorption profile. The benefit of this approach is that it eliminates the influence of slowly wavelength dependent absorption and scattering features of the bulk medium in which the gas of interest is enclosed.

Although the techniques presented are general and can be applied to the detection of any gaseous species, in this thesis focus has been on

---

gaseous substances that to different amounts are present in the atmosphere. Examples of gases studied include oxygen (Papers VII, VIII, IX, X, XI, XII, and XIII), water vapor (Paper XII), sulfur dioxide (Paper V), mercury (Paper I, II, and III), methane and other hydrocarbons (Paper IV). Oxygen and water vapor are essential for the processes of life and of interest for food preservation. Sulfur dioxide and mercury are environmental pollutants, and hydrocarbons and water vapor are important industrial gases. Thus, the studies span over a wide range of gases that are of environmental, biological and industrial importance.

The light-absorbing gases studied are present in media that both absorb and scatter light to various extent. Several of the techniques explored take advantage of this. For instance, range resolution in remote mapping of air pollutants by laser-radar techniques is provided by time-resolved detection of backscattered light pulses. Environmental field monitoring of gaseous mercury emission around chlor-alkali industries in Sweden, Italy, and Poland based on this technique is presented in Papers I, II, and III. Furthermore, a scheme for laser-radar measurements of mixtures of gases with overlapping spectra is introduced in Paper IV.

Another benefit of scattering is present in the concept of **gas in scattering media absorption spectroscopy (GASMAS)** [VII], where the multiple scattering provides an increased absorption path length, resulting in a stronger absorption signal than without scattering. An approach to gas concentration measurements in porous materials is explored in Paper VIII and the assessment of gas transport in scattering porous materials is discussed in Paper XIII. The GASMAS concept has shown to offer several application opportunities related to gas in porous materials. In this thesis, issues related to the food packaging industry are illustrated by studies on gas exchange in fruits during the postharvest period (Papers X and XI). Furthermore, in Papers IX and XII wood and its drying processes are studied by the diode laser spectroscopic techniques of GASMAS.

The thesis consists of an introduction and 13 original scientific Papers. After this introduction to the introduction, Chapter 2 presents the tunable light sources used. In Chapter 3 light propagation under various influences of scattering are described. Chapter 4 presents various laser-based spectroscopic techniques and show how the light sources introduced in Chapter 2 can be employed to assess the optical parameters discussed in Chapter 3. Finally, Chapter 5 places the work presented in this thesis in a larger contemporary societal and industrial context.

# TUNABLE LIGHT SOURCES

---

Light from the sun is the driving force for most of the terrestrial life. Through history, we have become familiar with different aspects of light and even learnt how to produce it ourselves in various forms from fires with broad-band radiation already in the childhood of mankind to high-tech narrow-band tunable light sources of today. In this Chapter tunable laser sources for spectroscopic applications are discussed.

## 2.1 The nature of light

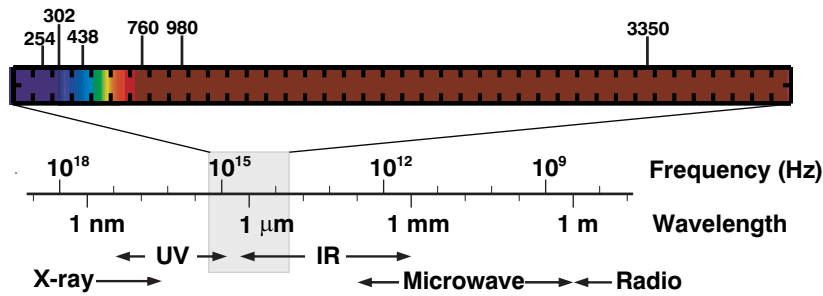


**Figure 2.1.** *The electromagnetic spectrum. The numbers indicated in the enlarged spectral range from the ultraviolet to the mid-infrared correspond to wavelengths in nanometers used for gas detection in this thesis.*

Light exhibits both wave and particle features. The wave nature is captured in the properties of wavelength,  $\lambda$ , and frequency,  $\nu$ , which are related by  $c = \lambda\nu$ , where the constant  $c$  is the speed of the light wave. Actually, visible light is only a specific range of the broad spectrum of electromagnetic radiation as is illustrated in Figure 2.1. The particle

nature is captured in the concept of light energy quanta, i.e., photons carrying the energy  $E = h\nu$ , where  $h$  is Planck's constant.

The light sources that we encounter in everyday life most often emit light in fixed broad wavelength regions. This kind of light can be used for spectroscopic studies provided that a wavelength selective detection device, e.g., an optical grating or prism is used. However, light sources that emit light of narrow spectral width around a specific wavelength that easily can be tuned have become available during the last decades. This has opened the opportunity for more sensitive spectroscopic measurements without the need of wavelength selective detection devices.

The research presented in the papers of this thesis, uses narrow-band light of various wavelengths. In Papers I, II, and III, ultraviolet radiation of 254 nm was used. Ultraviolet light was also used in Paper V, where light at 302 nm together with blue light at 438 nm and near infrared light at 975 nm was in action. Papers VI, VII, VIII, IX, X, XI, and XIII are all based on near-infrared light at 760 nm as is Paper XII, where also near-infrared light at 980 nm was used. Finally, Paper IV deals with the absorption of infrared light at around 3.4  $\mu\text{m}$ .

## 2.2 Lasers

### 2.2.1 Historical introduction

Nowadays we take lasers for granted in our everyday life. We store data, pictures, movies etc on optical storage media like CDs and DVDs utilizing lasers. We go to the supermarket where the cashier uses bar code readers based on lasers to collect the prices of the items we have bought. If we get some disease like diabetes retinopathy, lasers are routinely used for treatment. Even for cancer diagnostics and treatment, lasers are present in the modality of photodynamic therapy. In manufacturing of mechanical devices, powerful laser sources are responsible for cutting and welding. Lecturers have abandoned the mechanical pointers and use laser pointers, which in China can be bought for a fraction of a Euro. Additionally, there is a large flora of laser applications in both basic and applied science. One of these applications is laser spectroscopic detection of gases, which this thesis treats.

Back in the fifties, the scene was different. A device for **m**icrowave **a**mplification by **s**timulated **e**mission of **r**adiation (Maser) had recently been invented and the optical counterpart existed only in the minds of some researchers. A proposal for building such an optical Maser, now known as a Laser, was presented by Schawlow and Townes in 1958 [1]. Although there was some debate over the contribution of Gordon Gould to the invention of the laser, which resulted in lengthy patent fights [2], the laser, actually, was present long before that, since natural lasers have

been observed in astronomical objects [3]. After the laser proposal, there was a race of making the first laser. In 1960 Maiman succeeded. The ruby laser emitting pulsed laser light at 694.3 nm was invented [4]. At that time, the laser was a technology without a purpose and known as “a solution looking for a problem”, as is often the case with results springing from curiosity-driven basic research.

### 2.2.2 Operating principles of lasers

Although the first laser was invented in 1960, the underlying concept of stimulated emission was introduced already about half a century earlier by Albert Einstein. Here, only a brief introduction to the physics of lasers is given. For further reading, textbooks like for instance Refs [5, 6] can be recommended.

#### Absorption and stimulated emission

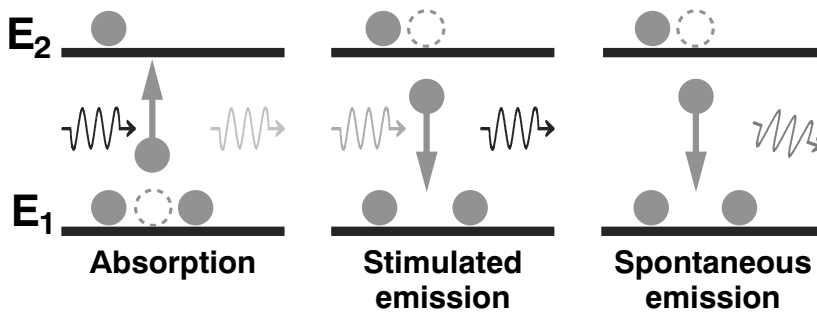


**Figure 2.2.** A schematic energy level picture of absorption, stimulated emission, and spontaneous emission.

Light can be absorbed with some probability when propagating through a medium of atoms or molecules having two energy levels  $E_1$  and  $E_2$  separated by the same energy as the energy of the light photon, e.g.  $E_2 - E_1 = hc/\lambda$ , which is further treated in Section 3.1. In the absorption process the energy of the vanishing photon is conserved by exciting one atom to the upper state as illustrated in Figure 2.2. This upper state has some finite lifetime and the excited system relaxes after some time to the lower state by spontaneously emitting a photon. However, it could also be that the transition from the upper to the lower state is stimulated by a resonant photon passing by. The stimulated emission of radiation has the same wavelength, phase and direction of propagation as the incident radiation, i.e., it is coherently radiated.

## Population inversion

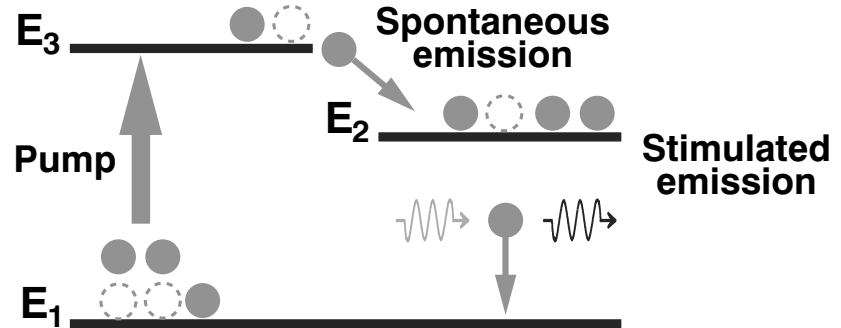


**Figure 2.3.** A schematic picture of a three level laser.

The question is what determines if stimulated emission or absorption of radiation occurs. According to the Einstein analysis, the probability of absorption is proportional to the number of atoms in the lower state  $N_1$  and the probability of stimulated emission is proportional, with the same constant of proportionality, to the number of atoms in the upper state  $N_2$ .

Systems in thermodynamic equilibrium tend not to be more excited than necessary and thus the lower state is normally more populated than the upper state. This results in a net absorption of the incident light. However, if the upper state is more populated than the lower state, the probability of stimulated emission becomes larger than the probability of absorption, which is a prerequisite for laser action. One way to achieve this is to employ a third energy level, denoted 3 in Figure 2.3, with short lifetime that spontaneously relaxes to the upper level 2 of our laser transition candidate. If the pump rate from level 1 to level 3 is fast enough compared to the rate of spontaneous emission rate from level 2, an inverted population between level 1 and level 2 can be achieved, as illustrated in Figure 2.3.

### Resonator

If we find an atomic system in which we can achieve an inverted population, we have an optical gain medium. In order to generate a substantial amount of coherent light we need to place the gain medium in a so-called resonator. This can be as simple as two mirrors that make the light go back and forth through the gain medium. The resonance criteria is that the light interferes constructively, i.e., after one round trip in the cavity the light should have the same phase as before the round trip. This means that a resonant wavelength,  $\lambda$ , fulfills the relation

$$L = q \frac{\lambda}{2n}, \quad (2.1)$$

where  $L$  is the length of the cavity,  $n$  the refractive index in the cavity and  $q$  is a large integer number. To make use of the laser light in exciting applications, part of the laser light can be transmitted through one of the cavity mirrors.

## 2.3 Diode lasers

Diode lasers are nowadays a widely used laser variety. In fact, their world wide commercial sales revenue of \$3,230 millions accounted for 59 % of the total laser market in 2005. Optical-storage and telecommunications segments are dominating and responsible for 54 % and 33 % of the diode laser sales, respectively. The total number of the diode version of a device, that 4 decades ago was “a solution looking for a problem”, sold last year was amazingly 800 millions. The trade journal *Laser Physics World*, that so far yearly has summarized the laser markets [7], provides a source for following future trends.

Laser prices are continuously dropping and are for a high-volume CD-type laser at 780 nm less than \$1 and for 660-nm lasers used in rewritable DVD applications around \$5. Prices for telecommunication lasers range from less than \$50 for Fabry-Pérot devices to \$500 - \$1,000 for more advanced fiber pigtailed distributed-feedback (DFB) lasers [7]. However, diode lasers for spectroscopic applications at non commercial wavelengths can be even more expensive.

This extreme diode laser development was initiated just two years after the invention of the laser. Almost simultaneously in the autumn of 1962, laser action in semiconductor junctions was announced by four different research groups [8–11]. Those diode lasers and all other early diode lasers shared the drawback of being of the so-called homostructure type. This meant that they had high losses and had to be operated in a pulsed mode at cryogenic temperatures in order not to be damaged.

Although already in 1963 a more efficient double-heterostructure scheme was proposed by Kroemer and Alferov independently [12, 13], it took all the time until 1970 before room-temperature operated continuous-wave diode lasers based on this technology were fabricated [14, 15]. An interesting aspect to note is that Kroemer first was refused the resources to develop the technology on the grounds that “this device could not possibly have any applications” [16]. By that, the possibility for all different diode laser applications that continually emerge and drive the diode laser development forward was opened up. Apparently, it was “for great benefit on mankind”, since Herbert Kroemer [16] and Zhores I. Alferov [17] were awarded the Nobel prize in physics in the year 2000.

### 2.3.1 Operating principles of diode lasers

As other lasers, diode lasers need an inverted population, see Section 2.2.2, for the formation of stimulated emission of radiation. The inverted population is located at the junction between semiconductor materials of different types. To understand how this can occur, we might need the small refreshment of the solid-state physics that follows. For further reading, see for instance textbooks like Refs [18, 19].

A semiconductor material is characterized by an electrical resistivity intermediate between that of an electrical conductor and of an insulator. Especially, the resistivity is sensitive to impurities and temperature. In a semiconductor crystal, the outer valence electrons of the atoms are forming covalent bonds with the electrons of neighboring atoms. If all electrons are bound, no electrical current can be transported through the material and the material acts as an insulator. However, the valence electrons can be released and become movable if the thermal energy becomes large enough. If impurities have one extra electron that is not covalently bond to the neighboring atoms, the material is said to be n-doped and movable electrons are available. If, on the other hand, the impurities do not have enough valence electrons, movable electron vacancies called holes occur and the material is of p-type, i.e. p-doped.

It is at the junction of such p-doped and n-doped materials that the active diode laser region is located. If the junction is part of an outer electrical circuit such that the p-doped material is at a high electrical potential and the n-doped material at a low electrical potential, i.e., the junction is forward biased, a current flows from the p-region to the n-region. Holes are moving from the p-region across the junction to the n-region and electrons are moving from the n-region across the junction to the p-region. At the junction, holes and electrons recombine and the energy corresponding to the difference between the energy of the conduction and valance band is emitted as a photon of light. So far, we have described a light emitting diode (LED) of homojunction type.

Except from population inversion, the accomplishment of laser action requires a resonant cavity, as discussed in Section 2.2.2. In fact, the semiconductor crystal itself provides the cavity by the reflectivity caused by the large change in refractive index between the crystal and the surrounding medium. Laser action is obtained when the optical gain exceeds the optical losses for one round trip of the light in the cavity. If the injection current is increased, break-even between gain and loss will, hopefully, eventually occur. This particular current is denoted as the threshold current for laser action.

The problem with homojunctions used in the childhood of the diode lasers was the high loss, which did not permit laser action at realistic currents. Reduced losses were accomplished by the development of the

heterostructure, which provided confinement of charge carriers and light in the active region. In the heterostructure, the active region is surrounded by a semiconductor material of higher bandgap, which forms a potential that confines the charge carriers in the material of lower bandgap as illustrated in Figure 2.4.

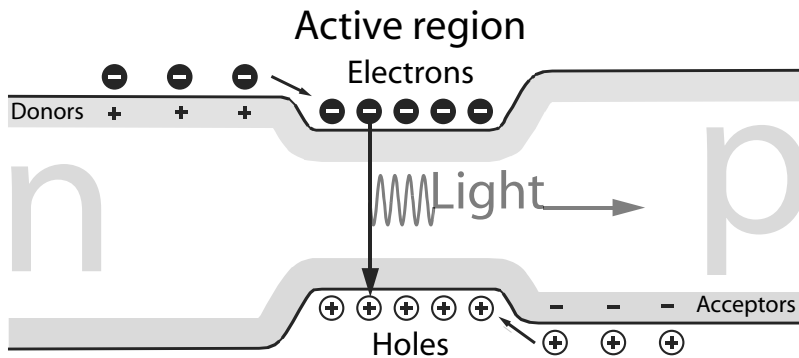


**Figure 2.4.** Laser action in a *pn*-junction of a double-heterostructure, which confines electrons and holes in the active region. Modified from [16].

The lifetime of a diode laser of today can be counted in tens of thousands hours. However, laser diodes are delicate devices that might suddenly be destroyed due to electrostatic discharges or due to high injection currents. Normally, the diodes are operated by an electronic driver that safeguards against fast electrical transients and limits the injection current. Special attention is required if the diode laser is directly modulated at high frequencies without an active injection current limiter. Generally, diode lasers should be handled with care and ebonite clogs at catskin carpets are prohibited.

### 2.3.2 Wavelength tunability

The emitted wavelength in diode lasers is roughly determined by the bandgap of the semiconductor material used. Combinations of semiconductor materials from groups III (Al, Ga, In) and V (N, P, As, Sb) of the periodic table have bandgaps that correspond to visible and near-infrared light.

Diode lasers emitting light in the near-infrared and red region of the spectrum were the first to be commercially available. In fact, the red color has become intimately connected with lasers to such an extent that some flea-market sellers of laser pointers claim that the light has to be red if it is a real laser. However, the wavelength coverage is increasing and in 1996 Shuji Nakamura and collaborators at the Nichia corporation demonstrated III-V nitride-based laser diodes emitting blue light [20,

21]. Today diode lasers emitting violet light at 365 nm are commercially available [22]. By adding aluminium to the gallium nitride the bandgap can be increased, and short ultraviolet radiation down to 200 nm can be achieved - at least in theory [23].

### Wavelength tuning

Since the bandgap is slightly temperature dependent, the temperature can be used to tune the wavelength of the emitted laser light. The tuning rate is typically about  $0.3 \text{ nm}/^\circ\text{C}$ , which means that the emitted wavelength can be changed about 10 nm by a reasonable temperature scan.

The cavity length and the refractive index of the semiconductor material are also changing with temperature. This results in that the resonance frequency of the optical resonator is changing. Unfortunately, the rate of wavelength change is different, typically  $0.06 \text{ nm}/^\circ\text{C}$ , from the corresponding rate for the bandgap change. This leads to mode hops, i.e., the wavelength cannot be continuously scanned across the whole wavelength region offered by the temperature change of the band gap. In fact, a large part of the wavelength range is inaccessible due to this drawback.

However, diode lasers with built-in **d**istributed **f**eedback (DFB) have provided a remedy for mode hopping, but on the expense of an increased device cost and limited tunable span. Enhanced tunability can also be accomplished by placing the diode laser in an external cavity that has some built in wavelength selective device, e.g., a grating that feeds back light into the active medium. A third alternative is offered by the **v**ertical **c**avity **s**urface **e**mitting lasers (VCSELs) that have an extremely short resonance cavity.

For large wavelength scans, see for instance Paper VI, the temperature can be used to change the wavelength. However, this is usually a slow process and most often the wavelength tuning is accomplished by scanning the injection current of the diode laser. This approach was used in Papers V, VII, VIII, IX, X, XI, XII, and XIII utilizing diode lasers.

## 2.4 Nonlinear optical frequency conversion

If we turn up the volume of a loud speaker system, the sound normally sounds equally good as at lower volumes, but just louder. This means that the amplification system has a linear response, i.e., if a signal at one frequency is sent into the system, a signal at the same frequency is sent out of the system. However, it might happen that the sound becomes distorted if the volume is turned up too much. In that case, a nonlinearity in the amplification process is present.

Here, we will deal with the optical analogy of this phenomenon and see how we can take advantage of it for converting light of certain wavelengths into light of other wavelengths. This approach provides an opportunity to generate light at wavelengths where no other light sources are readily available. Only a short introduction is given and for a full theoretical description, see for instance textbooks like Ref. [24]. A broad fun-to-read historical survey of the developments in nonlinear frequency conversion and solid-state lasers is given by Ref. [25].

### 2.4.1 Nonlinear optical media

Electrical dipoles in a material are swinging with the electrical field of the light wave present, and the material becomes polarized. In turn, the oscillating dipoles act as sources of light at the frequency of their oscillations as will be discussed in connection with Rayleigh and Mie scattering in Section 3.2. If the oscillation amplitude of the electrical field is not too high, the dipoles are swinging together at the same frequency and nothing exciting happens. However, if the light is too intense, the oscillating dipoles are not able to follow the oscillation closely and the generated light field becomes distorted and gets other frequency components than the initial.

The polarization  $P$  of a nonlinear optical medium can be expanded in a power series of the electrical field strength,  $E$ , of the optical radiation as

$$P(t) = \epsilon_0 \left( \chi_1 E(t) + \chi_2 E^2(t) + \chi_3 E^3(t) + \dots \right), \quad (2.2)$$

where  $\epsilon_0$  is the permittivity of free space and  $\chi_i$  are the electric susceptibilities. The linear polarization term is dominating and is closely related to the refractive index,  $n$ , of the medium ( $\chi_1 = n^2 - 1$ ) responsible for classical linear optics phenomena. The higher order polarization terms are much weaker, but nevertheless hide a large range of exciting nonlinear optical phenomena of which only a few will be mentioned here.

We will focus on the second-order nonlinear polarization term and especially on how it affects the wavelength of the re-radiated light. Suppose we have an incident optical field composed of two different sharp wavelengths corresponding to two optical frequencies  $\omega_1$  and  $\omega_2$ , respectively, which can be expressed by

$$\begin{aligned} E(t) &= E_1 \cos(\omega_1 t) + E_2 \cos(\omega_2 t) = \\ &= \frac{E_1}{2} \left( \exp(i\omega_1 t) + \exp(-i\omega_1 t) \right) + \frac{E_2}{2} \left( \exp(i\omega_2 t) + \exp(-i\omega_2 t) \right), \end{aligned} \quad (2.3)$$

where the second row is just a reformulation of the first row, to make the following calculations more transparent.

The field  $E(t)$  given in Eq. (2.3) induces a second-order polarization,  $P_2(t)$ , according to,

$$\begin{aligned}
 \frac{P_2(t)}{\epsilon_0 \chi_2} &= E^2(t) \\
 &= \frac{E_1^2}{4} (\exp(i2\omega_1 t) + \exp(-i2\omega_1 t) + 2) \\
 &\quad + \frac{E_2^2}{4} (\exp(i2\omega_2 t) + \exp(-i2\omega_2 t) + 2) \\
 &\quad + \frac{E_1 E_2}{2} (\exp(i(\omega_1 + \omega_2)t) + \exp(-i(\omega_1 + \omega_2)t)) \\
 &\quad + \frac{E_1 E_2}{2} (\exp(i(\omega_1 - \omega_2)t) + \exp(-i(\omega_1 - \omega_2)t)) \\
 &= \underbrace{\frac{E_1^2 + E_2^2}{2}}_{OR} + \underbrace{\frac{E_1^2}{2} \cos(2\omega_1 t)}_{SHG} + \underbrace{\frac{E_2^2}{2} \cos(2\omega_2 t)}_{SHG} \\
 &\quad + \underbrace{E_1 E_2 \cos((\omega_1 + \omega_2)t)}_{SFG} + \underbrace{E_1 E_2 \cos((\omega_1 - \omega_2)t)}_{DFG}, \quad (2.4)
 \end{aligned}$$

where we see that light at all sum and difference frequency combinations of the original frequencies are generated.

When powerful light sources in the form of the newly invented lasers became available in the beginning of the sixties the first observations of nonlinear optical frequency conversion phenomena were made. The observation of second-harmonic generation (SHG) was reported in 1961 [26] followed by the optical rectification (OR) [27] and sum-frequency generation (SFG) [28] by the same research group in 1962. Finally, optical difference-frequency generation (DFG) was reported early in 1963 [29].

### 2.4.2 Phase matching

The frequency conversion process, of all those captured in Eq. (2.4), that dominates in a particular case is determined by a phase matching criterion. As the incident light propagates through a nonlinear crystal, polarization is induced at different locations along the path. If there should be some converted light delivered at the end of the crystal, the light produced at different locations must not interfere destructively. This poses the requirement that the light at the original wavelength has the same phase velocity as the light at the generated wavelength. However, this needs some precautions since most often materials are dispersive, which is manifested by, e.g., the spectral decomposition of white light by prisms, i.e., the refractive index is wavelength dependent.

One way of fulfilling the phase matching criterion is to take advantage of the birefringence present in some crystals, i.e., the refractive index is dependent on the direction of polarization relative to some axes of the crystal. Thus, phase matching can be achieved by adjusting the polarization and the angle of the beam relative to the nonlinear crystal. Another approach is offered by the concept of quasi-phase-matching in which the nonlinearity of the crystal is periodically poled along the direction of light propagation.

### 2.4.3 Optical frequency conversion applications

Radio-frequency mixers are commonly used devices in the telecommunications business. With the introduction of optical communication, there is a need for an optical counterpart, which is offered by nonlinear optical frequency conversion [30]. Nowadays sensing applications in the terahertz spectral range are reported and such radiation can be generated by optical rectification. Sensing applications in the intermediate mid-infrared region using available laser sources in the visible and near-infrared region are also a reality by the help of nonlinear difference-frequency generation [31]. Sum-frequency generation can be used to reach into the other end of the spectrum, i.e., the ultraviolet region. For instance, mercury has been detected at 254 nm by an all-diode-laser based spectrometer utilizing sum-frequency generation [32].

In this thesis, nonlinear frequency conversion was used to achieve light for optical sensing of gases. Difference-frequency generation was used for generating infrared radiation at about 3.4  $\mu\text{m}$  for hydrocarbon measurements in Paper IV. In Papers I, II and III second-harmonic generation was used to achieve light at 254 nm for mercury monitoring. Finally, in Paper V sum-frequency generation of near-infrared light at about 980 nm and blue light at 437 nm was used to produce ultraviolet light at 302 nm for sulfur dioxide detection. These applications are summarized in Figure 2.5.

## 2.5 Optical parametric oscillators

The optical gain by population inversion of lasers have a relatively limited wavelength tunability for a particular laser and in order to reach wavelengths in a broad range several lasers are often needed. Contrary to this, there exist light sources that have such a wide tuning range that the whole spectral range from the ultraviolet to the infrared can be covered by a single device. The light source we are talking about is the **optical parametric oscillator** (OPO), which first was demonstrated in 1965 [33]. Since then, an extensive flora of OPOs based on various nonlinear materials and schemes have been developed [34].

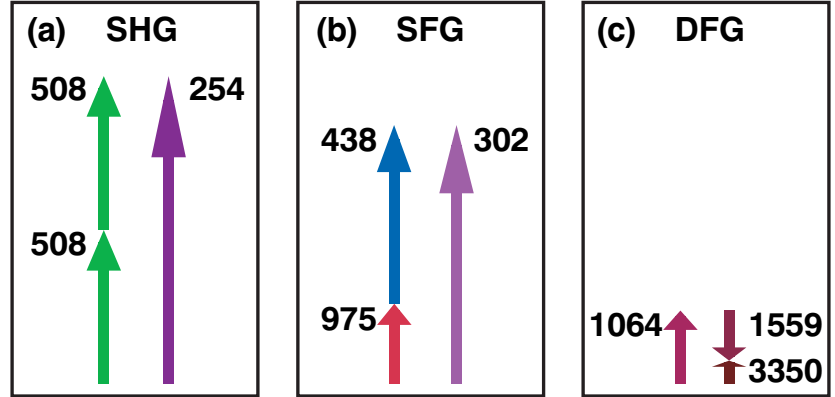


**Figure 2.5.** Some optical frequency conversions used for generation of light at; a) 253.6 nm for mercury monitoring by second-harmonic generation in Paper II, b) 302 nm for sulfur dioxide detection by sum-frequency generation in Paper V, c) 3.4  $\mu\text{m}$  for hydrocarbon measurements by difference-frequency generation in Paper IV.

### 2.5.1 Operating principles of OPO

The gain mechanism in the laser-like light source we are discussing is not population inversion between physical energy levels as for the laser. Rather, it is a nonlinear phenomenon called parametric gain. This concept was utilized in the microwave region in electrical circuits well before the optical counterpart was considered.

We can understand the parametric gain by considering Eq. (2.4). If an intense laser pump beam of frequency  $\omega_p$  is sent into a nonlinear crystal together with a weak signal at frequency  $\omega_s$ , light at the difference frequency  $\omega_i$  might, under appropriate phase matching conditions, be generated. As the formed *idler* light of frequency  $\omega_i$  propagates together with the pump light, more light at the *signal* frequency  $\omega_s$  will be generated at the expense of the pump light. If the pump light is much stronger than the signal and idler light, it can support a considerable gain of the signal and idler light and optical parametric amplification is accomplished.

As we saw in Section 2.2.2 two key components in the laser concept are the gain and the resonator. Similar to this, an OPO is formed by placing the nonlinear parametric gain process, just described, inside an optical cavity resonant with, e.g., the signal light. In the OPO, the signal starts from spontaneous noise and only strong pump light is needed. The next Section briefly describes the OPO implementation used in Papers I, II, III, and IV. For further reading about general aspects of optical parametric oscillators, the reviews presented in Refs [34, 35] are suitable starting points.

## 2.5.2 The implementation used

Here, a brief description of the OPO-based light source used for the remote measurements of mercury and hydrocarbons presented in Papers I, II, III, and IV is given. More details about the system performance can be found in Refs [36, 37].

A pulsed Nd:YAG laser (Spectra Physics GCR-290) emits near-infrared light at 1064 nm, which can be frequency doubled and mixed to supply frequency tripled ultraviolet pump light at 355 nm. The light pulses are delivered 20 times per second and last only a few nanoseconds.

The beam of the 355 nm laser light is sent into an OPO (Spectra Physics MOPO-730), where a smaller part goes into the master oscillator and a larger part into the power oscillator. For a schematic picture of the OPO, see figure 2 of Paper II. The master oscillator is a Littman cavity with a nonlinear  $\beta$ -barium borate (BBO) crystal in which an ultraviolet pump photon is converted to a *signal* photon and an *idler* photon of longer wavelengths.

The crystal angle and the angle of the tuning mirror determine which wavelengths the *signal* and *idler* actually get. For coarse wavelength changes this is adjusted by stepper motors, which provide a relatively slow tuning rate. For faster but smaller wavelength changes piezoelectric adjustment is beneficially used and allows a shot-to-shot shift of up to  $160\text{ cm}^{-1}$ .

The *signal* light generated in the master oscillator propagates into the power oscillator where it interacts with the larger part of the original pump light in order to boost the pulse energy. The generated *signal* is in the wavelength range 440-690 nm whereas the *idler* is in the range 730–1800 nm.

For the mercury measurements, Papers I, II, and III, ultraviolet light of 254 nm was achieved by frequency doubling of the light generated by the OPO, which extends the tuning range all down to 220 nm. In the other end of the spectrum the absorption lines of hydrocarbons could be accessed, see Paper IV, by a difference-frequency generation scheme.

Infrared light in the wavelength range 2600–4300 nm is achieved by difference-frequency generation of the idler light (1370–1800 nm) and the Nd:YAG light (1064 nm) in a nonlinear  $\text{LiNbO}_3$  crystal. The light at the difference frequency is amplified by optical parametric amplification (OPA) in a second  $\text{LiNbO}_3$  crystal pumped by 1064 nm light rendering an output pulse energy of up to 20 mJ [36].



# LIGHT PROPAGATION

---

---

In this chapter the basic principles of light propagation in the presence of absorption and scattering are discussed. We will start by light absorption only and then as the chapter proceeds, first add single scattering, and at the end include multiple scattering.

All Papers of this thesis deal with light absorption by gases under various influences of light scattering. Papers V and VI are solely about light absorption aspects. Papers I, II, III, and IV all rely on the presence of some backscattered light, whereas the regime of heavy multiple scattering is present in Papers VII, VIII, IX, X, XI, XII, and XIII.

## 3.1 Light absorption

Suppose we place an ordinary broad-band incandescent lamp inside a, e.g., blue armature. Then, the part of the white light that propagates through the armature will look blue. This is a manifestation of slowly wavelength dependent absorption with lowest absorption in the blue range of the spectrum.

Similarly, white light that is sent through a cloud of nitrogen dioxide gas will appear brownish. Although light sent through most gases will not have any particular color that can be seen by the naked eye, with the aid of spectroscopic instrumentation with much more specific sensitivity for a particular change, we can resolve the imprint of various gases upon light that has passed by. For instance, watching the sky radiation with a spectrometer will reveal several dark wavelength regions that is due to wavelength selective absorption by various gases. In this Section, we will discuss absorption of light, especially by gases.

### 3.1.1 Optical transitions

The electrons of atoms and molecules can only be arranged in certain well-defined configurations, which can be described by quantum mechanics [38]. Each configuration has an energy associated with it and often the atomic or the molecular system is represented by an energy level diagram that depicts the energy levels of various configurations. The energy structure can in some sense be seen as a staircase, where electrons tend to have as low energy as possible, but not the same as another electron, because they are asocial fermions.

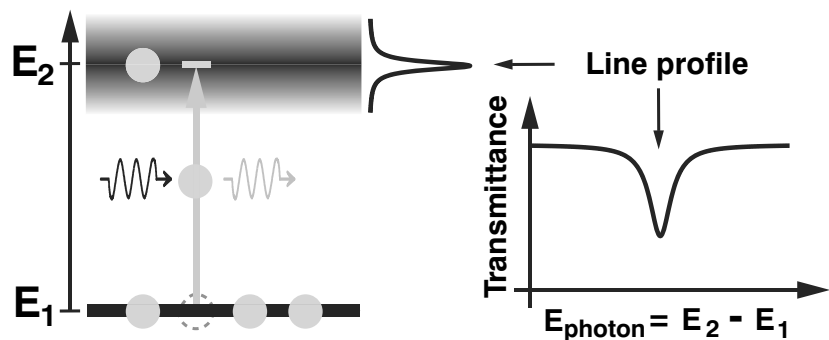


**Figure 3.1.** Absorption of light by an optical transition involving a diffuse energy level gives rise to an absorption line profile.

Let us take a look at two such energy levels with energies  $E_1$  and  $E_2$ , respectively, as seen in Figure 3.1. If the energy of an impinging photon of light fits this energy gap, i.e.,  $E_2 - E_1 = hc/\lambda$ , the photon might be absorbed and the energy of the photon is used to change the configuration from energy  $E_1$  to energy  $E_2$  as already discussed in Section 2.2.2. The energy level structures are different for different substances, which means that the corresponding spectra of wavelengths that are absorbed act as atomic or molecular fingerprints.

### 3.1.2 Line shapes

The absorption does not occur at infinitely sharp wavelengths although we often talk about absorption lines of gases. Rather, the absorption lines are broadened and have finite extension around their central frequency,  $\nu_0$ , of maximum absorption as illustrated in Figure 3.1. This frequency dependent absorption is described by line profiles,  $g(\nu - \nu_0)$ , that describe the relative absorption strength at different frequencies,  $\nu$ . The line broadening is due to several different mechanisms as we will see soon.

### Natural broadening

The minimal linewidth of an absorption transition is fundamentally set by the Heisenberg uncertainty principle due to the finite lifetime of the upper state of the transition. This gives rise to the so-called Lorentzian line shape, which basically is the Fourier transform of an exponential decay. However, in most practical situations the linewidth is much broader than this so-called natural linewidth due to other broadening mechanisms.

### Doppler broadening

When we are approached by, e.g., an ambulance, the frequency of the sirens drops at the moment of passage, i.e., the frequency is higher when the sound source moves towards us than when it moves away from us. This phenomenon is called the Doppler effect of sound. The optical counterpart means that the frequency of light has to be lower for the case when atoms or molecules are moving towards the light source compared to if they are at rest in order to be resonant with a specific transition.

Gaseous atoms and molecules are moving around due to thermal motion, with various velocities given by the Maxwellian velocity distribution [39]. Thus, a sharp absorption line becomes Doppler broadened. This broadening is said to be inhomogeneous since different atoms contribute to different parts of the line shape. From the Maxwellian velocity distribution we can derive the Gaussian Doppler line profile,  $g_D(\nu - \nu_0)$ , according to

$$g_D(\nu - \nu_0) = \frac{1}{\Delta\nu_D} \sqrt{\frac{\ln(2)}{\pi}} \exp\left(-\frac{\ln(2)(\nu - \nu_0)^2}{\Delta\nu_D^2}\right), \quad (3.1)$$

where the width,  $\Delta\nu_D$ , defined as the Half Width at Half the Maximum value of the line profile (HWHM) is given by

$$\Delta\nu_D = \nu_0 \sqrt{\frac{2kT}{Mc^2} \ln(2)} = 1.074 \cdot 10^{11} \frac{1}{\lambda_0} \sqrt{\frac{T}{M}}. \quad (3.2)$$

Here,  $\lambda_0$  is the wavelength [nm] at line center,  $M$  is the molecular mass, and  $T$  is the temperature [K]. In the case of molecular oxygen at 760 nm and room temperature this means that  $\Delta\nu_D \approx 600$  MHz.

### Pressure broadening

The natural line profile due to the finite lifetime of the upper state of the transition is, as previously discussed, Lorentzian. Another mechanism that reduces the effective lifetime is collisions with other atoms or molecules. As the pressure increases, the collision probability increases

and the linewidth becomes larger. Consequently, this broadening is called pressure broadening and results in a Lorentzian line profile,

$$g_L(\nu - \nu_0) = \frac{1}{\pi \Delta\nu_L \left(1 + \left(\frac{\nu - \nu_0}{\Delta\nu_L}\right)^2\right)}, \quad (3.3)$$

with a halfwidth,  $\Delta\nu_L$ , that depends upon pressure according to

$$\Delta\nu_L = \sum_i \gamma_i p_i, \quad (3.4)$$

where  $p_i$  is the partial pressure of the gas species  $i$  and  $\gamma_i$  is the corresponding pressure broadening coefficient.

The pressure-induced linewidth is also temperature dependent according to the following expression

$$\Delta\nu_L(T) = \Delta\nu_L(T_0) \left(\frac{T_0}{T}\right)^n, \quad (3.5)$$

where  $T_0$  is a reference temperature and  $n$  is a coefficient that has different values for different gas transitions. For instance, it assumes the value of 0.70 in the case of molecular oxygen.

### Combined broadening

From what we have discussed so far in this Section, Doppler broadening dominates at low pressure, whereas pressure broadening dominates at high pressure. In the intermediate pressure regime, the contributions from these two mechanisms are of the same order of magnitude and the line profile becomes the convolution between the Lorentzian and the Gaussian line profile. This general Voigt line profile,  $g_V(\nu - \nu_0)$ , is given by

$$\begin{aligned} g_V(\nu - \nu_0) &= \frac{1}{\sqrt{\pi} \Delta\nu'_D} \frac{y}{\pi} \int_{-\infty}^{+\infty} \frac{\exp(-\xi^2)}{y^2 + (x - \xi)^2} d\xi \\ &\equiv \frac{1}{\sqrt{\pi} \Delta\nu'_D} V(x, y) \\ &= \frac{1}{\sqrt{\pi} \Delta\nu'_D} \text{Re}[w(x, y)], \end{aligned} \quad (3.6)$$

where the normalized parameters  $x \equiv (\nu - \nu_0)/\Delta\nu'_D$  and  $y \equiv \Delta\nu_L/\Delta\nu'_D$  are introduced and  $\Delta\nu'_D$  is the Doppler halfwidth at 1/e intensity, i.e.,  $\Delta\nu_D = \sqrt{\ln 2} \Delta\nu'_D$ . The Voigt line profile is in essence the real part of the complex probability function  $w(x, y)$ , and can easily be calculated using an algorithm given by Humlicek [40, 41].

In Figure 3.2 a comparison between the line shapes discussed is given. An experimental recording of the influence of pressure on absorption lines in sulfur dioxide can be found in Figure 3 and 4 of Paper V.

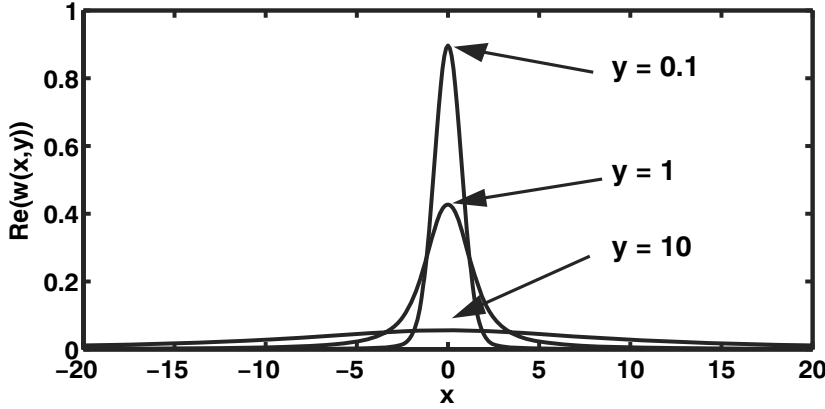


**Figure 3.2.** The complex probability function, Eq. (3.6), is evaluated in different broadening regimes.  $y=0.1$  and  $y=10$  approximately corresponds to a Gaussian and a Lorentzian line profile, respectively.

## Applications

The summary of this Section about line shapes is that the absorption line shape carries information that offers the opportunity of remote non-invasive contact-free assessment of temperature and pressure. For instance, in Paper VII an illustration of pressure assessment by the use of the line shape can be found.

### 3.1.3 Beer-Lambert's law

#### Lambert's law

The Swiss-German natural scientist Johann Heinrich Lambert (1728-1777) found that light of incident intensity  $I_0$  attenuates to  $I(r)$  after passing through an absorbing slab of thickness  $r$  according to what is now known as Lambert's law

$$I(r) = I_0 \exp(-\mu_a r), \quad (3.7)$$

where the linear absorption coefficient  $\mu_a$  [ $\text{m}^{-1}$ ] depends on both the absorbing material and the wavelength of the light. In modern mathematical language we see that Eq. (3.7) is the solution to the simple differential equation

$$\frac{dI(r)}{dr} = -\mu_a I(r), \quad (3.8)$$

which expresses that the amount of light absorbed in an infinitesimal short distance  $dr$  is proportional to the amount of incoming light with an absorption probability per unit path length of  $\mu_a$ .

**Beer's law**

Another German physicist, August Beer (1825-1863), found that  $\mu_a$  in Lambert's law in the case of stain colored solutions is proportional to the concentration  $c$  of the absorbing stain, i.e.,

$$\mu_a = \sigma c, \quad (3.9)$$

where the constant of proportionality is often denoted  $\sigma$  and called the cross-section, although in some cases the constant of proportionality appears as an absorptivity or extinction coefficient. This relation is generally true for a wide range of absorbing systems provided that there is no saturation in the absorption.

**Beer-Lambert's law**

The combination of Eq. (3.7) and Eq. (3.9),

$$I(r) = I_0 \exp(-\sigma(\lambda)cr), \quad (3.10)$$

is naturally called Beer-Lambert's law, although other names exist.

The fraction of the incident light that is transmitted through a distance  $r$  of the absorbing medium is called the transmittance and is given by  $T(r) = I(r)/I_0$ . Correspondingly, the fraction that is absorbed is called the absorption and is given by  $A = 1 - T$ . However, it is often convenient to have an absorption quantity that is linear with the concentration of the absorber. Such a quantity is the absorbance,  $a$ , which can be introduced by

$$A = 1 - \exp(-a). \quad (3.11)$$

**The linear regime**

In cases where the absorption,  $A$ , is small, it is approximately equal to the absorbance,  $a$ , which easily can be seen from a Maclaurin expansion of Eq. (3.11),

$$A = 1 - \exp(-a) = 1 - \left(1 + \frac{1}{1!}(-a) + \frac{1}{2!}(-a)^2 + \dots\right) \cong a, \quad (3.12)$$

as illustrated in Figure 3.3.

**3.2 Light scattering**

Scattering means that the direction of propagation of light is changed in some way. Scattering can be caused by reflection, refraction and diffraction of light from macroscopic borders between regions of different refractive indices. Another origin involves the absorption of light by atoms

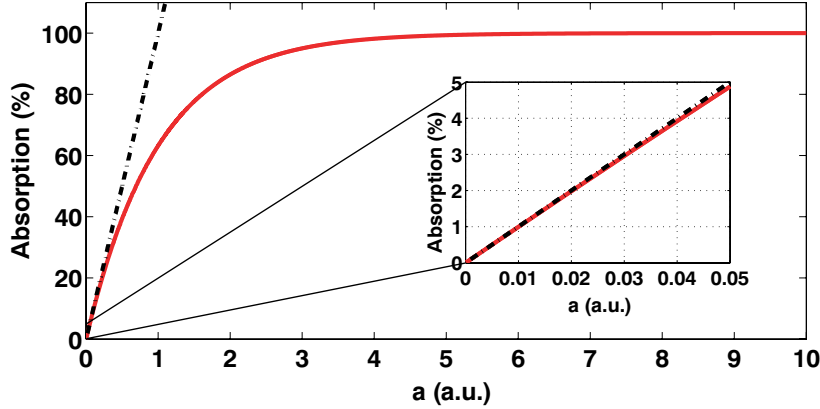


**Figure 3.3.** The absorption as a function of absorbance according to Beer Lambert's law and a linear approximation corresponding to Eq. (3.11) and Eq. (3.12), respectively.

or molecules that after the absorption event re-radiates light in other directions than the direction of the incident light.

Due to scattering, a collimated beam of light will be attenuated similar to the absorption attenuation given by Eq. (3.7), i.e.,

$$I(r) = I_0 \exp(-\mu_s r), \quad (3.13)$$

where the linear scattering coefficient  $\mu_s$  [ $\text{m}^{-1}$ ] expresses the probability per unit path length that light is scattered out of the collimated beam. Note, that this description assumes that the light initially scattered out of the beam will not be scattered back into the beam. However, multiple scattering will be further discussed in Section 3.4.

Scattering of light by particles much smaller than the wavelength is called Rayleigh scattering whereas scattering by particles larger than the wavelength of the light is denoted Mie scattering. Here, only a brief overview will be given. For further reading about single light scattering by small particles see, e.g., Refs [42, 43].

### 3.2.1 Rayleigh and Raman scattering

The mechanism of Rayleigh scattering is that the oscillating electric field of the light wave induces oscillating dipoles in the particles, which act as sources of re-radiated light. The most probable process is that the re-emitted light has the same wavelength as the incident light, which means that the scattering is elastic. The Rayleigh scattering is stronger at shorter wavelengths and has a wavelength dependence in the form of  $\lambda^{-4}$ , which shows its manifestation in the blue color of the sky.

Although much weaker, slightly wavelength shifted inelastic scattering might also occur. This so-called Raman scattering involves the interaction between the incident light and vibrational or rotational energy levels of molecules. The frequency of the incident light is high compared to the small frequency separation between vibrational or rotational levels. Analogous to the process of nonlinear frequency conversion, see Section 2.4.1, light at the sum and difference frequencies are generated. Scattering resulting in re-emitted light of longer wavelength than the wavelength of the incident light is called Stokes. Correspondingly, anti-Stokes is the name for scattering resulting in a wavelength shift towards shorter wavelengths.

### 3.2.2 Mie scattering

Scattering by particles considerably larger than the wavelength is denoted Mie scattering. Although Gustav Mie only considered scattering by homogenous spherical particles in his original work 1908, generalizations to other shapes of scatterers can be made. Typical Mie scatterers for visible light are aerosol particles, cloud droplets and ice particles.

Mie scattering has the property of being stronger for shorter wavelengths in common with Rayleigh scattering. Although the exact strength of this wavelength dependence is related to several factors, such as the wavelength, refractive index mismatch between scatterer and surrounding medium, probability of absorption, particle shape etc in a complicated way, an often useful approximation is  $\sigma(\lambda) \sim \lambda^{-2}$ .

### 3.2.3 Scattering phase function

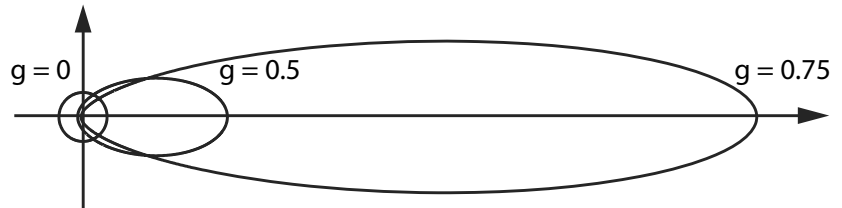


**Figure 3.4.** The Henyey-Greenstein function, Eq. (3.14), evaluated for  $g=0$ ,  $0.5$ , and  $0.75$ .

In a scattering event the direction of propagation of the light is often altered in some way characteristic for the specific scattering process. This angular deviation is described by a scattering phase function,  $P(s, s')$ , that gives the probability of scattering from direction  $s$  to direction  $s'$ . A widely used analytical scattering phase function is the Henyey-Greenstein function [44],

$$P(\cos \theta) = \frac{1 - g^2}{4\pi(1 + g^2 - 2g\cos\theta)^{3/2}}, \quad (3.14)$$

which only depends on one parameter  $g$  describing the asymmetry or anisotropy of the scattering. The parameter  $g$  is defined as the mean value of the cosine of the scattering angle, i.e.,

$$g = \langle \cos \theta \rangle = \frac{1}{2} \int_{-1}^1 P(\cos \theta) \cos \theta d \cos \theta. \quad (3.15)$$

Isotropic scattering is described by a  $g$ -value of zero, whereas  $g$ -values close to 1 describe forward scattering as can be seen in Figure 3.4.

### 3.2.4 Reduced scattering

Even if the scattering is strongly forward-peaked it can be treated as isotropic if we study the scattering process on another length scale. Such a re-scaling is captured in the concept of the reduced scattering coefficient,

$$\mu'_s = (1 - g)\mu_s. \quad (3.16)$$

The meaning of the reduced scattering coefficient is illustrated in Figure 3.5.

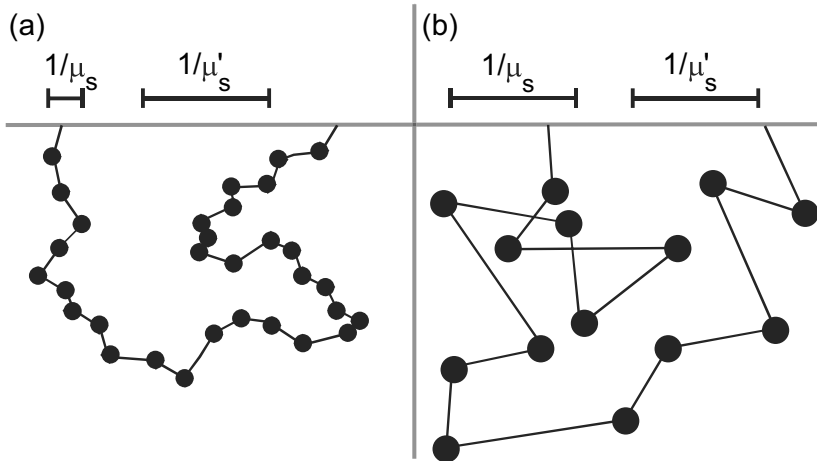


**Figure 3.5.** Although a) depicts a forward scattering process and b) an isotropic scattering process, both processes can be considered isotropic on a length scale defined by the reduced scattering coefficient, which is the same in both cases. Modified from [45].

### 3.3 Light absorption and scattering

#### 3.3.1 Spatial dependent attenuation

Absorption and scattering both lead to attenuation of a collimated beam that is sent through a scattering or absorbing medium as was expressed by Eq. (3.7) and Eq. (3.13), respectively. The obvious generalization of Lambert's law for the case of spatially dependent simultaneous absorption and scattering is,

$$I_T(\lambda, r) = I_0 \exp\left(-\int_0^r (\mu_a(\lambda, s) + \mu_s(\lambda, s)) ds\right), \quad (3.17)$$

where the absorption coefficient,  $\mu_a$ , in the general case is due to the absorption of a mixture of absorbing species  $i$ , i.e.,

$$\mu_a(\lambda, s) = \sum_i \sigma_i^A(\lambda) c_i(s). \quad (3.18)$$

The scattering coefficient,

$$\mu_s(\lambda, s) = \sigma_m^S(\lambda) c_m(s) + \int_0^\infty \sigma_a^S(\lambda, x) c_a(s, x) dx, \quad (3.19)$$

contains contributions from molecular Rayleigh scattering as well as the integrated contribution of Mie scattering from a size distribution of scatterers.

#### 3.3.2 Range-resolved absorption

So far, we have been dealing with the transmitted part of a collimated beam after propagating a distance  $r$  in a scattering and absorbing medium. However, in a scattering event a distance  $r$  from the light source there might be some probability for the light to be scattered within an angle element close to the opposite direction of the initial direction of propagation.

The backscattered light will as it propagates back be attenuated in the same way as prior to the scattering event and in addition be spread out over an area proportional to the square of the distance traveled. Thus, the backscattered light detected at a position near the light source is given by

$$I_R(\lambda, r) = I_0(\lambda) \frac{c_b(r) \sigma_b(\lambda) \Delta r}{r^2} \exp\left(-2 \int_0^r (\mu_a(\lambda, s) + \mu_s(\lambda, s)) ds\right), \quad (3.20)$$

where the probability of backscattering within a short range  $\Delta r$  at  $r$  is dependent on the cross-section for backscattering,  $\sigma_b(\lambda)$ , and the concentration of scatterer,  $c_b(r)$ , i.e., the probability is  $c_b(r) \sigma_b(\lambda) \Delta r$ .

A special laser spectroscopic technique that deals with the assessment of spatial distributions of for instance gases in the atmosphere is the light detection and ranging technique (lidar) that has been utilized in Papers I, II, III, and IV and is further presented in Section 4.2.

### 3.3.3 Differential absorption

In the various forms of Beer-Lambert's law presented above, the detected amount of light compared to the initial amount of light prior to passage of a scattering and absorbing medium has been treated. However, it is often difficult to measure the incident amount of light.

In this context, it is beneficial to note that the cross-section for scattering in the atmosphere as well as in for instance porous materials has a slow wavelength dependence. This property is shared also with the cross-section for absorption by solid and liquid materials. In sharp contrast to this, free atomic and molecular gases have sharp energy levels and thus absorption features of very narrow wavelength width, which can be summarized in,

$$\mu_{total} = \mu_s^{broad} + \mu_a^{broad} + \mu_a^{narrow}. \quad (3.21)$$

This separation of the total attenuation coefficient used in the Beer-Lambert law-like Eq. (3.17) gives

$$I_T(\lambda, r) = I_0^{broad}(\lambda) \exp\left(-\int_0^r \mu_a^{narrow}(\lambda, s) ds\right), \quad (3.22)$$

where all slowly wavelength dependent factors have been lumped together in

$$I_0^{broad}(\lambda) = I_0 \exp\left(-\int_0^r (\mu_s^{broad}(\lambda, s) + \mu_a^{broad}(\lambda, s)) ds\right). \quad (3.23)$$

This representation highlights the fact that the absorbance due to a narrow absorption feature can be determined without the knowledge of the incident amount of light. If the light is detected at a wavelength  $\lambda_{off}$  just outside a narrow absorption line, the  $\mu_a^{narrow}$  is zero meaning that  $I_0^{broad}$  is measured. Since the wavelength dependence of  $I_0^{broad}$  is slow, the measured value is practically the same as within the nearby gaseous absorption feature. Thus, the differential absorbance profile due to the gas of interest can be calculated as:

$$a(\lambda, r) = -\ln \frac{I_T(\lambda, r)}{I_T(\lambda_{off}, r)}. \quad (3.24)$$

The concept of differential absorption is used in various forms in all Papers included in this thesis.

## 3.4 Light transport in multiple scattering media

So far, we have considered single scattering out of a collimated beam with basically no probability for the light to be scattered back into the original direction of propagation. However, during certain atmospheric conditions such as fog, heavy plumes and clouds, multiple scattering does occur. Light propagating in porous materials, living tissue or similar scattering media is also subject to heavy multiple scattering, which will be treated in this Section.

### 3.4.1 Radiative-transport theory

From simple conservation principles, we can often in physics derive a partial differential equation that describes the problem at hand. One fundamental quantity that is conserved is energy or some quantity related to energy. Here we will make use of a quantity denoted radiance,  $L$ , which is the radiant energy per unit time and unit solid angle that flows in a certain direction  $\mathbf{s}$  through a unit area perpendicular to  $\mathbf{s}$ , i.e.,  $L$  has the unit of  $[\text{W}/(\text{m}^2\text{sr})]$ .

Considering the conservation of energy expressed as radiance, we note that in a small volume there are several contributions to the change of the radiance. One contribution is due to the difference between inflow and outflow of radiance over the borders of the volume. The radiance can be changed due to absorption within the volume or scattering out of the propagation direction within the volume. Furthermore, there is the possibility that light propagating in another direction is scattered into the direction treated. Finally, there can be a source inside the volume. If we set up this balance and let the volume be infinitesimally small, we obtain the radiative transport equation,

$$\begin{aligned} \frac{1}{c} \frac{\partial}{\partial t} L(\mathbf{r}, \mathbf{s}, t) = & \underbrace{-\mathbf{s} \cdot \nabla L(\mathbf{r}, \mathbf{s}, t)}_{\text{Influx}} - \underbrace{\mu_a L(\mathbf{r}, \mathbf{s}, t)}_{\text{Absorption}} - \underbrace{\mu_s L(\mathbf{r}, \mathbf{s}, t)}_{\text{Scattering-out}} \\ & + \underbrace{\mu_s \int_{4\pi} L(\mathbf{r}, \mathbf{s}', t) p(\mathbf{s}, \mathbf{s}') d\Omega'}_{\text{Scattering-in}} + \underbrace{S(\mathbf{r}, \mathbf{s}, t)}_{\text{Source}}, \quad (3.25) \end{aligned}$$

where the time derivative of the radiance (left side) is the sum of the net influx due to the spatial gradient, the negative contribution from radiance absorbed or scattered out of direction  $\mathbf{s}$ , radiance of another direction  $\mathbf{s}'$  scattered into  $\mathbf{s}$  with a probability given by the phase function  $p(\mathbf{s}, \mathbf{s}')$ , and, finally, the production of radiance by a local light source.

### 3.4.2 The diffusion approximation

The general transport equation, Eq. (3.25), most often becomes difficult to solve analytically. However, physics is in a sense the art of approximations and therefore we make an approximation in this case too. If the light is multiply scattered, there is basically no preferred direction of propagation and it can be anticipated that a good approximation could be obtained by expanding the radiance in spherical harmonics,

$$\begin{aligned} L(\mathbf{r}, \mathbf{s}, t) &= \sum_{l=0}^{\infty} \sum_{m=-l}^l \sqrt{\frac{2l+1}{4\pi}} L_{lm}(\mathbf{r}, t) Y_{lm}(\mathbf{s}) \\ &\approx \frac{1}{4\pi} \phi(\mathbf{r}, t) + \frac{3}{4\pi} \mathbf{F}(\mathbf{r}, t) \cdot \mathbf{s}, \end{aligned} \quad (3.26)$$

where the radiance is described by one isotropic term,  $\phi$ , and one term,  $\mathbf{F}$ , describing the angular dependence of the radiance, with higher terms neglected.

The radiant energy fluence rate  $\phi$  [W/m<sup>2</sup>] [46] is the integral of the radiance over all angles at a point  $\mathbf{r}$  at time  $t$ , i.e.,

$$\phi(\mathbf{r}, t) = \int_{4\pi} L(\mathbf{r}, \mathbf{s}, t) d\Omega, \quad (3.27)$$

and the radiant flux vector  $\mathbf{F}(\mathbf{r}, t)$  [W/m<sup>2</sup>] [46], i.e. the flow of the power per unit area, is introduced as,

$$\mathbf{F}(\mathbf{r}, t) = \int_{4\pi} L(\mathbf{r}, \mathbf{s}, t) \mathbf{s} d\Omega. \quad (3.28)$$

Within this so-called diffusion approximation of the radiative-transport equation, the Fick law of diffusion,

$$\mathbf{F} = -D\nabla\phi, \quad (3.29)$$

is applicable. Here,  $D$  is the diffusion coefficient defined as [47],

$$D = \frac{1}{3(\mu_a + (1-g)\mu_s)} \quad (3.30)$$

Thus, the radiative transport equation, Eq. (3.25), simplifies to the more manageable lossy diffusion equation for the photon fluence rate [47],

$$\frac{1}{c} \frac{\partial}{\partial t} \phi(\mathbf{r}, t) = D\nabla^2 \phi(\mathbf{r}, t) - \mu_a \phi(\mathbf{r}, t) + S(\mathbf{r}, t). \quad (3.31)$$

### 3.4.3 Time-dependent solutions

Here, some solutions to the time-dependent diffusion equation for light transport in scattering media, Eq. (3.31), are presented.

#### Infinite medium

We start by the generic solution for an isotropic point source in an infinite medium, which gives the Green function for free light diffusion [47],

$$\phi(\mathbf{r}, t) = c(4\pi Dct)^{-3/2} \exp\left(-\mu_a ct - \frac{\mathbf{r}^2}{4Dct}\right). \quad (3.32)$$

#### Boundary conditions

Most often the scattering media studied have finite extension and at the boundary there are some conditions that have to be fulfilled. A boundary condition often used is to let the fluence rate be zero at the boundary or at an extrapolated boundary a small distance,  $z_{eb}$ , outside the physical boundary [48].

#### Infinite half space

In reflection measurements, the medium probed can often be approximated as a half space, e.g. infinite extension in the x and y directions and extending from a boundary at  $z = 0$  to infinity. If a light beam enters such a medium, the incident light can be modeled as an isotropic point source at a depth  $z = z_0$  corresponding to one mean free path for isotropic scattering, i.e.,

$$z_0 \equiv \frac{1}{\mu'_s} = \frac{1}{(1-g)\mu_s}, \quad (3.33)$$

where  $\mu'_s$  is the reduced scattering coefficient discussed in Section 3.2.4.

This problem can be solved by making use of the solution for an isotropic point sources in an infinite medium, Eq. (3.32). The secret is to reflect the point source in the boundary or the extrapolated boundary in order to fulfill the boundary conditions. By introducing a negative isotropic point source at  $z = -2z_{eb} - z_0$  and sum this contribution to the contribution of the positive source at  $z = z_0$  the boundary condition of zero fluence rate is fulfilled. Thus, the fluence rate in the half space discussed can be expressed as [47]:

$$\begin{aligned} \phi(\rho, z, t) = & c(4\pi Dct)^{-3/2} \exp(-\mu_a ct) \\ & \left\{ \exp\left(-\frac{(z - z_0)^2 + \rho^2}{4Dct}\right) - \exp\left(-\frac{(z + 2z_{eb} + z_0)^2 + \rho^2}{4Dct}\right) \right\}. \end{aligned} \quad (3.34)$$

### Diffuse reflectance

Most often it is convenient to measure the diffusely transmitted or reflected light at the boundary. This diffuse remittance is basically the output flux [47], which can be found by using Fick's law for light diffusion, Eq. (3.29). Thus, for the half space discussed, we can express the diffuse reflectance as

$$\begin{aligned}
 R(\rho, t) = D \frac{\partial \phi}{\partial z} \Big|_{z=0} &= \frac{1}{2} (4\pi Dc)^{-3/2} t^{-5/2} \exp(-\mu_a ct) \exp\left(-\frac{\rho^2}{4Dct}\right) \\
 &\times \left\{ z_0 \exp\left(-\frac{z_0^2}{4Dct}\right) + (2z_{eb} + z_0) \exp\left(-\frac{(2z_{eb} + z_0)^2}{4Dct}\right) \right\}.
 \end{aligned}
 \tag{3.35}$$

### Infinite slab

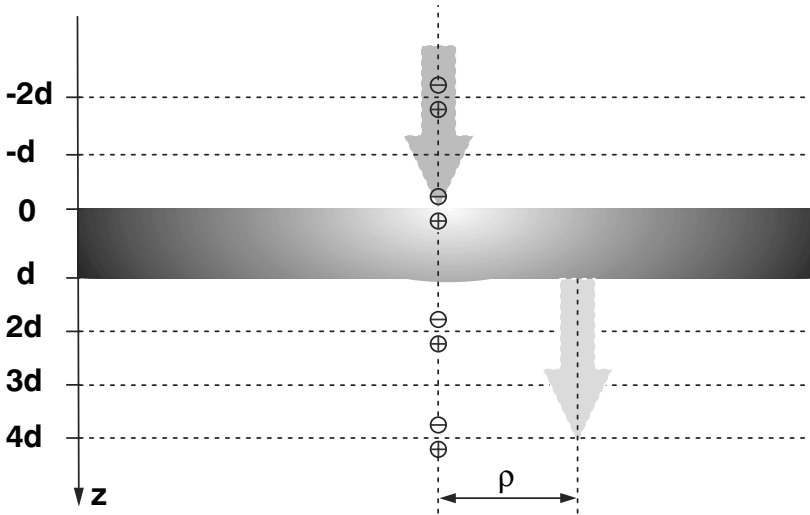


**Figure 3.6.** A schematic view of image sources. The detailed locations of the positive and negative sources are determined by Eq. (3.36) and Eq. (3.37), respectively.

If we would like to measure light transmitted through a scattering medium, a slightly more complicated geometry than the infinite half space is needed. An appropriate model is provided by a slab of thickness  $d$  in the  $z$  direction and infinite extensions in the  $x$  and  $y$  directions, which presents an additional boundary at  $z = d$ . The first pair of sources that was introduced for the infinite half space are now mirrored in this new boundary. In turn, this new pair of mirrored sources are mirrored in the

first boundary at  $z = 0$  and so on, as illustrated in Figure 3.6, where the positive and negative sources, respectively, have the  $z$ -coordinates

$$z_{kp} = 2k(d + 2z_{eb}) + z_0 \quad (3.36)$$

and

$$z_{kn} = 2k(d + 2z_{eb}) - 2z_{eb} - z_0, \quad (3.37)$$

where  $k = \dots, -3, -2, -1, 0, 1, 2, 3, \dots$

The fluence rate in slab geometry, thus, can be expressed as

$$\begin{aligned} \phi(\rho, z, t) &= (4\pi Dct)^{-3/2} \exp(-\mu_a ct) \exp\left(-\frac{\rho^2}{4Dct}\right) \\ &\times \sum_{k=-\infty}^{\infty} \left\{ \exp\left(-\frac{(z - z_{kp})^2}{4Dct}\right) - \exp\left(-\frac{(z - z_{kn})^2}{4Dct}\right) \right\}. \end{aligned} \quad (3.38)$$

### Diffuse remittance from an infinite slab

Following the same procedures as for the infinite half space, we obtain the diffuse reflectance from an infinite slab according to

$$\begin{aligned} R(\rho, t) &= D \frac{\partial \phi}{\partial z} \Big|_{z=0} = \frac{1}{2} (4\pi Dc)^{-3/2} t^{-5/2} \exp(-\mu_a ct) \exp\left(-\frac{\rho^2}{4Dct}\right) \\ &\times \sum_{k=-\infty}^{\infty} \left\{ z_{kp} \exp\left(-\frac{z_{kp}^2}{4Dct}\right) - z_{kn} \exp\left(-\frac{z_{kn}^2}{4Dct}\right) \right\}. \end{aligned} \quad (3.39)$$

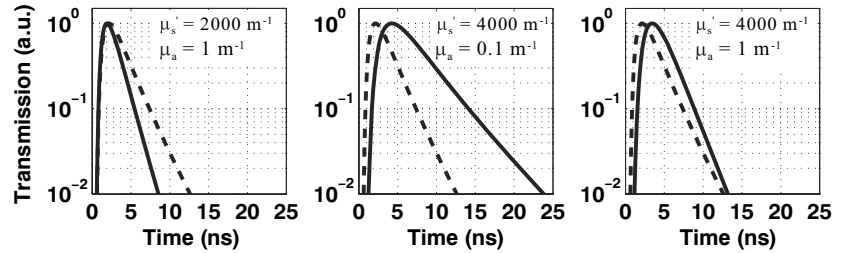


**Figure 3.7.** Time dispersion curves for transmission in a multiple scattering slab according to Eq. (3.40) are displayed for three combinations of scattering and absorption coefficients. Each curve is compared with a dashed curve corresponding to  $\mu'_s = 2000 \text{ m}^{-1}$  and  $\mu_a = 0.1 \text{ m}^{-1}$ .

The transmittance is described by a similar expression,

$$T(\rho, t) = -D \frac{\partial \phi}{\partial z} \Big|_{z=d} = \frac{1}{2} (4\pi Dc)^{-3/2} t^{-5/2} \exp(-\mu_a ct) \exp\left(-\frac{\rho^2}{4Dct}\right) \times \sum_{k=-\infty}^{\infty} \left\{ (d - z_{kp}) \exp\left(-\frac{(d - z_{kp})^2}{4Dct}\right) - (d - z_{kn}) \exp\left(-\frac{(d - z_{kn})^2}{4Dct}\right) \right\}. \quad (3.40)$$

In Figure 3.7 the influence of scattering and absorption on the temporally resolved transmission in a heavily scattering slab calculated by Eq. (3.40) is given. Similar experimental recordings can be found in, e.g. Paper VIII.

### 3.4.4 Steady-state solutions

For continuous wave applications, the steady-state form of the diffusion equation Eq. (3.31),

$$0 = D\nabla^2 \phi(\mathbf{r}) - \mu_a \phi(\mathbf{r}) + S(\mathbf{r}), \quad (3.41)$$

is of interest. Similar to the time-dependent case, the solutions in simple geometries can be found by the use of the relevant Green's function for infinite space together with appropriately placed mirror sources to fulfill the boundary conditions.

#### Infinite medium

The Green function for steady-state diffusion of light from an isotropic point source in infinite space is given by [49]

$$\phi(\mathbf{r}) = \frac{1}{4\pi D} \frac{\exp(-\mu_{eff} r)}{r}, \quad (3.42)$$

where the solution depends on only one single effective attenuation coefficient,

$$\mu_{eff} = \sqrt{3\mu_a(\mu_a + \mu'_s)} = \sqrt{\frac{\mu_a}{D}}, \quad (3.43)$$

that entangles the scattering and absorption coefficients.

#### Infinite slab

Following the procedure outlined for the time-dependent solution, we can solve the corresponding steady-state problems. An entering light beam is still represented by an isotropic point source at the depth of one mean free path for isotropic scattering,  $z = z_0$ . The fluence in a scattering slab

of thickness  $d$  in the  $z$ -direction and infinite extensions in the  $x$  and  $y$  directions can thus be expressed as

$$\phi(\rho, z) = \frac{1}{4\pi D} \sum_{k=-\infty}^{\infty} \left( \frac{\exp(-\mu_{eff} r_{kp}(\rho, z))}{r_{kp}(\rho, z)} - \frac{\exp(-\mu_{eff} r_{kn}(\rho, z))}{r_{kn}(\rho, z)} \right), \quad (3.44)$$

where

$$r_{kp}(\rho, z) = \sqrt{(z - z_{kp})^2 + \rho^2} \quad (3.45)$$

and

$$r_{kn}(\rho, z) = \sqrt{(z - z_{kn})^2 + \rho^2} \quad (3.46)$$

are the distances from the point of interest,  $(\rho, z)$ , to the positive and negative sources placed at  $\rho = 0$  at

$$z_{kp} = 2k(d + 2z_{eb}) + z_0 \quad (3.47)$$

and

$$z_{kn} = 2k(d + 2z_{eb}) - 2z_{eb} - z_0, \quad (3.48)$$

respectively.

The solution for the infinite half space is obtained by retaining only the sources placed in  $z = z_{0p}$  and  $z = z_{0n}$ .

### Diffuse remittance from an infinite slab

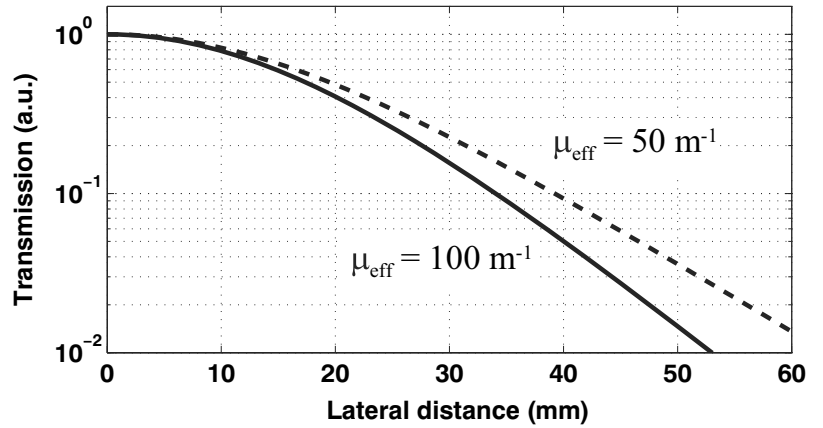


**Figure 3.8.** The influence of the effective attenuation coefficient upon the spatial dependence of the steady-state transmission in a multiple scattering slab calculated by Eq. (3.50).

As in the time-dependent case, the reflectance is found by the use of Fick's law for light diffusion, Eq. (3.29). Following that procedure, we obtain the reflection,

$$\begin{aligned}
 R(\rho) &= D \frac{\partial \phi}{\partial z} \Big|_{z=0} = \\
 &= + \frac{1}{4\pi} \sum_{k=-\infty}^{\infty} z_{kp} \left( 1 + \mu_{eff} r_{kp}(\rho, 0) \right) \frac{\exp(-\mu_{eff} r_{kp}(\rho, 0))}{r_{kp}^3(\rho, 0)} \\
 &\quad - \frac{1}{4\pi} \sum_{k=-\infty}^{\infty} z_{kn} \left( 1 + \mu_{eff} r_{kn}(\rho, 0) \right) \frac{\exp(-\mu_{eff} r_{kn}(\rho, 0))}{r_{kn}^3(\rho, 0)}.
 \end{aligned} \tag{3.49}$$

Correspondingly, the transmittance is described by a similar expression,

$$\begin{aligned}
 T(\rho) &= -D \frac{\partial \phi}{\partial z} \Big|_{z=d} = \\
 &= + \frac{1}{4\pi} \sum_{k=-\infty}^{\infty} (d - z_{kp}) \left( 1 + \mu_{eff} r_{kp}(\rho, d) \right) \frac{\exp(-\mu_{eff} r_{kp}(\rho, d))}{r_{kp}^3(\rho, d)} \\
 &\quad - \frac{1}{4\pi} \sum_{k=-\infty}^{\infty} (d - z_{kn}) \left( 1 + \mu_{eff} r_{kn}(\rho, d) \right) \frac{\exp(-\mu_{eff} r_{kn}(\rho, d))}{r_{kn}^3(\rho, d)}.
 \end{aligned} \tag{3.50}$$

In Figure 3.8 the influence of scattering and absorption on the spatially resolved steady-state transmission in a heavily scattering slab, as calculated with Eq. (3.50), is given. Similar experimental recordings can be found in, e.g., Paper VIII.

### 3.4.5 Absorption path length

If the differential absorption coefficient, see Section 3.3.3, is small, the differential absorbance from a multiply scattering sample is the product of the path length traveled and the absorption coefficient. For an experimental elucidation of this, see for instance Paper VIII.

Generally, the mean time of flight for diffusely remitted light is given by

$$\langle t \rangle(\xi) = \frac{\int_0^{\infty} t \Gamma(\xi, t) dt}{\int_0^{\infty} \Gamma(\xi, t) dt}, \tag{3.51}$$

where  $\xi$  is a point on the boundary of the scattering sample and  $\Gamma$  is the remittance, e.g., transmittance or reflectance.

The mean traveled distance for light transmitted through a scattering slab is given by

$$\langle ct \rangle = \frac{\sum_{k=-\infty}^{+\infty} \left\{ (d - z_{kp}) \frac{\exp(-\mu_{eff} r_{kp}(\rho, d))}{r_{kp}(\rho, d)} - (d - z_{kn}) \frac{\exp(-\mu_{eff} r_{kn}(\rho, d))}{r_{kn}(\rho, d)} \right\}}{8\pi DT(\rho)}, \quad (3.52)$$

where  $T$  is given by Eq. (3.50).

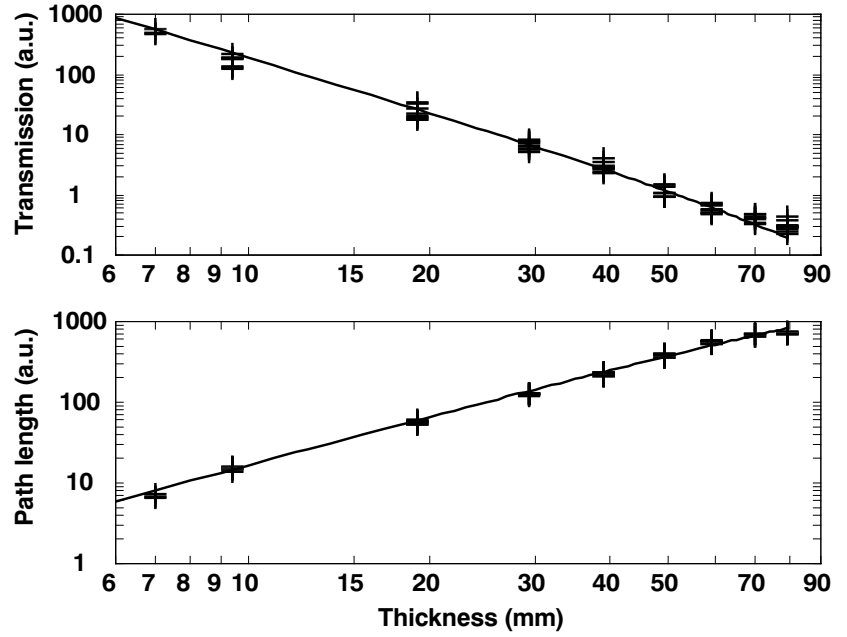


**Figure 3.9.** The thickness dependence of the absorption path length and the transmitted amount of light in slabs of white polystyrene foam is presented in the upper and lower part of the figure, respectively. Experimental data obtained by continuous wave tunable diode laser spectroscopy are given together analytical curves based on Eq. (3.52) and Eq. (3.50) for the path length and the transmission, respectively.

In the limit of small absorption, the mean time of flight is proportional to the square of the slab thickness  $d$ ,

$$\langle t \rangle \propto d^2, \quad (3.53)$$

whereas the transmitted amount of light is inversely proportional to the cube of the slab thickness,

$$T \propto \frac{1}{d^3}. \quad (3.54)$$

The experimentally obtained thickness dependence of the absorption path length and the transmitted amount of light in slabs of white polystyrene foam are given in Figure 3.9. Further information about the experimental techniques used are provided in Section 4 and Paper VIII. A collection of solutions to the diffusion equation of light for various simple geometries, including expressions for the mean time of flight, is compiled in Ref. [50].



# SPECTROSCOPIC TECHNIQUES

---

---

Optical spectroscopy has long traditions. Since this thesis work was accomplished at Lund University, we recognize the well-known Johannes (Janne) Robert Rydberg [51], who more than 100 years ago analyzed emission spectra of hydrogen and other simple atoms and found a theoretical description of the spectra that is still applicable. This thesis focuses on optical absorption spectroscopic techniques, which for a long time were based on broad-band light sources combined with wavelength selective detection schemes, e.g. gratings or prisms. However, the invention of the laser offered the opportunity to use non-wavelength selective detection systems. Instead, the wavelength selectivity is on the source side in the form of tunable narrow-band light.

In this Chapter we will make use of the tunable narrow-band light sources introduced in Chapter 2 and apply these sources for spectroscopic analysis of atmospheric gases under various influences of scattering. The techniques presented rely on the framework of light-matter interactions outlined in Chapter 3. The focus of the presentation in this Chapter is on the laser-based spectroscopic techniques applied in the Papers accompanying this thesis. For a comprehensive survey on most aspects of spectroscopic techniques see, e.g., Ref. [39].

## 4.1 Tunable diode laser spectroscopy

As we saw in Section 2.3.2, diode lasers can be easily wavelength tuned by changing the injection current or the temperature. This forms the basis for tunable diode laser spectroscopy, which this Section treats. The International Conference on Tunable Diode Laser Spectroscopy (TDLS) devoted to this field has been held biannually [52] five times and attracts an increasing number of researchers. Proceedings are published as special

issues in *Spectrochimica Acta: Part A*, and give glimpses of the ongoing activities within this research field.

The current trends are towards the exploration of the infrared region by the relatively recently introduced quantum cascade lasers. Schemes for lowering the detection limits of various gases are a constant theme in this field of research. Obviously, there are two ways of increasing the signal-to-noise ratio (SNR). Either the signal can be increased or the noise decreased. The absorption signal can be increased by choosing a stronger transition of the atoms or molecules of interest, longer absorption path length, higher gas concentration or by increasing the amount of detected light. In practice, the concentration and path length is often determined by the non-ideal sample under investigation. Further, the light source emits a limited amount of light and the transition strengths of the gas species are quite often low, which means that there is a demand for low levels of noise in order to obtain an acceptable signal-to-noise ratio.

#### 4.1.1 Modulation techniques

The observation that noise is lower at higher frequencies has led to the popularity of a number of modulation techniques that all share the property of shifting the detection band to higher frequencies. Already Moses performed wavelength modulation spectroscopy together with Tang [53]. Since then, a number of different modulation schemes have emerged [54–56]. At the Atomic Physics Division in Lund there is also a tradition in using various modulation techniques in combination with diode lasers [57–60]. Generally, the modulation techniques can increase the detection sensitivity several orders of magnitude compared to direct absorption.

#### 4.1.2 Phase modulation

Diode lasers are particularly convenient to use when performing modulation spectroscopy since the emitted wavelength can easily be modulated by varying the injection current of the diode laser as we discussed in Section 2.3.2. If the injection current is sinusoidally modulated at a frequency  $\nu_m$ , the modulated optical field  $E(t)$  with carrier frequency  $\nu_0$  emitted can generally, neglecting amplitude modulation, be expressed as [61]

$$\begin{aligned} E(t) &= E_0 \exp\left(i(2\pi\nu_0 t + \beta \sin(2\pi\nu_m t))\right) \\ &= E_0 \exp\left(i2\pi\nu_0 t\right) \sum_{-\infty}^{+\infty} J_n(\beta) \exp\left(in2\pi\nu_m t\right), \end{aligned} \quad (4.1)$$

where  $\beta$  is the frequency modulation index and the optical field has been expanded into a series of  $n$ th-order Bessel functions  $J_n(\beta)$ .

By examining the Bessel functions  $J_n(\beta)$ , we realize that higher side bands at frequencies  $\nu_n = \nu_0 + n\nu_m$  become more significant if the modulation index  $\beta$  is increased. Further, the spacing between the side bands obviously increases with the modulation frequency  $\nu_m$ .

The effect of the gas sample under investigation on each frequency component of the optical field, Eq. (4.1), can be characterized by a complex transmission function  $T(\nu_n)$ , where  $\nu_n = \nu_0 + n\nu_m$ . Thus, the resulting transmitted optical field is given by

$$E_T(t) = E_0 \exp(i2\pi\nu_0 t) \sum_{-\infty}^{+\infty} T(\nu_n) J_n(\beta) \exp(in2\pi\nu_m t). \quad (4.2)$$

The detector does not record the electrical field but rather the intensity, which is proportional to  $|E_T(t)|^2$  that varies in time due to the differential absorption. By the use of a phase-sensitive detector, e.g., a lock-in amplifier or a radio frequency mixer, it is possible to detect a Fourier component of the transmitted intensity at a multiple of the modulation frequency  $\nu_m$ . This component can, theoretically, be calculated by taking the square of Eq. (4.2) and only retaining the terms that vary in time with the desired harmonic of the modulation frequency.

By this, we have a general description of the modulation spectroscopy. However, the general modulation formulas obtained often become very complex to handle [57], and different approximations are normally made [61]. Depending on the value of the ratio between the modulation frequency and the half width of the absorption feature, different approximations can be made and, correspondingly, different names have been given to the general modulation technique. Techniques using modulation frequencies much smaller than the width of the absorption feature are normally denoted **wavelength modulation spectroscopy** (WMS) [53]. On the other hand, techniques using modulation frequencies larger than or comparable to the width of the absorption feature are normally called **frequency modulation spectroscopy** (FMS) [55].

### 4.1.3 Wavelength modulation

In Papers VII, VIII, IX, X, XI, XII, and XIII a modulation frequency in the kHz range was applied for sensitive detection of gas absorption features having spectral widths in the GHz range. Thus, the modulation techniques used are classified as wavelength modulation spectroscopy (WMS). In this Section we will discuss why the WMS signals present in the Papers mentioned have their characteristic appearance.

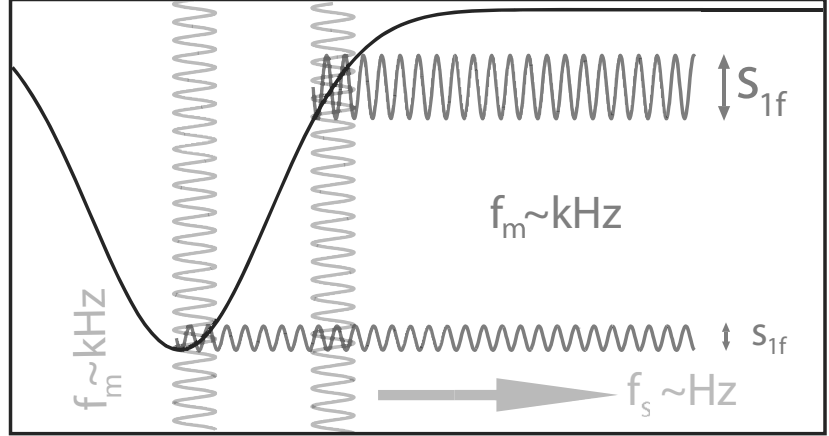


**Figure 4.1.** An intuitive schematic illustration of  $1f$  wavelength modulation spectroscopy signal generation. Rapidly wavelength modulated light is slowly tuned through an absorption profile resulting in a signal at the modulation frequency with an amplitude that is dependent on the derivative of the profile.

### Derivative spectroscopy

The general approach presented above becomes complicated in the case of WMS since there is a large number of sidebands separated by the modulation frequency only. Instead, WMS is preferably described by an intensity based model, where the closely spaced discrete sidebands instead are seen as a wavelength continuum.

We start the description by introducing the momentary frequency,

$$\nu_i \equiv \frac{1}{2\pi} \frac{d}{dt} \left( 2\pi\nu_0 t + \beta \sin(2\pi\nu_m t) \right) = \nu_0 + \Delta F \cos(2\pi\nu_m t), \quad (4.3)$$

as the time derivative of the phase seen in Eq. (4.1) [61]. Here  $\Delta F = \beta\nu_m$  is the maximum frequency deviation from the carrier frequency  $\nu_0$ . Typically, the carrier frequency  $\nu_0$  is swept across a gas absorption profile at a Hertz rate while the momentary frequency  $\nu_i$  is rapidly oscillating around the carrier frequency at a kHz rate. An intuitive picture of the generation of signals that resemble the derivative of the profile probed is shown in Figure 4.1. The intensity  $I(\nu)$  detected can, inspired by [61], be expanded into a Taylor series around the carrier frequency  $\nu_0$  according to

$$I(\nu) = I(\nu_0) + \left. \frac{dI}{d\nu} \right|_{\nu_0} (\nu - \nu_0) + \frac{1}{2!} \left. \frac{d^2 I}{d\nu^2} \right|_{\nu_0} (\nu - \nu_0)^2 + \frac{1}{3!} \left. \frac{d^3 I}{d\nu^3} \right|_{\nu_0} (\nu - \nu_0)^3 \dots \quad (4.4)$$

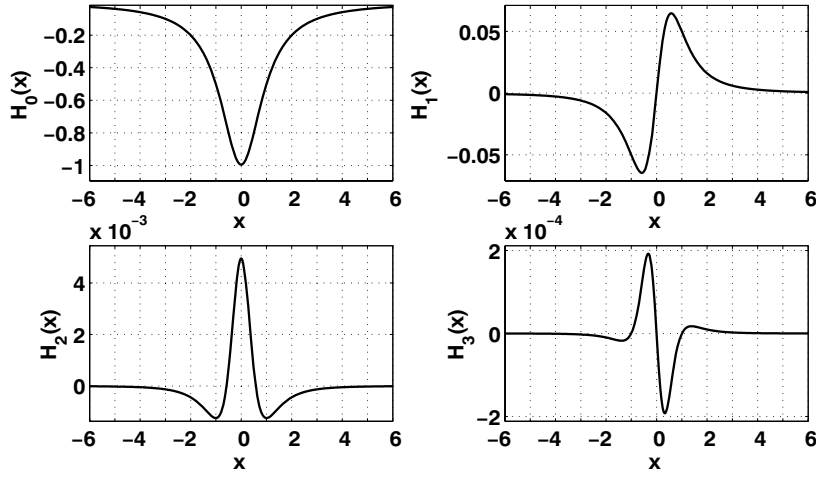


**Figure 4.2.** The direct signal together with the first, second and third derivative of a Lorentzian lineshape.

Inserting Eq. (4.3) into Eq. (4.4) and by using the Euler relations and the binomial theorem [62], it is simple to expand the powers of the cosine functions which yields

$$\begin{aligned}
 I(\nu) &= I(\nu_0) + \left. \frac{dI}{d\nu} \right|_{\nu_0} \Delta F \cos(2\pi\nu_m t) \\
 &+ \frac{1}{2!} \left. \frac{d^2 I}{d\nu^2} \right|_{\nu_0} (\Delta F)^2 \frac{1}{2} (1 + \cos(2\pi\nu_m t)) \\
 &+ \frac{1}{3!} \left. \frac{d^3 I}{d\nu^3} \right|_{\nu_0} (\Delta F)^3 \frac{1}{4} (3 \cos(2\pi\nu_m t) + \cos(2\pi 3\nu_m t)) + \dots
 \end{aligned} \tag{4.5}$$

If all terms oscillating at the same frequencies are collected in Eq. (4.5), it can be written as

$$I(\nu) = I(\nu_0) + A_0(\nu_0) + A_{\nu_m}(\nu_0) \cos(2\pi\nu_m t) + A_{2\nu_m}(\nu_0) \cos(2\pi 2\nu_m t) + \dots \tag{4.6}$$

where the perturbation amplitudes are given by

$$\begin{aligned}
 A_0(\nu_0) &= \left. \frac{d^2 I}{d\nu^2} \right|_{\nu_0} \frac{1}{2} (\Delta F)^2 + \left. \frac{d^4 I}{d\nu^4} \right|_{\nu_0} \frac{1}{32} (\Delta F)^4 + \left. \frac{d^6 I}{d\nu^6} \right|_{\nu_0} \frac{1}{768} (\Delta F)^6 + \dots \\
 A_{\nu_m}(\nu_0) &= \left. \frac{dI}{d\nu} \right|_{\nu_0} \Delta F + \left. \frac{d^3 I}{d\nu^3} \right|_{\nu_0} \frac{1}{8} (\Delta F)^3 + \left. \frac{d^5 I}{d\nu^5} \right|_{\nu_0} \frac{1}{192} (\Delta F)^5 + \dots \\
 A_{2\nu_m}(\nu_0) &= \left. \frac{d^2 I}{d\nu^2} \right|_{\nu_0} \frac{1}{4} (\Delta F)^2 + \left. \frac{d^4 I}{d\nu^4} \right|_{\nu_0} \frac{1}{48} (\Delta F)^4 + \left. \frac{d^6 I}{d\nu^6} \right|_{\nu_0} \frac{1}{1536} (\Delta F)^6 + \dots
 \end{aligned} \tag{4.7}$$

The intensity detected, Eq. (4.7), is a series of cosine terms, i.e., it is in a sense a Fourier expansion.

Provided the frequency deviation  $\Delta F$  is sufficiently small, the signal at the  $n$ th harmonic of the modulation frequency is proportional to the  $n$ th derivative of the detected intensity, which is illustrated in Figure 4.2. This property has given wavelength modulation spectroscopy, in the limit of small modulation, the additional name derivative spectroscopy [63].

### Larger modulation

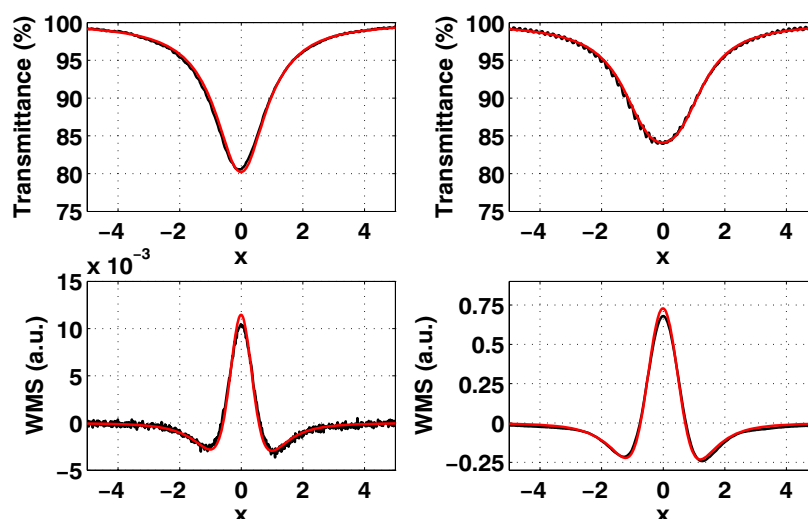


**Figure 4.3.** Experimentally obtained direct and WMS signals from long-path absorption of the molecular oxygen R7R7 line at around 761 nm together with theoretical signals. Left column: low modulation. Right column: high modulation.

From the intensity expansion, Eq. (4.7), we also learn that the harmonic signals increase with increasing modulation index. In the case of second-harmonic detection, the detected signal is proportional to the modulation squared at low modulation amplitudes. With increasing modulation, however, terms of higher order become prominent and the second-harmonic signal is no longer proportional to the pure second derivative of the absorption feature as can be seen in Figure 4.3. Although the signal is similar to the derivative, it is broader and other less transparent modeling approaches is normally used.

More general theoretical WMS curves are presented in Figure 4.3 together with experimental curves of both direct signals and second-harmonic WMS signals. The experimental signals originate from an

oxygen absorption line at about 761 nm and were recorded in a long-path setting using two different modulation amplitudes. The theoretical model used was the zeroth and second-order Fourier component of a wavelength modulated Lorentzian line profile at sloping baseline given by Ref. [64]. (Please note that an exponent of 2 is obviously missing in the expression provided in [64]).

The  $n$ th harmonic component of an arbitrary line profile at any modulation strength can be calculated numerically by a Fourier integral approach [65]. However, it is always reassuring to have an analytical expression, and such expressions have been presented for the second and  $n$ th harmonic component of the Lorentzian line profile without sloping baseline by Reid and Labrie [66] and Arndt [65], respectively. An expression for the more general case of linear baseline and a Voigt line profile has been given [64], where the Voigt function was approximated by something called a generalized Lorentzian function [67, 68]. Recently, a general Fourier-series-based formalism capable of providing analytical solutions for all harmonics of the three commonly used line profiles was presented by a research group in Umeå. A comprehensive review of this formalism is provided by Ref. [69].

### Intensity normalization

The WMS signals are proportional to the amount of light detected, which has to be accounted for in the case of varying light attenuation. This can be accomplished by normalizing the WMS signal to the amount of light detected, e.g., the direct signal. A practical measure of the gas absorbance is provided by the ratio of the peak-to-peak value of the WMS signal to the interpolated light intensity at the peak absorption wavelength.

## 4.2 Light detection and ranging (lidar)

In Section 3.3.2 Eq. (3.20) for the amount of light backscattered at a distance  $r$  from the source in an atmosphere with spatially dependent scattering and absorption was introduced. Here, the laser spectroscopic technique called lidar, i.e., light detection and ranging, that remotely can assess these spatially dependent absorption and scattering distributions range-resolved is presented.

The acronym lidar directs the association towards the similar acronym radar that is the radio-frequency counterpart to lidar. However, what is now called radar, was before 1947 known as radiolocation, which had a break through in the aircraft warning service during the second world war [70]. Actually, lidar is sometimes called laser radar

or optical radar. In some rare occasions lidar is the acronym used to emphasize that a laser is in use.

Early lidar experiments were focused on ranging applications like measuring the distance to the moon [71]. Since then a number of sophisticated lidar applications comprising the monitoring of air pollution, temperature and wind velocities have emerged. The International Laser Radar Conference (ILRC) has been held biannually 23 times and attracts hundreds of contributions.

The essence of the lidar principle is that a short pulse of light is sent out in the atmosphere and the backscattered light is detected time-resolved. Since the light has a known velocity, the distance from where the light was scattered can be calculated. Although most lidar applications utilize backscattering from atmospheric constituents, topographic targets can also be used as back reflectors [72].

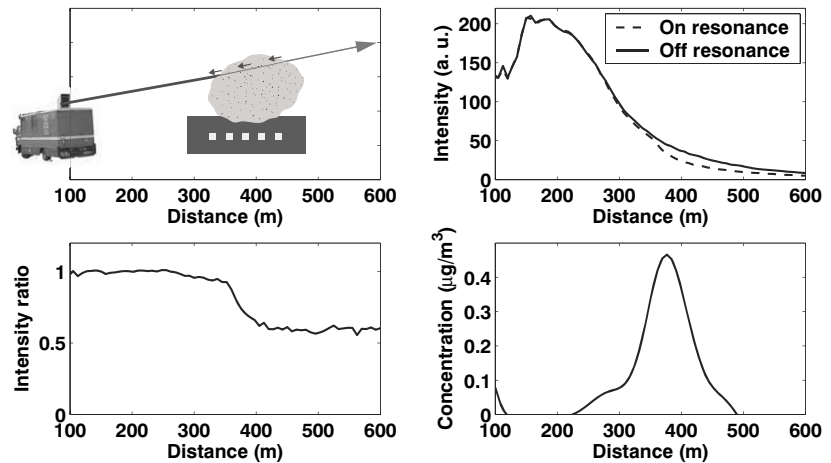


**Figure 4.4.** The principle of DIAL. From the spatial slope of the ratio between the intensity on an absorption line and the intensity slightly off that resonance line, the range-resolved gas concentration can be determined. The data are from field measurements of mercury presented in [73].

The concept of differential absorption introduced in Section 3.3.3 is fruitful in a vast number of spectroscopic applications. In the lidar branch the technique of differential absorption lidar (DIAL) was proposed by R. M. Schotland in 1966 [74].

In DIAL measurements, see Figure 4.4, light pulses are emitted alternately at a wavelength that is *on* an absorption feature and a nearby wavelength that is *off* that absorption feature. If the wavelength difference between the *on* and *off* wavelengths is small, the optical properties of the atmosphere, except the absorption due to the gas of interest, are the same for the two wavelengths. This provides the opportunity to

eliminate several of the factors in Eq. (3.20) resulting in

$$\frac{I(\lambda_{on}, r)}{I(\lambda_{off}, r)} = \exp\left(-2(\sigma_{on} - \sigma_{off}) \int_0^r c(s) ds\right), \quad (4.8)$$

from which the range-resolved concentration profile can be assessed by differentiation, i.e.,

$$c(r) = \frac{d}{dr} \left( \frac{1}{2\Delta\sigma} \ln \frac{I(\lambda_{off}, r)}{I(\lambda_{on}, r)} \right). \quad (4.9)$$

For some environmental DIAL applications see, e.g., Papers I, II, III, and IV.

#### 4.2.1 The lidar system

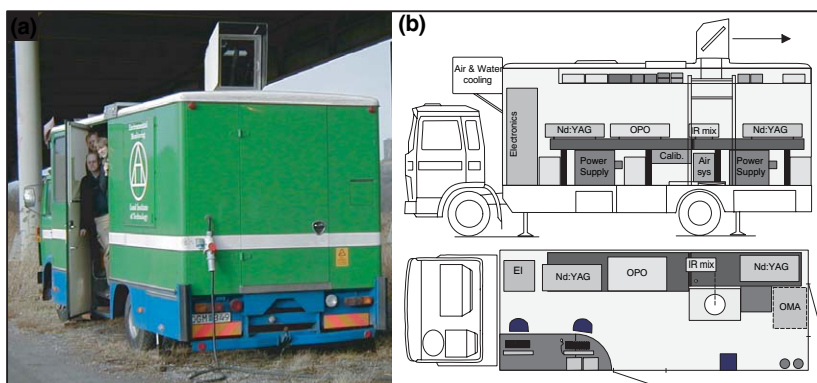


**Figure 4.5.** (a) The lidar truck and its crew are ready for field measurements of mercury. (b) Schematics of the mobile lidar lab, modified from Ref. [37].

The light pulses in the DIAL system used in Papers I, II, III, and IV are generated by the optical parametric oscillator described in Section 2.5.2. The few nanosecond long light pulses are sent through a Galilean beam expander and directed out into the atmosphere by a folding mirror that can be tilted and rotated by computer controlled stepper motors.

Backscattered light from the atmosphere is collected by a Newtonian telescope that focuses the light into a photo multiplier tube detector. The electrical signal from the detector is digitized by a 12 bit 20 MHz analog transient digitizer, corresponding to an atmospheric range resolution of 7.5 meters.

The whole lidar laboratory is 6 m × 2.3 m and is housed in a Volvo F610 truck, see Figure 4.5, that is accompanied by a trailer containing a Diesel-powered electric generator allowing true field monitoring. Stable

operating conditions for the laser system are assured by the climate control system that keeps the indoor temperature within 2°C in the outdoor temperature interval between -20°C and 30°C [37]. For further technical reading about the lidar system, see Refs [36, 37].

Except from remote differential absorption measurements of atmospheric gases, e.g., Papers I, II, III, and IV, the lidar system is capable of remote fluorescence assessments of both historical buildings, e.g., [75, 76] and high voltage insulators [77–79]. The system has recently also been adapted for remote imaging and cleaning of historical monuments by laser induced breakdown spectroscopy (LIBS)[80].

### 4.2.2 Flux measurements

With the tilting mirror in a fixed position, the lidar system provides the concentration profile along the laser beam direction. However, by changing the angles of the tilting mirror, concentration profiles along several lines can be obtained and a two dimensional concentration map can be generated.

In environmental surveillance not only the concentration distribution of a certain pollutant is of interest. The total flux emitted by the source under investigation is often the crucial information, which can be assessed by multiplying the integrated concentration in the measurement plane with the wind velocity orthogonal to that plane. For instance, assume that a concentration map is obtained in a  $yz$ -plane at a certain  $x$ , then the total flux through that plane is given by

$$F = \int_{z=0}^{\infty} \int_{y=0}^{\infty} v_x(y, z) c(y, z) dy dz, \quad (4.10)$$

where  $v_x(y, z)$  is the  $x$ -component of the wind velocity and  $c(y, z)$  is the concentration of the pollutant in the point  $(y, z)$ .

### Wind measurements

The wind velocity can be measured by various more or less complex methods ranging from simple and cheap combined wind vanes and anemometers to expensive and advanced laser Doppler or sound based Doppler systems (SODAR) [81].

In Papers I, II, and III the wind was measured by wind vanes and anemometers and the data were acquired by an analogue data acquisition card in a standard computer. The approach used did not provide the spatially resolved wind velocity but rather velocities only at a few locations close to the center of gravity of the mercury plume. In order to elucidate the influence of altitude dependent velocities, a comparison with a Doppler lidar system provided by Michael Bennett from University

of Manchester was undertaken during a mercury measurement campaign in Italy. The inter-comparison suggested that the flux determinations obtained by using wind vanes and anemometers agreed with the Doppler lidar based results to within 20 % [82].

### 4.3 Calibration techniques

In direct absorption measurements, the absorbance can be assessed in a straight-forward manner from the recorded signals. If the absorption cross-section is known, then, the concentration can be calculated. Cross-sections are available in the literature and in spectroscopic data bases, although the effective cross-sections depend on the instruments used, e.g., the linewidth of the light source. Additionally, modulation techniques are not providing direct information about the absorbance. However, the fact that “Nobody knows a molecular absorption spectrum better than the gas itself” [83] can resolve the problem as we briefly will see in this Section.

#### 4.3.1 Wavelength calibration

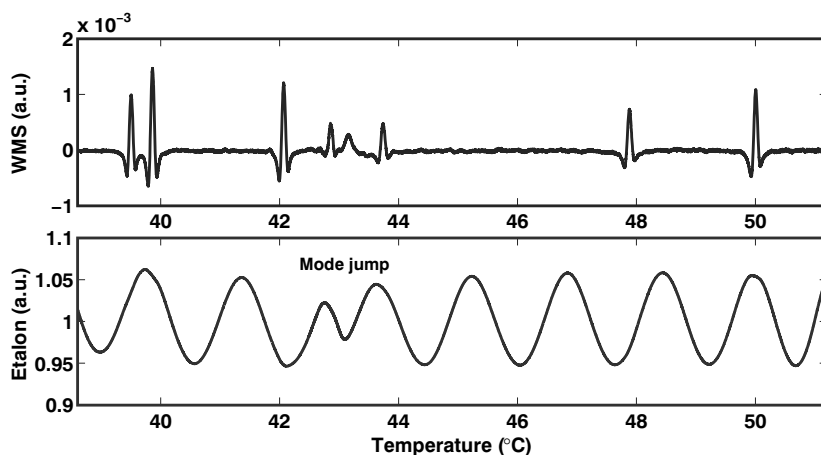


**Figure 4.6.** Etalon fringes can provide a frequency scale in tunable laser spectroscopy. Here, oxygen lines at around 760 nm are assessed by diode-laser-based wavelength modulation spectroscopy. The tuning range is, as indicated, interrupted by a mode jump.

Before we focus on the absorbance and concentration calibrations, we will discuss something about calibration along the wavelength axis. A rough estimate of the wavelength can be obtained by the naked eye by determining the color of the light. Obviously, this method has its limitations and calibrated spectrometers and wavemeters can provide more

accurate wavelength determinations. However, for absolute calibration of wavelength the most accurate result is provided by the position of a known absorption line combined with a precise relative wavelength scale generated by, e.g., an etalon, as illustrated in Figure 4.6. An etalon has two parallel surfaces between which the light is reflected as in a resonance cavity and the light transmittance varies periodically in wavelength with a period equal to the free spectral range of the etalon given by Eq. (2.1).

### 4.3.2 Concentration calibration

#### Standard addition

Most often reference cells with well-defined concentrations of the gas of interest are used in order to establish an effective cross section that can be used to calculate unknown concentrations. A commonly employed approach is the method of standard addition, where known amounts of the gas of interest are added to the original unknown amount. If the recorded signal, e.g., absorbance, responds linearly with the added known amounts of gas, the original unknown amount can be calculated. Typically, cells of various lengths containing a well-defined concentration of the substance under investigation are inserted in the light path. An example of such a linear response can be seen in, e.g., Figure 5 of Paper V. In the case of oxygen in porous materials, different long paths in the ambient standard air were the “reference cells” readily available. These kinds of linear standard-addition curves are shown in, e.g., Figure 2 of Paper VII, Figure 5 of Paper VIII, and Figure 2 of Paper X.

#### Univariate techniques

A quantity of an isolated absorption line that is linear with the concentration is, e.g., the peak absorbance at line center in the case of direct absorption measurements or the peak-to-peak value of the second-harmonic WMS signal in the case of modulation spectroscopy. Under noisy conditions, increased precision can be obtained by making use of the whole spectral profile by fitting a theoretical expression to the experimentally recorded wavelength scan. The fitting factor, then, is a linear measure of the concentration. However, the influence of instrumental effects on the theoretical curve is not always simple to deal with. An alternative is to record, with identical instrumental settings, the spectral absorption profile under the condition of high signal-to-noise ratio and use this curve as a fitting function. Such an approach was used for, e.g., detection of isolated oxygen and water vapor absorption lines in Papers IX, X, XI, XII, and XIII.

## Multivariate techniques

An extension of the calibration method based on an experimental fitting function previously discussed is the concept of partial least squares (PLS) in multivariate analysis. This concept is especially useful in situations of overlapping spectra where it is not, *a priori*, obvious how the recorded complex spectral signature is related to each of the absorbing constituents present. However, by performing calibration measurements of various combinations of the absorbing species present, a PLS model can be built for predicting the concentrations in an unknown mixture of absorbers. In Paper IV the PLS method was successfully used for concentration determination of light hydrocarbons in a remote gas mixture.

## 4.4 Optical techniques for scattering media

In Section 3.4 multiple light scattering was treated. Here some experimental techniques for retrieving optical properties of multiple scattering media are described. The techniques can be divided into three different categories; continuous wave spatially resolved measurements, time domain measurements and frequency domain measurements. Main applications of these techniques are within the biomedical field, e.g., optical mammography [84–86], dosimetry for photodynamic therapy [87], and concentration determinations for tissue and blood constituents [88, 89].

### 4.4.1 Temporal domain techniques

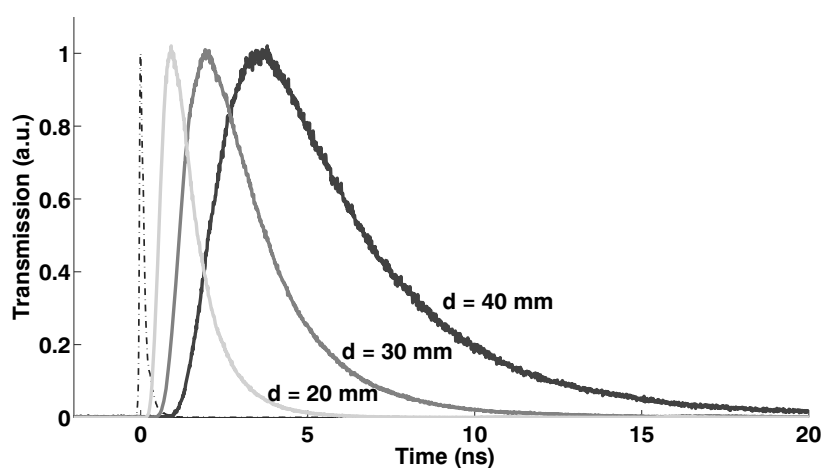


**Figure 4.7.** Time dispersion curves for light transmitted through polystyrene slabs of different thicknesses measured by the time-correlated single-photon counting technique.

One approach of assessing the scattering and absorption properties of scattering media is to send a short pulse of light into the material and record the escaping diffuse light time-resolved. The absorption and the reduced scattering coefficients can then be obtained by fitting analytical expressions, see Section 3.4.3, to the time dispersion curves recorded. A benefit of time-resolved techniques is that they provide direct information about the mean time spent by a photon in the sample, which is of interest in some applications, see e.g. Section 4.5.

These kinds of time-resolved measurements are commonly accomplished by the **time-correlated single-photon counting** technique (TCSPC) [90] employed in Paper VIII. The operational principle is that short pulses of light are repetitively sent into the scattering medium under study and part of the escaping light is directed into a sensitive and appropriately fast detector. It is made sure that the light is attenuated to such a low level that no more than one photon per pulse is detected. The electrical pulse originating from the detection of a photon is sent into a constant fraction discriminator (CFD) which provides a well-defined time for the pulse. Then, a **time-to-amplitude converter** (TAC) produces a signal with an amplitude proportional to the time difference between the pulse originating from the sample and a pulse originating from light sent directly from the light source to a detector. This time-to-amplitude converted signal addresses a certain channel in a **multi-channel analyzer** (MCA). The count of the channel addressed is increased by one unit and together with a large number of other pulses a distribution of arrival times, i.e. a time dispersion curve, will build up.

In Figure 4.7 TCSPC recordings of light diffusely transmitted through polystyrene foam slabs of various thicknesses are displayed. However, TCSPC techniques are not only used for studies of multiple light scattering [84], but also for measurements of fluorescence lifetimes and decay rates in various atomic and molecular systems [91].

#### 4.4.2 Frequency domain techniques

Generally, a system can be described equivalently in the time domain and in the frequency domain and the descriptions are linked by the Fourier transform. This is also true for the description of light transport in scattering media offering an alternative to the time-resolved techniques treated in the previous Section.

The principle of the phase-sensitive frequency domain techniques is that amplitude modulated light is sent into the multiple scattering sample under study and the phase shift and attenuation of the diffuse escaping light are measured [92]. For instance, the frequency domain counterparts to the theoretical expressions presented in Section 3.4.3 can be fitted to the frequency dependent phase shifts recorded in order to re-

trieve the absorption and reduced scattering coefficients of the scattering medium. Such measurements related to gas in scattering media, see Section 4.5, have been initiated and promising results are so far presented in Ref. [93].

### 4.4.3 Spatial domain techniques

In the previous Sections we encountered the time domain and the frequency domain techniques. Here, a third simpler alternative based on continuous-wave light will be presented briefly.

These steady-state techniques rely on the spatial dependence of the diffuse escaping multiple scattered light [49]. For instance, theoretical expressions for the escaping light at a series of different injection-detection separations, see Section 3.4.4, can be fitted to the corresponding recordings rendering information about the optical parameters as was done, e.g., in Paper VIII. However, the method only provides the effective attenuation coefficient  $\mu_{eff}$  if the injection-detection separation is large.

## 4.5 Gas in scattering media absorption spectroscopy (GASMAS)

This final Section about spectroscopic techniques is devoted to a concept denoted GASMAS, developed within this thesis work, that deals with absorption spectroscopy of gases in scattering media.

### 4.5.1 General aspects

The GASMAS concept is based on the fact that gas absorption features are extremely sharp compared to the spectral absorption and scattering structures of solids and liquids. Traditionally, such materials have only been studied at low spectral resolution not revealing any gas absorption signatures. However, the gas can readily be measured *in situ* by the use of spectrally narrow-band laser light that is scanned across an absorption line of the gas of interest. Since a short wavelength range of only a fraction of a nanometer is scanned, the slowly varying absorption and scattering properties of the bulk material stays constant and the gas concentration can be assessed by a differential approach. The benefit of the method is that the optical path length inside the absorbing and scattering medium becomes long compared to the geometrical dimensions of the sample, which means that the gas absorption is enhanced.

### 4.5.2 The small case

In Paper VII the GASMAS concept was first introduced by proof-of-principle measurements on various organic and manufactured porous materials. In a second publication, Paper VIII, time-resolved measurements, see e.g. Section 4.4.1, were employed to study the path distribution of diffusely transmitted multiply scattered light and the gas concentration in a porous material was estimated. The method of measuring gas inside porous materials introduced in Paper VII was in addition picked up by, e.g., a research group in Potsdam that later reported in *Technisches Messen* about gas absorption measurements in porous foams incorporating frequency domain techniques instead of temporal domain techniques [94].

So far, the spectroscopic absorption detection technique used by us has mainly been wavelength modulation spectroscopy, see Section 4.1.3, with modulation frequencies in the kHz range. Several applications have been reported in Papers IX, X, and XI using an absorption line of oxygen at about 760 nm, and in Paper XII water vapor was also measured at about 980 nm in studies of wood drying.

Gas exchange processes are of particular interest and such studies have been illustrated in several of the Papers mentioned, in particular in Paper XIII. The principle is that a porous sample is subjected to an anomalous atmosphere and the dynamics of the transient gas signature are studied.

Other opportunities of the concept discussed are assessments of temperature and pressure inside porous materials by analyzing the gas absorption lineshapes. An experiment on pressure assessment inside a porous glue is for instance presented in Paper VII. Tomographic studies of GASMAS type, possibly incorporating means of spatially varying the absorption profile, could be a prosperous modality.

Issues regarding the influence of the interactions between the gas and the hosting porous material in extremely tiny pores upon the absorption line shape are of fundamental interest. Resulting absorption line broadening and shifts can be expected to carry diagnostic information about the porous material. Another fundamentally interesting issue is how various parameters affect the light partitioning between the different phases of a porous medium.

### 4.5.3 The large case

#### Large absorption

The previous subsection discussed the case of relatively small samples, on the length scale of centimeters, and small fractional absorptions, often orders of magnitude lower than a percent. In that case, the absorption is

basically the same as the absorbance and the absorption signal obtained is in essence the product of the gas concentration and the path length traveled by the diffusing light inside the scattering medium, which was utilized in, e.g., Paper VIII. In particular, the path length traveled by light at the line center of a gas absorption profile is the same as for light at the wings of the profile. This is true since the differential absorption coefficient is small compared to the total absorption coefficient.

If the gas-related differential absorption coefficient is large, however, the path length traveled by the multiple scattered photons will vary with the wavelength position within the absorption line shape of the gas transition. This, since the path lengths traveled become longer if the absorption is low. Line shape analysis could then, possibly, reveal information about the path length traveled within the scattering medium. Studies on a strong absorption line of gaseous rubidium in a scattering slab of porous aluminium oxide are now pursued [95].

### **Large spatial scale**

So far, we have discussed GASMAS measurements on a small spatial scale with small differential absorption as well as large differential absorption. Another regime is the one occurring on a large spatial scale under influence of either small or large relative differential absorption. Such large-scale studies in the atmosphere can preferably be performed utilizing active lidar techniques.

Normally, lidar measurements are performed using a small detection field of view directed coaxially with the direction of the light transmitted. By this procedure, multiply backscattered light is efficiently rejected. Additionally, most often in ground based tropospheric applications the volume probed is clear, which further makes the measurements truly single scattering with the detection geometry used.

However, fog and clouds are inherently heavy scattering media in which the light is multiply scattered. If the coaxial part of the backscattered light is blocked and larger fields of view are used, the detected part of the light will be increasingly more multiply scattered. The mental step from the small scale spatially resolved measurements of gas in multiple scattering slabs of polystyrene foam presented in Paper VII to off-axis large scale lidar measurements of, e.g., stratus clouds is small. These kind off measurements are planned [73] and have prospects of being helpful in the elucidation of the earth's radiation budget, which is the essence of the climate change issue, see e.g. Section 5.1.1.



# GAS IN NATURE AND INDUSTRY

---

The gases dealt with in the Papers included are important in the larger contemporary societal and industrial contexts as outlined in this Chapter. This is not a complete survey of all aspects related to the gases, but rather a review of some prospective gas application areas of the techniques presented in the thesis.

## 5.1 Atmospheric pollution

The environmental concerns have increased dramatically in the Western world during the last half century. Here, three major environmental issues, i.e., climate change, acidification, and release of heavy metals in the ecosystems, all related to atmospheric gases studied in this thesis, are considered.

### 5.1.1 Climate change

Change of the climate in the form of global warming is a frequently discussed environmental issue. The consequences of an increased global average temperature is not only limited to environmental changes, but also include human health issues [96]. However, the global warming is a complex problem encompassing debate about the origin of the increased average temperatures observed, i.e., either natural fluctuations or an effect of anthropogenic activities [97, 98], which calls for further research.

Generally, the global warming phenomenon is about the radiative balance of the atmosphere and is often called the extended greenhouse effect [99], since short wavelengths of the sun light are transmitted down to the earth whereas certain compounds in the atmosphere block, like a glass window of a greenhouse, the longer wavelengths of terrestrial radiation from escaping.

### Monitoring techniques

To understand the mechanisms of global warming, the large-scale complex interplay between light absorption and scattering at various wavelengths in the atmosphere has to be fully understood. Similar to the small-scale laboratory experiments on gas in scattering media absorption spectroscopy presented in, e.g., Paper VIII, a large scale counterpart utilizing lidar techniques could have prospects of revealing interesting aspects of light transport in the atmosphere.

Compounds in the atmosphere contributing to the warming are infrared absorbing species such as carbon dioxide and methane. An interesting aspect in studying the origin of green-house gases is to investigate the amount of different carbon isotopes in atmospheric carbon dioxide, see e.g. [100] or hydrocarbons, see e.g. [101]. These amounts could be studied by for instance high resolution diode laser spectroscopy. The origin of the compounds can in this way be revealed, since the isotopic ratio is different for carbon originating from fossil fuels than for carbon fixated in recent biological processes.

Lidar techniques, e.g. the one presented in Paper IV, for remote range-resolved measurements of gas species, e.g. hydrocarbons like methane, ethane, propane, etc, that absorb radiation in the infrared spectral region can find fields of application in this global warming context. They are tools that can reveal emission sources and also quantify the emission, as was done in Papers I, II, and III in another context.

### 5.1.2 Acidification

The acidity of many aquatic and terrestrial ecosystems has increased due to human activities during the last century [102]. Acidification effects are visible on, e.g., trees that are displaying symptoms such as discoloration, defoliation, growth decline, and increased vulnerability to stress caused by, e.g., drought, cold, and various diseases [103].

The main cause of acidification is the deposition of sulfur and nitrogen compounds, i.e., nitric and sulfuric acid from the atmosphere. Although the atmosphere naturally has more acidic gases than basic gases, extensive fossil fuel combustion has led to anthropogenic emissions of nitrogen oxides and sulfur dioxide that exceed the natural emissions by about an order of magnitude [102]. This calls for emission allowance trading of nitrogen oxides and sulfur dioxide [104] as well as efficient monitoring techniques.

### Monitoring techniques

Remote range-resolved measurements of sulfur dioxide emissions from volcanoes around the Mediterranean sea have been performed by lidar

techniques [105]. In Paper V a diode laser based spectrometer for sulfur dioxide is introduced. In addition, the system presented has the opportunity of simultaneous nitrogen dioxide and water vapor detection. Cheaper systems for sulfur dioxide detection utilizing broad-band light sources are also currently emerging in China [106].

### 5.1.3 Heavy metals

Heavy metals, e.g., mercury (Hg), lead (Pb), cadmium (Cd), chromium (Cr), nickel (Ni), and arsenic (As) are of concern for the public health due to their toxicological effects. They are released into the atmosphere from, e.g., volcanoes, mines, geothermal fields, deposits, and industrial activities. For instance, elemental mercury is extracted from cinnabar (HgS), which occurs in, e.g., mines in Almaden (Spain), Abbadia S. Salvatore (Italy), and Idrija (Slovenia). In the industry, mercury has been employed for various purposes such as chlor-alkali production, instrument components, dental fillings and pesticides.

Actions to reduce the anthropogenic emission of heavy metals are taken, e.g., the United Nations Economic Commission for Europe (UNECE) Aarhus protocol on heavy metals from 1998 targeting cadmium, lead and mercury emissions [107]. Currently a European Union financed project about the estimation of willingness-to-pay to reduce risks of exposure to heavy metals and cost-benefit analysis for reducing heavy metals occurrence in Europe (ESPREME) is pursued [108].

#### **Mercury from the chlor-alkali industry**

Mercury monitoring is of general interest [109] and another European Union financed project exactly focused on mercury and in particular **European mercury emission from chlor-alkali plants (EMECAP)**. In that industry, mercury is used as an electrode in electrochemical cells producing sodium hydroxide and chlorine from salt solution, see Figure 5.1. The objective of the project was to provide decision makers with an innovative and integrated tool, including both technologies and methodologies, for the understanding of the atmospheric mercury pollution problem [110, 111].

The project was truly cross-disciplinary and international, encompassing participants from Italy, Norway, Poland, Romania, Slovenia, and Sweden with a large spectrum of competencies within epidemiology, chemical mercury analysis, sensor and instrument design, laser spectroscopic monitoring, dispersion modeling, software development, etc. [112].

In this context, remote mapping of elemental gaseous mercury emissions at chlor-alkali plants in Bohus (Sweden), Rosignano Solvay (Italy), and Tarnow (Poland) were performed and are presented in Papers I, II,



**Figure 5.1.** A mercury cell chlor-alkali plant (Tarnów, Poland).  
Photo: Stanisław Hławiczka.

and III. Based on the actual measurements, dispersion models including the weather influence were used to predict yearly average values of mercury in the surroundings of the industries [113].

## 5.2 Gases of life

Several gases are essential for the life processes and in this Section a few of them are reviewed with special emphasis on their relation to porous living structures.

### 5.2.1 Gas in porous plants

#### Porous structures

Plants contain substantial amounts of gas since their structures are porous to various extent. The gas filled volumes are either intracellular spaces present in, e.g., dead wood and cork or intercellular spaces found between living cells in for instance mesophyll and aerenchymatic tissues [114–116].

The pore volume fraction of plants spans over a large range of values from less than one percent in potato tubers to above 70 percent in the leaves of some *Doronicum* species [117]. Intermediate leaf porosities of 20 percent and 40 percent are found in *Phaseolus vulgaris* and *Oryza*

*sativa*, respectively [118]. Apple fruits, which have been studied in Papers X and XI, have porosities of around 15-25 percent [119].

One function of the gas filled porous structure is its mechanical benefit in that the construction becomes relatively light weighted in relation to the mechanical strength provided [120]. For instance, water plants like the Water Hyacinth (*Eichhornia crassipes*) are mainly built up of extremely porous aerenchymatic tissue that provides excellent floatability.

Another function of porous structures is found in the mesophyllic tissue of leaves where the light distribution within the leaf is optimized by light reflections at the airspace boundaries [121], which has been studied by time-resolved light transmittance techniques, see Section 4.4.1, [122]. Probably, however, the most important function of the intercellular air space is related to the exchange of life gases.

### **Gas exchange**

Plants are known for their ability to store the energy of light in complex organic molecules formed in several steps starting from atmospheric carbon dioxide and water vapor under the release of oxygen. Thus, this photosynthetic process demands an efficient inflow of carbon dioxide and water vapor and an outflow of molecular oxygen.

If the gas exchange between the active cells and the surrounding atmosphere had relied only on gas diffusion in liquid phase, the gas transport had been a severely limiting factor in the ongoing processes. However, gas diffusion in gas phase is several orders of magnitude faster than gas diffusion in liquid phase. Thus, plant tissues with internal continuous networks of air-filled spaces have better gas exchange capabilities.

The reverse of the photosynthetic process is the respiration process, in which the living cells release energy from organic molecules under the consumption of molecular oxygen and release of carbon dioxide and water vapor. The respiration process is dominating in the dark and in bulky storage organs and its metabolic pathways are profoundly influenced by the rate of gas exchange.

### **Plant physiological processes**

Various organic substrates can be degraded by different metabolic pathways in the respiration process. The difference related to gas exchange is the ratio between the amount of carbon dioxide deliberated and oxygen consumed. This ratio is denoted the respiratory quotient (RQ) and is less than 1 for lipids, about one for carbohydrates, and larger than 1 for organic acids. Thus, if there is a deficiency in oxygen supply the degradation of organic substrates of high RQ is preferred. If extremely low

levels of oxygen are available, i.e. anaerobic conditions, the metabolic pathway can even become fermentative resulting in alcohol production from carbohydrates.

The respiration rate is for instance important for the postharvest degradation rate of produce. It is traditionally assessed by measuring the accumulated gas outside the plant tissue placed in a sealed container. The crucial internal gas composition has, so far, been assessed intrusively by analyzing removed plugs of tissue, or gas sucked out by the use of hypodermic needles [123]. By such methods it has been found that the concentration of carbon dioxide in the air inside ripening apples can be as high as 5-10% [124]. However, these methods destroy the tissue and disturb the internal gas environment. Alternative non-intrusive *in vivo* techniques for internal gas measurements are introduced in Papers X and XI.

### 5.2.2 Gas of human health

Contrary to plants, humans do not rely on gas diffusion from the skin through porous structures to the respiring oxygen consuming living cells. Instead, oxygen is supplied bound to hemoglobin by the blood vascular system. However, during certain physiological states free gas might occur in human tissue.

A disease called decompression sickness is caused by rapid decrease in ambient pressure, which can affect divers, and pilots of unpressurised aircraft. When the ambient pressure is decreased, the gas solubility is also decreased resulting in gas release in the tissue. Other gas generating diseases are, e.g., gas gangrene, which is an infection caused by *Clostridium perfringens*. There might be prospectives for diode-laser-based gas absorption techniques in monitoring the onset of such diseases.

Although free gas is not normally distributed throughout the human tissue, there are gas filled cavities inside the human body. Such cavities are the sinuses, whose mucosa often is affected by inflammations, i.e., sinusitis. The diagnostic tools used so far for sinusitis are cost consuming, e.g. x-ray, ultrasound and computerized tomography. This has attracted some attention to the possibility of human sinus cavity diagnostics using non-intrusive cost effective diode-laser-based gas spectroscopy [125, 126].

## 5.3 Prospectives of performed porous projects

In this Section a few final applications using diode-laser-based techniques for gas assessment in porous materials mainly related to industrial processes are presented.

## 5.3.1 Pharmaceutical physics

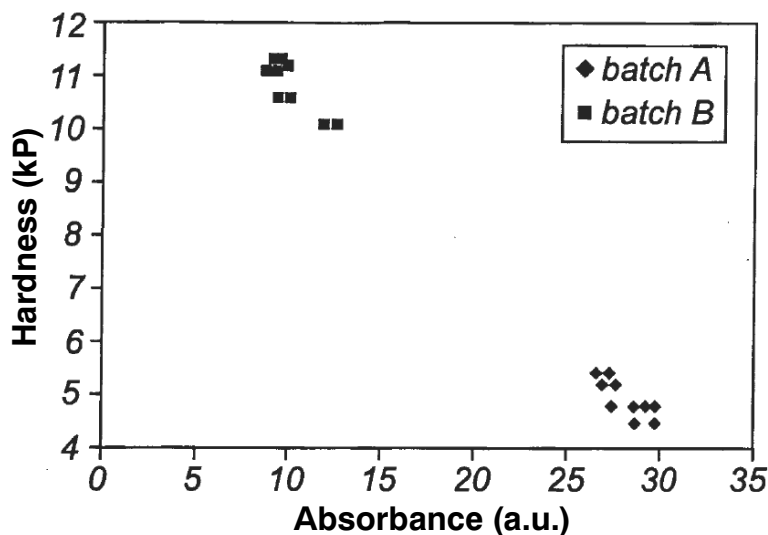


**Figure 5.2.** Experimental correlation between the GASMAS signal and the conventionally measured hardness of several pharmaceutical tablets. Adopted from [127].

The content of active substances in pharmaceutical samples, e.g. tablets, powders etc, are routinely analyzed by conventional near-infrared spectroscopy. Developments in scattering media techniques, see e.g. Section 4.4, now also offer the opportunity to account for multiple light scattering influence on the spectra recorded [128].

Contrary to the analysis of chemical content, there is still a lack of fast, non-destructive, and flexible analysis techniques for physio-mechanical properties such as structure, hardness, density, porosity, diffusivity of gas, dissolution ability, compressibility, flowability etc of a sample. Several of these properties are cumbersome to measure, but they can often be correlated to other more conveniently measured properties. For instance, it is time consuming to measure the property of disintegration and release of active substance *in vivo*, which is of utmost importance. A faster, but still slow, off-line and destructive, alternative is to measure the hardness by mechanical means, since the hardness, in some way, is related to the disintegration ability.

However, a prospective alternative optical technique that is fast, non-destructive and flexible is offered by the concept of GASMAS, introduced in Paper VII, [127, 129]. For instance, Figure 5.2 displays an experimental correlation between the hardness, obtained by a conventional mechanical testing procedure, and the GASMAS signal, related to light absorbance of molecular oxygen, of porous pharmaceutical tablets.

### 5.3.2 Drying diagnostics

Drying processes are present in a large range of settings, e.g., agricultural, food processing, pulp and paper, pharmaceutical, textile, wood, and building industries. The removal of moisture by various means such as, for instance, thermal heating, microwave radiation heating, and freezing are energy consuming and thus there is an economic incentive to make the drying processes more efficient [130].

Automatic control is routinely used in many industrial operations to improve their performance and has prospects of optimizing drying processes also. However, drying research is still mainly only on the level of understanding drying mechanisms and their influence on product quality [131, 132]. Nevertheless, for on-line control especially, the availability of accurate, fast and reliable sensors is crucial.

In this perspective, the in Ref. [133] and Paper XII recently introduced diode-laser-based non-destructive, *in situ*, and possibly remote spectroscopic technique offers an interesting moisture and water vapor sensor alternative. In Paper XII the technique was applied to wood drying and, for instance, the point in time when all free water is evaporated is readily provided.

### 5.3.3 Packaging processes

The respiration rate in, e.g., fruits during postharvest storage is crucial for the shelf life of the product. Generally, the respiration rate is lower at lower temperatures and can in addition be controlled by the ambient oxygen and carbon dioxide concentrations. For instance, lower oxygen concentration and higher carbon dioxide concentration lower the respiration rate. However, if the oxygen levels are too low, fermentation is induced which is often a disadvantage in fruit storage. From these facts we recognize refrigeration as an obvious and simple method of prolonging the shelf life.

More advanced methods take notice of the gas influence on the respiration rate and use, e.g., an actively controlled ambient storage atmosphere (CA) of relatively high carbon dioxide concentration and low oxygen concentration.

The gas composition approach is also used in a passive implementation in the form of modified atmosphere packaging (MAP), where the produce is sealed by a semi-permeable plastic film that makes the surrounding atmosphere modified due to the ongoing respiration process. These packages can also be pre-filled with a certain gas mixture in order to optimize the internal atmosphere. Additionally, the plastic film preserves the moisture in the produce and guards against bacterial access.

Not only fruits, but also other foodstuffs such as meat and beverages are packaged products of importance.

Prediction of the resulting atmosphere in MAP is a complex problem, since the respiration rate is most often not constant in time. Rather, the respiration rate in ripening fruits follow a time pattern dependent on the maturity as well as ambient factors. Especially so-called climacteric fruits such as apple, banana, tomato, pear, plum and avocado are sensitive to ethylene gas and has a pronounced rise in respiration rate during ripening [123, 134].

In this context non-intrusive, *in situ* measurement techniques for the internal gas composition make large impact. As demonstrated in Papers X and XI, diode-laser-based GASMAS techniques have prospects in this area.

### 5.3.4 Developing devices

A benefit of diode-laser-based techniques is the affordability. This has made it possible to transfer, e.g., GASMAS research systems to scientist in developing countries such as Zimbabwe, Ecuador, Ghana, Kenya, and Sri Lanka for exploration of various local applications. A compact diode laser based fluorescence system [135] was also transferred to each of these places except for Sri Lanka but instead also to Sudan and Senegal.

The concepts were introduced at a training workshop at the Atomic Physics Division at Lund University [136] and later on African PhD students, i.e., Benjamin Anderson, Kimari Wangai, and Robinson Ndegwa Gathoni started to sandwich their PhD studies between Lund and their laboratories at home. Furthermore, the establishment of the Ecuadorian laboratory for diode-laser-based gas studies was facilitated by a Master's Thesis project of students from Lund Institute of Technology [137].

So far fluorescence studies for tropical plants, and fluorescence based crop yield assessment of cowpea have been reported from Senegal [138] and Ghana [139], respectively. Future results from, e.g., tropical applications might be presented at the International Workshop on the Physics and Modern Applications of Lasers that so far has been organized seven times by The African Laser, Atomic, Molecular and Optical Sciences Network (LAM Network) [140].

Another aspect of developing devices is related to the business exploration of diode-laser-based techniques for gas in non-pharmaceutical scattering porous materials. This is pursued in the recently founded spin-off company GasPorOx AB, which stems from research presented in Papers VII–XIII and Ref. [125].



# SUMMARY OF PAPERS

---

---

## **Paper I. Atmospheric mercury near a chlor-alkali plant in Sweden**

The results from the first field measurement campaign within the cross-disciplinary European Union funded project about mercury emission from chlor-alkali plants (EMECAP) are presented. An intercomparison between the lidar system and mercury point monitoring instruments (TEKRAN and GARDIS) showed excellent agreement.

### **Contribution:**

Substantial part of preparations and the lidar field measurements. I. Wängberg, R. Ferrara, E. Lanzillotta, J. Munthe, and J. Sommar were responsible for the point monitoring. Minor part of manuscript preparation.

## **Paper II. Atomic mercury flux monitoring using an optical parametric oscillator based lidar system**

The application of an optical parametric oscillator (OPO) based differential absorption lidar (DIAL) system to the monitoring of atomic gaseous mercury is introduced. Approaches to meet the spectral stability demands on the light source are presented together with field results from measurement campaigns at chlor-alkali plants in Bohus (Sweden) and Rosignano Solvay (Italy). The Paper includes some time series of mercury flux and animations of vertical and horizontal concentration distributions that all are important input parameters for the environmental community.

### **Contribution:**

Substantial part of preparations and lidar measurements during all field campaigns. Responsible for data evaluation and manuscript preparation.

---

**Paper III. Elemental mercury emission from chlor-alkali plants measured by lidar techniques**

The Paper summarizes the lidar measurements of elemental gaseous mercury performed within the cross-disciplinary European Union funded project about mercury emission from chlor-alkali plants (EMECAP). Results from in total six two-week field campaigns at chlor-alkali plants in Bohus (Sweden), Rosignano Solvay (Italy), and Tarnow (Poland) are presented. The results indicate large differences in mercury emission between summer and winter as well as between different industries.

**Contribution:**

Substantial part of preparations and lidar measurements during all field campaigns. Minor part of data evaluation and manuscript preparation.

**Paper IV. Multi-component chemical analysis of gas mixtures using a continuously tuneable lidar system**

The Paper introduces an extension of the two-wavelength differential absorption lidar method, see e.g. Paper II, to a multiple-wavelength counterpart, which allows simultaneous remote measurement of substances with overlapping spectra in, e.g., the infrared spectral region. The method relies on a frequency agile optical parametric oscillator based light source combined with genetic variable selection and multivariate statistical techniques. Validation measurements on mixtures of hydrocarbons both in reference cells and in a remote artificial smokestack are presented.

**Contribution:**

Substantial part of the experimental work. Responsible for the remotely controlled gas handling. Minor part of manuscript preparation.

**Paper V. All-diode-laser ultraviolet absorption spectroscopy for sulfur dioxide detection**

A diode-laser-based scheme for high-resolution detection of sulfur dioxide at a wavelength of 302 nm is presented. The ultraviolet light is generated by sum-frequency mixing of blue and near-infrared diode laser light in a nonlinear crystal of beta-barium borate. The spectra are evaluated by a differential absorption method and the spectra recorded at various low pressures as well as ambient atmospheric pressure reveals the pressure influence on the sulfur dioxide absorption lineshape.

**Contribution:**

Responsible for data acquisition and evaluation. Part of manuscript preparation, discussions on experimental issues and measurements.

**Paper VI. Temporal correlation scheme for spectroscopic gas analysis using multimode diode lasers**

The Paper reports on a scheme for gas analysis based on temporal correlation between absorption signals from an unknown external gas concentration and, simultaneously recorded, known reference gas concentrations. The concept is illustrated by temperature induced diode laser wavelength scans in the molecular oxygen A-band around 760 nm. A discussion about the benefit, that the procedure does not require any knowledge of the exact spectrum of either the gas or the light is also presented.

**Contribution:**

Developed the LabVIEW based control, data acquisition and evaluation software. Part of the measurements, evaluation and manuscript preparation and minor part of system integration.

---

## Paper VII. Analysis of gas dispersed in scattering media

A novel concept of tunable-laser-based *gas in scattering media absorption spectroscopy* (GASMAS) measurements is introduced. Proof of principle diode-laser-based measurements on molecular oxygen embedded in porous materials like wood, apple, sugar, granulated salt, wheat flour, and polystyrene foam are presented. Sensitive detection is allowed by utilizing wavelength modulation spectroscopy. The prospective ability for characterization and diagnostics in organic and synthetic materials are illustrated by internal gas pressure and gas exchange measurements on porous materials.

### **Contribution:**

Substantial part of system integration, measurements, data evaluation and manuscript preparation.

## Paper VIII. Concentration measurement of gas embedded in scattering media by employing absorption and time-resolved laser spectroscopy

A procedure for gas concentration assessment in porous materials by laser spectroscopic techniques is presented. The light absorption caused by the gas of interest is measured by the GASMAS technique introduced in Paper VII. The gas concentration is estimated from the gas absorption measurements provided the path length traveled by the multiply scattered light is known. Time-resolved measurements employing the time-correlated single-photon counting technique (TCSPC) provides this information. It is shown that the mean path length of the multiply scattered light is proportional to the square of the straight distance between the light source and the detector.

### **Contribution:**

Substantial part of system integration, theory, measurements, data evaluation and manuscript preparation.

**Paper IX. Laser spectroscopy of free molecular oxygen dispersed in wood materials**

The GASMAS technique introduced in Paper VII is applied to the study of wood. Molecular oxygen is sensitively detected by wavelength modulation diode laser absorption spectroscopy. Anisotropy related to the fibre structure of wood, influence of the material density, and gas diffusion properties are studied. Finally, prospective extensions of the GASMAS techniques related to, e.g., the building industry are also discussed [141].

**Contribution:**

Substantial part of system integration, measurements, data evaluation and manuscript preparation. Developed the LabVIEW based data acquisition and evaluation software.

**Paper X. Diode laser absorption spectroscopy for studies of gas exchange in fruits**

Non-intrusive *in vivo* studies of gas inside fruits and its exchange with the surrounding is presented. In particular transport of molecular oxygen in apples is assessed by wavelength modulation diode laser absorption spectroscopy. The applicability of the techniques is demonstrated by studies of the influence on the internal oxygen balance by the natural apple skin and an artificial cling film, respectively. Furthermore, applications within food packaging, e.g., studies of modified atmosphere packaging processes are discussed [141].

**Contribution:**

Substantial part of manuscript preparation, discussions on experimental issues and measurements. Developed the LabVIEW based data acquisition and evaluation software.

---

**Paper XI. Studies of gas exchange in fruits using laser spectroscopic techniques**

The gas content and transport in horticultural produces, e.g., fruits are studied, in relation to modified atmosphere packaging, non-intrusively in real-time by diode laser based absorption spectroscopy. Preliminary studies of non-intrusive maturity determination of avocados are also presented. The prospects of compact devices, based on the techniques presented, for providing new types of information in postharvest fruit management are discussed.

**Contribution:**

Substantial part of system integration, measurements and manuscript preparation. Developed the LabVIEW based data acquisition and evaluation software.

**Paper XII. Spectroscopic studies of wood-drying processes**

A non-intrusive *in situ* technique for studying drying processes of porous materials by diode laser based absorption spectroscopy is introduced [133]. Wavelength modulation spectroscopy of water vapor and molecular oxygen absorption lines at the wavelengths 980 nm and 760 nm, respectively are employed in the implementation presented. The results suggest that the technique demonstrated can give information that are not provided by commercially available moisture meters. In particular, the time when all the free water has evaporated from the wood can be readily identified.

**Contribution:**

Developed the LabVIEW based data acquisition and evaluation program with Graphical Object Oriented Programming (GOOP). Part of system integration and experiments and minor part of manuscript preparation.

**Paper XIII. Gas diffusion measurements in porous media by the use of a laser spectroscopic technique**

The assessment of gas diffusion properties of porous materials by the GASMAS technique, i.e., wavelength modulation diode laser absorption spectroscopy of gases in scattering media, is treated. A porous sample is exposed for an anomalous atmosphere and the transient time-dependent gas absorption is recorded. A theoretical attempt to understand the time dependence of these transient gas signals is introduced and directions for further research are indicated.

**Contribution:**

Substantial part of system integration, theory, measurements, data evaluation and manuscript preparation. Developed the LabVIEW based data acquisition and evaluation program.



# ACKNOWLEDGEMENTS

---

---

Hösten är, liksom alla andra år, så här års i antågande. Men i år är det inte bara sommaren som nått sin ände utan även epoken som doktorand. När våren på nytt kommer åter med nya utmaningar är det förhoppningsvis som doktor jag tar mig dem an. Vid detta skede vill jag passa på att framföra mitt tack till alla som på något sätt bidragit till avhandlingens tillblivelse.

Jag vill börja med att tacka *Anders Sjödahl*, min högstadielärare i fysik och matematik, som med humor och glädje inför sina ämnen startade min färd på fysikens fascinerande farled vilken förde mig via Teknikum i Växjö till teknisk fysik i Lund. Väl i Lund tedde sig valmöjligheterna oändliga vilket resulterade i en stor flora av avklarade kurser.

Det var dock speciellt en professor som fångade mitt intresse. En professor som formligen flödade över av entusiasm inför sitt ämne när han expressivt och pedagogiskt illustrerade laserspektroskopins breda spektrum av möjligheter inom fysik, medicin och biologi. Det var *Sune Svanberg* som sedermera blev min handledare. Ett stort tack Sune för Din enastående förmåga att se kopplingar mellan till synes helt olika saker resulterande i många intressanta idéer. Tack för Din aldrig sinande entusiasm och för Ditt tålamod med forskningsresultat i ett arbetsklimat präglad av stor frihet och möjlighet att själv skaffa sig sina egna erfarenheter och insikter. Det har varit en lärorik tid.

Den biträdande handledaren *Hans Edners* gedigna kunnande inom bland annat optisk miljömätteknik och realistiska förhållningssätt till diverse problem har uppskattats. Dessvärre har han de senaste åren inte haft så stor del av sin tjänst förlagd till avdelningen. Tack för Din praktiska erfarenhet och Ditt trevliga umgänge i lidarbussen under fältkampanjerna i Bohus (Sverige), Rosignano Solvay (Italien) och Tarnow (Polen). *Stefan Andersson-Engels* har också varit biträdande handledare. Tack för Ditt gedigna kunnande inom bland annat den biomedicinska optiken och trevligt umgänge under resan till Kamerun.

Jag vill tacka gruppens tidigare doktorander *Ulf Gustafsson* och *Jonas Sandsten* för värdefulla råd och hjälp under den allra första tiden

på avdelningen. En stor läromästare har varit den äldre doktoranden *Petter Weibring*. Tack för allt praktiskt Du lärt mig om bland annat lidarsystemet och för att Du introducerade det grafiska programmeringspråket LabVIEW för mig. Så här efteråt kan jag nog hålla med om Ditt råd att inte gräva ner sig för mycket i programmeringen. Tack för trevligt samarbete under lidarfältkampanjerna och de flera dygn långa mätningarna hemma i Lund. Ett tack även till *Din far* för hans frukost.

*Gabriel Somesfalean* och jag har samarbetat intensivt och delat kontor under flera år. Tack för alla långa samtal och nätter vi tillbringat på kontoret och i labbet. Tack för att Du har stått ut med alla mina sokratiska frågor, och för alla skratt och all frukt Du bjudit på. Gästdoktoranden *Janis Alnis* från Lettland har också varit en samarbetspartner. Tack för inspirationen i det laborativa arbetet och det experimentella problemlösandet. Tack även till *Magnus Bengtsson* som med sitt alltid glada leende spridit glädje och tips om allt möjligt.

På senare tid har vår grupp fått förstärkning med flera nya doktorander som alla nu även delar samma kontor. Tack *Rasmus Grönlund* för gott samarbete i lidarbussen och trevligt resesällskap på fältmätningar, konferenser och projektmöten runt om i Europa. Tack även för Ditt lugn i vårt kontorslandskap. Tack *Linda Persson* för samarbete i diodlaserlabbet. Din arbetsflit, Ditt estetiska sinne och trevliga sällskap på tjänsteresor världen över har uppskattats. Tack *Mats Andersson* för att Du delar med Dig av dina industriella erfarenheter inom bland annat mät- och instrumenteringsteknik och för att Du har introducerat det objektorienterade synsättet på grafisk programmering för mig.

Vår grupp har även kopplingar till medicingruppen. Tack *Claes af Klinteberg* för inledande praktiska tips om tidsupplösta mätningar. Tack *Jonas Johansson*, *Christoffer Abrahamsson* och *Tomas Svensson* för samarbete kring farmaceutiska tillämpningar. Tack Tomas för Ditt kritiska och nyfikna förhållningssätt samt trevligt umgänge på konferensresor.

Utan *Bertil Hermansson* hade livet med våra datorer varit krångligare. Tack för att Du snabbt och effektivt uppgraderar våra datorer och ger bra tips i datorspörsmål. Vi saknar alla Bertils långvarige runskamrat *Åke Bergquist* som nu lämnat avdelningen för ett liv i USA. Tack Åke för alla elektronikprylar Du fixat. Tack *Jan Hultqvist*, *Göran Werner* med flera på den akademiska verkstaden för alla märkliga mekaniska prylar Ni fått tillverka åt oss. Tack Göran även för att Du på bumpiga vägar kört vår lidarlastbil med dålig fjädring ända till Italien och Polen. Tack *Anders Persson* för tips och råd om tekniska frågor och tack *Per Johnsson* för råd om avhandlingsskrivande med Latex.

Minnet av vår sekreterare *Laila Lewin* som bringade klarhet i de snåriga administrativa frågorna och effektivt hanterade ett stort antal reseräkningar samt dekorerade vår avdelning på ett trivsamt sätt kommer

alltid att vara ljust. Tack även våra nya sekreterare *Minna Ramkull* och *Henrik Steen* för hjälp med administrationen inför disputationen. Tack *Britt-Marie Hansson* för noggrann hantering av alla fakturor och vår ekonomi. *Elsie Nilsson* är den verkliga trotjänaren som sett många doktorander och även professorer komma och gå. Tack för att Du håller vår arbetsplats ren och fin och för att Du alltid tar Dig tid att växla ett par ord. Nu blir det snart lättare för Dig att städa vid mitt skrivbord.

Ett stort tack till *Marianne Madsen-Hult*, *Tora Kristiansen* och *Kristina Lindgren* vid fysik- och astronomibiblioteket för effektiv hjälp med att skaffa fram artiklar och böcker som ständigt måste lånas om.

Tack för hjälp av *personalen på kurslab* i samband med laborationsundervisning. Speciellt tack till *Sven-Göran Pettersson* för många givande diskussioner om pedagogik och till *Lennart Nilsson* för att han lockade med många nya laborationsundervisningstillfällen och höll föredömligt reda på den tid man undervisat. Det har även varit kul och lärorikt att få hjälpa examensarbetarna i vår grupp. Tack *Billy Kaldvee*, *Henrik Fält*, *Mats Lundqvist*, *Märta Cassel-Engquist* och *Christoffer Björkwall* för att Ni valde att göra era examensarbeten hos oss.

The research work has been truly international with several visiting scientists in the lab. I would like to thank our Chinese friends *Zhang Zhiguo*, *Gao Hong*, and *Zhang Yungang* for nice joint laboratory work and for the hospitality during the visit at your home base in Harbin in the north east of China. Thanks also to the helpful *students of professor Zhang Zhiguo* who made us feel really welcome to their town.

Our lab has also been visited by the PhD student *Benjamin Anderson* from Ghana during longer periods. Thanks for nice joint work and interesting discussions. I am sorry that I was not so supportive as I wished to be during your last stay due to my parental leave of absence. Thanks also to the PhD students *Kimari Wangai* and *Robinson Ndegwa Gathoni* from Kenya as well as *Omar Marcillo* from Ecuador who visited our lab for longer periods. Thanks to the senior scientists *Kenneth Kaduki* from Kenya, *Ahmadou Wague* from Senegal, *Paul Kingsley Buah-Bassuah* from Ghana, and *Manny Mathuthu* from Zimbabwe for nice interactions not at least during the Workshop of Laser Spectroscopy in Development in Lund and the International Workshop on the Physics and Modern Applications of Lasers in Cameroon.

The collaboration within the EU financed cross-disciplinary research project about mercury emission from chlor-alkali plants managed by *Barbara Mazzolai* is highly appreciated. Thanks for the nice interactions and interdisciplinary exchange of knowledge during the project meetings in Göteborg, Bled, Pisa and Oslo. Thanks to *Ingvar Wängberg*, *John Munthe*, *Jonas Sommar*, *Romano Ferrara* and *Enrica Lanzillotta* for nice collaboration during the field campaigns in Sweden and Italy and to *Urszula Zielonka*, *Stanisław Hławiczka* and *Janina Fudala* for collab-

oration during the field campaign in Poland. Thanks also to the Doppler Lidar expert *Michael Bennett* for nice joint work in Italy. The support from *Göran Andersson* and *Janne Pettersson* and their co-workers at Eka Chemicals is also appreciated.

Utan ekonomiska bidrag av varierande storlek från olika håll hade inte forskningen varit möjlig. I detta sammanhang vill jag passa på att tacka *Fredrik Magnusson* på Fellessons byggvaror i Växjö för att han skänkte mig en massa frigolit att studera. Knut and Alice Wallenbergs stiftelse har generöst bidragit till vetenskaplig utrustning. Vetenskapsrådet har stått för en stor del av min finansiering liksom EU genom EU-DG XII Commission on Quality of Life and Management of Living Resources som stöttat arbetet inom det tidigare omnämnda tvärvetenskapliga projektet om kvicksilverutsläpp. Svenska rymdstyrelsen, svenska biståndsorganet SIDA samt det internationella programmet för fysikvetenskaper i Uppsala har också ekonomiskt gett stöd i projekt jag deltagit i. Avslutningsvis vill jag tacka för resestipendium från Landshövding Per Westlings minnesfond.

Sist men inte minst ett stort tack till *mina föräldrar, svärföräldrar och familj* för allt stöd genom åren. Tack *Josefin* för att Du har fått stå ut med mig under dessa ganska schemalösa år som doktorand med sena nätter i labbet och intensivt avhandlingskrivande på slutet. Vår lille *Albert* lyser ädlare än världens alla lasrar. Nu får pappa förhoppningsvis mer tid att tillsammans med Dig utforska vår omvärld.

# REFERENCES

---

1. A. L. Schawlow and C. H. Townes, "Infrared and optical masers," *Physical Review* **112**, 1940–1949 (1958).
2. J. Hecht, *Laser Pioneers* (Academic Press, 1991).
3. S. Johansson and V. S. Letokhov, "Astrophysical lasers operating in optical Fe II lines in stellar ejecta of  $\eta$  Carinae," *Astronomy & Astrophysics* **428**, 497–509 (2004).
4. T. H. Maiman, "Stimulated optical radiation in ruby," *Nature* **187**, 493–494 (1960).
5. A. E. Siegman, *Lasers* (University Science Books, Mill Valley, 1986).
6. O. Svelto, *Principles of lasers*, 4th ed. (Plenum Press, New York, 1998).
7. R. V. Steele, "Price erosion puts diodes in the doldrums - Review and forecast, part 2: Diode lasers," *Laser Focus World* (2006).
8. R. N. Hall, G. E. Fenner, J. D. Kingsley, T. J. Soltys, and R. O. Carlson, "Coherent light emission from GaAs junctions," *Physical Review Letters* **9**, 366–368 (1962).
9. M. I. Nathan, W. P. Dumke, G. Burns, F. H. Dill, Jr., and G. Lasher, "Stimulated emission of radiation from GaAs p-n junctions," *Applied Physics Letters* **1**, 62–64 (1962).
10. N. Holonyak, Jr. and S. F. Bevacqua, "Coherent (visible) light emission from  $Ga(As_{1-x}P_x)$  junctions," *Applied Physics Letters* **1**, 82–83 (1962).
11. T. M. Quist, R. H. Rediker, R. J. Keyes, W. E. Krag, B. Lax, A. L. McWhorter, and H. J. Zeigler, "Semiconductor maser of GaAs," *Applied Physics Letters* **1**, 91–92 (1962).
12. H. Kroemer, "A proposed class of heterojunction injection lasers," *Proc. IEEE* **51**, 1782 (1963).
13. Z. I. Alferov and R. F. Kazarinov, "Semiconductor laser with electric pumping," Inventor's certificate No. 181737 (U.S.S.R.), Application No. 950840, priority as of March 30 (1963).

14. Z. I. Alferov, V. M. Andreev, D. Z. Garbuzov, Y. V. Zhilyaev, E. P. Morozov, E. L. Portnoi, and V. G. Trofim, "Investigations of the influence of the AlAs-GaAs heterostructure parameters on the laser threshold current and the realization of continuous emission at room temperature," *Soviet Physics Semiconductors-USSR* **4**, 1573 (1971).
15. I. Hayashi, M. B. Panish, P. W. Foy, and S. Sumski, "Junction lasers which operate continuously at room temperature," *Applied Physics Letters*. **17**, 109–111 (1970).
16. H. Kroemer, *The 2000 Nobel lecture in physics: "Quasi-electric fields and band offsets: Teaching electrons new tricks"*, Nobel Lectures, Physics 1996-2000 (World Scientific Publishing Co, Singapore, 2002).  
<http://nobelprize.org>.
17. Z. I. Alferov, *The 2000 Nobel lecture in physics: "Double heterostructure concept and its applications in physics, electronics and technology"*, Nobel Lectures, Physics 1996-2000 (World Scientific Publishing Co, Singapore, 2002).  
<http://nobelprize.org>.
18. H. Ibach and H. Lüth, *Solid-state physics - An introduction to principles of materials science*, 3rd ed. (Springer-Verlag, Berlin Heidelberg NewYork, 2003).
19. J. R. Hook and H. E. Hall, *Solid state physics*, 2nd ed. (John Wiley & Sons Ltd, West Sussex, 1991).
20. S. Nakamura, M. Senoh, S. Nagahama, N. Iwasa, T. Yamada, T. Matsushita, H. Kiyoku, and Y. Sugimoto, "InGaN-based multi-quantum-well-structure laser diodes" *Japanese Journal of Applied Physics* **35**, 74 -76(1996).
21. S. Nakamura, "III-V Nitride based light-emitting devices," *Solid State Communications* **102**, 237–248 (1997).
22. "The Nichia Corporation," <http://www.nichia.co.jp/>.
23. H. Hirayama, T. Kyono, K. Akita, T. Nakamura, and K. Ishibashi, "High-efficiency uv LEDs using quaternary InAlGaN," *Electrical Engineering in Japan* **157**, 43–51 (2006).
24. R. W. Boyd, *Nonlinear optics* (Academic Press, New York, 1992).
25. R. L. Byer, "Nonlinear optics and solid-state lasers: 2000," *IEEE Journal On Selected Topics in Quantum Electronics* **6**, 911–930 (2000).
26. P. A. Franken, A. E. Hill, C. W. Peters, and G. Weinreich, "Generation of optical harmonics," *Physical Review Letters* **7**, 118–119 (1961).
27. M. Bass, P. A. Franken, J. F. Ward, and G. Weinreich, "Optical rectification," *Physical Review Letters* **9**, 446–448 (1962).
28. M. Bass, P. A. Franken, A. E. Hill, C. W. Peters, and G. Weinreich, "Optical mixing," *Physical Review Letters* **8**, 18 (1962).
29. A. W. Smith and N. Braslau, "Observation of an optical difference frequency," *Journal of Applied Physics* **34**, 2105–2106 (1963).
30. M. H. Chou, "Optical frequency mixers using three-wave mixing for optical fiber communications," Ph.D. dissertation, Stanford Univ., Stanford, CA (1999).

- 
31. U. Gustafsson, J. Sandsten, and S. Svanberg, "Simultaneous detection of methane, oxygen and water vapour utilizing near-infrared diode lasers in conjunction with difference frequency generation," *Applied Physics B* **71**, 853–857 (2000).
  32. J. Alnis, U. Gustafsson, G. Somesfalean, and S. Svanberg, "Sum-frequency generation with a blue diode laser for mercury spectroscopy at 254 nm," *Applied Physics Letters* **76**, 1234–1236 (2000).
  33. J. A. Giordmaine and R. C. Miller, "Tunable coherent parametric oscillation in  $\text{LiNbO}_3$  at optical frequencies," *Physical Review Letters* **14**, 973–976 (1965).
  34. M. H. Dunn and M. Ebrahimzadeh, "Parametric generation of tunable light from continuous-wave to femtosecond pulses," *Science* **286**, 1513–1517 (1999).
  35. S. E. Harris, "Tunable optical parametric oscillators," *Proceedings of the IEEE* **57**, 2096–2113 (1969).
  36. P. Weibring, J. N. Smith, H. Edner, and S. Svanberg, "Development and testing of a frequency-agile optical parametric oscillator system for differential absorption lidar," *Review of Scientific Instruments* **74**, 4478–4484 (2003).
  37. P. Weibring, H. Edner, and S. Svanberg, "Versatile mobile lidar system for environmental monitoring," *Applied Optics* **42**, 3583–3594 (2003).
  38. B. H. Bransden and C. J. Joachain, *Physics of atoms and molecules*, 2nd ed. (Pearson Education Limited, Essex, 2003).
  39. S. Svanberg, *Atomic and molecular spectroscopy - basic aspects and practical applications*, 4th ed. (Springer-Verlag, Berlin Heidelberg, 2004).
  40. J. Humlicek, "An efficient method for evaluation of the complex probability function: The Voigt function and its derivatives," *Journal of Quantitative Spectroscopy & Radiative Transfer* **21**, 309–313 (1979).
  41. J. Humlicek, "Optimized computation of the Voigt and the complex probability function," *Journal of Quantitative Spectroscopy & Radiative Transfer* **27**, 437–444 (1982).
  42. H. C. van de Hulst, *Light scattering by small particles* (Wiley, New York, 1957).
  43. H. C. van de Hulst, *Light scattering by small particles* (Dover publications, New York, 1981).
  44. L. G. Henyey and J. L. Greenstein, "Diffuse radiation in the galaxy," *Astrophys. J.* **93**, 70–83 (1941).
  45. J. Swartling, "Biomedical and atmospheric applications of optical spectroscopy in scattering media," PhD Thesis, Lund Reports on Atomic Physics **LRAP-290**, Lund University (2002).
  46. A. J. Welch, M. J. C. van Gemert, W. M. Star, and B. C. Wilson, *Optical-thermal response of laser-irradiated tissue*, chap. Definitions and overview of tissue optics (Plenum Press, New York, 1995).
  47. M. S. Patterson, B. Chance, and B. C. Wilson, "Time resolved reflectance and transmittance for the non-invasive measurement of tissue optical properties," *Applied Optics* **28**, 2331–2336 (1989).

48. R. C. Haskell, L. O. Svaasand, T. T. Tsay, T. C. Feng, M. S. McAdams, and B. J. Tromberg, "Boundary-conditions for the diffusion equation in radiative-transfer," *Journal of the Optical Society of America A* **11**, 2727–2741 (1994).
49. T. J. Farrell, M. S. Patterson, and B. Wilson, "A diffusion theory model of spatially resolved, steady-state diffuse reflectance for the noninvasive determination of tissue optical properties," *Medical Physics* **19**, 879–888 (1992).
50. S. R. Arridge, M. Cope, and D. T. Delpy, "The theoretical basis for the determination of optical path lengths in tissue: temporal and frequency analysis," *Physics in Medicine and Biology* **37**, 1531–1560 (1992).
51. I. Martinsson and L. J. Curtis, "Janne Rydberg - his life and work," *Nuclear Instruments and Methods in Physics Research B* **235**, 17–22 (2005).
52. "The International Conference on Tunable Diode Laser Spectroscopy," <http://tdls.conncoll.edu/>.
53. E. I. Moses and C. L. Tang, "High-sensitivity laser wavelength-modulation spectroscopy," *Optics Letters* **1**, 115–117 (1977).
54. G. C. Bjorklund, "Frequency-modulation spectroscopy: a new method for measuring weak absorptions and dispersions," *Optics Letters* **5**, 15–17 (1980).
55. W. Lenth, "High frequency heterodyne spectroscopy with current-modulated diode lasers," *IEEE Journal of Quantum Electronics* **QE-20**, 1045–1050 (1984).
56. G. R. Janik, C. B. Carlisle, and T. F. Gallagher, "2-tone frequency-modulation spectroscopy," *J. Opt. Soc. Am. B* **3**, 1070–1074 (1986).
57. P. Kauranen, "Near-infrared diode laser frequency-modulation spectroscopy for high-sensitivity gas analysis," PhD Thesis, Lund Reports on Atomic Physics **LRAP-185**, Lund University (1995).
58. V. G. Avetisov, "High-sensitivity high-resolution diode laser spectroscopy in the near-infrared region," PhD Thesis, Lund Reports on Atomic Physics **LRAP-189**, Lund University (1996).
59. U. Gustafsson, "Diode laser spectroscopy in extended wavelength ranges," PhD Thesis, Lund Reports on Atomic Physics **LRAP-253**, Lund University (2000).
60. G. Somesfalean, "Environmental monitoring using diode-laser-based spectroscopic techniques," PhD Thesis, Lund Reports on Atomic Physics **LRAP-329**, Lund University (2004).
61. J. M. Supplee, E. A. Whittaker, and W. Lenth, "Theoretical description of frequency modulation and wavelength modulation spectroscopy," *Applied Optics* **33**, 6294–6302 (1994).
62. L. Råde and B. Westergren, *Beta Mathematics Handbook*, 2nd ed. (Studentlitteratur, 1993). 118.
63. J. A. Silver, "Frequency-modulation spectroscopy for trace species detection: theory and comparison among experimental methods," *Applied Optics* **31**, 707–717 (1992).

- 
64. M. De Rosa, A. Ciucci, D. Pelliccia, C. Gabbanini, S. Gozzini, and A. Lucchesini, "On the measurement of pressure induced shift by diode lasers and harmonic detection," *Optics Communications* **147**, 55–60 (1998).
  65. R. Arndt, "Analytical line shapes for Lorentzian signals broadened by modulation," *Applied Physics* **36**, 2522–2524 (1965).
  66. J. Reid and D. Labrie, "Second-harmonic detection with tunable diode lasers comparison of experiment and theory," *Applied Physics B* **26**, 203–210 (1981).
  67. P. Martin and J. Puerta, "Generalized Lorentzian approximations for the Voigt line shape," *Applied Optics* **20**, 259–263 (1981).
  68. J. Puerta and P. Martin, "Three and four generalized Lorentzian approximations for the Voigt line shape," *Applied Optics* **20**, 3923–3928 (1981).
  69. P. Kluczynski, J. Gustafsson, Å. M. Lindberg, and O. Axner, "Wavelength modulation absorption spectrometry – an extensive scrutiny of the generation of signals," *Spectrochimica Acta Part B* **56**, 1277–1354 (2001).
  70. "Försvarets historiska telesamlingar," <http://www.fht.nu/>.
  71. L. D. Smullin and G. Fiocco, "Optical echoes from the Moon," **194**, 1267 (1962).
  72. C. González Alonzo, T. Gasmi, and A. G. Urena. "Dial remote sensed ethylene and ozone-ethylene correlation in presence of urban NO<sub>x</sub>," *Journal of Atmospheric Chemistry* **50**, 159–169 (2005).
  73. R. Grönlund, L. Persson, M. Sjöholm, M. Andersson, and S. Svanberg, "Studies of free gas in scattering media at micro- and macroscopic scales," *International Symposium on Biophotonics, Nanophotonics and Metamaterials in Hangzhou, China* (2006).
  74. R. M. Schotland, "Some observations of the vertical profile of water vapor by laser optical radar," *Proceeding 4th Symposium on Remote Sensing of the Environment, Univ. of Michigan, Ann Arbor* (1966).
  75. P. Weibring, T. Johansson, H. Edner, S. Svanberg, B. Sundnér, V. Raimondi, G. Cecchi, and L. Pantani, "Fluorescence lidar imaging of historical monuments," *Applied Optics* **40**, 6111–6120 (2001).
  76. R. Grönlund, J. Hällström, S. Svanberg, and K. Barup, "Fluorescence lidar multispectral imaging for diagnosis of historical monuments – Övedskloster a Swedish case study," *Proceedings LACONA VI (Lasers in CONservation of Artworks)* (2005).
  77. A. D. Dernfalk, M. Bengtsson, R. Grönlund, M. Sjöholm, P. Weibring, H. Edner, S. M. Gubanski, S. Kröll, and S. Svanberg, "Laser-induced fluorescence spectroscopy for detection of biological contamination on composite insulators," *XIIIth International Symposium on High Voltage Engineering, Delft* (August 2003) .
  78. M. Bengtsson, R. Grönlund, M. Sjöholm, C. Abrahamsson, A. D. Dernfalk, S. Wallström, A. Larsson, P. Weibring, S. Karlsson, S. M. Gubanski, S. Kröll, and S. Svanberg, "Fluorescence lidar imaging of fungal growth on high-voltage outdoor composite insulators," *Optics and Lasers in Engineering* **43**, 624–632 (2005).

79. M. Bengtsson, S. Wallström, M. Sjöholm, R. Grönlund, B. Anderson, A. Larsson, S. Karlsson, S. Kröll, and S. Svanberg, "Fungus covered insulator materials studied with laser-induced fluorescence and principal component analysis," *Applied Spectroscopy* **59**, 1037–1041 (2005).
80. R. Grönlund, M. Lundqvist, and S. Svanberg, "Remote imaging laser-induced breakdown spectroscopy and remote cultural heritage ablative cleaning," *Optics Letters* **30**, 2822–2824 (2005).
81. W. F. Dabberdt, G. L. Frederick, R. M. Hardesty, W. C. Lee, and K. Underwood, "Advances in meteorological instrumentation for air quality and emergency response," *Meteorology and Atmospheric Physics* **87**, 57–88 (2004).
82. M. Bennett, H. Edner, R. Grönlund, M. Sjöholm, S. Svanberg, and R. Ferrara, "Joint application of Doppler Lidar and differential absorption lidar to estimate the atomic mercury flux from a chlor-alkali plant," *Atmospheric Environment* **40**, 664–673 (2006).
83. S. Svanberg, "Environmental and medical applications of photonic interactions," *Physica Scripta* **T110**, 39–50 (2004).
84. S. Andersson-Engels, R. Berg, S. Svanberg, and O. Jarlman, "Time-resolved transillumination for medical diagnostics," *Optics Letters* **15**, 1179–1181 (1990).
85. G. Müller, B. Chance, R. Alfano, S. Arridge, J. Beuthan, E. Gratton, M. Kaschke, B. Masters, S. Svanberg, and P. van der Zee, eds., *Medical optical tomography: Functional imaging and monitoring*, vol. 11 of *SPIE Institute Series* (Society of Photo-Optical Instrumentation Engineers, Bellingham, Washington, 1993).
86. J. C. Hebden, S. R. Arridge, and D. T. Delpy, "Optical imaging in medicine: I. Experimental techniques," *Physics in Medicine and Biology* **42**, 825–840 (1997).
87. W. M. Star, "Light dosimetry *in vivo*," *Physics in Medicine and Biology* **42**, 763–787 (1997).
88. Y. Mendelson, A. C. Clermont, R. A. Peura, and B.-C. Lin, "Blood glucose measurement by multiple attenuated total reflection and infrared absorption spectroscopy," *IEEE Transactions on Biomedical Engineering* **37**, 458–465 (1990).
89. A. Roggan, M. Friebel, K. Dörschel, A. Hahn, and G. Müller, "Optical properties of circulating human blood in the wavelength range 400–2500 nm," *Journal of Biomedical Optics* **4**, 36–46 (1999).
90. G. Hungerford and D. J. S. Birch, "Single-photon timing detectors for fluorescence lifetime spectroscopy," *Measurement Science & Technology* **7**, 121–135 (1996).
91. J. Karolczaka, D. Komara, J. Kubickia, T. Wróźowa, K. Dobeka, B. Ciesielska, and A. Maciejewski, "The measurements of picosecond fluorescence lifetimes with high accuracy and subpicosecond precision," *Chemical Physics Letters* **344**, 154–164 (2001).
92. B. Chance, M. Cope, E. Gratton, N. Ramanujam, and B. Tromberg, "Phase measurement of light absorption and scatter in human tissue," *Review of Scientific Instruments* **69**, 3457–3481 (1998).

- 
93. H. Fält, "Determination of optical path lengths in scattering media by intensity modulated light in connection with gas in scattering media absorption spectroscopy," Master's Thesis, Lund Reports on Atomic Physics **LRAP-323**, Lund University (2004).
  94. F. Schael and O. Reich, "In-situ analysis of heterogeneous media with frequency and intensity modulated diode lasers," *Technisches Messen* **68**, 448–455 (2001).
  95. M. Sjöholm, G. Somesfalean, J. Alnis, and S. Svanberg, "Strongly absorbing gas in scattering media studied by diode laser based spectroscopy," Manuscript in preparation (2006).
  96. A. J. McMichael, R. E. Woodruff, and S. Hales, "Climate change and human health: present and future risks," *Lancet* **367**, 859–869 (2006).
  97. M. L. Khandekar, T. S. Murty, and P. Chittibabu, "The global warming debate: A review of the state of science," *Pure and Applied Geophysics* **162**, 1557–1586 (2005).
  98. T. M. Lenton, "Climate change to the end of the millenium," *Climatic Change* **76**, 7–29 (2006).
  99. S. K. Foong, "An accurate analytical solution of a zero-dimensional greenhouse model for global warming," *European Journal of Physics* **27**, 933–942 (2006).
  100. J. Zhang, T. J. Griffis, and J. M. Baker, "Using continuous stable isotope measurements to partition net ecosystem CO<sub>2</sub> exchange," *Plant, Cell and Environment* **29**, 483–496 (2006).
  101. M. E. Trudeau, P. Chen, G. de Andrade Garcia, L. W. Hollberg, and P. P. Tans, "Stable isotopic analysis of atmospheric methane by infrared spectroscopy by use of diode laser difference-frequency generation," *Applied Optics* **45**, 4136–4141 (2006).
  102. J. N. Galloway, "Acidification of the world: natural and antropogenic," *Water, Air, and Soil Pollution* **130**, 17–24 (2001).
  103. L. Rodríguez-Lado and F. Macías, "Calculation and mapping of critical loads of sulphur and nitrogen for forest soils in Galicia (NW Spain)," *Science of the Total Environment* **366**, 760–771 (2006).
  104. D. Burtraw, D. A. Evans, A. Krupnick, K. Palmer, and R. Toth, "Economics of pollution trading for SO<sub>2</sub> and NO<sub>x</sub>," *Annual Review of Environment and Resources* **30**, 253–289 (2005).
  105. P. Weibring, H. Edner, S. Svanberg, G. Cecchi, L. Pantani, R. Ferrara, and T. Caltabiano, "Monitoring of volcanic sulphur dioxide emissions using Differential Absorption Lidar (DIAL), Differential Optical Absorption Spectroscopy (DOAS) and Correlation Spectroscopy (COSPEC)," *Applied Physics B* **67**, 419–426 (1998).
  106. F. Xu, Z. Lv, Y. G. Zhang, G. Somesfalean, and Z. G. Zhang, "Concentration evaluation method using broadband absorption spectroscopy for sulfur dioxide monitoring," *Applied Physics Letters* **88**(231109) (2006).
  107. "The UNECE protocol on heavy metals," [http://www.unece.org/env/lrtap/hm\\_h1.htm](http://www.unece.org/env/lrtap/hm_h1.htm).

108. "The website of the ESPREME project," <http://espreme.iier.uni-stuttgart.de/>.
109. I. S. Osborne, "APPLIED PHYSICS: Monitoring Mercury," *Science* **303**(5665), 1733 (2004). (In Editors' Choice: Highlights of the recent literature, i.e., Paper II of this thesis).
110. "The website of the EMECAP project," <http://www.emecap.com/>.
111. "The final report of the EMECAP project," [http://ec.europa.eu/research/quality-of-life/ka4/pdf/report\\_emecap\\_en.pdf](http://ec.europa.eu/research/quality-of-life/ka4/pdf/report_emecap_en.pdf).
112. B. Mazzolai, V. Mattoli, V. Raffa, G. Tripoli, P. Dario, R. Ferrara, E. Lanzilotta, J. Munthe, I. Wängberg, L. Barregård, G. Sällsten, M. Horvat, D. Gibicar, V. Fajon, M. Logar, P. Pacyna, B. Denby, S. Svanberg, H. Edner, R. Grönlund, M. Sjöholm, P. Weibring, A. Donati, S. Baldacci, W. Vigano, A. Pannocchia, R. Fontanelli, S. La Manna, S. Di Bona, J. Fudala, U. Zielonka, S. Hławiczka, D. Jarosinska, A. Danet, and C. Bratu, "A multidisciplinary approach to study the impact of mercury pollution on human health and environment: the EMECAP project," in *Proceedings from the Seventh International Conference on Mercury as a Global Pollutant, Ljubljana* (2004).
113. I. Wängberg, L. Barregård, G. Sällsten, M. Haeger-Eugensson, J. Munthe, and J. Sommar, "Emissions, dispersion and human exposure of mercury from a Swedish chlor-alkali plant," *Atmospheric Environment* **39**, 7451–7458 (2005).
114. H. B. Stifton, "Air-space tissue in plants," *The Botanical Review* **XI**, 108–143 (1945).
115. H. B. Stifton, "Air-space tissue in plants II," *The Botanical Review* **XXIII**, 303–312 (1957).
116. M. Sjöholm, "Porositet hos kulturväxter - en vandring bland ihåligheter," in *Kulturväxtkurs 2000 specialarbeten* (Department of Crop Science, Swedish University of Agricultural Sciences, Alnarp, 2000).
117. A. G. Calbo and A. A. Nery, "Methods for measurement of gas volume of fruits and vegetables," *Journal of The American Society for Horticultural Science* **120**, 217–221 (1995).
118. I. Raskin, "A method for measuring leaf volume, density, thickness and internal gas volume," *Hortscience* **18**, 698–699 (1983).
119. H. Baumann and J. Henze, "Intercellular space volume of fruit," *Acta Horticulturae* **138**, 107–111 (1983).
120. K. J. Niklas, *Plant biomechanics* (The University of Chicago Press, Chicago & London, 1992).
121. J. T. Woolley, "Reflectance and transmittance of light by leaves," *Plant Physiology* **47**, 656–662 (1971).
122. J. Johansson, R. Berg, A. Pifferi, S. Svanberg, and L. O. Björn, "Time-resolved studies of light propagation in *Crassula* and *Phaseolus* leaves," *Photochemistry and Photobiology* **69**, 242–247 (1999).

- 
123. M. M. Blanke, "Respiration of apple and avocado fruits," *Postharvest News and Information* **2**, 429–436 (1991).
  124. S. P. Burg and E. A. Burg, "Gas exchange in fruits," *Physiologia Plantarum* **18**, 870–884 (1965).
  125. L. Persson, K. Svanberg, and S. Svanberg, "On the potential of human sinus cavity diagnostics using diode laser gas spectroscopy," *Applied Physics B* **82**, 313–317 (2006).
  126. L. Persson, M. Andersson, E. Kristensson, L. Simonsson, S. Andersson-Engels, K. Svanberg, and S. Svanberg, "Monte Carlo simulations of optical human sinusitis diagnostics," Manuscript in preparation (2006).
  127. J. Johansson, S. Folestad, S. Svanberg, M. Sjöholm, G. Somesfalean, C. Abrahamsson, and S. Andersson-Engels, "Method of analyzing a pharmaceutical sample," Patent Applications SE0200782D (2002), WO03078983 (2003), CA2475934 (2003), AU2003214401 (2003), MXPA04008719 (2004), EP1488213 (2004), JP2005520152T (2005), CN1643366 (2005), US2005173637 (2005), and NZ534526 (2006).
  128. C. Abrahamsson, J. Johansson, S. Andersson-Engels, S. Svanberg, and S. Folestad, "Time-resolved NIR spectroscopy for quantitative analysis of intact pharmaceutical tablets," *Analytical Chemistry* **77**, 1055–1059 (2005).
  129. T. Svensson, C. Abrahamsson, L. Persson, M. Sjöholm, G. Somesfalean, S. Andersson-Engels, S. Svanberg, J. Johansson, and S. Folestad, "Non-invasive determination of porosity in solids by diode laser oxygen spectroscopy: Application to pharmaceutical tablets," The 31st conference of the Federation of Analytical Chemistry and Spectroscopy Societies (FACSS), Portland, Oregon (2004).
  130. T. Kudra, "Energy aspects in drying," *Drying Technology* **22**, 917–932 (2004).
  131. P. Dufour, "Control engineering in drying technology: Review and trends," *Drying Technology* **24**, 889–904 (2006).
  132. C. Strumillo, "Perspectives on developments in drying," *Drying Technology* **24**, 1059–1068 (2006).
  133. M. Andersson, L. Persson, M. Sjöholm, and S. Svanberg, "Apparatus and method for determining the moisture content in porous media using optical spectroscopy," Swedish Patent Application (2006).
  134. H. G. Jones, "Carbon dioxide exchange of developing apple (*Malus pumila* Mill.) fruits," *Journal of Experimental Botany* **32**, 1203–1210 (1981).
  135. U. Gustafsson, S. Pålsson, and S. Svanberg, "Compact fiber-optic fluorosensor using a continuous-wave violet diode laser and an integrated spectrometer," *Review of Scientific Instruments* **71**, 3004–3006 (2000).
  136. S. Svanberg, "Laser spectroscopy in development," *Europhysics News* **33** (2002).
  137. C. Björkwall and M. Cassel-Engquist, "Establishing a diode laser absorption spectroscopy laboratory in Quito, Ecuador," Master's Thesis, Lund Reports on Atomic Physics **LRAP 347**, Lund University (2005).

138. A. S. Ndao, A. Konté, M. Biaye, M. E. Faye, N. A. B. Faye, and A. Wagué, “Analysis of chlorophyll fluorescence spectra in some tropical plants,” *Journal of Fluorescence* **15**, 123–129 (2005).
139. B. Anderson, P. K. Buah-Bassuah, and J. P. Tetteh, “Using violet laser-induced chlorophyll fluorescence emission spectra for crop yield assessment of cowpea (*Vigna unguiculata (L) Walp*) varieties,” *Measurement Science and Technology* **15**, 1255–1265 (2004).
140. “The LAM Network,” <http://www.lamnetwork.org>.
141. S. Svanberg, M. Sjöholm, and G. Somesfalean, “Method and device for investigation of a surface layer,” Patent Applications SE0201359D (2002), WO03093803 (2003), AU2003224589 (2003), EP1499873 (2005), and US2005148092 (2005).

# PAPERS



# PAPER I

## **Atmospheric mercury near a chlor-alkali plant in Sweden**

I. Wängberg, H. Edner, R. Ferrara, E. Lanzillotta, J. Munthe,  
J. Sommar, M. Sjöholm, S. Svanberg, and P. Weibring.

*The Science of the Total Environment* **304**, 29–41 (2003).





ELSEVIER

The Science of the Total Environment 304 (2003) 29–41

**the Science of the  
Total Environment**An International Journal for Scientific Research  
into the Environment and its Relationship with Man

www.elsevier.com/locate/scitotenv

## Atmospheric mercury near a chlor-alkali plant in Sweden

Ingvar Wängberg<sup>a,\*</sup>, Hans Edner<sup>b</sup>, Romano Ferrara<sup>c</sup>, Enrica Lanzillotta<sup>c</sup>, John Munthe<sup>a</sup>,  
Jonas Sommar<sup>d</sup>, Mikael Sjöholm<sup>b</sup>, Sune Svanberg<sup>b</sup>, Petter Weibring<sup>b</sup>

<sup>a</sup>*IVL Swedish Environmental Research Institute, P.O. Box 47086, Göteborg S-40258, Sweden*

<sup>b</sup>*Department of Physics, Lund Institute of Technology, P.O. Box 118, Lund S-22100, Sweden*

<sup>c</sup>*CNR-Institute of Biophysics (CNR-IB), Via G. Moruzzi, 1, Pisa 56124, Italy*

<sup>d</sup>*Inorganic Chemistry, Department of Chemistry, Göteborg University, Göteborg S-41296, Sweden*

Received 20 February 2002; accepted 15 October 2002

### Abstract

Atmospheric mercury species/fractions were measured near a chlor-alkali plant in Sweden during August 28 to September 4, 2001. The concentration of total gaseous mercury in the plume from the plant was measured using TEKRA and GARDIS instruments. Gaseous elemental mercury was measured using a light detection and ranging (LIDAR) technique. From vertical LIDAR sweeps through the plume from the chlor-alkali plant mercury emission rates could be calculated. The concentrations of reactive gaseous mercury (RGM) in the plume and also inside the cell house were measured using annular KCl coated denuders. The RGM emission constitutes 0.5–1.0% of the total mercury emitted from the plant. The mercury concentration adsorbed on particles was measured as well as the mercury flux from soil. The data presented also include an intercomparison showing an excellent agreement between TEKRA/GARDIS and LIDAR gaseous mercury measurements.

© 2003 Elsevier Science B.V. All rights reserved.

**Keywords:** Atmospheric mercury; Chlor-alkali; Emission rates

### 1. Introduction

Pollution of the environment by mercury remains a major concern in many regions. Measures to control releases to air and water have been implemented in many countries in Europe and North America. Despite this, mercury levels in freshwater fish remain elevated and further cuts may be warranted. Recently, an international agreement on emission controls of mercury has been signed by 32 countries from Europe, the USA and

Canada, within the framework of the LRTAP convention of the UN-ECE (UN-ECE, 1998). As the requirements on industry and utilities to reduce mercury emissions to the atmosphere increases, the demand for quantitative descriptions of source–receptor relationships increases.

Mercury is an atmospheric pollutant with a complex biogeochemical cycle. The atmospheric cycling includes chemical oxidation/reduction in both gaseous and aqueous phases, deposition and re-emission from natural surfaces in addition to emissions from both natural and anthropogenic sources (Schroeder and Munthe, 1998).

\*Corresponding author. Fax: +46-31-725-6290.

E-mail address: Ingvar.Wangberg@ivl.se (I. Wängberg).



Fig. 1. The river valley of Göta älv.

In the atmosphere, mercury exists in three different forms; elemental mercury vapour ( $\text{Hg}^0$ ); gaseous divalent compounds [ $\text{Hg}(\text{II})$ ]; and associated with particulate matter [ $\text{Hg}(\text{p})$ ]. The three different species have different atmospheric behaviour and lifetimes.  $\text{Hg}^0$  is stable with a lifetime in the range of 0.5–2 years and is thus capable of distribution on a global scale.  $\text{Hg}(\text{II})$  and  $\text{Hg}(\text{p})$  are more readily deposited on local to regional scales via wet or dry processes.

The results presented here are the outcome of a measurement campaign made at the Eka Chemicals in Bohus, Sweden. The measurements were made within the on-going EU-project EMECAP (European Mercury Emission from Chlor-Alkali Plants). The mercury emission from chlor-alkali industry in Europe constitutes 14% of the total anthropogenic mercury emission (Pacyna et al., 2001). Part of the project is aimed at investigating the environmental impact of mercury emission within the local environment of one chlor-alkali plant in Sweden and one in Italy.

The Eka Chemicals plant in Bohus, is situated in the river valley of Göta älv, 20-km north of the city of Göteborg (see Fig. 1). The company is part of the great Akzo Nobel nv concern with headquarters in the Netherlands. Apart from the chlorine and alkali production, bulk industrial chemicals for pulp and paper, pharmaceutical and plastic industry are also manufactured. The industrial unit consists of many factories as well as

administrative and laboratory buildings located on a 200 000  $\text{m}^2$  large area along the Eastern Shore of the Göta älv River.

The chlor-alkali production in Bohus started 1924 and uses the mercury method. Today the annual chlorine production amounts to 80 000 t. Great efforts have been made to reduce the emissions of mercury. Hence, the direct emission of mercury to air from the chlor-alkali production is according to the companies own measurements, approximately 0.4 g per ton of chlorine produced. This number is low in comparison to 1.5–2 g per ton of chlorine as reported to be valid for European chlor-alkali producers (Ayres, 1997; Ferrara et al., 1992a).

Here we present the result from measurements of mercury in the plume from the cell house of the chlor-alkali unit as well as some measurements made inside of the cell house. Elemental gaseous mercury, oxidised and particulate mercury was measured. Mercury degassing rates from soil at two selected places is also presented.

A LIDAR technique was used to measure the concentration of mercury in the plume from the plant. With this method the total atomic mercury flux from the plant can be measured. The result of this measurement will be presented and compared with Eka Chemicals own regular measurements.

Three different techniques were employed to measure mercury vapour ( $\text{Hg}^0$ ) and based on the data an intercomparison is presented.

## 2. Methods

A small part of the Eka Chemicals industrial area is shown in Fig. 2. The cell house building where the chlor-alkali is produced is indicated as well as the sampling site where mercury air samples were collected. Mercury vapours are exhausted via an opening in the ceiling. The ceiling vent is 13 m above the ground and is protected by a roof, see Fig. 2. The air is ventilated out on both sides of the long ceiling vent. The distance between the measurement site and the cell house is approximately 70 m. Since, the buildings immediately to the left of the sampling site are low (only 4 m), the mercury plume from the cell house

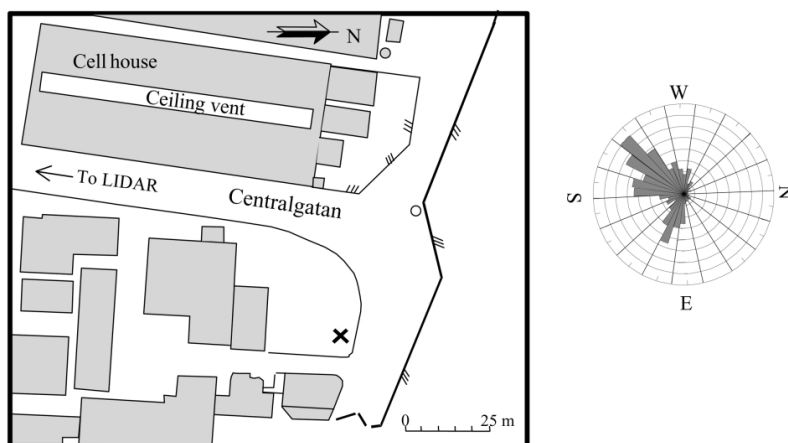


Fig. 2. The Northern end of the Eka Chemicals plant. The measurement site where TGM, TPM and RGM measurements were performed is indicated as (x). Also shown is a frequency plot showing the prevailing wind directions during the measurement campaign.

occasionally passes over the measurement site without interferences.

### 2.1. Sampling and analysis of total gaseous mercury (TGM) and gaseous elemental mercury (GEM)

Total gaseous mercury (TGM) refers to gaseous elemental mercury ( $\text{Hg}^0$  hereafter denoted GEM) and small contributions, in this context  $<1\%$  (see below), from other gaseous mercury species that also may be trapped by the sampler and detected as  $\text{Hg}^0$ . To measure TGM two different instruments were used, the TEKRA and the GARDIS instruments, both of which utilise the Au-amalgamation principle during accumulative sampling cycles. Additionally, a mobile LIDAR set-up was employed to measure GEM. These three techniques are described below.

The Tekran mercury vapour analyser (Model 2537A) is an automatic instrument. The pre-filtered sample air stream is pulled through gold cartridges where the mercury is collected. The mercury is then thermally desorbed in an argon gas stream and detected by an integrated atomic fluorescence spectrophotometer (AFS) (Tekran,

1998). The instrument utilises two gold cartridges in parallel, with alternating operation modes (sampling and desorbing/analysing) on a predefined time base of 5 min. A 47-mm diameter Teflon pre-filter protects the sampling cartridges against contamination by particulate matter. A sampling flow rate of  $1.5 \text{ l min}^{-1}$  was used. Under these conditions the detection limit is roughly  $0.15 \text{ ng m}^{-3}$  and the precision  $\pm 10\%$  calculated as 1 S.D. The accuracy and precision of this instrument has recently been assessed in measurements inter-comparisons performed at various locations (Schroeder et al., 1995; Munthe et al., 2001). TGM data with 5-min time resolution were continuously obtained during the campaign.

The mercury vapour analyser GARDIS-3 is a portable automatic instrument. The sampled air is pre-filtered using a 25-mm diameter PTFE membrane filter to protect the analyser gas inlet from contamination by aerosol particles. Atmospheric mercury is collected on a concentrating gold trap, thermally desorbed and recollected on an analytical gold trap. A second thermal desorption step allows mercury determination by atomic absorption spectrophotometry. A sampling flow rate of  $0.5 \text{ l min}^{-1}$  and a sampling time of 10 min

were used. The time interval between two consecutive mercury determinations was 30 min. Under these conditions the detection limit was  $0.1 \text{ ng m}^{-3}$ . The accuracy and precision of this instrument has recently been assessed in measurements inter-comparisons performed at various locations (Ebinghaus et al., 1999; Munthe et al., 2001).

The GARDIS and the TEKRAN instruments were operated in parallel measuring at the same spot, 1.5 m above ground, 70 m north-east of the cell house, as indicated in Fig. 2, throughout the whole campaign. Both instruments were calibrated on site by injecting known amount of elemental mercury saturated air from a mercury vapour generator kept at a constant temperature of  $4.0 \pm 0.02 \text{ }^\circ\text{C}$  using a  $50 \text{ }\mu\text{l}$  Hamilton gas-tight micro-syringe.

The mobile LIDAR system was most of the time positioned approximately 350 m south of the main cell-house. This enabled measurements to be performed at low heights along the main street within the plant, Centralgatan, and with a possibility to perform vertical scans through the plume during southwest/northwest wind directions. Another position at Strandgatan near the Göta älv River was occasionally used during easterly winds.

Basic descriptions of the LIDAR system and measurement technique have been published (e.g. Edner et al., 1995; Weibring et al., 1998). Differential absorption LIDAR (DIAL) measurements were performed during this campaign using an optical parametric oscillator as the tuneable laser source. The laser transmitter operates at 20-Hz repetition frequency with wavelength switching for the on- and off-resonance transmission between every shot. After frequency doubling a pulse energy of typically 5 mJ was achieved in the UV region. The mercury resonance line near 254 nm was used as the absorption wavelength, which means that only the atomic form of mercury, i.e. GEM is detected. An internal calibration unit using small Hg cells with known lengths and temperatures was used to monitor and compensate for small laser wavelength and linewidth changes. The outgoing laser beam is directed coaxially with a vertically mounted telescope and transmitted into the atmosphere via a large flat mirror in a retract-

able transmitting/receiving dome on the roof. Stepping motors are used to turn the dome and to tilt the mirror. The DIAL measurements resulted in range-resolved data of the mercury concentration profile along the laser beam direction. Two-dimensional images of the mercury distribution in the spreading plume can be produced by scanning the laser beam in a vertical plane. Combined with wind data, such vertical scans were used to evaluate the mercury flux from the plant. The mercury emission obtained was compared with Eka Chemical's own emission measurements. Two separate systems are in use in the ceiling vent. With the first, air is drawn through impingers containing  $\text{KMnO}_4/\text{H}_2\text{O}_4$  aqueous solutions. Six such impingers are placed along the narrow ceiling vent. The airflow and the temperature at each measurement point is also measured. A 24-h sample is collected once a week and the total flux is calculated based on the mercury concentrations and airflows at these six points along the ceiling vent. Hence, 52 such 24-h average emission values are obtained per year and used to calculate annual average mercury emission values. In addition to this, an UV-absorption Hg-detector (HG-Monitor 3000, Seefelder Messtechnik), allowing high time resolved continuous Hg measurements, is mounted on a mobile system. Normally, the Hg-detector is slowly moving back and forth along the ceiling vent. Mercury concentrations together with airflow and the air temperature are also continuously monitored with the mobile unit. Mercury concentrations, the mercury flux and the position of the monitor are displayed in the control room of the cell house. This system is mainly used to quickly detect leaking cells etc.

During some hours in the end of the campaign a comparison was made using GARDIS, TEKRAN and the LIDAR set-up. During this experiment the GARDIS and TEKRAN instrument were fed with air from 3 m above ground at a location 30 m north of the cell house. The LIDAR was adjusted to measure the average concentration of GEM in a volume centred close to same spot as the intake of the two other instruments. An open circle in Fig. 2 indicates the location of this place.

## 2.2. Sampling and analysis of total particulate mercury (TPM)

A new method for sampling and analysis of TPM was used. The method is based on the AES mini trap developed by Lu et al. (1998). A quartz micro-fibre filter (Munktell MK 360), of 7-mm diameter is housed in a quartz glass tube of 140-mm length. The filter is supported by a pure Ni-screen grid. The sampling device serves as both particulate trap and pyrolyzer for airborne particulate species. Air is drawn through the quartz tube at a flow rate of 4–6 l min<sup>-1</sup>. After sampling, the Hg content is analysed via pyrolysis where the trap is heated to 900 °C in a stream of argon or nitrogen. In this step, the Hg is reduced to GEM and is subsequently transferred to the gas phase and detected by conventional amalgamation—thermal desorption-atomic fluorescence spectrometric detection or alternatively using atomic absorption. To bring down blanks to a minimum the TPM traps were cleaned by pyrolysis at the sampling site prior to sampling. Parallel samples were collected and analysed at the site using atomic fluorescence spectrometric detection (IVL) and atomic absorption detection (CNR). Sampling periods were varied between 1 and 21 h.

## 2.3. Methods for the determination of reactive gaseous mercury (RGM) in ambient air

RGM is an operational defined gaseous mercury fraction present in ambient air. However, it is believed that RGM to the most part consist of mercury dichloride (HgCl<sub>2</sub>), but other divalent mercury species are also conceivable. In the vicinity of the plant, RGM is likely to mainly constitute of mercury chlorides like HgCl<sub>2</sub> and Hg<sub>2</sub>Cl<sub>2</sub>. The term reactive mercury refers to mercury compounds that easily undergoes reduction to elemental mercury in the analysis step. These species adsorb to solid KCl matrixes and RGM can, therefore, be sampled using KCl coated denuders. Tubular as well as annular denuder techniques have previously been used. The analysis of RGM trapped on denuders may consist of extraction with MQ-water, followed by SnCl<sub>2</sub> reduction, pre-concentration and measurement by CVAFS. Alternatively, the denuder can be analysed by heating to 500 °C, which converts the RGM to GEM, which is subsequently measured using the standard CVAFS procedure. Automated sampling techniques with annular denuders and thermo-reduction-CVAFS detection are also in use (Tekran 1998; Sommar et al., 1999). Mist chambers, con-

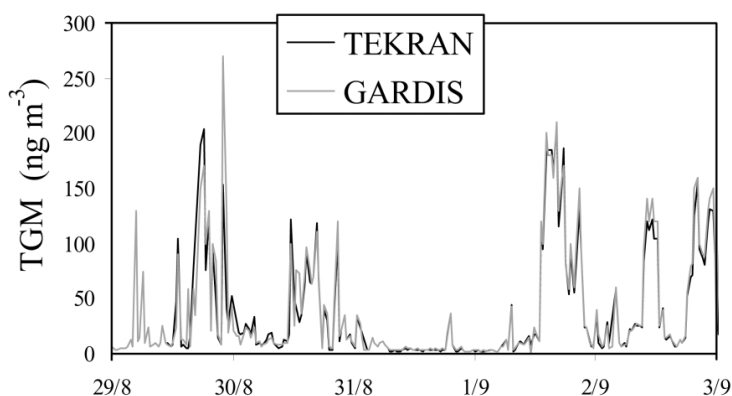


Fig. 3. TGM measured with two different automated instruments. The values were obtained 1.5 m above the ground on the site 70-m north-east of the cell house building as indicated in Fig. 2.

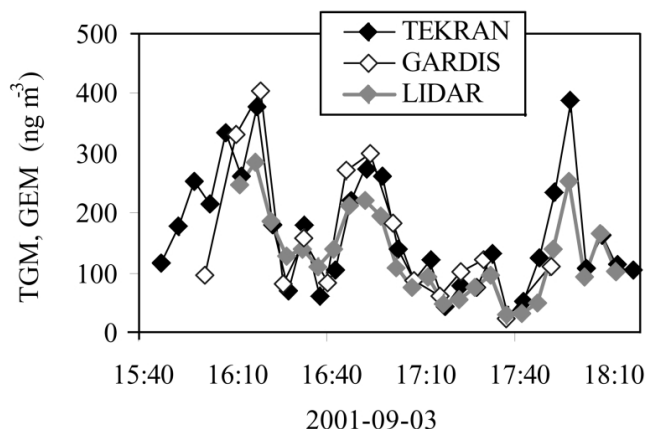


Fig. 4. Mercury time series obtained using three different measurement techniques.

taining a KCl/HCl solution may also be used to trap RGM. With this approach air is drawn through a glass chamber containing a fine dispersed liquid aerosol that continuously is formed from a refluxing KCl/HCl solution. The solution is then analysed by SnCl<sub>2</sub> reduction and CVAFS. During the campaign both manual and automated denuder techniques (Sommar et al., 1999) were used as well as mist chambers. The denuders were purchased from University Research Glass, USA.

2.4. Determination of mercury degassing rate (MDR) from soil

Mercury flux from soil was measured using the flux chamber technique (Xiao et al., 1991; Kim and Lindberg, 1995). A small area of soil surface is covered by a box. The increase in mercury concentration inside the box is measured as a function of time. An inlet port allows ambient air to enter into the chamber. An outlet port serves

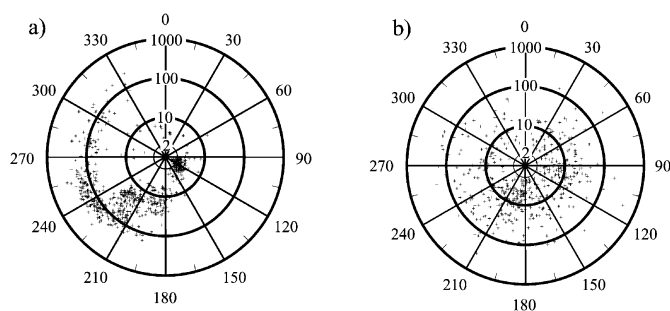


Fig. 5. TGM concentration (logarithmic scale) as a function of wind direction (a) TGM values obtained at wind speeds  $\geq 1.5$  m s<sup>-1</sup>. (b) TGM values obtained at wind speeds  $< 1.5$  m s<sup>-1</sup>.

both as sampling port for collection of mercury on a gold trap and to maintain a constant flow rate inside the chamber. Both the air from the chamber and part of the airflow entering into the chamber are drawn through gold traps by means of membrane pumps. The chamber, placed on the ground, was carefully sealed using surrounding soil to limit the infiltration of outside air.

Two different flux chambers were used:

Teflon chamber: dimension  $30 \times 60 \times 30 \text{ cm}^3$ ; sampling time 4 min; mercury sampling flow rate  $0.25 \text{ l min}^{-1}$ ; flushing flow rate  $8 \text{ l min}^{-1}$ ;

Plexiglas chamber: a semi-cylinder (diameter: 19.0 cm, length: 62.0 cm); mercury sampling flow rate:  $0.05 \text{ l min}^{-1}$ ; flushing flow rate:  $10.6 \text{ l min}^{-1}$ .

Fluxes ( $F$ ) were calculated according to:

$$F = \frac{f(C - C_0)}{A} \text{ ng m}^{-2} \text{ h}^{-1} \quad (1)$$

where  $f$  and  $A$  are the flushing flow rate through the chamber and the soil area covered, respectively.  $C$  and  $C_0$  are the mercury concentrations in the air leaving and entering the chamber, respectively. An automated system, employing a Gardis mercury analyser, was used in conjunction with the Teflon chamber measurements. Mercury in air leaving and entering the chamber was measured in sequence. The sampling times for  $C_0$  and  $C$  were varied to obtain optimal detection. At contaminated sites, 4- and 1-min sampling time were used to measure  $C$  and  $C_0$ , respectively. With this set-up a semi continuous flux value was obtained every 13 min. Measurements with the Plexiglas chamber was made manually, with sampling periods of 8 min.

### 3. Results

Due to the proximity to the cell house TGM concentrations at the measurement site sometimes reached concentrations two orders of magnitude greater than the ambient. TGM concentrations obtained at the measurement site is shown in Fig. 3. As shown, an excellent agreement between TEKRAN and Gardis data was obtained. The

TEKRAN instrument sampled air continuously for 5-min durations, while the GARDIS data consist of a 10-min long active sampling interval every 30 min. The two data sets were also compared by calculating averages of two adjacent 5-min TEKRAN values to obtain 10-min averages corresponding to the same time intervals as the GARDIS data. A set of 220 such individual TGM data were examined by linear regression analysis yielding a straight line with the slope  $0.94 \pm 0.03$ . The precision given is random and expressed as the 95% confidence limit.

In order to make a comparison between TEKRAN/GARDIS and the LIDAR instrument, the laser beam was directed close to the inlet position of the stationary instruments. The actual beam height over the ground was measured to 6 m, which was 3 m over the air intake of the instruments. The LIDAR data were evaluated with a time resolution of 1 min, but also averaged to 5-min values to match the other instruments. The measured values are the mean concentration of GEM over a horizontal path of 40 m ( $\pm 20$  m around the air intake position). Fig. 4 shows the results of all three instruments during a 2.5-h period. The LIDAR result compares favourably with that from Gardis and TEKRAN. Furthermore, considering that the LIDAR values corresponds to the average concentration of mercury in a much larger volume than with the other two instruments. The somewhat lower concentrations obtained with the LIDAR, is not likely to be due to difference between TGM and GEM that will be discussed below.

As can be seen in Fig. 3 and Fig. 4, the TGM concentration show a strong variation with time. In Fig. 5a and b, TGM concentrations are plotted as function of wind direction. High TGM values are obtained with winds within the southwest to west wind sector. That is the direction towards the cell house building. Hence, the high values are likely to correspond to the TGM concentration in the plume from the cell house. According to Eka's own measurements of the air leaving the cell house via the ceiling vent the mercury concentration is varying between 3 and  $15 \mu\text{g m}^{-3}$  during the measurement period. Hence, the mercury concen-

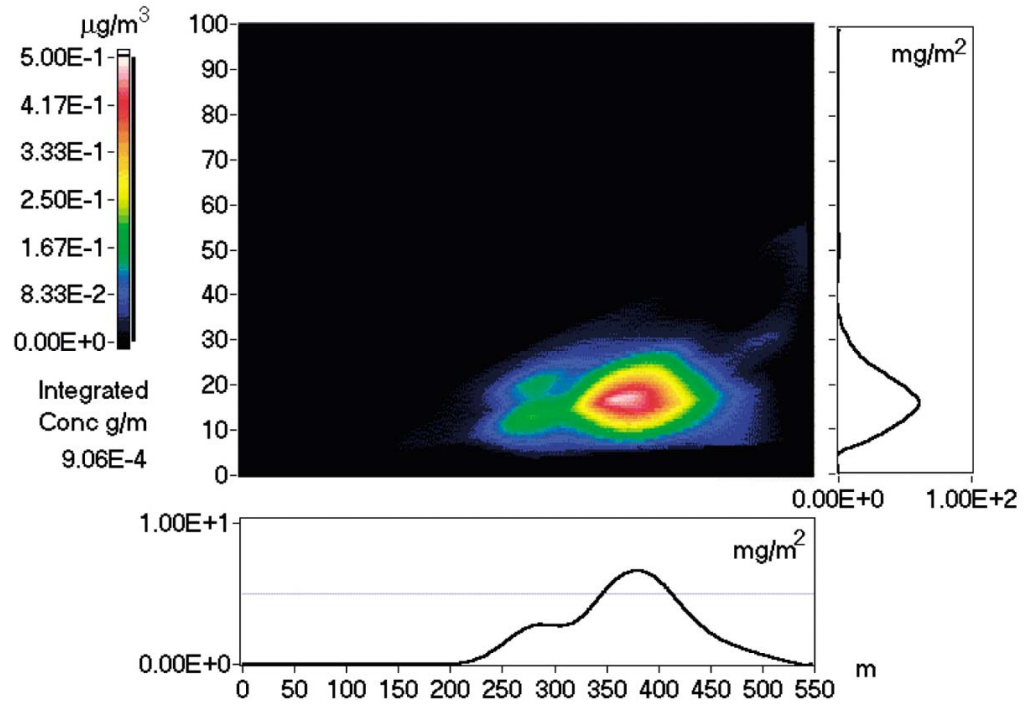


Fig. 6. Concentration map of the Hg plume, evaluated from a vertical LIDAR scan.

tration in the plume leaving the ceiling vent is approximately 50 times higher than the highest value measured at the outdoor sampling site. As is shown in Fig. 5b, during occasions with zero or very low wind speeds a more random distribution is obtained. The cell house is probably the principal source also in this case, but diffuse sources of mercury may also contribute. As also is shown in Fig. 5a, intrusion of ambient levels of TGM ( $<2 \text{ ng m}^{-3}$ ) to the site appears to be restricted to conditions with easterly advective flows.

Some LIDAR measurements of the mercury flux from the plant were performed during the measurement campaign. Unfortunately, most of the days the wind conditions were not favourable for such measurements, with unstable and too low wind speeds. Therefore, only one period was considered good enough to accurately evaluate the flux. Fig. 6 shows the result of a 3-min vertical sweep

downwind from the cell house. The concentration levels in the plume cross-section are displayed together with the horizontal and vertical integrated values. Fig. 6 shows that most of the plume could be measured. Only a limited area in the bottom of the plume escaped detection. However, as is evident from Fig. 6 the concentration in this part of the plume is low. For the flux determination, the area-integrated concentration is multiplied with the wind speed normal to the vertical plane. Due to changes in the wind field during individual scans, the results of several scans are then averaged to produce hourly mean flux values. Wind direction and speed were received from a monitor at a single height inside the factory area. This was positioned approximately 800 m south of the cell house at 30-m height, which is higher than the normal plume height of approximately 15 m (vertical centre of gravity). Since the flux calculated is

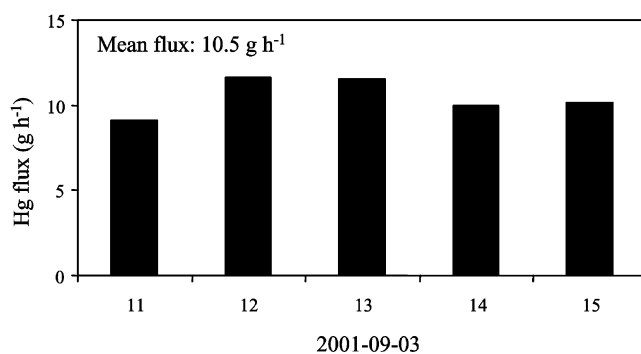


Fig. 7. Mercury flux obtained with the LIDAR system.

directly proportional to the wind speed, this parameter preferably should be measured at the same place and height as the plume. Therefore, the wind data was modified by help of a later comparison of the wind fields at the two positions. The resulting mercury emission is displayed in Fig. 7. As shown a mean flux of  $10.5 \text{ g h}^{-1}$  was obtained which can be compared with  $5 \text{ g h}^{-1}$  as was obtained from Eka Chemicals own flux measurements. This number is from the mobile system in the ceiling vent and was obtained during the same time period. Hence, the flux obtained with the LIDAR is approximately a factor of 2 higher in comparison to company's measurements. The discrepancy may partly be due to an overestimation

of the wind speed of the plume. On the other hand, the LIDAR measurement covers a greater source area. The present and an earlier measurement (Edner et al., 1989) clearly identified significant mercury emissions from surrounding buildings, i.e. a former cell house. The additional plume is clearly seen in Fig. 6.

The result from the TPM measurements is shown in Fig. 8. Very high TPM values were occasionally measured. As a comparison the average background concentration in this part of Sweden is  $10 \text{ pg m}^{-3}$ . The parallel measurements were made using the same type of sampling traps, but analyses were carried out on two different systems. An examination of the data reveals that the TPM

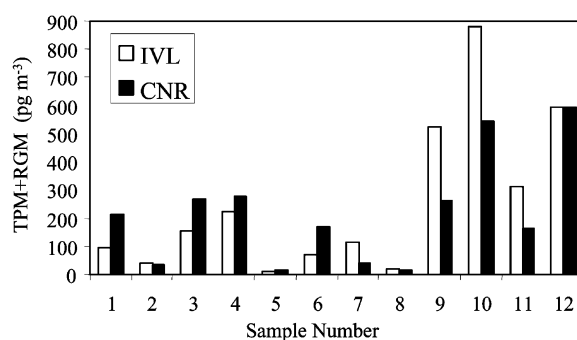


Fig. 8. Parallel TPM (total particulate mercury) samples measured at the sampling site (X) in Fig. 2. As is discussed in the text the TPM values are occasionally greatly overestimated due to adsorption of RGM.

Table 1  
RGM trapped on TPM traps

Sampling method	Place	Date	Start time	Stop time	TPM $\text{pg m}^{-3}$	RGM $\text{pg m}^{-3}$
TPM	At the sampling site	01–09–01	15:00	16:55	882	–
RGM/TPM	At the sampling site	01–09–01	15:00	16:55	69	380
TPM	*In the cell house	01–09–02	15:34	15:45	86 965	–
RGM/TPM	*In the cell house	01–09–02	15:34	15:45	4365	43 062
RGM/TPM	Inside the ceiling vent	01–09–03	13:35	13:37	4622	101 655

\* Measurements were made in the stairway inside the cell house leading to the ceiling vent.

values varies with wind direction in the same manner as for TGM. Hence, the high values correspond to the concentration in the plume from the cell house building. As is shown individual measurements often differ significantly. Some separate measurements were made using RGM denuders and TPM traps in series. With this set-up RGM was removed by adsorption on the KCl denuder before the particles were trapped on quartz glass filter. The result is shown in Table 1. The sampling methods RGM/TPM and TPM denote sampling with and without RGM denuder, respectively. One test was made at the outdoor sampling site and two inside the cell house. The result indicates that more than 90% of the measured TPM corresponds to RGM. As also is shown in

Table 1, TPM+RGM obtained with the RGM/TPM method only corresponds to 50% of TPM obtained with the TPM method. We have no explanation for this difference at the present. It is concluded that especially the high TPM values are erroneous due to the presence of RGM. This artefact may also explain the difference between paired samples shown in Fig. 8. Moreover, since the agreement between sample pairs corresponding to background concentrations (sample 2, 5 and 8) is good.

RGM was measured using both mist chamber and a denuder technique. Unfortunately the mist chamber measurements failed. The reason is likely to be contamination of the mist chamber at the site. Therefore, only denuder data is presented.

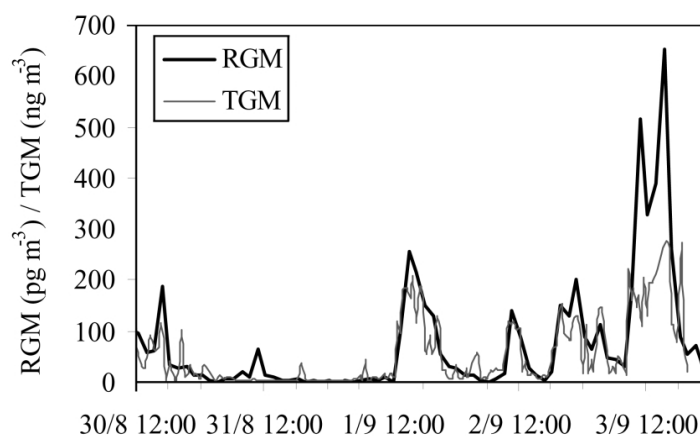


Fig. 9. RGM measured with a time resolution of 1.5 h at the outdoor measurement site. Simultaneous TGM values are also included in the plot.

Table 2  
Mercury degassing rates from soil

Date	Site	Institute	Starting time	Hg flux (ngm <sup>-2</sup> h <sup>-1</sup> )	Soil temp. (°C)	Air temp. (°C)
30/08/01	Behind the cell house	CNR-IB	14:30	3857	29.3	29.0
		CNR-IB	14:50	2367		
		CNR-IB	15:15	2154	26.3	
		CNR-IB	15:40	2535		
		CNR-IB	16:00	1747		
		CNR-IB	16:45	1151	25.1	23.3
		CNR-IB	17:30	1943	23.7	22.5
		IVL		13 700	22.8	21.5
31/08/01	Grass lawn	CNR-IB	11:00	39.2	17.9	17.1
		CNR-IB	11:30	22.3		
		CNR-IB	12:30	18.5	18.1	19.7
		CNR-IB	14:00	18	19.3	20.7
		CNR-IB	15:30	5.3	21.3	20.5
		CNR-IB	16:15	7.71		
		IVL		97.5		

RGM time series measured with the automatic denuder set-up is shown in Fig. 9. The temporal correlation with TGM shows that RGM also stems from the cell house. According to Fig. 9, RGM concentrations in the plume above the measurement site may reach 600 pg m<sup>-3</sup>. This value is approximately 50 times higher than the average background concentration in this area. Moreover, the divalent mercury only constitutes 0.1–0.2% of the total mercury. The origin of RGM is not known, but it may be formed in the electrolysis process or by photolytical-induced reactions between chlorine gas and elemental mercury in the cell house. Comparing the ratio between RGM and TGM measured inside and outside the cell house, (i.e. 0.01 and 0.0015, respectively), RGM appears to be depleted to a much larger extent than TGM. In contrast to TGM, RGM is likely to undergo removal due to deposition. However, deposition alone cannot account for this large difference. More work is needed to solve this inconsistency.

The soil around a chlor-alkali plant is generally highly contaminated by mercury partly because of deposition of mercury from the plume from the cell house but mostly from spread of mercury containing waste in the past. Mercury degassing rates are reported in Table 2. The data consist of values measured with the Teflon and Plexiglas flux

chamber at two sites (gravel covered soil on the west side of the cell house and on grass near the measurement site). The area near the cell house constitutes a source of mercury with a high degassing rate (Teflon chamber: 1950 ng m<sup>-2</sup> h<sup>-1</sup>; Plexiglas chamber: 13 700 ng m<sup>-2</sup> h<sup>-1</sup>). The mercury concentration in the soil at this area was determined to 8.5 µg g<sup>-1</sup>. A much lower mercury-degassing rate was obtained at the grass lawn. Mean values of 18.5 ng m<sup>-2</sup> h<sup>-1</sup> and 97.5 ng m<sup>-2</sup> h<sup>-1</sup> were obtained with the two chambers, respectively. It seems like very high mercury concentration in the soil makes flux measurements difficult. This first approach to measure mercury-degassing rates calls for modifications of the measurement technique. However, it seems like the continuous measurement method employed by CNR is favourable since it allows a series of measurements where the collecting time can be optimised—thereby avoiding risk of contamination from manual handling Au-traps as with the IVL method.

#### 4. Conclusions

An excellent agreement between different TGM and GEM measurements techniques was obtained. A comparison between LIDAR mercury measurements and mercury sampling on Au-traps using a

manual method has been reported previously (Ferrara et al., 1992b). However, this is for the first time a direct comparison between LIDAR and other automatic measurements techniques like TEKRAN or GARDIS is reported. The cell house and some nearby buildings constitute the principal mercury source at the plant from which air with high mercury content is emitted. However, the plume from the cell house is rapidly diluted. Hence, at the sampling site 70-m north-east of the cell house the TGM concentration already is reduced by a factor of approximately 50. The emission of TGM is likely to have a negligible impact on the local environment, as it quickly will be mixed into the troposphere. The mercury emission from the ceiling vent of the cell house was monitored during a 5-h long period using a LIDAR system and the result was compared with Eka Chemicals own measurements covering the same time period. The flux obtained by the LIDAR was a factor of two higher in comparison to the company's measurement. This difference may partly be explained by that the LIDAR measurements covered a greater source area. However, this work as well as an earlier investigation (Edner et al., 1989) indicates that the emission from this chlor-alkali plant is comparatively low.

Reactive gaseous mercury (RGM), most likely mercury chloride homologues, is also present in the air leaving the cell house. Some additional measurements made in the cell house indicated that the formation of RGM corresponds to 0.5–1% of the total mercury. However, it should be mentioned that the RGM fraction might vary considerably from time to time. In contrast to TGM, RGM easily dry deposits to ground and vegetation and due to its great water solubility it is efficiently being washed out by precipitation. A significant part of the RGM is, therefore, likely to be deposited in the local environment.

The experiments show that the TPM sampling method gives erroneous values in the presence of RGM. During occasions with high RGM concentrations more than 90% of the TPM signal seem to be due to RGM. The RGM fraction is likely to be trapped on the quartz glass fibre filters. This artefact may also explain the somewhat poor correlation between IVL and CNR TPM samples.

Consequently, background air samples with low RGM content compared favourably. The overall TPM result suggests that the particulate mercury fraction that was emitted during the measurement period was very small, contributing less than 0.05% to the total mercury emission.

Measurements of mercury degassing rate from soil around the chlor-alkali plant reveals very high fluxes from some surfaces. The experiments also indicated that automatic sampling is preferable since it prevents manual handling of samples, something that is likely to be crucial at contaminated sites. An estimation of the flux from the soil of the whole area taking the average of the CNR measurements at the contaminated site gives a value of  $0.045 \text{ g h}^{-1}$ . This number, as should be considered as an upper limit, suggests that the flux from soil is negligible in comparison to the total flux from the plant.

One interesting aspect of this work is the emission of RGM. It appears that the RGM/GEM ratio from Eka Chemicals is very low. The RGM fraction from other European chlor-alkali plants has been estimated to be 30% of the total atmospheric emission (Pacyna et al., 2001). Although, RGM constitutes a small fraction of the total mercury emitted from Eka Chemicals, its ability to readily deposit makes it unique. It is likely that the deposition of RGM constitutes the greatest impact on the environment close to chlor-alkali plants. A study aiming to investigate how RGM is formed in the process is required since such findings may give a hint as to how further reduction could be accomplished.

#### Acknowledgments

Göran Andersson and Janne Pettersson and their co-workers at Eka Chemicals are greatly acknowledged for their valuable support during the measurements. The EMECAP project is supported financially by the European Commission DG XII.

#### References

- Ayres R. The life-cycle of chlorine, part-1, chlorine production and the chlorine-mercury connection. *J Ind Ecol* 1997;1:81–94.

- Ebinghaus R, Jennings SG, Schroeder WH, Berg T, Donaghy T, Guentzel J, Kenny C, Kock HH, Kvietkus K, Landing W, Munthe J, Prestbo EM, Schneeberger D, Slemr F, Sommar J, Urba A, Wallschläger D, Xiao Z. International field intercomparison measurements of atmospheric mercury species at Mace Head Ireland. *Atmos Environ* 1999;33:3063–3073.
- Edner H, Faris GW, Sunesson A, Svanberg S. Atmospheric atomic mercury monitoring using differential absorption lidar technique. *Appl Opt* 1989;28:921–930.
- Edner H, Ragnarsson P, Wallinder E. Industrial emission control using lidar techniques. *Environ Sci Technol* 1995;29:330–337.
- Ferrara R, Maserti BE, Edner H, Ragnarsson P, Svanberg S, Wallinder E. Mercury emissions into the atmosphere from a chlor-alkali complex measured with LIDAR technique. *Atmos Environ* 1992a;26A:1253–1258.
- Ferrara R, Maserti B.E, Edner H, Ragnarsson P, Svanberg S, Wallinder E. Atmospheric mercury determinations by LIDAR and point monitors in environmental studies. Selected papers from the Fourth IAEA Workshop on Toxic Metal Compound (Interrelation between Chemistry and Biology) at Les Diabes (Switzerland), March 4–8, 1991. Merian E, Haerdi W editors. *Sci Technol Lett* 1992b; Nortwood, Middlesex, 29–37.
- Kim KH, Lindberg SE. Design and initial tests of a dynamic enclosure chamber for measurements of vapour-phase mercury fluxes over soils. *Sci Total Environ* 1995;80:1059–1068.
- Lu JY, Schroeder WH, Berg T, Munthe J, Schneeberger D, Schaedlich F. A device for sampling and determination of total particulate mercury in ambient air. *Anal Chem* 1998;70:2403–2408.
- Munthe J, Wangberg I, Pirrone N, Iverfeldt A, Ferrara R, Ebinghaus R, Feng X, Gardfeldt K, Keeler G, Lanzillotta E, Lindberg SE, Lu J, Mamane Y, Prestbo E, Schmolke S, Schroeder WH, Sommar J, Sprovieri F, Stevens RK, Stratton W, Tuncel G, Urba A. Intercomparison of methods for sampling and analysis of atmospheric mercury species. *Atmos Environ* 2001;35:3007–3017.
- Pacyna EG, Pacyna JM, Pirrone N. European Emissions of atmospheric mercury from anthropogenic sources in 1995. *Atmos Environ* 2001;35:2987–2996.
- Schroeder WH, Keeler G, Kock H, Roussel P, Schneeberger D, Schaedlich F. International field intercomparison of atmospheric mercury measurement methods. *Water Air Soil Poll* 1995;80:611–620.
- Schroeder WH, Munthe J. Atmospheric mercury—an overview. *Atmos Environ* 1998;29:809–822.
- Sommar J, Feng XB, Gardfeldt K, Lindqvist O. Measurements of fractionated gaseous mercury concentrations over north-western and central Europe 1995–1999. *J Environ Monit* 1999;1:435–439.
- Tekran. Tekran home page; Model 2357A-Principles of operation; <http://tekran.com/2357/2357poi.html>, 1998.
- UN-ECE. Protocol on heavy metals. Convention Long-range Transboundary Air Pollution, United Nations Economic Commission for Europe, 1998.
- Weibring P, Andersson M, Edner H, Svanberg S. Remote monitoring of industrial emissions by combination of lidar and plume velocity measurements. *Appl Phys* 1998;B66:383–388.
- Xiao ZF, Munthe J, Schroeder WH, Lindqvist O. Vertical fluxes of volatile mercury over forest soil and lake surfaces in Sweden. *Tellus* 1991;43B:267–279.



## PAPER II

### **Atomic mercury flux monitoring using an optical parametric oscillator based lidar system**

M. Sjöholm, P. Weibring, H. Edner, and S. Svanberg.

*Optics Express* **12**, 551–556 (2004).



# Atomic mercury flux monitoring using an optical parametric oscillator based lidar system

Mikael Sjöholm, Petter Weibring, Hans Edner and Sune Svanberg

Atomic Physics Division, Lund Institute of Technology, P.O. Box 118, 221 00 Lund, Sweden  
<http://www-atom.fysik.lth.se>

**Abstract** A newly developed optical parametric oscillator (OPO) based differential absorption lidar (DIAL) system has been applied to the monitoring of atomic mercury emissions at several chlor-alkali plants in Europe. The versatility of the system is illustrated by measured time series of mercury flux and movies of vertical and horizontal concentration distributions, which yield important input parameters for the environmental community. Long term measurements of the resonance absorption of mercury at 253.65 nm poses special demands, i.e. long term stability, on the light source that often have been hard to fulfill, in different respects, for standard OPO and dye laser based systems. Here, approaches to meet these demands are presented.

©2004 Optical Society of America

**OCIS codes:** (280.1120) Air pollution monitoring; (280.1910) DIAL, differential absorption lidar; (300.6210) Spectroscopy, atomic; (190.4970) Parametric oscillators and amplifiers; (140.3580) Lasers, solid state; (280.3640) Lidar; (010.3640) Lidar; (010.1120) Air pollution monitoring.

## References and Links

1. W. H. Schroeder, J. Munthe, "Atmospheric mercury - an overview," *Atmos. Environ.* **32** No. 5, 809 (1998).
2. K. von Rein, L. D. Hylander, "Experiences from phasing out the use of mercury in Sweden," *Reg. Environ. Change* **1**, 126 (2000).
3. E.G. Pacyna, J.M. Pacyna and N. Pirrone, "European emissions of atmospheric mercury from anthropogenic sources in 1995," *Atmos. Environ.* **35**, 2987 (2001).
4. <http://www.emecap.com>
5. S. Svanberg, "Differential Absorption Lidar (DIAL)," in *Air Monitoring by Spectroscopic Techniques*, M. Sigrist (ed) (Wiley, New York 1994).
6. M. Aldén, H. Edner, and S. Svanberg, "Remote measurements of atmospheric mercury using differential absorption lidar," *Opt. Lett.* **7**, No. 5, 221 (1982).
7. H. Edner, G. W. Faris, A. Sunesson and S. Svanberg, "Atmospheric atomic mercury monitoring using differential absorption lidar techniques," *Appl. Opt.* **28**, No. 5, 921 (1989).
8. G. Egret, A. Fix, V. Weiss, G. Poberaj, T. Baumert, "Diod-laser-seeded optical parametric oscillator for airborne water vapor DIAL application in the upper troposphere," *Appl. Phys B* **67**, 427 (1998).
9. P. Weibring, H. Edner, and S. Svanberg, "Versatile Mobile lidar System for Environmental Monitoring," *Appl. Opt.* **42**, 3583 (2003).
10. P. Weibring, J. N. Smith, H. Edner, and S. Svanberg, "Development of a frequency agile optical parametric oscillator system for differential absorption lidar," *Rev. Sci. Instr.* **74**, 4478 (2003).
11. <http://www.tekran.com/2505/2505fea.html>
12. T. Lindström, U. Holst, P. Weibring, and H. Edner, "Analysis of LIDAR Measurements Using Nonparametric Kernel Regression Methods," *Appl. Phys. B* **74**, 155 (2002).
13. U. Holst, O. Hössjer, C. Björklund, P. Ragnarsson and H. Edner, "Locally weighted least squares kernel regression and statistical evaluation of lidar measurements," *Environmetrics* **7**, 401-416 (1996).
14. P. Weibring, M. Andersson, H. Edner and S. Svanberg, "Remote monitoring of industrial emissions by combination of lidar and plume velocity measurements," *Appl. Phys. B* **66**, 383 (1998).
15. I. Wängberg, H. Edner, R. Ferrara, E. Lanzillotta, J. Munthe, J. Sommar, S. Svanberg, M. Sjöholm and P. Weibring, "Mercury emissions from a chlor-alkali plant in Sweden," *Sci. Tot. Environ.* **304**, 29 (2003).

## 1. Introduction

The increased awareness of the impact of mercury on the environment and human health has caused stronger regulations against mercury emissions [1,2]. This calls for more powerful measurement techniques for surveillance of the emissions from different sources and for monitoring the local dispersion of the mercury released. In the most commonly employed chlor-alkali production scheme in Europe, mercury is still used as a liquid cathode in the electrolytic cells where chlorine, sodium hydroxide and hydrogen are formed in the electrolysis of sodium chloride. Due to the high vapor pressure of mercury already at low temperatures, considerable amounts of mercury are released into the atmosphere in the process. Thus, the chlor-alkali industry constitutes a large mercury polluter, responsible for about 12% (41 tonnes/year) of the anthropogenic total mercury emissions in Europe [3]. In this context a large cross-disciplinary project, financed by the European Union, concerning the European mercury emission from chlor-alkali plants (EMECAP) has been initiated. The goal of the project is to provide decision-makers with an improved tool for evaluating the risk to the human health and the environment around mercury cell chlor-alkali (MCCA) plants [4]. Two key inputs in this assessment are the initial plume extension and the emitted flux of gaseous elemental mercury at the source industries. Such measurements, performed within the EMECAP project, utilizing the DIAL (Differential Absorption Lidar) technique [5], are treated in the present paper.

DIAL measurements of mercury have been performed for a long time using dye laser systems [6,7], that have the disadvantage of having a fast degrading gain medium needing frequent service. A more convenient alternative in this respect is an all-solid-state laser system. However, the drawback of such systems is that they generally have problem producing light with stable and narrow linewidth, which is important for measurements of spectrally sharp absorption features like the one in atomic mercury. One way of dealing with this problem is by injection seeding with a narrow-banded light source, e.g. a diode laser, at the desired wavelength [8]. Unfortunately, the availability of such narrow-banded laser sources is limited to certain wavelength regions, which makes that solution not always feasible. However, a general approach to deal with the linewidth problem was recently implemented in an all-solid-state lidar system in Lund. The new system, developed on the same mobile platform as an earlier dye laser based lidar system, employs a Nd:YAG pumped Optical Parametric Oscillator (OPO) that, combined with frequency doubling and mixing stages, can generate pulsed radiation ranging from the deep-UV to the mid-IR regions [9]. The system has the possibility to present concentration maps and flux in real time during the measurement. Movies of the concentration distribution are easily made to study the temporal variation of the emission pattern during long times.



Fig. 1. The mobile lidar system in a field campaign in Rosignano Solvay, Italy.

## 2. The system

The measurements presented in this paper were performed with the newly developed mobile lidar system, Fig.1, at Lund University [9]. A key component of the system is the light source, which is a modified Optical Parametric Oscillator laser system (Spectra Physics MOPO-730) that is pumped by a frequency-tripled injection seeded Nd:YAG laser (Spectra Physics Model GCR-290) and equipped with doubling and mixing crystal units.

The main modification of the OPO is the introduction of piezo-electric control of all nonlinear crystals and the mirror in the Littman cavity master oscillator, as illustrated in Fig. 2. This modification makes it possible to tune the wavelength up to  $160\text{ cm}^{-1}$  between each shot, i.e. within a period of 50 ms, in the wavelength ranges 220-690 nm, 730-1800 nm and 2600-4300 nm [10].

Although the average spectral linewidth of the generated pulses is better than  $0.2\text{ cm}^{-1}$ , the linewidth can reach  $0.4\text{ cm}^{-1}$  due to fluctuations in the Littman cavity, which allows several modes to be simultaneously amplified. If the linewidth becomes broad compared to the width of the spectral feature under study the measurement is impaired. Therefore, the system is equipped with two on-line surveillance systems for monitoring the spectral quality of the emitted light. One Fabry-Pérot based system monitors the wavelength, linewidth and power in real time. Based on the linewidth measured, the backscattered light pulse from the atmosphere can be sorted into an appropriate linewidth category, which can be individually evaluated with an appropriate absorption cross-section, and if the pulse is too broad the corresponding data is not used in the evaluation process.

Moderate linewidth and wavelength fluctuations can also be handled by splitting off a small fraction of the UV pulse to an internal gas cell system, where the light is divided into two paths. One beam is passing through an absorption cell with a drop of mercury at atmospheric pressure, and the other one is passed through a cell without mercury. By measuring the mercury cell temperature, the internal mercury vapor concentration can be calculated [11]. This, together with the length of the cell and the mercury cell absorption detected gives, in real time during the DIAL measurement, the effective absorption cross section, which compensates for fluctuations in wavelength and linewidth.

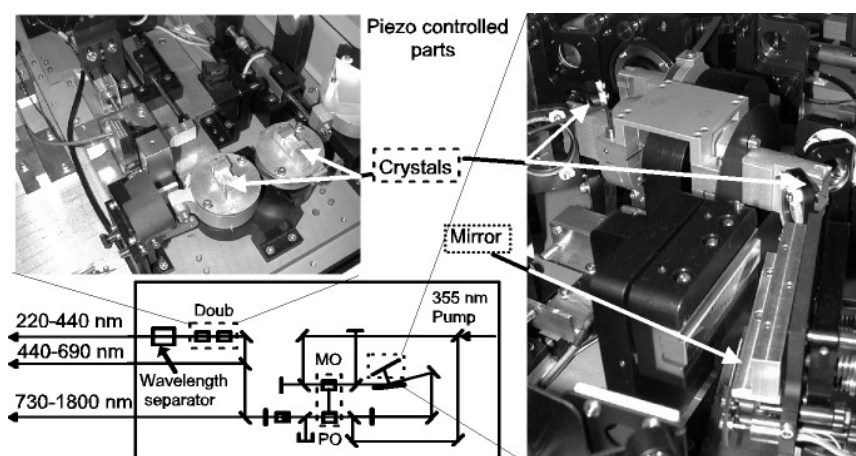


Fig. 2. Schematic overview of the master oscillator (MO) and power oscillator (PO) transmitter.

The mercury probing UV-light pulse duration is about 3-4 ns and the typical pulse energy is 12 mJ. However, the energy is normally lowered to about 5 mJ and a comparatively large

beam divergence of about 2 mrad (full angle) of the transmitted light is set by a variable Galileian beam expander to avoid stimulated emission on the atomic line, which would result in a different effective absorption cross-section. Proper operation conditions were determined in a separate investigation [7]. The laser pulses are directed into the atmosphere by the use of a computer controlled optical dome, and a coaxial receiving Newtonian telescope collects the back-scattered photons. Before the received probing light enters a photo multiplier tube (PMT), an interference filter attenuates the background light. Furthermore, the gain of the PMT is modulated in order to suppress the signal due to intense light coming from closer distances. A 12-bit analogue digitizer unit (Licel) operating at 20 MHz, corresponding to a 7.5-m spatial resolution, then digitizes the signal from the PMT.

The mobile lidar system is accompanied by a 45 kVA diesel powered electrical generator, which makes it possible to select the appropriate measurement positions during field campaigns without being limited by stationary electrical supply facilities.

### 3. Measurements and results

DIAL measurements at the resonance absorption line at 253.65 nm of gaseous elemental mercury were performed with the mobile lidar system, during several field campaigns at different MCCA plants in Europe. The purposes of the measurement campaigns were to estimate the total emission of elemental mercury into the atmosphere and to make an inter-calibration with other mercury monitoring techniques as well as to provide input for the modeling of mercury dispersion. To achieve this the lidar light beam was scanned in 7-15 directions in a vertical plane, down wind of the mercury emitting cell houses, and in a horizontal plane, resulting in 2-D concentration maps. The detection range was limited to about 800 m or less depending on the scattering and absorption properties of the local atmosphere at the UV wavelengths used. Each map was, in most cases, acquired during 3-5 minutes in order to obtain a good signal to noise ratio. The radial concentration distributions were evaluated by locally weighted polynomial regression [12] using a global bandwidth [13]. The resulting radial concentration distributions for different angles of direction was then transformed into a Cartesian (x,y) coordinate system and interpolated to give 2-D concentration maps.

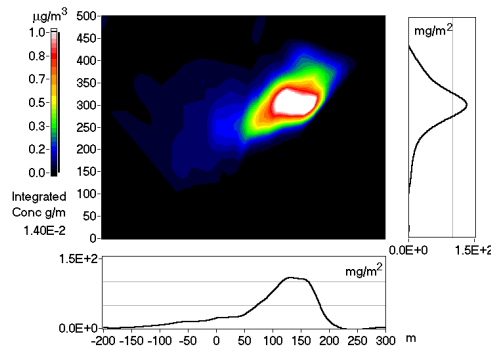


Fig. 3. (417 KB) Movie of horizontal concentration maps from the MCCA plant in Rosignano Solvay 2002-02-03, 12:11-12:38.

As an example of a concentration map, a horizontal mercury plume distribution at the MCCA plant in Rosignano Solvay (Italy) is given in Fig. 3, where a movie based on three horizontal concentration maps, recorded within half an hour with interpolated maps in between, is presented. It can be seen that the peak concentration in the plume is in the order of  $\mu\text{g}/\text{m}^3$  and that the concentration level decreases a whole order of magnitude within a few hundred meters.

An insight into the mercury plume dynamics is given in Fig. 4 and Fig. 5, where movies of consecutive vertical concentration maps, without time interpolation, from the MCCA plants in Bohus (Sweden) and Rosignano Solvay (Italy), respectively, are presented for measurements of a few hours. The concentration ( $\mu\text{g}/\text{m}^3$ ) was integrated to give an area-integrated concentration ( $\mu\text{g}/\text{m}$ ), which was multiplied by the wind component orthogonal to the measured plane to render the flux ( $\text{g}/\text{h}$ ).

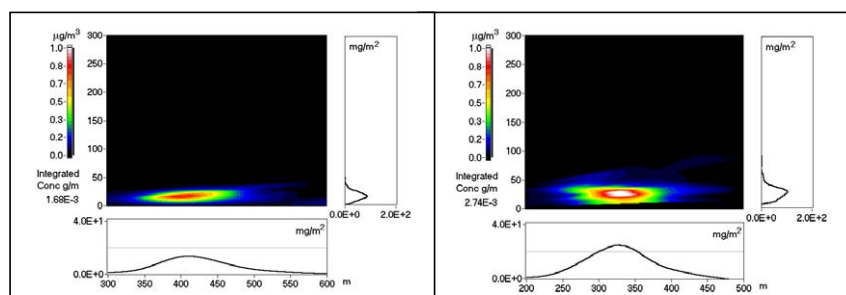


Fig. 4. (611 KB) Movie of vertical concentration maps from the MCCA plant in Bohus 2002-01-18, 12:00-15:27.

Fig. 5. (467 KB) Movie of vertical concentration maps from the MCCA plant in Rosignano Solvay 2002-02-04, 14:35-17:57.

The over-all accuracy in the flux measurements is limited by the accuracy of the wind measurements [14]. Since the accuracy is decreased for wind directions nearly parallel with the direction measured, the system was moved to the most appropriate positions regarding the mercury source and the prevailing wind directions. However, the wind direction unavoidably is changing and because there is a certain set up time after the system has been moved there are still flux data from less favorable wind conditions. For this reason, the results of measurements during wind directions more parallel to the scan direction than 25 deg was excluded from the final flux compilation. A wind vane and anemometer, placed on the roof of the cell house, monitored the wind at approximately the center height of the mercury plume with a time resolution of 30 s. Due to the lower accuracy of this instrument at lower wind speeds, data obtained at wind speeds less than 1 m/s was excluded from the final compilation also.

As examples, time series of mercury flux, evaluated as mentioned above, from Bohus and Rosignano Solvay, respectively, are presented in Fig. 6. In the lower part of the figure hourly mean values are presented. The mean values were only calculated if there were more than three accepted flux measurements during the period, since it is important that the wind conditions is fairly stable during the averaging period. The influence of wind fluctuations can be seen in the large variation in the flux during the first half of the measurement period on January 30. Later that day, the wind became more stable and also more perpendicular to the laser beam, resulting in more stable flux data. During the winter campaigns average fluxes of 6 g/h and 20 g/h were measured at the two MCCA plants in Bohus and Rosignano Solvay, respectively.

An inter-calibration between the lidar system and two point-monitoring systems was performed during an initial autumn campaign at the MCCA plant in Bohus [15]. The two point monitors were based on gold amalgamation of the mercury followed by thermal desorption and atomic fluorescence spectrophotometry (TEKRAN) and atomic absorption spectrophotometry (GARDIS), respectively. During the inter-comparison the GARDIS and TEKRAN instrument were sampling air in a point located 3 m above ground, while the lidar sampling volume ( $\sim 40\text{m} \times 0.5\text{m}^2$ , in this particular case) was placed as near (6 m above ground) that sampling point as obstructing building elements made possible. Remembering the slight difference in sampling volumes, an excellent agreement between the instruments could be seen [15].

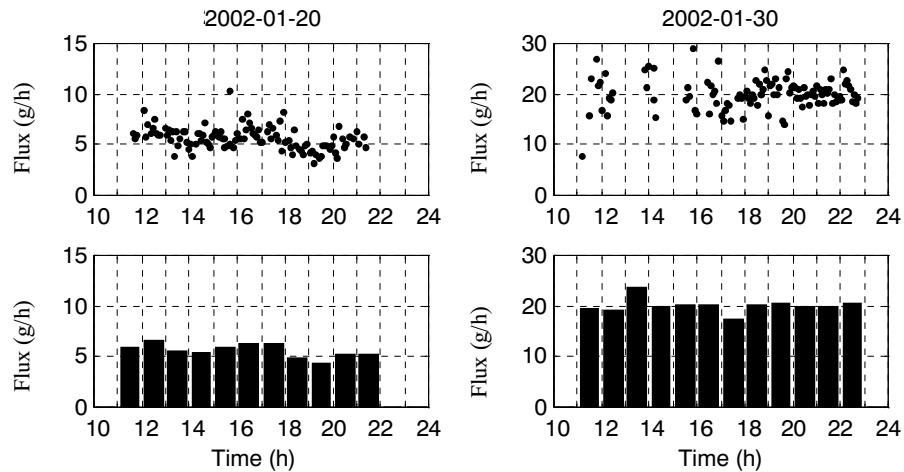


Fig. 6. Typical mercury fluxes from Bohus (left) and Rosignano Solvay (right), respectively.

#### 4. Conclusions

The OPO based lidar system has proven to be an efficient tool for measurements of mercury in the field. Long time series of flux and concentration distributions can readily be obtained, constituting an essential input for dispersion modeling of the pollutant. The concentration values measured by the lidar system are in good agreement with corresponding values obtained by standard point monitoring systems and the accuracy in the flux measurements is normally limited by the accuracy of the wind field measurements.

#### Acknowledgments

The authors gratefully acknowledge Romano Ferrara, Enrica Lanzillotta, John Munthe, Jonas Sommar and Ingvar Wängberg for their collaboration during the field campaigns. The EMECAP project is supported financially by the European Commission DG XII. We also acknowledge the Knut and Alice Wallenberg Foundation for generous support.

## PAPER III

### **Elemental mercury emission from chlor-alkali plants measured by lidar techniques**

R. Grönlund, M. Sjöholm, P. Weibring, H. Edner, and S. Svanberg.

*Atmospheric Environment* **39**, 474–7480 (2005).



Available online at [www.sciencedirect.com](http://www.sciencedirect.com)

SCIENCE @ DIRECT®

Atmospheric Environment 39 (2005) 7474–7480

ATMOSPHERIC  
ENVIRONMENT[www.elsevier.com/locate/atmosenv](http://www.elsevier.com/locate/atmosenv)

## Elemental mercury emissions from chlor-alkali plants measured by lidar techniques

Rasmus Grönlund\*, Mikael Sjöholm, Petter Weibring,  
Hans Edner, Sune Svanberg

*Department of Physics, Lund Institute of Technology, P.O. Box 118, SE-221 00 Lund, Sweden*

Received 15 October 2004; accepted 23 June 2005

### Abstract

Differential absorption lidar (DIAL) techniques have been utilized to measure elemental gaseous mercury fluxes from mercury cell chlor-alkali (MCCA) plants as a part of the European Union funded European mercury emissions from chlor-alkali plants (EMECAP) project. Three plants have been selected as study objects and a total of six measurement campaigns have been performed, one intercalibration campaign and five flux evaluation campaigns, in both winter and summer. The measurements were carried out using the Swedish optical parametric oscillator- (OPO) based mobile lidar system developed at Lund Institute of Technology. The study shows large differences in the mercury emissions measured in winter or summer and at the different plants. The average values for the campaigns ranged from  $6 \text{ g h}^{-1}$  in the winter campaign at the Swedish plant to  $54 \text{ g h}^{-1}$  in the summer campaign at the Italian plant.

© 2005 Elsevier Ltd. All rights reserved.

*Keywords:* DIAL; Atmospheric mercury flux; EMECAP; Chlor-alkali plant; OPO

### 1. Introduction

Mercury cell chlor-alkali (MCCA) plants use liquid mercury as a cathode in electrolytic cells to produce chlorine, sodium hydroxide and hydrogen by electrolysis of brine solution. In this process, very large quantities of mercury are handled and because of the high-vapor pressure of mercury already at low temperatures, considerable amounts of mercury is emitted to the atmosphere, due to spills, leakage from mercury cells or pumps, maintenance activities, etc. (Southworth et al., 2004). Although the MCCA technique is in many places being replaced by alternatives, it is still the most commonly used in Europe.

Over the last decades, increased awareness of the environmental and human health impacts of mercury has led to stronger regulations against mercury emissions, leading to decreased emissions (Schroeder and Munthe, 1998). However, the chlor-alkali industry still constitutes a large mercury polluter, in 1995 responsible for about 12% ( $41.3 \text{ tonnes year}^{-1}$ ) of the anthropogenic total mercury emissions in Europe (Pacyna et al., 2001). More recent estimates reports emissions from the chlor-alkali industry to be responsible for about 17% ( $40.4 \text{ tonnes year}^{-1}$ ) of anthropogenic total mercury emissions in the year 2000 (Pacyna, 2003). A report from the Euro-Chlor Association (Anon, 2001) shows constantly decreasing, but still significant, emissions from chlor-alkali plants.

In this context a large cross-disciplinary project, financed by the European Union, concerning the European mercury emission from chlor-alkali plants

\*Corresponding author. Tel.: +46 46 222 41 38;  
fax: +46 46 222 42 50.

E-mail address: [rasmus.gronlund@fysik.lth.se](mailto:rasmus.gronlund@fysik.lth.se)  
(R. Grönlund).

(EMECAP) has been pursued. The goal of the project is to provide decision-makers with an improved tool for evaluating the risk to the human health and the environment around MCCA plants (Mazzolai et al. 2004; <http://www.emecap.com>). Within the project, epidemiological studies of people living in the vicinity of MCCA industries are performed (Barregård et al., to appear) and linked to the levels of mercury in the environment, which are assessed by point monitoring of mercury in air, soil and living organisms around the mercury emitters (Wängberg et al., 2003). These data are managed by a data mining-based software (Fayyad et al., 1996) which, interrogating dedicated epidemiological and environmental data bases, provides high-level information in terms of health risk.

For understanding the regional atmospheric dispersion of mercury a mathematical model is being developed (Munthe et al., 2001). Two key inputs in this model are the initial plume extension and the emitted flux of gaseous elemental mercury at the source industries. Such measurements, performed within the EMECAP project, utilizing the Differential absorption lidar (DIAL) technique (Svanberg, 1994), are treated in the present paper. The model also needs input on the chemical composition of the emitted mercury, i.e. elemental mercury ( $\text{Hg}^0$ ) versus reactive gaseous mercury (RGM,  $\text{Hg}^{2+}$ ), etc. Such measurements were also performed and are presented in Wängberg et al. (2005).

Although flux estimation is an important issue, few techniques for flux measurements exist. Recently, Differential optical absorption spectroscopy (DOAS) measurements in the air vent from a US MCCA plant combined with wind measurements were used to assess mercury flux from the cell house (Kinsey et al., 2004). Here, the concentration is integrated over the measured path between the light-source and the detector. Using the DIAL technique, range-resolved measurements of atomic mercury concentrations and fluxes can be measured. Our group has previously reported on this kind of measurements from MCCA plants, employing different laser systems, but the same mercury absorption line at 253.65 nm (Edner et al., 1989; Ferrara et al., 1992; Edner et al., 1995; Wängberg et al., 2003; Sjöholm et al., 2004). In the present report mercury fluxes from summer and winter campaigns at three different European MCCA plants, Eka Nobel in Bohus, Sweden, Solvay in Rosignano Solvay, Italy and Zakłady Azotowe in Tarnów, Poland, are presented.

## 2. Measurement technique

DIAL measurements were performed on atomic mercury, using two wavelengths, one *on* the absorption line (253.65 nm) and the other slightly *off*. The *off* wavelength was chosen at a longer wavelength than the

*on* wavelength to avoid interference with a close-lying, weak oxygen absorption line (Edner et al., 1989). Some unsaturated hydrocarbons and aromatic compounds absorb light in the same wavelength region, but these elements have quite slow absorption features compared to the *on/off*-wavelengths and are not considered to be abundant enough to affect the signal. This was verified by measurements outside the plume not showing elevated mercury concentrations. The lidar signal was collected time-resolved to obtain a range-resolved measurement. By forming the ratio between the *on* and *off* signals, the DIAL curve is obtained, being flat where no mercury is present and sloping downwards in the presence of mercury. Since the *on* and *off* wavelengths are chosen close to each other, no other differences than the mercury absorption are expected. The output energy may be slightly different for the two wavelengths; however, this does not matter since the slope of the normalized DIAL curve is the only pertinent factor when analyzing the mercury concentrations. Particulate mercury and different Hg(II) species do not have any absorption of light at 253.65 nm, thus not being detected by the technique presented.

Each DIAL measurement, in a certain direction, gives the range-resolved mercury concentration along the laser beam. By vertical scanning of the laser beam downwind from a pollution source, in this case a chlor-alkali plant, a concentration cross-section of the mercury plume is found. The mercury flux is estimated by area integration of the concentration and multiplication by the wind speed component perpendicular to the cross-section surface.

The measurements were performed using the Swedish optical parametric oscillator (OPO) based mobile lidar system, built inside a Volvo F610 truck (Weibring et al., 2003). The OPO (Spectra-Physics MOPO-730) is pumped by a pulsed (20 Hz) frequency-tripled Nd:YAG laser at 355 nm and gives output in the wavelength range 440–1800 nm which can be frequency doubled to reach wavelengths down to 220 nm. The OPO is modified with piezo-electric elements so that the wavelength can be switched within a range of  $160\text{ cm}^{-1}$  between consecutive shots. The average linewidth of the transmitter is normally better than  $0.2\text{ cm}^{-1}$  and the pulse length is typically 3–4 ns. An absorption cell system is used to compensate for fluctuations in wavelength and linewidth of the emitted laser light pulses.

The laser radiation is sent into the air through the dome, hoisted to the roof of the truck, which can be rotated  $360^\circ$  and by using a folding mirror the beam can be tilted vertically from  $-10^\circ$  to  $55^\circ$ . The backscattered radiation is collected using the on-axis, 40-cm-diameter Newtonian telescope and focused onto a photomultiplier tube. An interference filter is used to suppress background light, since only elastic scattering is of interest. The retrieved signal is then digitized at a

sampling frequency corresponding to a range resolution of 7.5 m. The entire system is controlled by a LabVIEW-based computer program, which also is used for data analysis.

### 3. Measurements

A total of six measurement campaigns have been performed at the three test sites. Initially, intercalibration measurements were performed during a campaign at the Swedish test site in September 2001. In this inter-comparison, a good agreement between lidar and conventional mercury point-monitoring concentration measurements was shown (Wängberg et al., 2003). DIAL measurement campaigns of the flux have been performed in Sweden, Italy and Poland in summer and additionally, in winter in Sweden and Italy. Each measurement campaign lasted for about 2 weeks and in this time a substantial number of scans were performed, rendering an average value representative

for the campaign period. Maps over the measurement areas along with a picture of the mobile lidar system are seen in Fig. 1.

A single sweep is gathered in 3–5 min, yielding a concentration map and, combined with wind data, a flux value. Over the course of each measurement campaign, the wind velocity was measured using wind vanes and anemometers, placed as close as possible to the center of the pollution plume. The horizontal direction of the sweep was not held constant over the entire measurement campaign, as indicated in Fig. 1, due to fluctuations of the wind direction, as it is always desired to have the measurement direction as perpendicular to the wind direction as possible.

All the different flux values were then averaged to give a mean flux value for each hour and ultimately for the measurement period. In the averaging, sweeps where the wind speed was less than  $1 \text{ m s}^{-1}$  or the wind direction was in a too acute angle to the measurement direction, giving rise to a large sine correction, have been excluded.

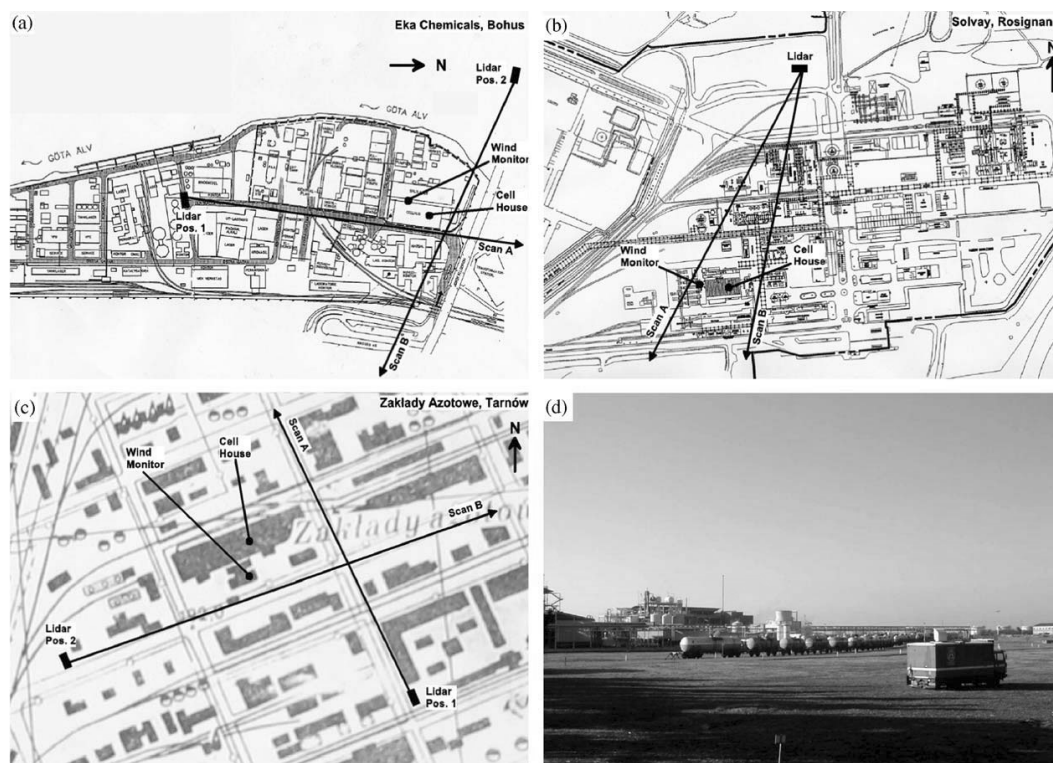


Fig. 1. Maps over the measurement sites (a) Bohus, (b) Rosignano Solvay, (c) Tarnów, with measurement directions indicated. (d) shows the lidar system on location in Rosignano Solvay.

#### 4. Results

Each vertical sweep gives a cross-section of the mercury plume, an example of which is given in Fig. 2 where the area-integrated concentration ( $\text{g m}^{-1}$ ) can also be seen. The daily elemental mercury flux averages from the different campaigns are given in Fig. 3. For each campaign a total average flux value was calculated, the result is given in Fig. 4. Here, the uncertainty bars correspond to one standard deviation of the different hourly averages and should not be considered solely as the error of the measurement technique, as the emissions most probably were not constant over the measurement campaign. For comparison, the fluxes may be normalized with respect to the chlorine production, as has been done in Fig. 5. However, it should be kept in mind that a substantial part of the flux may be independent of the chlorine production due to gassing from spills, as discussed below.

#### 5. Discussion

The results in Fig. 4 can be compared with earlier measurements by our group at the same plants rendering average elemental mercury flux values of  $43 \text{ g h}^{-1}$  in Rosignano Solvay in a september measurement campaign in 1990 (Ferrara et al., 1992) and  $31 \text{ g h}^{-1}$  in

Bohus in a may measurement campaign in 1992 (Edner et al., 1995). The present results indicate that, particularly in Bohus, new technologies and environmental awareness has decreased the emissions significantly.

It should be noted that the accuracy in the measured flux depends equally on the precision in the integrated mercury concentration obtained in the lidar vertical scan and on the accuracy in the wind speed determination. Wind speed assessment is clearly an important issue and in the present work data from vane anemometers appropriately placed were used. In order to estimate the accuracy of this procedure some joint measurements comparing vane anemometer data with data obtained with a Doppler lidar set-up, in which the Doppler-shifts in particulate backscattering were determined. The intercomparison suggests that the procedure adopted in the present flux determination project is good to about 20 percent (Bennett et al., to appear).

Emissions from the cell building may have a number of different origins, as discussed earlier (Southworth et al., 2004). However, it seems logical that there would be two types of emissions: forced leakage from pumps, cells, valves, etc. and gassing from spills. The second type is expected to be dependent on the wind speed over it, reducing the vapor pressure and thus allowing faster gassing, whereas a forced leakage is not expected to have this behavior. In respect of this it should be noted that the Italian plant has an open structure, ventilated by the

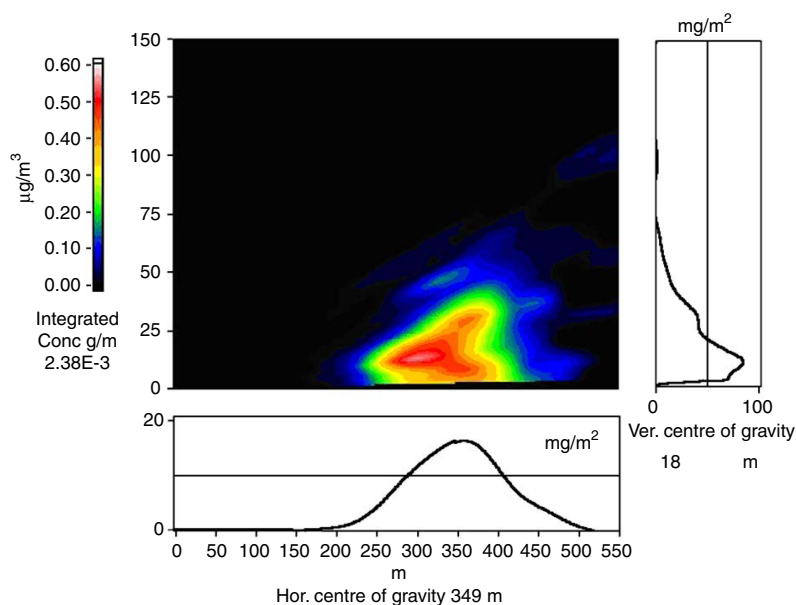


Fig. 2. Cross-section of the mercury plume, recorded at the Solvay plant in Italy, 04-07-2003, 11:29–11:34, corresponding to a mercury flux of  $74 \text{ g h}^{-1}$ .

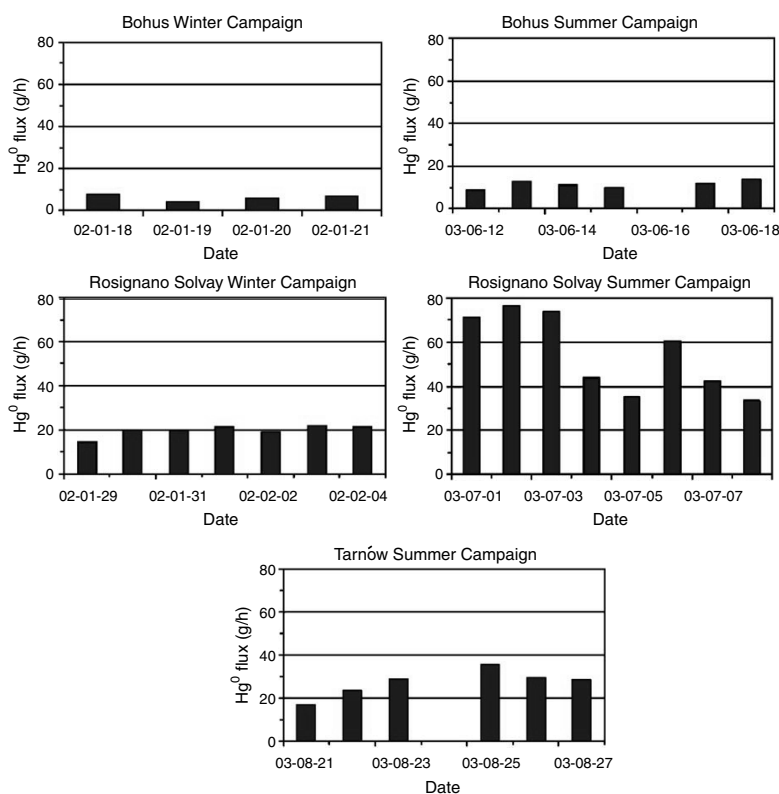


Fig. 3. Daily average elemental mercury flux values for the different campaigns.

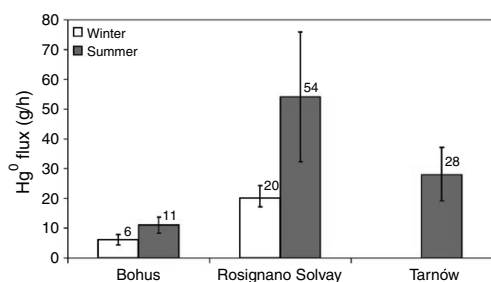


Fig. 4. Average mercury flux from the different campaigns. The error bars correspond to the standard deviation of the hourly measured values.

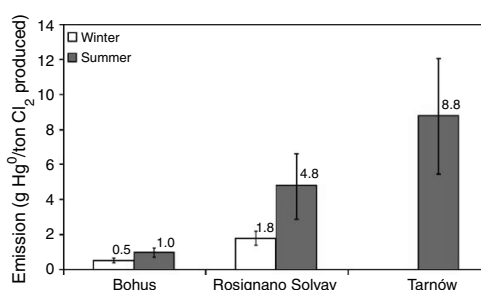


Fig. 5. Average mercury flux from the different sites, normalized to the chlorine production during the different campaigns.

wind blowing through the cell house, whereas both the Swedish and Polish plants are closed buildings with forced ventilation. The wind dependence is clearly largest at the Italian site as can be seen by comparing Fig. 6a–c where the flux as a function of the wind speed is given for the Italian, Swedish and Polish plant,

respectively. It could be argued that the large emissions from the Italian plant are only due to the fact that the wind speed happened to be particularly high at the time of the campaign. Assuming the fit in Fig. 6a–c are correct, the emissions if the wind conditions would have been the same at all sites can be calculated and are seen

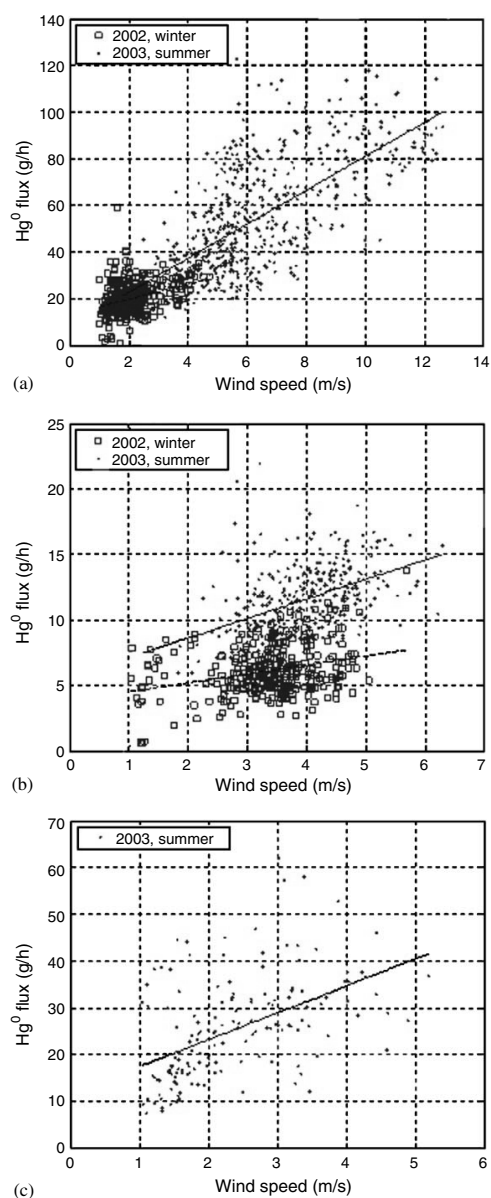


Fig. 6. Mercury flux as a function of wind speed at the different plants; Solvay plant in Italy (a), Eka plant in Sweden (b) and Zakłady Azotowe plant in Poland (c). The dashed lines correspond to regression of the results in the winter campaigns (the squares represent single sweep results) and the solid lines to the summer campaigns (the dots). The correlation for the different regressions are:  $r^2 = 0.10$  (Italy, winter)  $r^2 = 0.49$  (Italy, summer)  $r^2 = 0.09$  (Sweden, winter)  $r^2 = 0.20$  (Sweden, summer)  $r^2 = 0.25$  (Poland, summer).

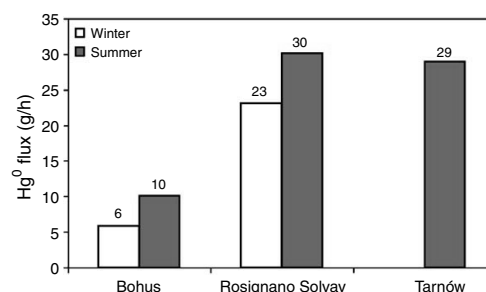


Fig. 7. Mercury emissions from the different plants, assuming a constant wind speed of  $3 \text{ m s}^{-1}$  in all campaigns.

in Fig. 7, assuming the wind speed to be  $3 \text{ m s}^{-1}$ . As can be seen, by comparing Fig. 7 with Fig. 4, only the Italian summer campaign is affected significantly by this normalization, in the other campaigns the wind dependence was not very pronounced. This indicates that it was only in the Italian summer campaign that the gassing from spills gave a large contribution to the total flux.

## 6. Conclusions

Total atomic mercury emissions to air from three mercury cell chlor-alkali plants were successfully assessed using the differential absorption lidar technique. It was found that the total fluxes from the three different plants differ widely, also when normalized on the chlorine production. This reflects differences in the technology being used. A hitherto undescribed wind velocity dependence of the total flux was also observed especially during high-ambient temperatures on the open cell house structure of Solvay. This is interpreted as indicative of a strong emission component from mercury spills in the electrolytic cell environment.

## Acknowledgments

The authors gratefully acknowledge support and encouragement from our EMECAP partners, in particular Dr. Barbara Mazzolai. The EMECAP project was supported financially by the European Commission DG XII.

## References

- Anon, 2001. Reduction of Mercury Emissions from the West European Chlor-Alkali Industry, 3rd Ed. Euro-Chlor Association, Brussels.

- Barregård, L., Horvat, M., Mazzolai, B., Sällsten, G., Gibicar, D., Fajon, V., diBona, S., Munthe, J., Wängberg, I., Haeger Eugensson, M., to appear. Urinary mercury in people living near point sources of mercury emissions. *Environmental Health Perspectives*, submitted.
- Bennett, M., Edner, H., Grönlund, R., Sjöholm, M., Svanberg, S., Ferrara, R., to appear. Joint application of Doppler Lidar and differential absorption Lidar to estimate the mercury flux from a chlor-alkali plant. *Atmospheric Environment*, submitted.
- Edner, H., Faris, G.W., Sunesson, A., Svanberg, S., 1989. Atmospheric atomic mercury monitoring using differential absorption lidar techniques. *Applied Optics* 28 (5), 921–930.
- Edner, H., Ragnarsson, P., Wallinder, E., 1995. Industrial emission control using lidar techniques. *Environmental Science and Technology* 29 (2), 330–337.
- Fayyad, U.M., Shapiro, G.P., Smyth, P., Uthurusamy, R., 1996. *Advances in Knowledge Discovery and Data Mining*. AAAI Press, Menlo Park, CA.
- Ferrara, R., Maserti, B.E., Edner, H., Ragnarsson, P., Svanberg, S., Wallinder, E., 1992. Mercury emissions into the atmosphere from a chlor-alkali complex measured with the lidar technique. *Atmospheric Environment* 26A (7), 1253–1258.
- <http://www.emecap.com>.
- Kinsey, J.S., Swift, J., Bursley, J., 2004. Characterization of fugitive mercury emissions from the cell building at a US chlor-alkali plant. *Atmospheric Environment* 38 (4), 623–631.
- Mazzolai, B., Mattoli, V., Raffa, V., Tripoli, G., Dario, P., Ferrara, R., Lanzillotta, E., Munthe, J., Wängberg, I., Barregård, L., Sällsten, G., Horvat, M., Gibicar, D., Fajon V., Logar, M., Pacyna, P., Denby, B., Svanberg, S., Edner, H., Grönlund, R., Sjöholm, M., Weibring, P., Donati, A., Baldacci, S., Viganò, W., Pannocchia, A., Fontanelli, R., La Manna, S., Di Bona, S., Fudala, J., Zielonka, U., Hlawiczka, S., Jarosinska, D., Danet, A., Bratu, C., 2004. A multidisciplinary approach to study the impact of mercury pollution on human health and environment: the EMECAP project. Proceedings from the seventh International Conference on Mercury as Global Pollutant, Ljubljana, June 28–July 2, 2004.
- Munthe, J., Kindbom, K., Kruger, O., Petersen, G., Pacyna, J., Iverfeldt, Å., 2001. Examining source–receptor relationships for mercury in Scandinavia. *Water, Air, and Soil Pollution: Focus* 1 (3), 299–310.
- Pacyna, J.M., 2003. Emissions of Hg in Europe in 2000, The EU Mercymys Project, e-mail: [jp@nilu.no](mailto:jp@nilu.no)
- Pacyna, E.G., Pacyna, J.M., Pirrone, N., 2001. European emissions of atmospheric mercury from anthropogenic sources in 1995. *Atmospheric Environment* 35 (17), 2987–2996.
- Schroeder, W.H., Munthe, J., 1998. Atmospheric mercury—an overview. *Atmospheric Environment* 32 (5), 809–822.
- Sjöholm, M., Weibring, P., Edner, H., Svanberg, S., 2004. Atomic mercury flux monitoring using an optical parametric oscillator based lidar system. *Optics Express* 12 (4), 551–556.
- Southworth, G.R., Lindberg, S.E., Zhang, H., Anscombe, F.R., 2004. Fugitive mercury emissions from a chlor-alkali factory: sources and fluxes to the atmosphere. *Atmospheric Environment* 38 (4), 597–611.
- Svanberg, S., 1994. Differential absorption lidar (DIAL). In: Sigrist, M. (Ed.), *Air Monitoring by Spectroscopic Techniques*. Wiley, New York, pp. 85–161.
- Wängberg, I., Edner, H., Ferrara, R., Lanzillotta, E., Munthe, J., Sommar, J., Sjöholm, M., Svanberg, S., Weibring, P., 2003. Atmospheric mercury near a chlor-alkali plant in Sweden. *Science of the Total Environment* 304 (1), 29–41.
- Wängberg, I., Barregård, L., Sällsten, G., Haeger-Eugensson, M., Munthe, J., Sommar, J., 2005. Emissions, dispersion and human exposure of mercury from a Swedish Chlor-Alkali plant. *Atmospheric Environment*, this issue.
- Weibring, P., Edner, H., Svanberg, S., 2003. Versatile mobile lidar system for environmental monitoring. *Applied Optics* 42 (18), 3583–3594.



## PAPER IV

### **Multi-component chemical analysis of gas mixtures using a continuously tuneable lidar system**

P. Weibring, Ch. Abrahamsson, M. Sjöholm, J. N. Smith, H. Edner, S. Svanberg.

*Applied Physics B* **79**, 525–530 (2004).



P. WEIBRING  
C. ABRAHAMSSON<sup>✉</sup>  
M. SJÖHOLM  
J.N. SMITH\*  
H. EDNER  
S. SVANBERG

## Multi-component chemical analysis of gas mixtures using a continuously tuneable lidar system

Department of Physics, Lund Institute of Technology, 22100 Lund, Sweden

Received: 26 September 2003/Revised version: 14 May 2004  
Published online: 7 July 2004 • © Springer-Verlag 2004

**ABSTRACT** Differential absorption lidar (DIAL) measurements are usually made on single compounds by alternately switching the wavelength between on and off a resonance line. The selection of more than two wavelengths is a mathematical necessity for simultaneous measurement of multiple species or for resolving interference effects between a compound of interest and a background gas such as water vapour or carbon dioxide. This is especially true in the mid-IR region, where many hydrocarbon compounds have important spectral features. We present a method for remote measurement of gas mixtures in the mid-IR region based on a newly developed fast-switching, frequency-agile optical parametric oscillator lidar transmitter. A multivariate statistical procedure has also been applied for this system, which combines a genetic algorithm for wavelength selection with a partial least squares method for identifying individual compounds from their combined absorption spectrum. A calibration transfer is performed for compounds of interest using reference spectra from an absorption spectra database. Both indoor absorption cell measurements and outdoor remote range resolved measurements of hydrocarbon mixtures were performed to explore the performance of the method.

PACS 42.62.Fi; 42.79.Qx; 02.50.Sk

### 1 Introduction

The increased awareness of the environmental impact of certain industrial activities, and more stringent regulations on emissions, call for more powerful measurement techniques for air pollution monitoring. Especially interesting are the hydrocarbons due to their absorption of terrestrial radiation in the infrared wavelength region, which contributes to the greenhouse effect [1]. The amount and composition of the anthropogenic hydrocarbon emissions from sources such as petrochemical industries, pipelines, road transportation, use of solvents, rice paddies, and biomass burning are also crucial

for understanding their impact on the chemistry of the atmosphere on regional and global scales.

In this context, optical remote sensing techniques [2] are particularly advantageous, allowing large-area monitoring and avoiding sample extraction and preparation difficulties. The mid-IR wavelength region is an important spectral range where many hydrocarbon compounds have fundamental rotational–vibrational transitions while major constituents such as N<sub>2</sub> and O<sub>2</sub> do not. In Fig. 1 the absorption spectra of some simple n-alkanes and water vapour are presented. It can be concluded that there are significant overlaps in the absorption spectra of the hydrocarbons, as well as interference effects from water vapour. Spectrometers have frequently been used for multiple-species detection over long atmospheric paths, utilising different multivariate techniques to overcome these interference effects. In these cases, the whole spectral signature, containing hundreds of measurement wavelengths, is utilised for the detection. In the case of lidar systems, it would be possible to scan the entire wavelength range using a tuneable, pulsed transmitter, but this is not feasible due to the limited repetition rate of most lasers. Still, a substantial number of different wavelengths need to be employed in the multi-species lidar measurement, rather than just a pair of on- and off-resonance wavelengths, as is customary in differential absorption lidar (DIAL). The multi-wavelength lidar concept raises new considerations, such as how many wavelengths and which wavelengths should be used during a particular measurement. In addition, the signal obtained from a single laser pulse in a lidar measurement is not sufficient for data extraction. On the contrary, a large number of shots have to be averaged for each measurement wavelength in order to get an acceptable signal-to-noise ratio. Thus, for a concentration measurement the total number of transmission wavelengths must be weighed by the time required to obtain a sufficient signal for each wavelength.

A few laser-based techniques have been proposed for remote measurements of spectrally overlapping species. Kasparian et al. applied a femtosecond white-light source and a time resolved spectrometer to record whole spectral signatures, ranging over hundreds of nanometers [3]. Presently, available intensity in the mid-IR wavelength region makes hydrocarbon monitoring impractical using this approach. Robinson et al. used a hybrid approach, consisting of DIAL measurements and gas sampling, to determine range resolved

✉ Fax: +46-46/222-4250,

E-mail: Christoffer.Abrahamsson@fysik.lth.se

\*On leave from: Department of Environmental Engineering Science, California Institute of Technology, Pasadena, CA 91125, USA;

Present address: Atmospheric Chemistry Division, National Center for Atmospheric Research, P.O. Box 3000, Boulder, CO 80307, USA

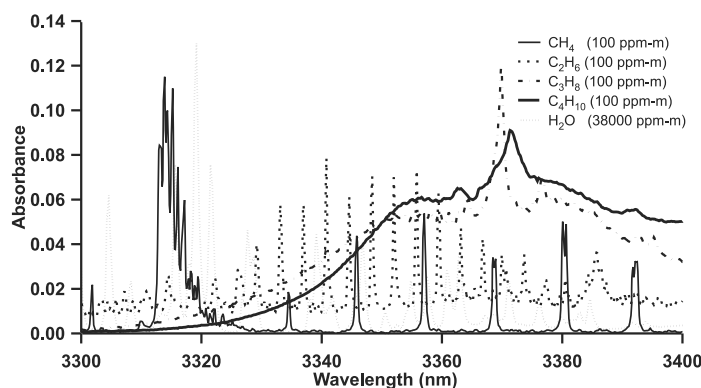


FIGURE 1 Example of overlapping hydrocarbon and water absorption spectra in the middle-IR region

concentrations of hydrocarbon mixtures [4]. Quagliano et al. employed a CO<sub>2</sub> laser in the wavelength range from 9 to 11  $\mu\text{m}$  to make long-path absorption measurements [5]. In that case the discrete nature of the tuning of this laser necessitates the limitation of a set of compounds that have interesting spectral features coinciding with the emitted laser wavelengths. The same group chose to use partial least squares techniques, which we also have explored, for analysing the composition of hydrocarbon mixtures from their combined absorption spectra. The most important distinction between previous papers on the subject and the present one is that our system can be tuned to any wavelength, in any order, in a range of 160  $\text{cm}^{-1}$ , and on a shot-to-shot basis providing on-line range resolved measurements of compound mixtures [6]. The systems overall tuning range, 220–4300 nm, enables measurements of a major part of the important trace gases in the atmosphere.

The quantitative identification of multiple, coexisting compounds from their combined spectrum requires not only a measurement system that has the ability to transmit and detect light at multiple wavelengths, but also the implementation of the appropriate evaluation tools and measurement procedures. To manage these requirements, we will present a method, based on a frequency agile transmitter, genetic variable selection and multivariate statistical techniques. The method is tested by absorption measurements in the laboratory and range resolved outdoor measurements on a remote artificial smokestack.

## 2 Measurement procedure

The task of the multivariate regression technique is to create a mathematical model that relates the absorption of the measurement wavelengths to the concentration of individual components in a gas mixture. This model can then be used to predict the composition of new gas samples.

The multivariate analysis starts with the acquisition of spectra from gas samples with known compositions. A regression model is then built, with the important constraint that the model should be built up using the individual and combined spectra of all compounds and concentrations that one would likely encounter in future measurements. Various methods exist for building a regression model, includ-

ing the well known multiple linear regression technique that is based on ordinary least squares regression. The problem with applying this technique to spectroscopic measurements is the requirement that the variables (spectra) must be linearly independent. In addition, ordinary least squares regression tends to over-fit noisy data. The partial least squares (PLS) technique [7] overcomes most of these problems by the virtue of being a projection technique, i.e., the PLS technique projects the information onto a lower dimensional subspace. The model is built in such way that the first component conveys as much of the variations in the data as possible, at the same time as it finds the relation between the two data blocks (spectra and gas concentrations). If a one-component model is not good enough, more components are added until the variations modelled by the last component is regarded as noise. The quality of the model is evaluated by predicting the gas concentrations of the samples in a test set and thereby calculate the mean prediction error (RMSEP) value:

$$\text{RMSEP} = \sqrt{\frac{\sum_{i=1}^n (y_i - c_i)^2}{n}} \quad (1)$$

where  $y_i$  is the predicted,  $c_i$  is the real concentration value of the sample and  $n$  is the total number of samples. In most studies that have been performed up to date, the multivariate regression technique of PLS has been shown to provide the most accurate predictive models [8] that are the least sensitive to background noise, and therefore this technique will be used for analysing the data in this work.

A recording of the whole spectrum would be desirable, but due to the limited repetition rate of the laser, such measurements could not be carried out in a reasonable time scale, during which the atmospheric circumstances and the compounds present could be considered as constant in the absorption path. Therefore there is a need to reduce the number of measured wavelengths, which is easily done when measuring mixtures containing only a few compounds. When the number of compounds increases, the selection of suitable measurement wavelengths gets more and more difficult, and in the case of severely overlapping spectral structures, it is not possible by the eye to determine which wavelengths to choose. Therefore a genetic algorithm (GA) can advantageously be used as

guidance when selecting which wavelengths to measure. The GA has proven to be a valuable tool for automated variable selection [9–11]. The drawback with GA is normally the substantial set-up preparations that have to be considered. For the present application only some basic set-up properties of the GA were explored, since the goal is not to optimise the GA but just to get some guidance when selecting wavelengths. The wavelengths selected by the GA could then be used as a base when measuring with the system.

For a fixed number of wavelengths the GA consists of four basic steps, where steps 2–4 are performed until a stop criterion is fulfilled:

1. A number of chromosomes (different wavelength sets) are constructed randomly. This is called the initial population. The number of wavelengths in each chromosome is locked to a certain number during the entire wavelengths selection procedure.
2. For each chromosome the response associated with the corresponding experimental conditions is evaluated. This is done by making a PLS model for each chromosome. The model is then evaluated by means of predicting a test set and thereby calculating the RMSEP-value. This value is used as the fitness value and is the criterion for guiding the GA to the global optimum.
3. The reproduction step creates a new population that can be considered as the next generation. The new generation of chromosomes is made up by recombination of the original chromosomes. The chromosomes with a good fitness value have a higher probability to reproduce than a chromosome with a bad fitness value, all in order to improve the overall fitness of the population. The chromosome with the best fitness value is always transferred unchanged to the next generation.
4. Mutations are necessary to overcome some problems that may occur. The most essential problem to be solved is that if a wavelength should not be selected in any of the original chromosomes, it would never be selected in the coming generation if mutations were not present. Another important aspect is that the mutations help the GA not to find local minima, but to find the global minimum. A mutation is simply an exchange of one of the wavelengths in the chromosome to a randomly chosen one.

Although it is optimal to experimentally record these absorption spectra using gases in a test cell, this is not practical for such a large set of compounds that normally can be found in a polluted atmosphere. A better alternative is to use spectroscopic databases, which include most species in the atmosphere. The database approach also has the advantage that it will allow the multivariate model to be modified in the field if a previously unidentified compound would be found to exist in the gas mixture. It is though important to adjust the database data so it also takes the instrumental parameters into account. For example, since field experiments are associated with noisy signals, white noise has to be added to the spectra included in the model. In addition, differences in laser linewidth, wavelength stability, wavelength offset, and wavelength slope lead to further differences in the recorded spectra. All above stated parameters can be taken into account through a calibration

transfer procedure, which establishes a relationship between the instrument and database responses.

Due to the above-mentioned considerations, a measurement must sometimes be performed in an iterative way, especially if there is no detailed knowledge about the composition of the pollution.

A systematic way of dealing with this is proposed in the following procedure.

- Building a model based on experience and basic knowledge of the source's emission inventory and atmospheric conditions. For instance, a petrochemical industry emits a wide range of hydrocarbons. Based on this knowledge the model is built on the expected existing compounds in the emission.
- A GA is used to select the appropriate wavelengths for later PLS determination of the concentrations of the different pollutants. The wavelength selection is made based on database spectra, with added noise etc.
- A PLS model is built from database spectra, with the GA selected wavelengths.
- The lidar measurement is performed with the required number of shots to reach the desired signal-to-noise ratio.
- Calibration transfer is performed between the instrument recording at the selected wavelengths and the database spectra.
- Prediction of the individual concentrations of the compounds in measured mixtures by importing the calibration transferred data to the model.
- Checking the model prediction error statistics. If the measurement gives large residuals, probably the compounds included in the model do not match the composition of the emission. The model is then rebuilt, based on experience, by either increasing or decreasing the number of included compounds until the residual information not described by the model is minimised.

### 3 Experimental set-up

Experiments for this investigation were performed with the Lund University mobile lidar system [12], which is shown schematically in Fig. 2. The key element of the system is a fast tuning lidar transmitter, using all-solid-state technology, providing range- and temporally resolved atmospheric measurements of gas concentrations. The instrument is based on a commercial OPO laser system (Spectra Physics MOPO-730) which has been redesigned introducing piezoelectric transducers mounted on the wavelength tuning mirror and on the crystal angle tuning element in the OPO. A piezoelectric transducer similarly controls the frequency-mixing and doubling stages, which have been implemented to extend system capabilities to the mid-IR and UV regions. The system is able to produce radiation, with an average linewidth better than  $0.2\text{ cm}^{-1}$  and a shot-to-shot tunability of  $160\text{ cm}^{-1}$ , with an accuracy better than the linewidth. For instance, this means that the fast tuning ability is within a range of 170 nm in the mid-IR wavelength region. The output power in the wavelength regions 220–1800 nm and 2600–4300 nm reaches 100 mJ and 20 mJ, respectively [12]. The system performance in terms of wavelength, linewidth and power stability is monitored on a shot-to-shot basis in real time by

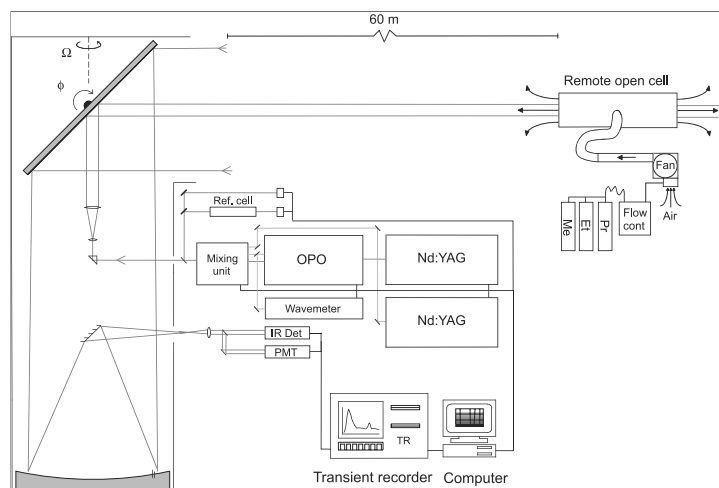


FIGURE 2 Optical schematics of the Lund University lidar system and outdoor open-ended flow cell

a surveillance system based on a Fabry–Pérot interferometer. If the desired requirements are not met for a specific light pulse the system discards the corresponding collected data and repeats the measurement until the requirements are fulfilled. For concentration and wavelength reference purposes, an absorption cell system is incorporated in the lidar system, enabling different reference mixtures to be measured at the same time as the lidar measurement is performed. The outgoing beam from the lidar system is expanded by a variable beam expander and transmitted out into the atmosphere by a computer controlled transmitting/receiving unit; see Fig. 2. A 40 cm diameter Newtonian telescope is used as a receiver. Two parallel detection channels enable full spectral coverage in the UV, VIS and mid-IR regions by utilizing both a PMT and a liquid-nitrogen-cooled InSb detector. A filter system in front of the detectors enables high signal-to-background ratios for compounds in the whole wavelength region. For an optimally adjusted IR lidar system, a measurement range of about 400 m can be estimated.

To test the potential of the measurement procedure in determining the concentration of different compounds in a mixture, two test stations were built. One station consisted of an ordinary absorption cell arrangement simulating an ideal measurement situation. The other test station consisted of an open-ended remote gas cell simulating a remote plume.

The absorption cell arrangement consisted of a 2 cm long cell. All optics including the cell windows were made of  $\text{CaF}_2$ . To eliminate interference fringes and achieve a similar power at both detectors, the beams for the cell and reference paths were split off by reflection from the beam line with separate wedged beam splitters. The detectors (PbSe) were tested to assure that the experiment was conducted in the linear regime of their response. To create a gas mixture the following steps were carried out: The absorption cell was flushed with nitrogen and then evacuated, after which it was filled with different partial pressures of methane, ethane, propane and butane (> 99% purity) using a pressure gauge. Following this, the cell was filled with nitrogen to atmospheric pressure resulting in concentrations of 0–140 ppm m of the above stated hydro-

carbons. For validation purposes a gas mixture was measured using a FTIR instrument (Mattsson Instruments), which showed a good agreement with the lidar system measurement.

In order to simulate a real-life measurement, an outdoor open-ended flow cell was built for testing the lidar system under conditions that closely resemble emission sources such as factory smokestacks. The facility was located 60 m from the lidar system, and consisted of a 3 m long, 40 cm diameter pipe, through which ambient air was forced from a side pipe using a fan. At the inlet of the fan, controlled flows of methane, ethane and propane were added to a controlled flow of carrier gas consisting of ambient air. This mixed gas was then introduced into the center of the main flow cell and allowed to pass out each open end of the pipe, as shown in Fig. 2. The total flow of the gas mixture was measured by a pressure gauge inserted in the side pipe. The concentration of the different gases in the cell was calculated by dividing the flow of the individual gases by the total flow. All flows could be set and monitored from a computer at the lidar system. The average flow data of the gases and air were stored on the computer disc every 10 s. The mass flow controllers were tested to have a maximum error of 15%, and the variation of the air flow was constantly measured and found to be within 2% which results in a total concentration error of approximately 15%. By firing the lidar beam through the open-ended flow cell, range resolved absorption measurements were performed. The maximal range-resolution allowed by the system is 7.5 m. The integrated gas contents (ppm m) due to the gas released was evaluated from the size of the resulting steps in the lidar curves, evaluated with some smoothing of the raw data, using an effective range interval of 15 m.

#### 4 Results

The measuring and analysis procedure for both the absorption cell and the open ended flow cell was performed according to the multivariate concept described above. To make a PLS model, first database spectra of methane, ethane, propane, butane and water were utilised to make 150 resulting

spectra, spanning the expected concentrations of the compounds (0–200 ppm m). Also 40% of white noise and a wavelength jitter of 0.2 nm were added to the spectra to enable a modelling resistant to noisy data and laser wavelength jitter. A GA was utilised to select the most significant wavelengths to use in the PLS model according to the procedure described above. The GA input properties were kept constant at 100 separate chromosomes (wavelength sets), 100 generations and a 5% mutation rate, with the exception of the number of selected wavelengths in order to examine the effect of that factor. Four different sets of wavelengths were compared: 10 and 20 wavelengths selected by the GA, 20 wavelengths selected manually based upon experience of a spectroscopist, and 20 wavelengths selected by a combination of the GA and a spectroscopist. These four sets of wavelengths and a fifth case, utilising all scanned wavelengths, were then used to build separate PLS models.

To validate the wavelength selection procedure and the potential of the different PLS models in determining the concentration of different compounds, an experiment with the indoor absorption cell was performed. The gas cell was filled with 0–140 ppm m of methane, ethane, propane and butane spanning all encountered concentration situations. After the cell was filled, a complete wavelength scan from 3305 to 3385 nm, with a resolution of 0.1 nm, was performed. A simple calibration transfer was then performed, consisting of re-scaling and offset adjustment in order to match the measured spectra to the resolution and spectral response of the database spectra. These data were then used to validate the above described PLS models created from the database. The result from this experiment is summarised in Table 1. Also the models based on wavelength selections for 20 wavelengths selected by a spectroscopist (manual) and 20 wavelengths selected by a combination of the GA and a spectroscopist (GA & manual) are shown in Fig. 3. It can be concluded that a PLS model using 10 wavelengths based on a GA selection gives quite large residuals, but a PLS model based on a 20 wavelength GA

selection improves the predictive abilities. Further increase of the number of wavelengths, to e.g. 30–40, does not significantly increase the prediction capabilities. The automated GA selection of 20 wavelengths performs actually better for ethane than a manual selection of 20 wavelengths based on the selection of a spectroscopist. The GA & manual model with 10 wavelengths selected by a GA and 10 wavelengths added afterwards by a spectroscopist gives the best results, thus achieving a robust model with predictive powers only succeeded by the model based upon the complete spectrum. The prediction error in the combined model is about 7 ppm m for methane, and between 20 and 25 ppm m for the other species. The main improvement in accuracy of the combination model compared to the manual model is achieved for ethane and propane. For ethane, the selection of measurement wavelengths is completely different among the two models while for propane the number of measurement wavelengths around the main peak is increased in the GA & manual model. Here the aid from GA proves to be superior due to the fact that it is difficult to determine by eye only the wavelengths that enable a good de-convolution of the interference among the different species.

The sharp-featured substances can be modelled in a more accurate and robust way, as in the case of ethane, using a few wavelengths rather than using complete spectra, due to the fact that the errors introduced by varying interfering substances could be minimised. It can also be seen that substances with sharp features, such as methane and ethane, are easily modelled using just a few wavelengths whereas heavier compounds with broader spectral features such as propane and butane need a larger set of wavelengths to be modelled in a proper way.

The cell experiment showed that the combination of GA and manual selection gave the best wavelength selection; therefore, these 20 wavelengths were used when measuring on the outdoor cell. The outdoor cell system was set to deliver 0–100 ppm m of methane, ethane and propane for the differ-

	RMSEP methane (ppm m)	RMSEP ethane (ppm m)	RMSEP propane (ppm m)	RMSEP butane (ppm m)
10 wavelengths GA	15	37	43	32
20 wavelengths GA	9	21	37	25
20 wavelengths manual	9	35	33	25
20 wavelengths GA & manual	7	23	19	26
Complete spectra	6	27	14	15

**TABLE 1** Average errors (RMSEP) from the predictions of the samples measured in the indoor cell with variations of the different compounds 0–140 ppm m, showing the differences between the various wavelength selection cases

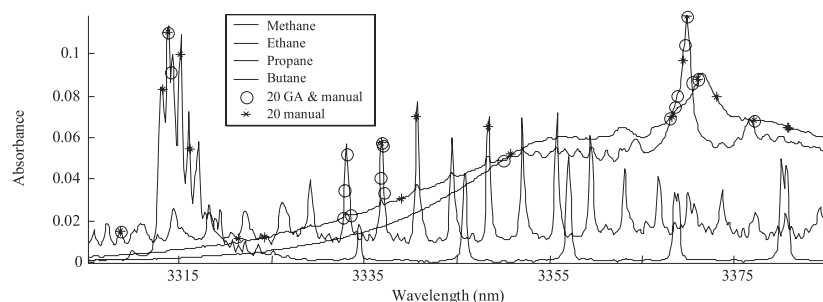


**FIGURE 3** Spectra of the four measured substances, with the selected wavelengths for the different wavelength selection cases marked

TABLE 2 Set values for the mass flow controllers and lidar system response for methane, ethane and propane

Mixture	Set methane concentration (ppm m)	Predicted methane concentration (ppm m)	Set ethane concentration (ppm m)	Predicted ethane concentration (ppm m)	Set propane concentration (ppm m)	Predicted propane concentration (ppm m)
1	0	18	50	46	50	64
2	50	53	100	104	0	0
3	0	10	100	118	0	-2
4	0	5	100	127	100	120
5	100	99	100	99	0	-7
6	100	120	100	120	0	14
7	100	101	100	107	100	109
8	50	56	50	63	50	53
9	0	24	0	-7	50	38
10	100	145	100	105	100	129
Average error		13		10		11

ent measurements. On this occasion the typical pulse energy of the emitted IR radiation was 8–10 mJ. The range resolved data were then used to calculate the absorption at the different wavelengths through the cell. The natural background concentration of methane was measured and taken into account during the calculations. The results from the outdoor cell measurements are summarised in Table 2. The prediction errors are comparable between the lidar and the indoor cell measurements, with some exceptions. The major factor for the disagreement is probably the wind conditions. The fact that the range resolution of the lidar system is only 7.5 m and that the wind speed and direction affects the effective length of the absorption path introduces large errors. The length of the absorption path could typically vary from 3 to 6 m between the extremes of the wind conditions. This was confirmed by introducing smoke to the inlet of the cell system and studying the resulting plumes out of the cell openings for different wind conditions.

## 5 Discussion

The concept of a multi-wavelength lidar system with multivariate analysing techniques for measuring hydrocarbon gas mixtures has been successfully implemented and tested. The tests were carried out with the light hydrocarbons methane, ethane, propane and butane. When larger hydrocarbons such as heptane, hexane, and octane are measured, the spectral overlap will be more severe and it can be difficult to determine the individual concentrations of the different hydrocarbons without increasing the number of wavelengths substantially. Recording all spectral structures over a range of hundreds of nanometers is not possible due to prolonged measurement time compared to the time constants of source emission and atmospheric variability. Thus establishing the concentration of different groups of hydrocarbons, using fewer wavelengths, could be the target for such a measurement. The extension of the multivariate techniques employed in the current study to other classes of compounds is thus one area for future development.

Multi-wavelength measurements can be advantageously applied in other spectral regions as well. In the ultraviolet wavelength region, overlapping aromatic hydrocarbons are more easily measured due to less interfering species. High accuracy measurements of sulphur dioxide with interference of ozone in the ultraviolet wavelength region have been performed with specially designed three wavelength systems [13]. By utilising even more wavelengths, an increase in the accuracy of both sulphur dioxide and ozone could be expected. In the same way one could achieve higher measurement accuracy for isolated species that have been traditionally measured by standard two wavelength measurements (DIAL).

**ACKNOWLEDGEMENTS** This work was supported by the Swedish Space Board, the Knut and Alice Wallenberg Foundation and the Lund/Caltech Academic Exchange Programme. A fruitful collaboration with Spectra Physics, Inc., is gratefully acknowledged.

## REFERENCES

- 1 J.H. Seinfeld, S.N. Pandi: *Atmospheric Chemistry and Physics* (John Wiley & Sons, New York 1988)
- 2 M.W. Sigrist: Air monitoring by spectroscopic techniques, In: *Chemical Analysis*, vol. 127 (John Wiley & Sons, New York 1994)
- 3 J. Kasparian, M. Rodriguez, G. Méjean, J. Yu, E. Salmon, H. Wille, R. Bourayou, S. Frey, Y.-B. André, A. Mysyrowicz, R. Sauerbrey, J.-P. Wolf, L. Wöste: *Science* **301**, 61 (2003)
- 4 R.A. Robinson, P.T. Woods, M.J.T. Milton: *SPIE* **2506**, 140 (1995)
- 5 J.R. Quagliano, P.O. Stoutland, R.R. Petrin, R.K. Sander, R.J. Romero, M.C. Whitehead, C.R. Quick, J.J. Tjee, L.J. Jolin: *SPIE* **2702**, 16 (1996)
- 6 P. Weibring, J. Smith, H. Edner, S. Svanberg: *Rev. Sci. Instrum.* **74**, 4478 (2003)
- 7 P. Geladi, B.R. Kowalski: *Anal. Chim. Acta* **185**, 1 (1986)
- 8 S.J. Haswell, A.D. Walmsley: *Anal. Chim. Acta* **400**, 399 (1999)
- 9 R. Leardi, R. Boggia, M. Terrile: *J. Chemom.* **6**, 267 (1992)
- 10 A.S. Bangalore, R.E. Shaffer, G.W. Small, M.A. Arnold: *Anal. Chem.* **68**, 4200 (1996)
- 11 L. Davies: *Handbook of Genetic Algorithms* (Van Nostrand Reinhold, New York 1991)
- 12 P. Weibring, H. Edner, S. Svanberg: *Appl. Opt.* **42**, 1 (2003)
- 13 T. Fujii, T. Fukuchi, N. Goto, K. Nemoto, N. Takeuchi: *App. Opt.* **40**, 949 (2001)

# PAPER V

## **All-diode-laser ultraviolet absorption spectroscopy for sulfur dioxide detection**

G. Somesfalean, Z. G. Zhang, M. Sjöholm, and S. Svanberg.

*Applied Physics B* **80**, 1021–1025 (2005).



G. SOMESFALEAN  
Z.G. ZHANG\*  
M. SJÖHOLM  
S. SVANBERG✉

## All-diode-laser ultraviolet absorption spectroscopy for sulfur dioxide detection

Department of Physics, Lund Institute of Technology, P.O. Box 118, 221 00 Lund, Sweden

Received: 15 November 2004 /

Revised version: 25 March 2005

Published online: 31 May 2005 • © Springer-Verlag 2005

**ABSTRACT** Ultraviolet radiation around 302 nm was produced by sum-frequency generation in beta-barium borate employing a blue and a near-infrared diode laser. The diode-laser-based spectrometer has a mode-hop-free tuning range of 50 GHz and was used for high-resolution spectroscopic detection of sulfur dioxide. Differential measurements of several gas concentrations, at low pressure as well as at ambient atmospheric pressure, were demonstrated. The detection limit in the first implementation of the instrument was about 20 ppm m at atmospheric pressure, essentially limited by interference fringes. Methods for greatly improving this limit are suggested.

PACS 42.55Px; 42.65.Ky; 42.62.Fi; 42.68.Ca; 33.20.Lg

### 1 Introduction

Strives to extend the available wavelength range of semiconductor lasers have led to the development of new laser types, which have become useful tools for spectroscopic measurements. For instance, a wide access to the mid-infrared (mid-IR) wavelength region (2–15  $\mu\text{m}$ ), where most molecules have fundamental rotational–vibrational transitions, has been achieved by the recent introduction of quantum cascade lasers [1]. Presently, diode laser and LED sources for direct generation of blue and violet radiation down to 365 nm are readily available by use of InGaN and GaN materials [2]. However, at shorter ultraviolet (UV) wavelengths (200–350 nm), there is still a need for efficient continuous-wave (cw) light generation by compact and comparatively inexpensive semiconductor lasers. This would facilitate the widespread application of UV absorption spectroscopy for in situ and remote gas measurements, which has so far been largely prevented by the size, weight, cost, power consumption, and complexity of existing sources. The UV region is important for spectroscopy since electronic transitions of most atoms and molecules occur in this spectral range, and the line strengths of these transitions are several orders of magnitude

larger than those of rovibrational transitions in the infrared [3].

A common approach to generate light in wavelength regions not accessible by direct laser sources is to use different non-linear optical frequency conversion procedures. A particularly powerful approach is a mixing scheme where both the primary pumping laser wavelengths and the generated mixing wavelength can be simultaneously tuned to absorption lines of several species. Such a three-gas-monitoring scheme employing diode lasers has previously been demonstrated for difference-frequency generation (DFG) at 3.4  $\mu\text{m}$  (methane) by mixing a 760 nm (oxygen) and a 980 nm (water vapor) source [4]. In the UV range, recently available blue/violet diode lasers have been successfully employed in frequency mixing with visible and near-infrared diode lasers to produce 254 nm for mercury spectroscopy [5] and 309 nm for hydroxyl radical detection [6], respectively. Alternative diode laser strategies for producing tunable sources of UV light have been demonstrated utilizing second-harmonic generation to 325 nm for copper spectroscopy [7] and to 308 nm for hydroxyl radical detection [8]; and by a combination of frequency doubling and sum-frequency mixing to 283 nm for absorption measurements of lead [9].

In the present work, we report the generation of 6.9 nW of tunable UV radiation in the wavelength interval between 302 and 303 nm by sum-frequency generation (SFG) in a  $\beta\text{-BaB}_2\text{O}_4$  (BBO) crystal employing an external cavity blue diode laser emitting light at 437.84 nm, and a near-infrared (near-IR) Fabry–Pérot diode laser operating around 975 nm. Ultraviolet light, with a continuous 50-GHz mode-hop-free tuning range, was used for spectroscopic detection of molecular sulfur dioxide ( $\text{SO}_2$ ). The moderately strong absorption band around 300 nm has absorption cross sections about 100 times higher than above 365 nm available today for direct diode laser and LED sources. Additionally, in this spectral region no essential interferences from ordinary constituents of air are present [10], except for ozone ( $\text{O}_3$ ), formaldehyde ( $\text{H}_2\text{CO}$ ), and nitrogen dioxide ( $\text{NO}_2$ ), which have one to two orders of magnitude smaller absorption cross sections than  $\text{SO}_2$  [11].

To our knowledge, this is the first all-diode-laser-based UV spectrometer used for  $\text{SO}_2$  detection. An interesting aspect of our optical-frequency-conversion scheme is that in addition to monitoring of the UV-absorbing pollutant  $\text{SO}_2$ , the two driving lasers can be made resonant with transitions

✉ Fax: +46-46-2224250, E-mail: sune.svanberg@fysik.lth.se

\*Permanent address: Department of Applied Physics, Harbin Institute of Technology, P.O. Box 406, Harbin 150001, P.R. China

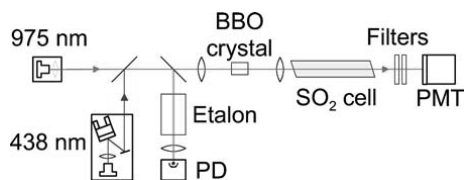


FIGURE 1 Experimental setup for sum-frequency generation at 302 nm used for sulfur dioxide spectroscopy

in nitrogen dioxide (blue laser) and water vapor (near-IR laser). This simultaneous detection scheme can be anticipated to be of interest for studies of chemical processes in the atmosphere and for combustion research. Possible spectral interference between  $\text{NO}_2$  and  $\text{SO}_2$  in the UV range could also be accounted for by monitoring the concentration of  $\text{NO}_2$  in the blue wavelength region.

## 2 Experimental

The experimental setup used for SFG and subsequent  $\text{SO}_2$  detection is shown schematically in Fig. 1. The blue diode laser (Nichia NDHB500APAE1) had a nominal operating wavelength at room temperature of 438 nm and a maximum cw output power of 5 mW. It was assembled into a home-made monolithic brass holder in a Littrow-geometry arrangement with active temperature control to ensure stable single-longitudinal-mode operation. While coarse wavelength tuning was performed by changing the temperature around the diode laser capsule, fine tuning to the desired wavelength was accomplished by changing the angle of the 2400 lines/mm holographic grating (Edmund Scientific 43224) by means of a high-accuracy piezo-translator and driver (Thorlabs MDT-690). With the present coupled-cavity configuration and the particular diode laser type used, the blue laser light could be tuned without mode hops only over limited spectral intervals, probably due to insufficient optical feedback from the grating, and the wavelength was therefore held fixed at 437.84 nm. In order to achieve stable lasing conditions, the operating current  $I_{\text{op, blue}} = 35.5$  mA was chosen just below the threshold of the free-running laser  $I_{\text{th, blue}} = 36.3$  mA, resulting in an output power off the grating of 2.2 mW.

The 980-nm Fabry–Pérot-type diode laser (Power Technology LD1313) with a maximum output power of 200 mW was mounted in a thermoelectrically cooled holder (Thorlabs TCLDM9). The temperature and current variation of the near-IR diode laser wavelength are shown in Fig. 2. As displayed in the figure, a total discontinuous tuning range of about 10 nm for a temperature change of 30°C is achieved, corresponding to the frequency-converted wavelengths of the SFG scheme shown on the right-hand vertical axes. The most stable single-mode-operation conditions with the laser operating free running were found at a set temperature of 12°C. Wavelength scanning was performed by ramping the current (Hewlett-Packard 33120A) with 20-Hz repetition rate and 76-mA peak-to-peak amplitude symmetrically around the operating current  $I_{\text{op, n-ir}} = 120$  mA. This resulted in a continuous tuning range of more than 50 GHz, limited by mode hops, as indicated by the plateau in Fig. 2. At these operating

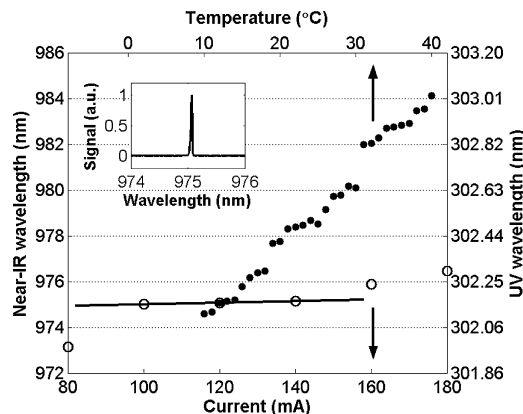


FIGURE 2 Variation of the wavelength output of the near-IR Fabry–Pérot laser with current (open circles, lower horizontal scale) at a temperature of 12°C, and with temperature (filled circles, upper horizontal scale) at a current of 120 mA. Mode hops are seen as discontinuities in the wavelength-tuning range occurring at specific temperatures. The current ramping for a continuous tuning range of 50 GHz used in the present study is indicated as a solid line. In the inset, the typical single-mode characteristic of the laser is shown

conditions, the average output power of the near-IR laser was 130 mW.

The temperature and current of both lasers were controlled by low-noise diode laser drivers (Melles Griot 06DLD 103), and the divergent output beams were collimated by anti-reflection-coated molded glass aspheric lenses (Geltech C230TM). The emitted radiation was diagnosed by a home-made and a commercial wavemeter (Burleigh WA-4500) for precise measurements of the diode laser wavelengths, and by a Czerny–Turner spectrometer (Jobin-Yvon, 1-m instrument) with CCD read out, in order to ascertain that the lasers were operating in a single longitudinal mode during the measurements. The inset in Fig. 2 illustrates the typical single-mode characteristic of the near-IR diode laser output.

Both lasers were vertically polarized, acting as ordinary beams in type I phase matching for a negative uniaxial crystal. The blue and the near-IR beams were combined and spatially overlapped through a dichroic beam splitter and then focused by an achromatic lens ( $f = 60$  mm) into a 13-mm-long BBO crystal, which was cut for type I phase matching at  $\theta \approx 37^\circ$  and  $\varphi = 90^\circ$ . Since both primary beams had comparable elliptical beam sizes, no circularization of the beam profiles was needed. After re-collimation by a plano-convex fused-silica lens with a focal length of 50 mm (Thorlabs LA4148-UV), the generated UV radiation was transmitted through an interference filter (centered at 300 nm), which was slightly tilted for accurately matching the produced UV wavelength, and through a colored glass filter (Schott UG11), before entering a large-area photomultiplier tube (PMT) (Hamamatsu R331). Thus, the non-converted blue and near-infrared radiation, as well as the background light, were effectively blocked from entering the detector. The signal from the PMT was sent via a preamplifier to a signal-averaging oscilloscope

(Tektronix TDS520B), from where the data was transferred to a computer for processing and evaluation.

In the experiments, the crystal was slowly rotated horizontally until phase matching was observed. Since the BBO crystal was cut at a slightly different angle than the one required for this particular combination of wavelengths, the primary beams were not incident normally on the crystal surface. This had the advantage of reducing the back reflections into the lasers. Additionally, all other transmissive optics were carefully angled by a few degrees. Since laser instabilities that might have been caused by optical feedback were not observed, no optical isolation in either beam path was required. The reflected part of the near-IR beam coming from the dichroic beam splitter was directed through a low-finesse solid-glass etalon, which allowed relative calibration of the frequency scale by the free spectral range between the fringes.

A 30-cm-long gas cell, equipped with quartz windows at Brewster angle, and connected to a gas-mixing manifold, could be inserted in the light path in front of the detector for high-resolution measurements of SO<sub>2</sub> at low and ambient atmospheric pressures. The sulfur dioxide, supplied in a steel cylinder as a 2% mixture in dry air (Air Liquid), was diluted with air to required concentrations and introduced into the absorption cell.

The primary generated UV light was estimated by photon counting, and yielded  $n = 0.15 \times 10^9$  pulses per second. Allowing for losses through the interference filter, the colored glass filter, and the quartz lens, which had transmissions of 0.09, 0.82, and 0.92, respectively, and accounting for the quantum efficiency of the PMT at 302 nm ( $\eta = 0.21$ ), means that approximately 6.9 nW was generated inside the crystal.

From the theory of SFG using focused Gaussian beams [12, 13] and assuming a lossless crystal, the UV power can be expressed as

$$P_3 = \frac{4\omega_1\omega_2\omega_3 d_{\text{eff}}^2 P_1 P_2 l h}{\pi \epsilon_0 c^4 n_3^2}, \quad (1)$$

where  $\omega_i$  ( $\omega_1 < \omega_2 < \omega_3$ ) are the angular frequencies,  $P_i$  are the powers,  $n_3 = 1.59$  is the refractive index of the crystal at 302 nm,  $d_{\text{eff}}$  is the effective non-linear coefficient,  $l$  is the crystal length, and  $h$  is a dimensionless focusing parameter. Using input powers measured before the crystal of  $P_1 = 1.6$  mW and  $P_2 = 108$  mW,  $d_{\text{eff}} = 1.24 \times 10^{-12}$  m/V according to the expressions in [14], and  $h = 0.02$  estimated from the plots presented in [12], and accounting for the approximately 7% reflection losses at the crystal input and output facets, a theoretical UV output of  $P_3 = 27$  nW was calculated. The deviation between measured and calculated UV powers could be attributed to imperfect beam overlap of the two input beams, inferior beam profile of the blue diode laser (caused by diffraction in the collimating lens), and deviation from the optimal cutting angle of the crystal.

The bandwidth of the generated UV radiation is expected to be dominated by that of the near-IR laser, because blue lasers in similar configurations were found to have bandwidths of 5 MHz [15] and 8.3 MHz [16], while the bandwidth of the Fabry–Pérot near-IR diode laser is estimated to be less than 100 MHz.

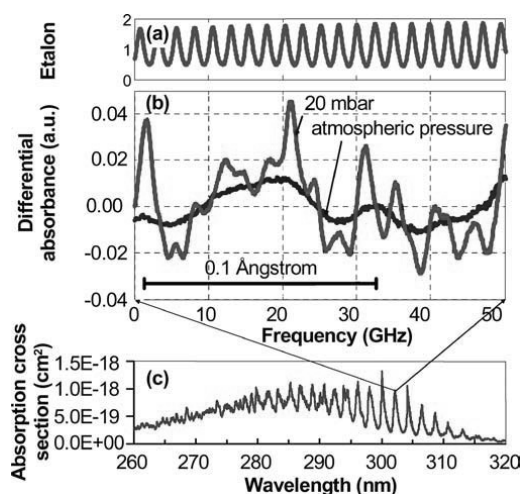


**FIGURE 3** a Etalon fringes from a 2.44-GHz Fabry–Pérot etalon used for frequency calibration. b Sulfur dioxide spectra recorded around 302 nm at low pressure (20 mbar) and at ambient atmospheric pressure. The recordings are 1024 scan averages, corresponding to a total sampling time of 52 s for each curve. c The wavelength location of the spectra in the broad UV absorption region of SO<sub>2</sub> is indicated in a spectral overview, obtained with a Fourier-transform spectrometer [17]

### 3 Measurements and results

The UV radiation wavelength was continuously scanned across a 50-GHz interval by tuning the near-IR laser, while the blue laser was kept at a fixed frequency. Data was averaged over 1024 scans on the digital oscilloscope, corresponding to an acquisition time of 52 s with the repetition rate of 20 Hz used. Attempts to reach higher repetition rates resulted in a decrease of the mode-hop-free tuning range. A portion of the SO<sub>2</sub> absorption spectrum around 302 nm was recorded, as shown in Fig. 3b. Comparison can be made with a Fourier transform spectrometer measurement, shown in Fig. 3c, which indicates the wavelength location of the selected UV scan, and presents an overview of the broad structures of the SO<sub>2</sub> absorption band in the 260–320-nm spectral region [17]. The differential absorption of the slowly-wavelength-dependent SO<sub>2</sub> structures is suitable to be probed with broad laser sources and has been utilized in, for example, differential absorption lidar (DIAL) measurements, where the on/off-resonance wavelength pair 300.5 nm/299.3 nm is normally chosen to achieve maximum contrast [18].

However, the pronounced band spectrum of SO<sub>2</sub> in the UV also has very sharp rotational structures visible only at high spectral resolution [11]. Until now, very few studies of the SO<sub>2</sub> absorption spectrum have been performed using high-resolution instruments. The best available data has a wavelength accuracy of about 0.01 nm and a resolution of  $2 \text{ cm}^{-1}$  (60 GHz) [17], which is more than 600 times broader than a usual diode laser bandwidth (10–100 MHz). There is a great interest in increasing the accuracy and the resolution of the spectrum, especially at temperatures and pressures that are different from NTP, where extremely little data has

been collected. These kind of data, needed for computation of the variation of the absorption cross sections with both temperature and pressure, are collected in spectroscopic databases such as HITRAN [3], and can potentially be useful for separation of stratospheric and tropospheric gas absorption in atmospheric spectra.

Recorded SO<sub>2</sub> spectra at the top of the 302-nm peak are shown in Fig. 3b for a low-pressure gas (20 mbar of a 2% SO<sub>2</sub> gas mixture in dry air) and at atmospheric pressure, in both cases for the same partial pressure of SO<sub>2</sub>. The effect of pressure broadening, with consequent reduction of the differential absorption, can be clearly seen. Given the absorption line density of about 10 lines/cm<sup>-1</sup>, visible in the low-pressure spectrum, lines are partially overlapped at atmospheric pressure due to broadening. However, as evident from the recording, the features remain sufficiently resolved to allow spectroscopic detection.

The spectra displayed were obtained by initial linearization of the slightly non-linear frequency scale using simultaneously recorded interference fringes from an etalon ( $\Delta\nu_{\text{FSR}} = 2.44$  GHz in the near-IR region). The frequency-linearized etalon fringes corresponding to the 975-nm radiation are displayed in Fig. 3a. Subsequent data evaluation consisted of subtraction of the corresponding background levels from all the signals, followed by normalization of the gas-related signals to signals recorded using an empty gas cell. The negative value of the natural logarithm of this ratio is proportional to the path-integrated concentration, i.e. the absorbance, according to the Beer–Lambert law. By subtracting the mean value of this quantity over the interval studied, a differential spectrum was obtained, as displayed in Figs. 3b and 4.

Differential spectra recorded at several low pressures (2, 5, 10, 20, 40, and 80 mbar, respectively) of a 2% SO<sub>2</sub> gas mixture are presented in Fig. 4. They demonstrate the good reproducibility of the spectral measurement, and the absence of a major pressure-broadening influence in this pressure range.

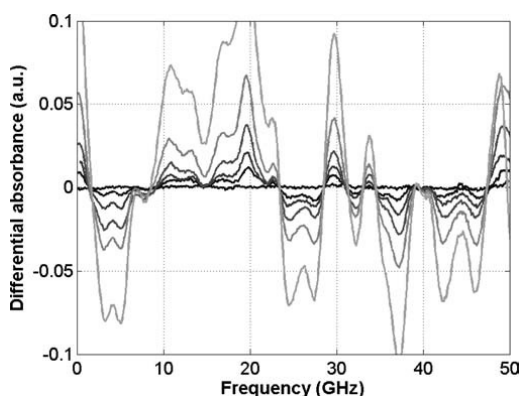


**FIGURE 4** Differential spectra of sulfur dioxide at several low gas pressures (2, 5, 10, 20, 40, and 80 mbar, respectively). The absorption cell was filled with a 2% sulfur dioxide gas mixture. The spectra were normalized to their mean values in the interval presented and the natural logarithm was used to calculate the differential absorbance

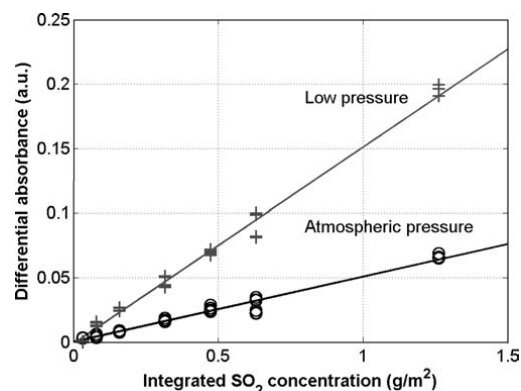


**FIGURE 5** Direct absorption as a function of sulfur dioxide concentration recorded at atmospheric pressure (*lower plot*) and at low pressures (*upper plot*), respectively. The calculation of the differential absorbance is based on the relatively large structure seen in Fig. 3 between 20 and 25 GHz. The slopes of the lines fitted to the experimental points were estimated to be  $5.0 \times 10^{-2}/(\text{g}/\text{m}^2)$  and  $1.5 \times 10^{-1}/(\text{g}/\text{m}^2)$  for high and low pressures, respectively

As a measure of the path-integrated SO<sub>2</sub> concentration, the ratio (i.e. the difference in the spectra of relative absorbance presented) between the signal on and off a gas absorption feature was formed, similarly to the procedure used in differential absorption lidar (DIAL) [18]. In this particular case the spectral feature between 20 and 25 GHz, seen in Fig. 3, was selected and the resulting differential absorbance was found to depend linearly on the path-integrated SO<sub>2</sub> concentration, as can be seen in Fig. 5. It can also be seen in the figure that the sensitivity is about three times higher at low pressures than at ambient atmospheric pressure. It was found that the SO<sub>2</sub> differential signals at atmospheric pressure and at a path-integrated concentration of about 50 mg/m<sup>2</sup>, equivalent to 20 ppm m, became comparable to the magnitude of unwanted interference fringes generated in the optical system, thereby defining the present detection limit of the diode-laser-based spectrometer.

#### 4 Discussion and conclusions

We have demonstrated high-resolution spectroscopic detection of molecular sulfur dioxide using a sum-frequency-generation scheme. Our detection scheme relies on the fact that the absorption spectrum of sulfur dioxide in the wavelength region around 300 nm consists of a complicated line structure superimposed on the typical broader structure that is normally used. The sensitivity of the diode-laser-based spectrometer in its present configuration is limited by interference fringes, induced by spurious reflections and scattering in the optical system. No attempt to minimize the influence of this type of noise was done so far. This can be performed by extensive use of anti-reflection coatings on the optical components, use of wedged windows (especially on the gas cell), dithering of optical components, and filtering techniques. Although the reported detection limit for SO<sub>2</sub> is too high for use in environmental monitoring, the present sensitivity could be

sufficient for industrial or volcanic SO<sub>2</sub> emission measurements. For example, average integrated gas concentrations around 100 ppm m and above have been readily observed in volcanic plumes [19].

As mentioned, the detectivity of the present setup was primarily limited by experimental circumstances, which implies that the interference fringes should be eliminated first. Consecutively, however, the fundamental noise sources should be reduced to achieve the best possible detection performance. Alternatively, the signal could be enhanced, for instance by increasing the UV power available. In the following, a survey of possible sensitivity-enhancement schemes is presented.

Since only direct absorption measurements were presently performed, the sensitivity can be improved by at least one order of magnitude using modulation schemes, which effectively reduce the influence of noise by moving the detection band to much higher frequencies, where the flicker ( $1/f$ ) noise is strongly reduced. In particular, frequency-modulation (FM) spectroscopy or two-tone frequency-modulation spectroscopy (see e.g. [20]) performed at 10 MHz or higher frequencies eliminates this type of noise, leaving the quantum shot noise as a fundamental limitation. FM spectroscopy in the UV region was demonstrated in [5]. With the UV intensities generated in the present experiments, modulation techniques are expected to improve the detectivity considerably.

Alternative sensitive detection schemes such as cavity ring-down spectroscopy (CRDS), intracavity laser absorption spectroscopy (ICLAS), and White cells are based on multipass arrangements which require comparatively high optical power in order to reduce the detection noise. In our case the advantage of such schemes would be limited due to the low UV laser power available. However, more careful overlapping of the beams by, for example, use of anamorphic prism pairs and collimation optics designed for the proper laser wavelength, and use of high-power blue diode lasers currently available (30 mW), have the potential to increase the emitted UV intensities. A very promising alternative is to use quasi-phase matching (QPM) in a periodically poled non-linear crystal to increase the efficiency of the frequency conversion. This has been demonstrated for frequency doubling of the 650-nm output of a dye laser using a QPM crystal [21]. At present, however, QPM crystals with short poling period – necessary for these short wavelengths – are not yet commercially available.

Inspecting Fig. 2 we notice that, by using the full tuning of the near-IR diode laser, a 1-nm UV tuning range can be achieved, thus accessing the large-scale differential effect available in the SO<sub>2</sub> spectrum. Clearly, this cannot be achieved without severe mode-jump problems. This would suggest great difficulties in achieving sensitive detection. However, as recently pointed out and demonstrated by us, a ‘misbehaving’ diode laser can still be utilized when applying a temporal gas correlation scheme, where fluctuations in the sample signal are correlated to a simultaneously recorded reference cell signal [22]. For large UV tuning ranges several tandem non-linear crystals achieving together broadband phase matching, or a multiple-period periodically poled non-linear material, must be used.

As mentioned in the introduction, the original idea was to detect three different gases – sulfur dioxide, nitrogen dioxide, and water vapor – simultaneously. Due to difficulties in scanning the blue diode laser, this was, however, not achieved here. With improving performance of the blue diode lasers, possibly by using an anti-reflection-coated device presently commercially available [23], the implementation of the proposed multi-species spectrometer should be possible. A less ambitious scheme would allow simultaneous NO<sub>2</sub> and SO<sub>2</sub> detection by frequency doubling of 635-nm radiation. As recently demonstrated, radiation at 635 nm weakly interacts with NO<sub>2</sub>, and by using FM spectroscopy realistic detection limits can be reached [24]. Simultaneous 317-nm FM spectroscopy efficiently addresses the weak bands of SO<sub>2</sub>, as indicated in Fig. 3.

**ACKNOWLEDGEMENTS** This work was supported by the Swedish Research Council, the SIDA/VR Research Link Programme, the SIDA Asian-Swedish Research Partnership Programme, and the Knut and Alice Wallenberg Foundation.

## REFERENCES

- 1 F. Capasso, *IEEE J. Sel. Top. Quantum Electron.* **38**, 511 (2002)
- 2 S. Nakamura, G. Fasol, *The Blue Laser Diodes* (Springer, Heidelberg, 1997)
- 3 L.S. Rothman, C.P. Rinsland, A. Goldman, S.T. Massie, D.P. Edwards, J.-M. Flaud, A. Perrin, C. Camy-Peyret, V. Dana, J.-Y. Mandin, J. Schroeder, A. McCann, R.R. Gamache, R.B. Wattson, K. Yoshino, K.V. Chance, K.W. Jucks, L.R. Brown, V. Nemtchinov, P. Varanasi, *J. Quantum Spectrosc. Radiat. Transfer* **60**, 665 (1998)
- 4 U. Gustafsson, J. Sandsten, S. Svanberg, *Appl. Phys. B* **71**, 853 (2000)
- 5 J. Alnis, U. Gustafsson, G. Somesfalean, S. Svanberg, *Appl. Phys. Lett.* **76**, 1234 (2000)
- 6 L. Corner, J.S. Gibb, G. Hancock, A. Hutchinson, V.L. Kasyutich, R. Peverall, G.A.D. Ritchie, *Appl. Phys. B* **74**, 441 (2002)
- 7 T. Laurila, R. Hernberg, *Appl. Phys. B* **83**, 845 (2003)
- 8 H.R. Barry, B. Bakowsky, L. Corner, T. Freearde, O.T.W. Hawkins, G. Hancock, R.M.J. Jacobs, R. Peverall, G.A.D. Ritchie, *Chem. Phys. Lett.* **319**, 125 (2000)
- 9 J. Franzke, R.W. Fox, L. Hollberg, *Spectrochim. Acta Part B* **53**, 1951 (1998)
- 10 K.P. Koch, W. Lahmann, *Appl. Phys. Lett.* **32**, 289 (1978)
- 11 J. Orphal, K. Chance, *J. Quantum Spectrosc. Radiat. Transfer* **82**, 491 (2003)
- 12 G.D. Boyd, D.A. Kleinman, *J. Appl. Phys.* **39**, 3597 (1968)
- 13 K. Sugiyama, J. Yoda, T. Sakurai, *Opt. Lett.* **16**, 449 (1991)
- 14 Y.X. Fan, R.C. Eckhardt, R.L. Byer, C. Chen, A.D. Jiang, *IEEE J. Quantum Electron.* **QE-25**, 1196 (1989)
- 15 R.S. Conroy, J.J. Hewett, G.P.T. Lancaster, W. Sibbett, J.W. Allen, K. Dholokia, *Opt. Commun.* **175**, 185 (2000)
- 16 H. Leinen, D. Glässner, H. Metcalf, R. Wynands, D. Haubrich, D. Meschede, *Appl. Phys. B* **70**, 567 (2000)
- 17 A.C. Vandaele, P.C. Simon, J.M. Guilmet, M. Carleer, R. Colin, *J. Geophys. Res.* **99**, 25 599 (1994)
- 18 S. Svanberg, in *Air Monitoring by Spectroscopic Techniques*, ed. by M.W. Sigrist (Wiley, New York, 1994), pp. 85–161
- 19 B. Galle, C. Oppenheimer, A. Geyer, A.J.S. McGonigle, M. Edmonds, L. Horrocks, *J. Volcanol. Geotherm. Res.* **119**, 241 (2002)
- 20 P. Kauranen, H.M. Hertz, S. Svanberg, *Opt. Lett.* **19**, 1489 (1994)
- 21 J.-P. Meyn, M.M. Fejer, *Opt. Lett.* **22**, 1214 (1997)
- 22 G. Somesfalean, M. Sjöholm, L. Persson, H. Gao, T. Svensson, S. Svanberg, *Appl. Phys. Lett.* **86**, 184102 (2005)
- 23 D.J. Lonsdale, A.P. Willis, T.A. King, *Meas. Sci. Technol.* **13**, 488 (2002)
- 24 G. Somesfalean, J. Alnis, U. Gustafsson, H. Edner, S. Svanberg, *Appl. Opt.*, in press (2005)



## PAPER VI

### **Temporal correlation scheme for spectroscopic gas analysis using multimode diode lasers**

G. Somesfalean, M. Sjöholm, L. Persson, H. Gao, T. Svensson, and S. Svanberg.

*Applied Physics Letters* **86**, 184102 (2005).



## Temporal correlation scheme for spectroscopic gas analysis using multimode diode lasers

G. Somesfalean, M. Sjöholm, L. Persson, H. Gao,<sup>a)</sup> T. Svensson, and S. Svanberg<sup>b)</sup>  
*Department of Physics, Lund Institute of Technology, P.O. Box 118, SE-221 00 Lund, Sweden*

(Received 9 November 2004; accepted 15 March 2005; published online 26 April 2005)

The reliability of diode lasers used in spectroscopic applications is limited by their intrinsic multimode and mode-jump behavior when wavelength-tuned by current or temperature. We report on a scheme for gas analysis based on temporal correlation between absorption signals from an unknown external and a known reference gas concentration, simultaneously recorded when the diode laser wavelength is temperature-tuned across absorption features of the gas of interest. This procedure, which does not require any knowledge of the exact spectrum, also eliminates light intensity fluctuations due to mode competition. The method is illustrated for atmospheric oxygen absorption applied to diffusion measurements.

© 2005 American Institute of Physics. [DOI: 10.1063/1.1921351]

Gas concentrations can be conveniently measured by high-resolution absorption spectroscopy employing single-mode tunable laser sources, especially diode lasers. The narrow-band laser radiation is scanned over an isolated absorption line, specific for the species to be studied, and the concentration is retrieved from the measured absorbance according to Beer–Lambert’s law. The technique, commonly referred to as tunable diode laser absorption spectroscopy (TDLAS), has applications ranging from, e.g., long-path absorption measurements of environmental pollutants<sup>1</sup> to probing of gas confined in porous materials.<sup>2</sup>

However, semiconductor diode lasers have intrinsic properties that often impair their spectroscopic applicability.<sup>3</sup> For example, several longitudinal modes can oscillate simultaneously, since the width of the spectral gain profile is much broader than the separation between adjacent longitudinal modes. The mode competition leads to interfering gas absorption signals from the submodes. Additionally, the tuning range of diode lasers is often not continuous and mode-hops occur, which causes light intensity fluctuations that can be misinterpreted as absorption. To cope with these problems, essentially single-mode operation can be achieved by employing distributed feedback, distributed Bragg reflector, or external cavity arrangements. All these technologies increase the degree of complexity and the cost of the systems. Additionally, the wavelength characteristics of the laser can change over time due to aging. Diode laser system realizations are frequently subject to thermal drift and active stabilization may be needed. These inconveniences as well as the need of expert operators have been major obstacles for the widespread application of TDLAS.

Another approach is used in the gas filter correlation (GFC) technique,<sup>4</sup> in which, frequently passive, broadband radiation is either passed directly through the external gas that is analyzed, or is additionally filtered through an optically thick reference cell filled with the target gas. The direct recording is strongly dependent upon the presence of the target gas in the external path, whereas the signal from the

reference cell is essentially the same, since the light at all characteristic wavelengths is anyway absorbed. The difference in spectral transmittance between the two paths is thus a sensitive indicator of the target gas concentration. Due to the inherent “holistic” property of the GFC technique, which matches out the unique spectral signature of the target gas, the presence of interfering gases does not affect the analysis. Notably, no knowledge of the gas spectrum is needed, which has been effectively used in, e.g., lidar gas monitoring<sup>5</sup> and gas imaging.<sup>6,7</sup>

In this letter a scheme for gas analysis, denoted temporal gas correlation spectroscopy (TEGACOS), is proposed. The technique combines the superior sensitivity and selectivity of the high-resolution TDLAS technique with the simplicity and robustness of a GFC spectrometer. The technique is particularly suited for analysis of gas with sharp absorption characteristics, and allows employment of multimode diode lasers. Similarly to the GFC technique, the radiation is split into one beam transmitted through the external gas, and another beam passed directly through a reference cell with a well-calibrated concentration of the target gas, as illustrated in the schematic setup shown in Fig. 1. Generally, the diode laser wavelength can be tuned across absorption structures of the target gas by changing the diode temperature or current. The simultaneously recorded signals from the two optical paths may contain gas absorption imprints, as well as intensity variations due to mode competition and mode hops, background fluctuations, and interference fringes. If the target gas is present in the external path, the gas signatures will correlate in time. Oppositely, mode-instability-induced fluctuations of the laser output will correlate differently, since they are independent of the presence of the gas. Thus, in order to discriminate between gas-related absorption and

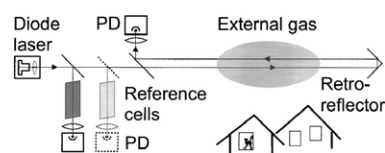


FIG. 1. Experimental setup for temporal gas correlation spectroscopy.

<sup>a)</sup>Present address: Department of Applied Physics, Harbin Institute of Technology, P.O. Box 406, Harbin 150001, People’s Republic of China.

<sup>b)</sup>Electronic mail: sune.svanberg@fysik.lth.se

mode instability, at each point in time both the external and the reference signals are normalized to the laser output power, which is conveniently monitored using the integrated photodiode in the diode laser case.

In conclusion, if the diode laser operates in a single longitudinal mode when scanned through the gas absorption structures, the temporal recording obtained constitutes the actual absorption spectrum of the gas. This is the ideal case used in conventional TDLAS. Oppositely, if the laser mode is unstable, the detected signal no longer corresponds to the actual spectrum. By using the temporal correlation scheme, information about the gas absorption can still be retrieved. It should be noted that the influence of laser frequency fluctuations due to thermal drift are automatically eliminated with the temporal correlation scheme, due to the simultaneousness of the measurement. Note also that external background and internal optical variations, including changes in the optical system alignment, and interference fringes generated by external feedback from optical surfaces, should be minimized, as in conventional TDLAS. If the perturbation widths are comparable to the linewidth of the absorbing species under investigation, they can obscure the detection and reduce system performance. Increased sensitivity is achieved with the suggested method, as in conventional GFC, in wavelength regions with strong differential absorption, i.e., where the gas spectrum has high contrast.

To demonstrate the TEGACOS concept, preliminary proof-of-principle measurements were performed on atmospheric oxygen, which has close-lying and well-resolved absorption lines in the A-band around 760 nm. An AlGaAs Fabry-Pérot-type diode laser (Sharp LT031MDO) with a nominal wavelength of 757 nm at 25 °C and a free running output power of 7 mW was scanned across a wide wavelength range including several oxygen absorption lines, by changing the laser temperature about 12 °C. Although temperature scanning by a Peltier element in a standard laser mount was slow (~20 s per scan), a faster method based on photothermal heating of the diode laser by pulsed radiation from an external laser<sup>8</sup> was also investigated. Many commercially available diode lasers are notoriously emitting light at multiple longitudinal modes. Enhanced multimode behavior of the diode laser used in our experiments was obtained by operating it at an injection current close to the lasing threshold. The widely tunable but spectrally noisy diode laser source, not suitable to use in conventional TDLAS, was diagnosed using a spectrometer. The output spectrum obtained had discontinuities and mode hops, as illustrated in Fig. 2(b). The experimental setup, shown schematically in Fig. 1, consisted of an external path of variable length and several reference paths, corresponding to different absorbancies, utilized for calibration. Figure 2(a) shows the simultaneously recorded direct-absorption signals normalized to the monitor current and divided by a fitted third order polynomial for display purposes. The signals displayed correspond to 138, 304, and 830 g/m<sup>2</sup> path-integrated concentration of oxygen, respectively. The absorption features observed (counted from left to right) correspond to the P3P3, P3Q2, R13Q14, R15R15, R15Q16, and R17R17 lines of the oxygen A band. However, it should be stressed that such a detailed spectral knowledge is not required using the present technique, which functions for any combination of gas absorption signals obtained when the diode laser source exhibits arbitrary frequency shifts or mode competition.

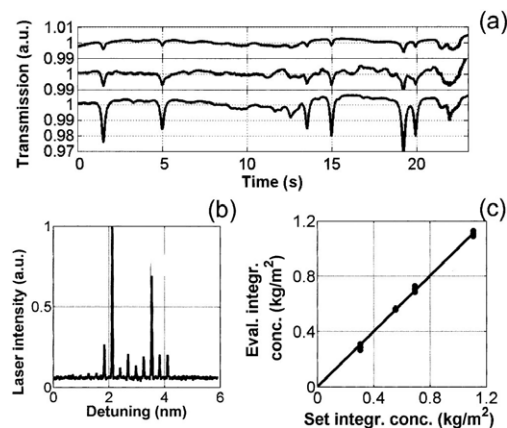


FIG. 2. (a) Simultaneously recorded single-scan time-correlated oxygen signals. The curves correspond to 138, 304, and 830 g/m<sup>2</sup> path-integrated concentrations of oxygen, equivalent to path lengths in air of 0.5, 1.1, and 3 m, respectively; (b) typical multimode diode laser spectrum around 760 nm; (c) evaluated vs set path-integrated oxygen concentrations in air, plotted with a linear fit.

Similarly to the broadband GFC technique, the reference cell provides an ultrasharp matching signature of the target gas. However, owing to the spectral sharpness of the laser source used in the temporal correlation scheme, the absorbed radiation is detected in a narrow wavelength interval at the time, and not integrated over all wavelengths as in the conventional case. Thus, in this scheme the reference cell is preferably not totally absorbing, and can also be used for calibration purposes. Since the reference gas concentration is well known, the external gas concentration can be related to it in a way that resembles the standard addition method. An important difference is that the standard addition calibration is usually not performed simultaneously, but in a time multiplexing procedure. To avoid line shape discrepancies of the absorption lines that would impair the correlation, the temperature and pressure in the reference path are kept as similar as possible to the conditions in the external gas. This can be achieved, e.g., by long-term temperature stabilization and pressure equilibrium in nonsealed reference cells.

The simple data processing consisted of initial subtraction of the background level, assessed by temporarily switching of the laser, followed by normalization of the signals to the laser output power. In order to remove the influence on the signals caused by path-differential variations due to, e.g., slowly wavelength-dependent transmission, a sliding pointwise-symmetric division was performed. The logarithms of the signals obtained were subject to a sliding correlation interval with a width corresponding to the expected width of the gas absorption features, resulting in a pointwise time-interval-integrated ratio between the signals. In a calibration procedure, a pair of reference signals of known concentration was used to single out points in time having the expected time-interval-integrated ratio, thus corresponding to the gas signature. Subsequently, the pointwise time-interval-integrated ratio between one of the reference signals and the external signal was used to determine the unknown gas concentration in the external path. The evaluated path-integrated concentrations obtained by the TEGACOS method versus

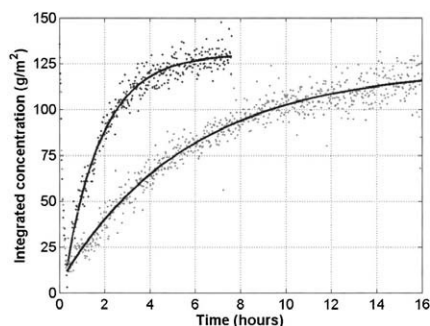


FIG. 3. Recording of the reinvasion of ambient air into a previously nitrogen-flushed glass container covered by polystyrene foam slabs of (a) 20 mm and (b) 10 mm thickness, respectively. An offset path-integrated concentration of  $73 \text{ g/m}^2$ , due to the air outside the container, was subtracted from the signals.

the corresponding set values from a multipath experiment are displayed in Fig. 2(c). The detection scheme was used to monitor gas exchange through differently thick slabs of polystyrene foam covering a glass container placed in ambient air after previously being flushed with pure nitrogen gas. The temporal variation of the path-integrated oxygen concentration in the container is shown in Fig. 3. Although the measurement lasted several hours, thermal drifts do not affect the measurement.

Improved signal-to-noise ratios can be achieved by averaging the concentrations evaluated from several wavelength scans. With the proposed temporal correlation scheme, as in conventional TDLAS, several orders of magnitude higher sensitivity compared to direct absorption could be obtained by employing modulation techniques. A large modulated signal proportional to the species concentration is generated, which can be temporally correlated in a similar

way as in the case presented. Multivariate statistical methods, such as the powerful partial least-squares (PLS) technique,<sup>9</sup> are expected to further improve the accuracy and speed of data processing.

Although demonstrated for oxygen, it is evident that the TEGACOS technique works in any wavelength region and for any gas with close-lying and fairly sharp absorption lines. For example, in the mid-IR region, molecular band heads of several environmentally and biologically important gases could be monitored using the proposed scheme in combination with quantum cascade lasers. The requirements on the system are less stringent, facilitating use of cheaper, high-power multimode diode lasers without need for frequency stabilization. Although the detection sensitivity is lower than for conventional TDLAS, its robustness and relaxed stabilization requirements promise to make the technique very versatile.

This work was supported by the Swedish Research Council, the Asian-Swedish Research Partnership Programme of the Swedish International Development Cooperation Agency (SIDA), and the Knut and Alice Wallenberg Foundation.

<sup>1</sup>H. I. Schiff, G. I. Mackay, and J. Bechara, in *Air Monitoring by Spectroscopic Techniques*, edited by M. W. Sigrist (John Wiley, New York, 1994), pp. 239–333.

<sup>2</sup>M. Sjöholm, G. Somesfalean, J. Alnis, S. Andersson-Engels, and S. Svanberg, *Opt. Lett.* **26**, 16 (2001).

<sup>3</sup>P. Werle, *Appl. Phys. B: Lasers Opt.* **60**, 499 (1995).

<sup>4</sup>T. V. Ward and H. H. Zwick, *Appl. Opt.* **14**, 2896 (1975).

<sup>5</sup>H. Edner, S. Svanberg, L. Unéus, and W. Wendt, *Opt. Lett.* **9**, 493 (1984).

<sup>6</sup>J. Sandsten, P. Weibring, H. Edner, and S. Svanberg, *Opt. Express* **6**, 92 (2000).

<sup>7</sup>J. Sandsten, H. Edner, and S. Svanberg, *Opt. Express* **12**, 1443 (2004).

<sup>8</sup>C. Klimcak and J. Camparo, *J. Opt. Soc. Am. B* **5**, 211 (1988).

<sup>9</sup>P. Weibring, Ch. Abrahamsson, M. Sjöholm, J. N. Smith, H. Edner, and S. Svanberg, *Appl. Phys. B: Lasers Opt.* **79**, 525 (2004).



# PAPER VII

## **Analysis of gas dispersed in scattering media**

M. Sjöholm, G. Somefalean, J. Alnis, S. Andersson-Engels, and  
S. Svanberg.

*Optics Letters* **26**, 16–18 (2001).



## Analysis of gas dispersed in scattering media

M. Sjöholm, G. Somesfalean, J. Alnis, S. Andersson-Engels, and S. Svanberg

Department of Physics, Lund Institute of Technology, P.O. Box 118, S-221 00 Lund, Sweden

Received August 7, 2000

Monitoring of free gas embedded in scattering media, such as wood, fruits, and synthetic materials, is demonstrated by use of diode laser spectroscopy combined with sensitive modulation techniques. Gas detection is made possible by the contrast of the narrow absorptive feature of the free-gas molecules with the slow wavelength dependence of the absorption and scattering cross sections in solids and liquids. An absorption sensitivity of  $2.5 \times 10^{-4}$ , corresponding to a 1.25-mm air column, is demonstrated by measurements of dispersed molecular oxygen. These techniques open up new possibilities for characterization and diagnostics, including internal gas pressure and gas-exchange assessment, in organic and synthetic materials. © 2001 Optical Society of America

OCIS codes: 300.6360, 290.7050, 290.5820, 170.3660, 020.3690, 160.4890.

We demonstrate, for what we believe to be the first time, how free gas dispersed in scattering materials can be detected and characterized by use of diode laser spectroscopy. The technique, provisionally denoted gas in scattering media absorption spectroscopy (GAS-MAS) opens up new possibilities for characterization and diagnostics of scattering solids and turbid liquids.

Many substances, frequently of organic origin, are porous and contain free gas that is distributed throughout the material. For instance, wood, plants, fruits, cheese, powders, sintered materials, and foams can be considered. A common way to analyze gas *in situ* is to use absorption spectroscopy that employs a sufficiently narrow-band light source in combination with the Beer–Lambertian law. However, the straightforward application of this method fails for turbid media, since the radiation is heavily scattered in the material containing the gas. Thus there are no well-defined path lengths as required by the Beer–Lambertian law, but light emerges diffusely. This situation has been much discussed in connection with light propagation in living tissue, which has applications to optical mammography,<sup>1–3</sup> dosimetry for photodynamic therapy,<sup>4</sup> and concentration determinations for tissue and blood constituents.<sup>5,6</sup>

In this Letter we consider solid or fluid bulk materials containing pockets or small bubbles of gas. Light scattering is caused by inhomogeneities in the optical properties of the medium. Even in the case of a clear liquid containing fine bubbles of gas, e.g., beer, a diffuse refraction occurs.<sup>7</sup> In the case of strong scattering, which is the most interesting aspect of the proposed gas-detection technique, a long effective path length is achieved, giving rise to a strong gas signature. Clearly, the gas-containing medium should not have substantial absorption of radiation in the wavelength range needed for monitoring of the particular gas. A consequence of this restriction is that materials containing liquid water, e.g., substances derived from living organisms, can be investigated only up to a limiting wavelength of  $\sim 1.4 \mu\text{m}$ . Generally, absorption and scattering properties of solids and liquids have a very slow wavelength dependence. In contrast, free gas exhibits extremely sharp absorptive

features. Thus bulk material will not influence the detected radiation when the frequency of a single-mode probing laser is slightly changed, whereas embedded gas gives rise to a tiny but narrow signal that can be picked up by use of modulation techniques even in the presence of a large background.

Diode lasers are particularly convenient sources of tunable radiation. Tunable diode lasers can easily be wavelength modulated by addition of an ac component to the driving current and are very suitable for monitoring of small but sharp absorptive features.<sup>8</sup> Modulation techniques can be used to increase detection sensitivity by typically several orders of magnitude compared with that of direct absorption.<sup>9,10</sup>

Two basic geometries can be considered when one is performing measurements with the proposed technique. In Fig. 1(a), a transillumination arrangement is presented, and in Fig. 1(b), a backscattering detection scheme is shown. In both cases optical fibers can be used for light injection and for collection of scattered radiation. In a medium with a homogeneous distribution of gas, the “history” of the photons

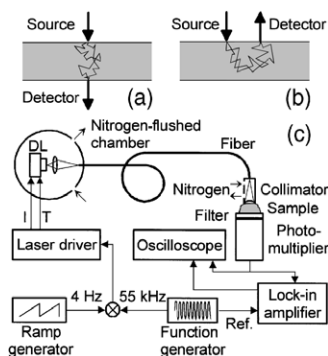


Fig. 1. (a), (b) Basic geometrical arrangements for monitoring of free gas in scattering media. (c) Experimental setup of the initial experiments. DL, diode laser; I, current; T, temperature control; Ref., reference.

can partially be followed by measurement of the relative amplitude of the sharp gas-absorption signal, which increases with the path length. The absorption and scattering properties of the bulk material can be deduced independently by spatially resolved, time-resolved, or frequency-domain measurements, as is frequently done in tissue optics studies.<sup>3</sup> Thus a mean path length of the impinging photons through the scattering material can be estimated, which together with the magnitude of the gas absorption determines the concentration of the dispersed gas.

In our exploratory proof-of-principle measurements we used the setup shown schematically in Fig. 1(c). A tunable diode laser with a nominal wavelength of 757 nm at 25 °C and a free-running output power of 7 mW was used as a spectroscopic source for molecular oxygen monitoring. The spectroscopic measurements were performed on a double line near 759.95 nm (*R17Q18* and *R19R19*) as well as on a strong isolated line at 761.003 nm (*R7R7*). These lines belong to the oxygen A band and were within the wavelength range of the diode laser that we used. Since oxygen is abundant in normal air, we placed the laser and a lens that focused the radiation into a 600- $\mu$ m quartz fiber in a nitrogen-flushed chamber to eliminate spurious oxygen signals. At the other end of the fiber, the output light was collimated by another lens fixed in a nitrogen-flushed adapter. Since the transmitted light intensities through the samples were usually very low, it was important to ensure high detection sensitivity. Thus a photomultiplier tube with a 50-mm-diameter photocathode was used for detection. The ambient room light was effectively suppressed by a Schott RG695 colored-glass long-pass filter attached directly to the photocathode, in combination with the sensitivity falloff of the photomultiplier tube toward longer wavelengths. The samples were placed directly between the colored-glass filter and the collimating lens, which could be freely positioned by a fine translation stage. The diode laser was operated in a thermoelectrically cooled mount and was current and temperature controlled by a precision diode laser driver. Wavelength scanning was achieved by repetitive application of a current ramp with a repetition rate of 4 Hz to the drive current, whereas a sinusoidal current at 55 kHz was superimposed for wavelength modulation of the diode laser. The photomultiplier tube signal was picked up phase-sensitively by a lock-in amplifier. The extracted second-harmonic component and the direct signal were then accumulated for 256 scans in a digital oscilloscope.

Experiments were performed on a variety of samples of different thicknesses. Data for a piece of dried pine wood are shown in Figs. 2(a) and 2(b). Measurements were performed with the collimator lens of the transmitter initially in contact with the surface of the sample and then retracted to add several free air paths of well-defined lengths. The oxygen contained in the scattering medium could be evaluated as illustrated in Fig. 2(a) by use of the standard addition method, which is well known from physical chemistry. Since the absorption is of the order of a few percent, the signal is expected to depend linearly on the

concentration. An equivalent mean path length in the sample, i.e., the mean distance that light travels through air dispersed in the sample, can be evaluated. For determination of the sensitivity of the oxygen concentration measurement, the specific absorption of oxygen was also measured in air with the laser beam strongly attenuated by a neutral-density filter. We also calibrated the wavelength-modulation signal by use of long-path direct absorption in air (measurable at a path length of 4.5 m), given the atmospheric oxygen concentration of 20.8%. In the present experiments we were able to detect an absorbance of  $2.5 \times 10^{-4}$ , which corresponds to a 1.25-mm column of air.

The signal that was due to oxygen dispersed in a 26-mm-thick slice of apple is displayed in Fig. 2(c), which shows that liquid water does not pose problems for measurement in this wavelength region. Finally, Fig. 2(d) shows signals from a bulk of turbid epoxy glue containing air bubbles embedded at an ambient pressure of 300 mbars. The pressure dependence of the line shape can clearly be seen, illustrating the potential of the technique for internal pressure assessment, e.g., in porous mineral samples or sintered ceramics. Measurement data for different samples are compiled in Table 1, in which the thicknesses of the samples are also given. Note that the evaluated air equivalent mean path lengths through the different samples are often several times longer than the geometrical dimension but can also be shorter, as in epoxy.

Our experiments show that it is possible to monitor small and sharp absorptive features that are due to free gas in strongly scattering solids by use of sensitive diode laser spectroscopy. Many applications of this new type of scattering spectroscopy for solids and

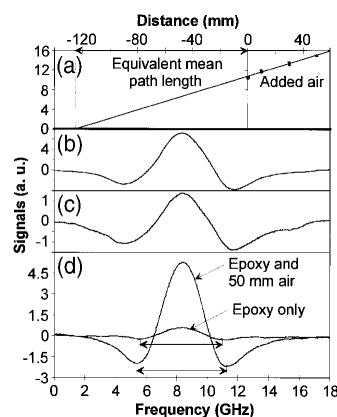


Fig. 2. Experimental data for lines in the molecular oxygen A band obtained by wavelength-modulation diode laser spectroscopy. (a) Standard addition plot for a 10-mm-thick piece of wood, (b) corresponding recorded line shape for wood only, (c) spectral recording for a 26-mm-thick slice of apple, and (d) spectra for a 19-mm-thick bulk of turbid epoxy containing air bubbles at low pressure and when 50 mm of background air is added. The isolated molecular oxygen line was used in these last two recordings.

**Table 1. Equivalent Mean Path Lengths for Oxygen-Containing Porous Media of Various Thicknesses**

Material	Thickness (mm)	Equivalent Mean Path Length (mm)
Wood	10	123
Apple	26	33
Lump sugar	12	20
Granulated salt	18	170
Wheat flour	18	380
Polystyrene foam	19	600
Turbid epoxy	19	5

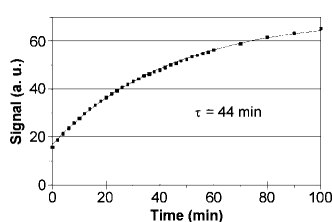


Fig. 3. Recording of the oxygen-signal increase of a 19-mm-thick piece of polystyrene foam while it is kept in ambient air but after it has been stored in a pure nitrogen atmosphere.

liquids can be envisaged. By use of these techniques it would be possible to monitor *in situ* physiological and degradation processes in various biological substances. Such measurements have been limited to extraction of emitted gas from, e.g., plants, fruits, and insects, measured by normal gas spectroscopic techniques.<sup>11,12</sup> The largest challenge would be to develop methods for monitoring minute amounts of free gas inside human tissue, possibly allowing development of new diagnostic techniques for diseases.

The new possibility of observing free gas in scattering media allows not only static gas assessment but also the study of dynamic processes, i.e., how embedded gas is exchanged with the environment. For instance, an object can be surrounded by a gas, and the successive gas penetration into the object can be studied. This example is demonstrated in Fig. 3. A piece of polystyrene foam was first subjected to a pure nitrogen atmosphere for 4 h. Invasion of oxygen into the material was observed to occur with a time constant ( $1/e$ ) of 44 min. This experiment suggests that radioactive labeling can sometimes be replaced by the new technique.

In the limit of very small (nanometer-scale) enclosures of free gas, additional collisional broadening and shifts of diagnostic value can be expected. Note also that tomographic reconstruction of the gas distribu-

tion in the material is possible by use of multiple fibers placed around the object.

Quantifying and fully exploiting diagnostic aspects of gas in scattering media require full modeling of the multiple-scattering material. The theoretical and experimental techniques developed for medical applications are useful in this respect.<sup>2,13</sup> Time-resolved measurements are particularly powerful, providing a direct and independent assessment of photon history.<sup>1,14,15</sup>

The authors gratefully acknowledge the assistance of U. Gustafsson in setting up the oxygen spectrometer and of J. Sandsten in HITRAN spectral identifications. This work was supported by the Swedish Research Council for Engineering Sciences, the Knut and Alice Wallenberg Foundation, and the Swedish Institute. S. Svanberg's e-mail address is [sune.svanberg@fysik.lth.se](mailto:sune.svanberg@fysik.lth.se).

## References

1. S. Andersson-Engels, R. Berg, S. Svanberg, and O. Jarlman, *Opt. Lett.* **15**, 1179 (1990).
2. G. Müller, B. Chance, R. Alfano, S. Arridge, J. Beuthan, E. Gratton, M. Kaschke, B. Masters, S. Svanberg, and P. van der Zee, eds., *Medical Optical Tomography: Functional Imaging and Monitoring*, Vol. 11 of SPIE Institute Series (Society of Photo-Optical Instrumentation Engineers, Bellingham, Wash., 1993).
3. J. C. Hebden, S. R. Arridge, and D. T. Delpy, *Phys. Med. Biol.* **42**, 825 (1997).
4. W. M. Star, *Phys. Med. Biol.* **42**, 763 (1997).
5. Y. Mendelson, A. C. Clermont, R. A. Peura, and B.-C. Lin, *IEEE Trans. Biomed. Eng.* **37**, 458 (1990).
6. A. Roggan, M. Friebel, K. Dörschel, A. Hahn, and G. Müller, *J. Biomed. Opt.* **4**, 36 (1999).
7. N. E. Shafer and R. N. Zare, *Phys. Today* **44**(10), 48 (1991).
8. H. I. Schiff, G. I. Macay, and J. Bechara, in *Air Monitoring by Spectroscopic Techniques*, M. W. Sigrist, ed., Vol. 127 of Chemical Physics Series (Wiley, New York, 1994), Chap. 5.
9. J. A. Silver, *Appl. Opt.* **31**, 707 (1992).
10. D. S. Bomse, A. C. Stanton, and J. A. Silver, *Appl. Opt.* **31**, 718 (1992).
11. F. G. C. Bijnen, H. Zuckermann, F. J. M. Harren, and J. Reuss, *Appl. Opt.* **37**, 3345 (1998).
12. F. J. M. Harren, in *Encyclopedia of Analytical Chemistry: Applications, Theory and Instrumentation*, R. A. Meyers, ed. (Wiley, New York, 2000), pp. 2203–2226.
13. S. Andersson-Engels, R. Berg, and S. Svanberg, *J. Photochem. Photobiol.* **16**, 155 (1992).
14. B. Chance, J. S. Leigh, H. Miyake, D. S. Smith, S. Nioka, R. Greenfeld, M. Finander, K. Kaufmann, W. Levy, M. Young, P. Cohen, H. Yoshioka, and R. Bortsky, *Proc. Natl. Acad. Sci. USA* **85**, 4971 (1988).
15. R. Berg, O. Jarlman, and S. Svanberg, *Appl. Opt.* **32**, 574 (1993).



## PAPER VIII

**Concentration measurement of gas embedded in scattering media by employing absorption and time-resolved laser spectroscopy**

G. Somesfalean, M. Sjöholm, J. Alnis, C. af Klinteberg, S. Andersson-Engels, and S. Svanberg.

*Applied Optics* **41**, 3538–3544 (2002).



# Concentration measurement of gas embedded in scattering media by employing absorption and time-resolved laser spectroscopy

Gabriel Somesfalean, Mikael Sjöholm, Janis Alnis, Claes af Klinteberg, Stefan Andersson-Engels, and Sune Svanberg

Diode-laser-based absorption spectroscopy for the evaluation of embedded gas concentrations in porous materials is demonstrated in measurements of molecular oxygen dispersed throughout scattering polystyrene foam, used here as a generic test material. The mean path length of light scattered in the material is determined with the temporal characteristics of the radiation transmitted through the sample. This combined with sensitive gas-absorption measurements employing wavelength-modulation spectroscopy yields an oxygen concentration in polystyrene foam of 20.4% corresponding to a foam porosity of 98%, which is consistent with manufacturing specifications. This feasibility study opens many possibilities for quantitative measurements by using the method of gas-in-scattering-media absorption spectroscopy. © 2002 Optical Society of America

OCIS codes: 290.7050, 300.1030, 290.4210, 300.6380, 300.6390.

## 1. Introduction

Embedded gas is often found in porous materials of both organic and synthetic origin. Monitoring the distributed free gas can convey the internal gas concentration, pressure, and temperature and can reveal useful information about the bulk material, e.g., internal structure and diffusion characteristics. Recently, we demonstrated a new technique, called gas in scattering media absorption spectroscopy (GASMAS),<sup>1</sup> used for the characterization and diagnostics of free gas in scattering solids and turbid liquids. Initial demonstrations included proof-of-principle measurements of the embedded oxygen concentration relative to an equivalent column of air and of the internal gas pressure as well as assessment of the gas exchange. We analyzed the dispersed gas *in situ* by using absorption spectroscopy, employing a single-mode probing diode laser tuned over a sharp absorption feature of the free gas molecule. The absorption and scattering cross sections of

the bulk material display slow wavelength dependence; thus these properties can be assumed to be constant over the wavelength range tuned. Wavelength modulation techniques<sup>2</sup> are used to increase the detection sensitivity and to discriminate effectively against background signals, allowing for detection of around  $10^{-4}$ – $10^{-5}$  absorption fractions of the light received.

Owing to inhomogeneities on the microscopic scale in the optical properties of the turbid medium, the radiation is scattered multiple times in the material. This prevents a straightforward application of the Beer–Lambert law, which requires well-defined path lengths. However, using a temporally resolved technique, as is routinely done in tissue optics studies,<sup>3,4</sup> a mean path length of the diffused light can be estimated, which together with the strength of the gas absorption determines the concentration of the dispersed gas. In this paper we demonstrate the possibility of quantitative concentration measurements by using polystyrene foam as a generic test material.

## 2. Theoretical Background

To extract the concentration of gas embedded in a turbid sample, we employ two independent measurements to obtain the gas absorbance  $a$  and the absorption path length  $L$ , respectively. The Beer–Lambert law yields the transmitted intensity over a free path length  $L$  of a species with a concentration

The authors are with the Department of Physics, Lund Institute of Technology, P.O. Box 118, Lund, Sweden. S. Svanberg can be reached at sune.svanberg@fysik.lth.se.

Received 23 July 2001; revised manuscript received 2 January 2002.

0003-6935/02/183538-07\$15.00/0

© 2002 Optical Society of America

$c$  and a wavelength-dependent absorption cross section  $\sigma(\lambda)$  according to

$$I(\lambda) = I_0(\lambda)\exp[-\sigma(\lambda)cL] = I_0(\lambda)\exp(-a), \quad (1)$$

where  $I_0(\lambda)$  is the initial injected intensity and  $I(\lambda)$  is the recorded intensity of the transmitted light. One obtains the gas absorbance using Eq. (1) by measuring the transmitted intensity through the sample at wavelengths on and off the gas absorption line. The expression  $cL$  can thus be determined from the transmission measurement, assuming that the absorption cross section is known. The optical path length in a scattering medium  $L_{sm}$  is, however, not simply the thickness of the sample but is determined by the absorption and scattering properties of the material as well as by measurement geometry. Independent measurements of both the absorbance and the optical path length are thus necessary to obtain the concentration. The absorption of the gas is often small compared with the bulk material absorption, and will thus essentially not influence the optical path length. The influence of gas absorption on the optical path length is neglected below.

The absorption path length can be estimated as the mean path length traveled by the photons  $\langle l \rangle$ . Two different approaches can be used to determine the path length, by a direct time-resolved measurement or indirectly by assessing the optical properties of the medium, making it possible to calculate  $L_{sm}$  with the use of a transport model for the light propagation within the sample. In the limit of small absorptions the mean traveled path length can be estimated from the experimentally determined average time of flight of the photons  $\langle t \rangle$  according to

$$L_{sm} = \langle l \rangle = v\langle t \rangle, \quad (2)$$

where  $v$  is the velocity of light in the scattering material. The material optical properties can be as-

slab with finite thickness and infinite expansion, the most common approach is to mirror an infinite set of imaginary positive and negative isotropic sources in an extrapolated boundary at some distance beyond the actual surface, to insure that the fluence rate of photons is fully canceled. It yields an analytic expression for the transmitted pulse shape in terms of the absorption coefficient  $\mu_a$  and the reduced scattering coefficient  $\mu_s'$  of the sample material. In the case of an infinitely extended slab of scattering material the time-dependent transmitted intensity can be expressed as<sup>5</sup>

$$I(\rho, d, t) = (4\pi Dv)^{-3/2} t^{-5/2} \times \exp\left(-\mu_a vt - \frac{\rho^2}{4Dvt}\right) \times \sum_{k=0}^{+\infty} \left[ z_{-k} \exp\left(-\frac{r_{-k}^2}{4Dvt}\right) - z_{+k} \exp\left(-\frac{r_{+k}^2}{4Dvt}\right) \right], \quad (3)$$

where  $\rho$  is the lateral injection-detection separation,  $d$  is the slab thickness,  $D = [3(\mu_a + \mu_s')]^{-1}$  is the diffusion coefficient,  $z_0 = (\mu_s')^{-1}$  is the mean free path of isotropic scattering,  $z_{\pm k} = (2k + 1)d \pm z_0$  is the depth of the imaginary sources used to fulfill the boundary conditions, and  $r_{\pm k} = (\rho^2 + z_{\pm k}^2)^{1/2}$  is the distance between the detector position and the sources used in the calculations. One can evaluate the optical properties of a sample by fitting such an analytical expression to the experimentally acquired temporal dispersion curve by adjusting the free parameters: the absorption, and reduced scattering coefficients. For a slab of thickness  $d$  the expression for the average time of flight of the photons, calculated by integration of Eq. (3), is given by<sup>6</sup>

$$\langle t \rangle = \frac{\sum_{k=0}^{\infty} \left[ \frac{z_{+k}}{r_{+k}} \exp(-\mu_{\text{eff}} r_{+k}) - \frac{z_{-k}}{r_{-k}} \exp(-\mu_{\text{eff}} r_{-k}) \right]}{2vD \sum_{k=0}^{\infty} \left[ \frac{z_{+k}}{r_{+k}^3} (1 + \mu_{\text{eff}} r_{+k}) \exp(-\mu_{\text{eff}} r_{+k}) - \frac{z_{-k}}{r_{-k}^3} (1 + \mu_{\text{eff}} r_{-k}) \exp(-\mu_{\text{eff}} r_{-k}) \right]}, \quad (4)$$

essed experimentally in three different ways: by time-resolved, spatially resolved, and frequency-domain measurements.

In this research the powerful technique of time-resolved measurements utilizing ultrashort light pulses and fast optical detection was used for studying photon propagation in multiple-scattering materials.<sup>3,4</sup> The analysis of the time-resolved data was based on the diffusion approximation to the radiative-transfer theory. When solving the diffusion equation, one must specify the boundary conditions. In the case of simple geometries, such as a

where  $\mu_{\text{eff}} = (\mu_a/D)^{1/2}$  is the effective attenuation coefficient. If the distribution of gas in the porous material is assumed to be homogeneous and the absorption is of the order of a few percent, the detected gas absorption signal can be considered the integrated contribution from all exiting photons. A typical theoretical time-dispersed curve for light transmitted through a 39-mm-thick sample with the optical parameters  $\mu_a = 0.002 \text{ cm}^{-1}$  and  $\mu_s' = 40 \text{ cm}^{-1}$  is shown in Fig. 1. The broad time-of-flight distribution of the photons, corresponding to the absorption path lengths through the embedded

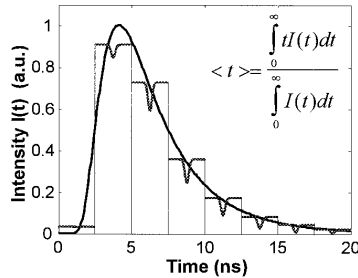


Fig. 1. Analytical time dispersion curve obtained for transillumination of a 39-mm-thick slab with optical parameters  $\mu_a = 0.002 \text{ cm}^{-1}$  and  $\mu_s' = 40 \text{ cm}^{-1}$  by using short-pulsed light. For clarity the direct absorption signals corresponding to photons that have traveled distances of different lengths in the material are intentionally exaggerated. The mean traveling time in the limit of small absorptions is shown in the inset.

gas, gives rise to varying absorption signal strengths, which are also schematically shown in Fig. 1. Thus the gas absorption can be used as a means to track the history of the photons in the material.

A simpler alternative to the time-resolved measurement technique, also explored in the present research, is to use a cw laser source and to spatially monitor the diffuse light-intensity distribution at the sample surface.<sup>7,8</sup> When the recorded light intensity is plotted versus, e.g., the injection-detection separation distance, the final slope of the curve at large distances is found to be determined by the effective attenuation coefficient  $\mu_{\text{eff}}$ . The spatially resolved measurement method also requires that the absolute intensities of the injected and scattered light be measured, which may be difficult to perform experimentally because of unknown conditions regarding the coupling of light at the medium boundary. Solving the diffusion equation in the steady-state case yields a transmitted intensity for an infinite slab of scattering material:

$$I(\rho, d) = \frac{1}{2\pi} \sum_{k=0}^{\infty} \left[ \frac{z-k}{r-k} (1 + \mu_{\text{eff}} r_{-k}) \exp(-\mu_{\text{eff}} r_{-k}) - \frac{z+k}{r+k} (1 + \mu_{\text{eff}} r_{+k}) \exp(-\mu_{\text{eff}} r_{+k}) \right]. \quad (5)$$

In our previous research on measurements of molecular oxygen,<sup>1</sup> we expressed the concentration of the gas in a scattering medium by introducing an equivalent mean path length  $L_{\text{eq}}$ . It is defined as the distance traversed by light in air, yielding a detected signal of the same magnitude as that from the absorption of photons by oxygen embedded in the porous material according to

$$c_{\text{air}} L_{\text{eq}} = c_{\text{sm}} L_{\text{sm}}, \quad (6)$$

where  $c_{\text{air}}$  is the oxygen concentration in air and  $c_{\text{sm}}$  is the oxygen concentration in the scattering medium. The purpose of the present paper is to demonstrate

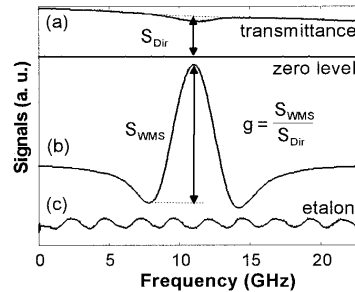


Fig. 2. (a) Direct absorption and (b) second-harmonic component of the WMS spectrum for the R7R7 line in the oxygen A band measured along a 10-m-long path in air. (c) Low-finesse fringes from a 2.43-GHz free spectral range Fabry-Perot etalon used for calibration of the frequency scale.

quantitative gas concentration measurements. Thus determination of an effective absorption path length can be performed by means of time-resolved and spatially resolved measurements.

### 3. Experiment

The experimental setup for GASMAS measurements has been described in detail.<sup>1</sup> Basic experiments of the GASMAS type are conveniently performed on molecular oxygen, because this gas is normally diffused from the surrounding atmosphere into porous materials. A near-IR single-mode diode laser (Sharp LT031MDO) was placed in a nitrogen-flushed chamber, and the light was brought to the sample through a 0.6-mm-core-diameter optical fiber to ensure that the ambient air did not influence the measurements. A transilluminating geometry was chosen, in that the samples were placed on a long-pass colored-glass filter (Schott RG 695) attached directly to the cathode surface of a photomultiplier tube 2 in. (~50 mm) in diameter (EMI 9558 QA). A very high sensitivity and a large dynamic range were achieved with this detector setup, which is necessary when only small and variable amounts of light seep through the scattering materials under observation. In the measurements performed in this study, relatively high transmitted light intensities were available, and it was thus possible to spatially limit the detection area by using a mask with a circular aperture 3 mm in diameter. Thus spatially resolved measurements could also be performed.

The experiments were performed on the strong, isolated R7R7 line at 761.003 nm in the oxygen A band. Wavelength-modulation spectroscopy (WMS) employing lock-in techniques was used to pick up the second-harmonic component, which produces a signal similar to the second derivative of the original absorption line shape. An experimental signal for oxygen in free air is shown in Fig. 2, where a direct absorption recording is also included. In our case modulation at 55 kHz (Philips PM5139) effectively discriminated the background signals by shifting the

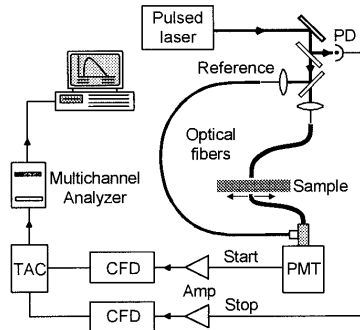


Fig. 3. Experimental setup used for time-resolved measurements: PD, photodiode; PMT, photomultiplier tube; Amp, amplifier; CFD, constant fraction discriminator; TAC, time-to-amplitude converter.

detection band to a high-frequency region where the noise level is low.<sup>2</sup> An absolute absorption calibration was established by performing a long-path measurement in free atmosphere, where the direct absorption signal could also be observed. Curves (a) and (b) in Fig. 2 are recordings obtained for a 10-m-long absorption path length in air. To compensate for variations in the detected light intensity, the experimental WMS signal  $S_{WMS}$  was normalized against the interpolated intensity of the diffused light at the line center  $S_{Dir}$ , defining a GASMAS differential absorption signal

$$g \equiv \frac{S_{WMS}}{S_{Dir}}, \quad (7)$$

determined for the selected modulation parameters. The Fabry-Perot etalon fringes in Fig. 2(c) allow the oxygen linewidth to be evaluated to  $\sim 3.6$  GHz.

Figure 3 shows a schematic diagram of the experimental setup used for the time-resolved measurements. Two different laser sources were used for generation of picosecond-long light pulses: a diode laser with a repetition rate of 10 MHz (Mitsubishi ML4405 with a Bios Quant DL4040 driver) and a mode-locked Ti:Sapphire laser with a repetition frequency of 76 MHz (Coherent MIRA 900). Diode lasers are particularly convenient to use in such applications because of their simple operation, compact size, and ability to produce short light pulses when high-frequency components are applied to the driving current. The average output power of the diode laser was less than 1 mW, while only a small fraction of the available radiation of the Ti:Sapphire laser was used. Both lasers were tuned near the selected absorption wavelength of oxygen around 761 nm. Owing to the broadened linewidths of the short-pulsed lasers and low gas absorption, the gas has no significant influence on the photon propagation through the scattering medium. A transillumination arrangement was used, as shown in Fig. 3, although a backscattering detection scheme can in

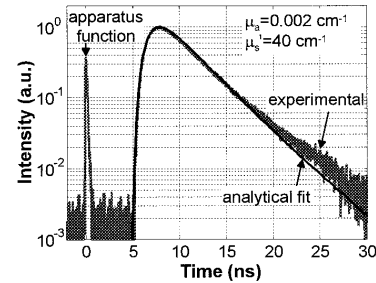


Fig. 4. Recorded time dispersion curve obtained when transilluminating a 39-mm-thick slab of polystyrene foam by using a diode laser source pulsed at 10 MHz. A fit of a theoretical curve and the instrumental transfer function are also depicted.

certain cases be more appropriate. Optical fibers with a core diameter of 0.6 mm were employed for light injection and for collection of scattered radiation, with the samples placed between the fiber ends. The injector-detector separation could be varied by translating the collecting fiber. The transmitted light was detected with a microchannel plate photomultiplier tube (Hamamatsu R2566U-07), which ensured high detection sensitivity. The time-correlated single-photon detection technique was employed, including a constant fraction discriminator, a time-to-amplitude converter TAC, and a multichannel analyzer.<sup>4,9</sup> The photon arrival time distribution was recorded, and the overall temporal response function of the system was  $\sim 140$  ps for the diode laser and  $\sim 60$  ps for the Ti:Sapphire laser. The latter number corresponds essentially to the electronic response time, since the Ti:Sapphire laser has a subpicosecond pulse length.

Spatially resolved gas absorption measurements of GASMAS type combined with transmitted light intensity measurements were also performed with transillumination geometry. The incident beam diameter was 3 mm, and the receiving photomultiplier tube, with a detection area masked down to 3 mm in diameter, could be translated sideways.

The measurements were performed on polystyrene foam samples of different thicknesses but of the same kind. We have chosen polystyrene foam as a model scattering material, owing to its relatively high homogeneity, strong scattering properties, and high gas content, i.e., factors that contribute to a strong gas signature. This material also has a great industrial and commercial importance since it is extensively used as an insulation and packaging material.

#### 4. Results

Figure 4 shows the recorded photon-arrival-time distribution curve for a 39-mm-thick slab of polystyrene foam measured with the diode laser. The time response of the system itself, the apparatus function, was obtained at time  $t = 0$  by using a separate fiber, transmitting part of the laser pulse directly to the detector (see Fig. 3). This signal also provided a

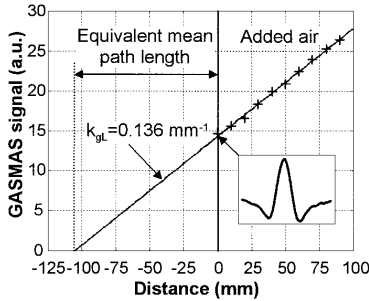


Fig. 5. Standard-addition plot for molecular oxygen obtained with the GASMAS setup showing the extrapolated equivalent mean path length for a 9.4-mm-thick slab of polystyrene foam. The WMS signal obtained with the light-injecting collimator in direct contact with the sample is shown in the inset.

time reference during the measurement. As can be seen from the time distribution curve, a certain fraction of the photons has traveled more than 15 ns through the material, i.e., corresponding to a path length of 4.5 m, although the physical thickness of the slab is only 0.039 m. The absorption and scattering coefficients of the polystyrene foam were determined by first convolving the solution of the diffusion equation, Eq. (3), to the impulse response of the system and then fitting the resulting curve to the detected time dispersion curve, as shown in Fig. 4. Note that the scale is logarithmic, causing small discrepancies in the low-intensity region at late times to be clearly visible. No extrapolated boundary condition was employed in the model owing to the resulting negligible corrections. In principle, laser-induced fluorescence could perturb the measurements. However, because of the long excitation wavelength, the fluorescence is negligible compared with the directly scattered light. The evaluated absorption coefficient is  $\mu_a = 0.002 \text{ cm}^{-1}$ , and the transport scattering coefficient is  $\mu_s' = 40 \text{ cm}^{-1}$ , yielding an effective attenuation coefficient  $\mu_{\text{eff}} = 0.5 \text{ cm}^{-1}$ .

Gas-absorption spectroscopy data for a 9.4-mm-thick slab of polystyrene foam embedded with atmospheric oxygen are shown in Fig. 5. It illustrates the amplitude variation of the GASMAS signal for several added free columns of air and is used to estimate an extrapolated equivalent mean path length in polystyrene foam according to the standard-addition method. Since the fraction of light absorbed by the gas within the medium is small, corresponding to only a few percent of the incident light, the absorption signal  $g$  is approximately linearly proportional to the concentration. We denote the slope of the curve

$$k_{gL} \equiv \frac{g}{L}, \quad (8)$$

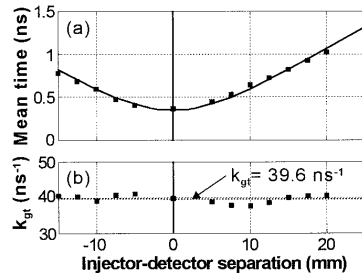


Fig. 6. (a) Recorded mean time of flight through a 9.4-mm-thick slab of polystyrene foam measured with a pulsed Ti:Sapphire laser. Solid curve, theoretical curve corresponding to the evaluated optical parameters ( $\mu_a = 0.002 \text{ cm}^{-1}$ ,  $\mu_s' = 40 \text{ cm}^{-1}$ ). (b) Dotted line, quotient between the GASMAS signal and the mean traveling time of the photons together with a least-squares fit of the factor  $k_{gt}$ .

where  $L$  is the absorption path length in air. The oxygen concentration in the polystyrene foam can now be estimated as

$$c_{\text{sm}} = \frac{c_{\text{air}} L_{\text{eq}}}{v \langle t \rangle} = \frac{g}{\langle t \rangle} \frac{c_{\text{air}}}{v k_{gL}}, \quad (9)$$

where Eqs. (2) and (6) and substitution of  $L = L_{\text{eq}}$  in Eq. (8) have been utilized. To minimize the influence of material inhomogeneities, temporal dispersion curves were also recorded for various lateral positions of the detector. The pulsed Ti:Sapphire laser was employed in such a measurement on a 9.4-mm-thick polystyrene foam slab. An experimental plot of the directly evaluated mean photon arrival time versus various injector–detector separations is shown in Fig. 6(a), derived from these measurements. A theoretical curve corresponding to the evaluated optical parameters is also plotted according to Eq. (4). In Fig. 6(b) the experimental value at different injection–detection separations of the ratio between the GASMAS signal and the mean time of flight,  $k_{gt} \equiv g/\langle t \rangle$ , is shown together with a least-squares fit. The uncertainty in the ratio was 1.3%, evaluated by using a 95% confidence interval of the experimental values. The only unknown factor left is the index of refraction of the scattering material  $n_{\text{sm}}$ , which determines the light velocity in the medium according to  $v = c_0/n_{\text{sm}}$  where  $c_0$  is the light velocity in vacuum. Owing to the homogeneous and isotropic nature of the porous material, the macroscopic index of refraction was estimated as a weighted mean of the refractive indices of the individual compounds contained, i.e.,

$$n_{\text{sm}} = P n_{\text{air}} + (1 - P) n_b, \quad (10)$$

where  $P$  is the material porosity,  $n_{\text{air}}$  and  $n_b$  are the indices of refraction of air and of the bulk material, respectively. In the case of gas equilibrium with the surrounding atmosphere we can derive the foam po-

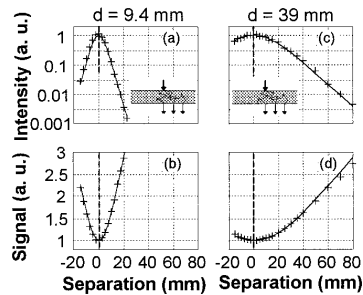


Fig. 7. Spatially resolved transmission recordings measured with the GASMAS setup on two polystyrene foam slabs (a), (b) 9.4 mm and (c), (d) 39 mm thick: upper curves, transmitted intensity; lower curves, detected oxygen absorption signal amplitude for different injector–detector separation distances. Fits according to the evaluated effective attenuation coefficient ( $\mu_{\text{eff}} = 0.5 \text{ cm}^{-1}$ ) are also indicated. A schematic of the transillumination setup is shown in the insets, and dashed lines at the zero position mark the symmetry axis.

rosity  $P$  from the embedded gas concentration by using

$$P = \frac{V_{\text{gas}}}{V_{\text{tot}}} = \frac{c_{\text{sm}}}{c_{\text{air}}}, \quad (11)$$

where  $V_{\text{gas}}$  is the volume of gas in the porous material and  $V_{\text{tot}}$  is the total volume of the porous material. With an index of refraction of the polystyrene bulk material,  $n_b = 1.4$ , and an atmospheric oxygen content of 20.8%, the oxygen concentration in the polystyrene foam can be evaluated accordingly with Eqs. (9)–(11) to yield  $c_{\text{sm}} \approx 20.4\%$  and the corresponding foam porosity  $P \approx 98\%$ .

The mean time of flight of the photons, and consequently the embedded gas concentration, can as described above also be evaluated indirectly by spatially resolved measurement techniques. Experimental curves recorded with the GASMAS setup are shown for a 9.4-mm-thick [Figs. 7(a), 7(b)], and a 39-mm-thick [Figs. 7(c), 7(d)] slab of polystyrene foam. Figures 7(a) and 7(c) show the total transmitted light intensity as a function of lateral displacement, where the zero separation corresponds to the position where the injector and the detector are placed opposite to each other. Figures 7(b) and 7(d) display the GASMAS signal of the embedded oxygen. Note that the transmitted light intensity falls off laterally as the GASMAS signal increases. The distributions are, as expected, broader in the case of the thicker slab. The experimental points are plotted in Fig. 7 together with theoretical curves [Eqs. (4) and (5)] where the effective attenuation coefficient evaluated above is used. In the general case the mean time of flight can thus be evaluated when we insert the obtained optical parameters into the analytical formula, Eq. (4). However, a fit of the theoretical curve to the spatially resolved steady-state data measured at long injection–detection separation ( $\rho \gg z_0$ ) can provide

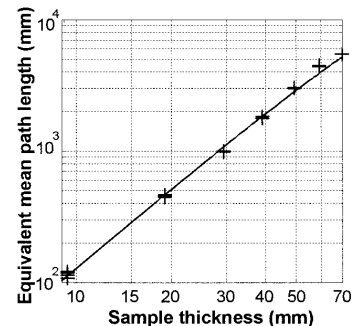


Fig. 8. Plot of the equivalent mean path length corresponding to oxygen absorption measured through slabs of polystyrene foam with different thicknesses by using a diode laser. The mean time of flight is proportional to the square of the slab thickness. Solid line, theoretical curve evaluated with  $\mu_a = 0.002 \text{ cm}^{-1}$  and  $\mu_s' = 40 \text{ cm}^{-1}$ .

only an unambiguous value for the lumped coefficient  $\mu_{\text{eff}}$  and not for  $\mu_a$  and  $\mu_s'$  separately. The embedded gas concentration can thus not readily be assessed by using only these kinds of steady-state measurements.

Measurements on polystyrene foam slabs of different thicknesses were also performed, and the variation in the equivalent mean path length with the slab thickness is plotted in Fig. 8. It can be seen in Fig. 8 that in the case of polystyrene foam, which has weak absorption and strong scattering properties, the mean time of flight related to the equivalent mean path length is proportional to the square of the thickness of the slab, i.e.,  $\langle t \rangle \propto d^2$ , as predicted by Eq. (4) for the case of low gas absorption. A similar relationship was also obtained by considering the related topic of light propagation through clouds.<sup>10</sup>

## 5. Conclusions and Discussions

We have shown that the embedded gas concentration can be estimated by using time-resolved measurements together with the newly developed GASMAS technique. The proof-of-principle measurements were performed on atmospheric oxygen at a wavelength characterized by weak absorption. The gas was embedded in polystyrene foam, which is a model material with high porosity and strong scattering properties. The evaluated porosity of polystyrene foam is comparable with manufacturing specifications. However, in the more general case of moderate porosity or of substantial gas absorption, it is still a subject for further investigation whether there is any preference for the photons to travel through the diffused gas or through the bulk material when being multiply scattered inside the porous material. This is a research topic that might reveal novel insights into the field of light propagation through confining media.

Note that some aspects of the GASMAS technique

do not require detailed knowledge about light propagation, as in the present case of an absolute concentration measurement. For example, gas pressure, temperature, and ratios between gas concentrations are quantities that can be readily evaluated, being largely independent of light scattering inside the porous medium.

Gas tomography is another possible application of the technique. This extension corresponds to the one done for optical mammography and skull hematoma detection.

An alternative to the time and spatially resolved techniques presented in this paper is to perform phase-sensitive measurements in the frequency domain.<sup>11,12</sup> A major advantage of such a method is that it needs only one single diode laser both for the GASMAS measurements and for determination of optical properties of the bulk material by using modulation techniques.

This research was supported by the Swedish Research Council for Engineering Sciences (TFR), the Knut and Alice Wallenberg Foundation, and the Swedish Institute.

#### References

1. M. Sjöholm, G. Somesfalean, J. Alnis, S. Andersson-Engels, and S. Svanberg, "Analysis of gas dispersed in scattering media," *Opt. Lett.* **26**, 16–18 (2001).
2. U. Gustafsson, G. Somesfalean, J. Alnis, and S. Svanberg, "Frequency-modulation spectroscopy with blue diode lasers," *Appl. Opt.* **39**, 3774–3780 (2000).
3. B. Chance, J. S. Leigh, H. Miyake, D. S. Smith, S. Nioka, R. Greenfeld, M. Finander, K. Kaufmann, W. Levy, M. Young, P. Cohen, H. Yoshioka, and R. Boretzky, "Comparison of time-resolved and unresolved measurements of deoxyhemoglobin in the brain," *Proc. Natl. Acad. Sci. USA* **85**, 4971–4975 (1988).
4. S. Andersson-Engels, R. Berg, S. Svanberg, and O. Jarlman, "Time-resolved transillumination for medical diagnostics," *Opt. Lett.* **15**, 1179–1181 (1990).
5. M. S. Patterson, B. Chance, and B. C. Wilson, "Time-resolved reflectance and transmittance for the noninvasive measurement of tissue optical properties," *Appl. Opt.* **28**, 2331–2336 (1989).
6. S. R. Arridge, M. Cope, and D. T. Delpy, "The theoretical basis for the determination of optical path lengths in tissue: temporal and frequency analysis," *Phys. Med. Biol.* **37**, 1531–1560 (1992).
7. T. J. Farrell, M. S. Patterson, and B. Wilson, "A diffusion theory model of spatially resolved, steady-state diffuse reflectance for noninvasive determination of tissue optical properties *in vivo*," *Med. Phys.* **19**, 879–888 (1992).
8. J. S. Dam, P. E. Andersen, T. Dalgaard, and P. E. Fabricius, "Determination of tissue optical properties from diffuse reflectance profiles by multivariate calibration," *Appl. Opt.* **37**, 772–778 (1998).
9. R. Berg, O. Jarlman, and S. Svanberg, "Medical transillumination imaging using short-pulsed diode laser," *Appl. Opt.* **32**, 574–579 (1993).
10. U. Platt, Institute for Environmental Physics, University of Heidelberg, Heidelberg, Germany (personal communication, 2000).
11. J. K. Link, "Measurements of the radiative lifetimes of the first excited states of Na, K, Rb, and Cs by means of the phase shift method," *J. Opt. Soc. Am.* **56**, 1195–1199 (1966).
12. J. B. Fishkin, E. Gratton, M. J. Vande Ven, and W. W. Mantulin, "Diffusion of intensity-modulated near-infrared light in turbid media," in *Time-Resolved Spectroscopy and Imaging of Tissues*, B. Chance and A. Katzir, eds., *Proc. SPIE* **1431**, 122–135 (1991).



# PAPER IX

## **Laser spectroscopy of free molecular oxygen dispersed in wood materials**

J. Alnis, B. Anderson, M. Sjöholm, G. Somesfalean, and  
S. Svanberg .

*Applied Physics B* **77**, 691–695 (2003).



J. ALNIS\*  
B. ANDERSON\*\*  
M. SJÖHOLM  
G. SOMESFALEAN  
S. SVANBERG✉

## Laser spectroscopy of free molecular oxygen dispersed in wood materials

Department of Physics, Lund Institute of Technology, P.O. Box 118, 22100 Lund, Sweden

Received: 29 January 2003/Revised version: 21 July 2003  
Published online: 30 September 2003 • © Springer-Verlag 2003

**ABSTRACT** The recently introduced Gas in Scattering Media Absorption Spectroscopy (GASMAS) technique is applied to the study of various wood samples. Molecular oxygen in the pores of the strongly scattering material is detected using diode laser spectroscopy around 760 nm. Diffuse light propagation in these media is studied by time-dispersion measurements. Furthermore, anisotropy related to the fibre structure of wood and gas diffusion properties are studied. Promising extensions of the experiments are discussed.

PACS 42.55.Px; 42.62.Fi; 81.05.Rm; 81.70.Fy; 87.64.Cc

### 1 Introduction

Solid-state and liquid materials exhibit only broad features in optical absorption spectroscopy due to the complex interaction of the atoms. Thus, the requirements for resolution in spectroscopic instrumentation are moderate in the study of such materials. On the other hand, many natural and artificial materials contain pores filled with gas, for which the associated absorptive signals are typically  $10^4$  times narrower, rendering them invisible in standard spectroscopy of solids and liquids. However, by using single-mode diode laser radiation combined with modulation techniques [1], even very weak and narrow gas absorption signals in open air can be retrieved. Recently, we demonstrated the first measurements with the Gas in Scattering Media Absorption Spectroscopy (GASMAS) technique [2] of gas embedded in porous media. In our first demonstrations, atmospheric oxygen was monitored in samples as diverse as wheat flour, polystyrene foam, and apple. Diode laser spectroscopy combined with sensitive modulation techniques was performed on an A-band line around 760 nm. Gas diffusion in polystyrene was studied by first placing the sample in pure nitrogen for several hours and subsequently observing the time constant for the re-invasion of the ambient air into the material.

A porous medium by nature scatters light, resulting in many different trajectories for the photons penetrating a sample. Thus, absorption experiments cannot be evaluated by a straightforward use of the customary Beer–Lambert law. Instead diffuse light propagation as encountered in tissue or cloud optics has to be considered. Concentration determination requires the effective path length through the medium to be known, an aspect that has been addressed in [3], where experimental techniques and theoretical approaches well known in the field of medical tissue optics [4–6] were employed. The distribution of short and long path lengths could be determined in time-resolved transillumination measurements and verified in continuous-wave experiments, in which the distance between the points of light injection into the sample and the photon pick-up by the receiver was altered.

Further aspects of the GASMAS technique are explored in the present paper, which focuses on gas in an important class of porous natural materials, wood, which has been addressed by others, although using intrusive methods (see, e.g. [7]). As in previous work, we restrict our gas studies to molecular oxygen, and use a diode laser source, although virtually any gas within the reach of tunable lasers with narrow enough linewidths can be used. The experimental arrangements and the measurement techniques presently used are briefly described in the next section. Then, measurements are described in Sect. 3, where a comparative study of eight different types of common woods is performed, and a study of the anisotropy induced by the orientation of the annual rings is presented. Air diffusion into wood is also elucidated, showing differences between wood of different types. Finally, a concluding section discusses the results and suggests some extensions to the techniques.

### 2 Experimental arrangements and procedures

#### 2.1 Continuous wave GASMAS spectroscopy

The experimental setup for GASMAS, shown schematically in Fig. 1a, has been described in detail elsewhere [2, 3]. The diode laser and the lens that coupled light into the fibre were placed in an enclosure flushed with nitrogen to eliminate oxygen from the ambient air. A 600- $\mu\text{m}$  fibre was used to bring the probe light via a collimating lens to the sample, which was illuminated with a 3-mm-diameter beam. In order to obtain a high photon collecting efficiency

✉ Fax: +46-46/2224250, E-mail: Sune.Svanberg@fysik.lth.se

\*Permanent address: Institute of Atomic Physics and Spectroscopy, University of Latvia, 19 Rainis Blvd., Riga LV-1586, Latvia

\*\*Permanent address: Laser and Fibre Optics Centre, University of Cape Coast, Cape Coast, Ghana

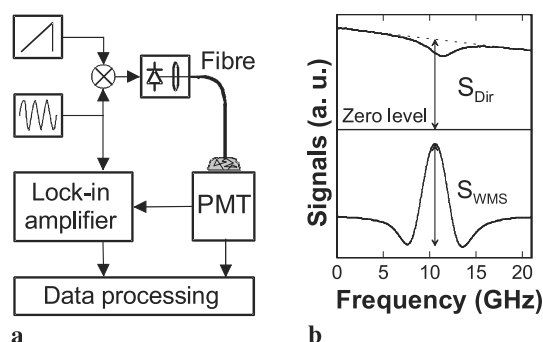


**FIGURE 1** a Schematic of the GASMAS setup. b WMS signal of oxygen recorded for a 10-m column of air and corresponding pure absorptive imprint

and a high dynamic range, the sample was placed directly on a photomultiplier tube (PMT; EMI9558 QA) cathode, which was protected from visible light by a blocking coloured glass filter (Schott RG695).

A diode laser (Sharp LT031MDO) with an output power of 7 mW was temperature tuned to the molecular oxygen line at 761.003 nm (R7R7 of the A-band). The laser injection current was swept at a repetition frequency of 4 Hz, allowing a linear scan over the absorption line. A 55-kHz sine-wave modulation was superimposed on the current ramp, and the absorption signal was detected by the use of a lock-in amplifier (EG&G Princeton Applied Research 5209) at the second harmonic of this modulation frequency, rendering a wavelength modulation spectroscopy (WMS) signal that was similar to the second derivative of the absorption profile. Signal averaging, of between 32 and 1024 scans depending on the level of noise, was performed on a computer-controlled digital oscilloscope. The maximum wavelength drift was less than 500 MHz/h. Thus, with a pressure-broadened oxygen linewidth of about 3.5 GHz at ambient pressure, the drift of the laser wavelength was negligible even during substantial averaging.

The wavelength modulation spectroscopy (WMS) signal of the absorbing oxygen in a 10-m column of air and the corresponding pure absorptive imprint are shown in Fig. 1b. The slight asymmetry of the WMS signal was caused by a variation of the modulation depth during the laser scan. The peak-to-peak value of the signal ( $S_{WMS}$ ) was, in the absorption regime explored, linearly proportional to the gas-related differential absorption and to the light intensity reaching the detector. Hence the WMS signal was always normalised by dividing it by the interpolated light intensity at the peak absorption wavelength ( $S_{Dir}$ ). The optical densities of the samples varied by several orders of magnitude and so did the light levels reaching the detector. The PMT gain was adjusted by changing the supply voltage to achieve high amplification and linearity in the detected signal. Clearly, oxygen concentration measurements in optically dense samples have less sensitivity because the weak signals vanish in the noise. In this case in particular, enhanced accuracy can be achieved by first performing a least squares linear fitting of an ideal WMS curve to the noisy recorded WMS curve. Thus, instead of directly using the peak-to-peak value of the noisy curve, the corresponding fitting factor constitutes a measure of the gas

absorption. One simple method for obtaining the ideal WMS curve is to use an experimental curve recorded with a good signal-to-noise ratio.

It could be checked that no spurious oxygen signal occurred and that the flushing with nitrogen of the diode laser chamber was adequate by replacing the sample with an appropriate absorptive filter, which attenuated the transmitted light to a level that could be detected linearly by the PMT, and by ensuring that there was no air gap between the filter and the collimator.

The oxygen concentration in the sample could be related to the oxygen in the ambient air by deliberately introducing an air gap between the fibre collimator and the sample (the standard addition method of analytical chemistry). The WMS signal, normalised to the intensity detected, could, in the regime of low absorption, be considered to be linear with the absorption path length.

## 2.2 Time-resolved photon propagation spectroscopy

The setup used for time-resolved measurements of photon path lengths in wood samples has been described previously [3] and is shown schematically in Fig. 2a. A 760-nm laser diode (Mitsubishi ML 4405) was used to generate short pulses having an average optical power of 0.3 mW at a 10-MHz repetition rate. Light from the laser was passed through a 600- $\mu\text{m}$ -thick optical fibre to one side of the sample and another similar fibre collected light on the opposite side and conveyed it to a cooled PMT (Hamamatsu R2566U-07). Part of the laser output was divided by a beamsplitter into a reference fibre coupled directly to the PMT to provide a time fiducial. The response function of the detection system, assessed by the use of sub-picosecond laser pulses, had a full width at half maximum of 60 ps. When using the diode laser, the corresponding width was found to be 140 ps.

A recorded photon distribution after passage through a 9-mm-thick sample of Portuguese marble, and the reference pulse, are shown in Fig. 2b. There were essentially no photons that got through the material directly (ballistic photons), and there were only a few photons that exited the sample very late because many were absorbed or scattered in the material. The evaluation of the photon mean path length in the mate-

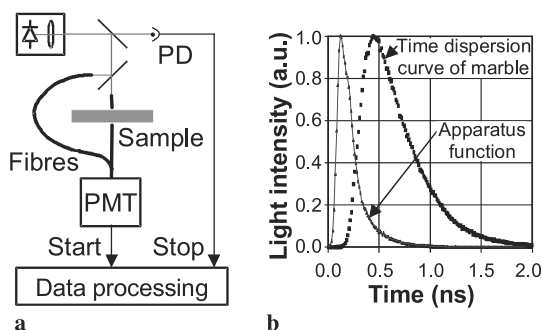


**FIGURE 2** a Schematic of the time-resolved measurement setup. b Photon distribution after transillumination of a 9-mm-thick slab of marble. The apparatus function is also included for the pulse only

rial requires an estimate of the effective index of refraction of the material, i.e. the local light velocity. Assuming that the mean light velocity in the sample is 2/3 the velocity of light, close to the values for glass and water, we note that 1 ns corresponds to 200 mm in the sample. For the 9-mm-thick sample illustrated, it is obvious that the mean photon path length was several times longer than the geometrical distance between the injection and detection fibres, emphasising the important role of scattering. For the natural samples we studied in the present investigation, the scattered photon distribution was only a few times broader than the apparatus function. In this case, the mean photon dwell time in the material can be obtained by a deconvolution of the apparatus function from the measured temporal distribution.

The linewidth of the pulsed laser is much larger than the absorption linewidth of the gas, and for the case of oxygen the differential absorption due to gas in the sample is less than a few percent. Thus, when studying the time delay and attenuation of light pulses in the bulk material, it does not matter whether the laser is tuned to the oxygen absorption line or not. However, the scattering properties are strongly wavelength dependent, meaning that the continuous wave and time-resolved measurements should be performed at approximately the same wavelength.

### 3 Measurements and results

Basic measurements of different aspects related to light propagation and embedded gas in wood were performed. By shining light through the samples and adding known distances of ambient air, the gas content in the porous samples could be expressed as an equivalent mean path length, that is, the path length in air rendering the same absorption as the encountered oxygen in the material. First, measurements of 6-mm-thick slabs of wood of different species and different densities were performed. In Fig. 3, the equivalent mean path lengths of oxygen in eight different types of wood are plotted versus the density of the material (ten different densities). The different species are listed in the figure caption. The annual rings in the measured samples had a uniform inclination of approximately 45° to the primary impinging laser beam. Each sample was measured at three different points, and at each point three different averages consisting of 512 individual scans were acquired using a circular detection area with a diameter of 25 mm. The error bars indicated correspond to  $\pm 2$  standard deviations. Note that the density of wood is an average of the whole sample, and that there could be local variations within the sample. However, it can clearly be seen that with increasing wood density the oxygen absorption decreased. Clearly the signal depends on both the gas content and the light transport properties (i.e. the effective path length) of the material. Measurements were also performed on denser species, Pear, Norway Maple, Beech, Pedunculate Oak, Wych Elm, Wild Cherry and Hornbeam, but the emerging light intensities were too low and consequently the gas absorption signals too noisy with the present detection system. The most optically dense sample that still gave a measurable gas absorption signal was that of Ash (see curve 8 in Fig. 3b).

The orientation of the annual rings relative to the direction of the impinging light could be anticipated to influence

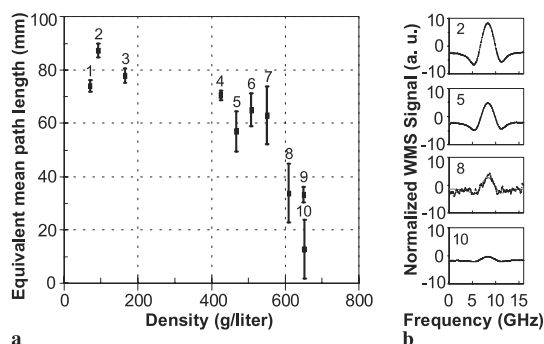


**FIGURE 3** a Equivalent mean path lengths of oxygen for eight different types of wood plotted versus the density of the material. The annual rings in the measured samples had an inclination of approximately 45° to the primary impinging laser beam. Data are given for Balsa (*Ochroma pyramidale*, curves 1–3), Norway Spruce (*Picea abies*, curve 4), European Larch (*Larix decidua*, curve 5), Alder (*Alnus glutinosa*, curve 6), Aspen (*Populus tremula*, curve 7), Ash (*Fraxinus excelsior*, curve 8), Birch (*Betula* sp., curve 9), and Scots Pine (*Pinus sylvestris*, curve 10). b Corresponding WMS signals for some of the samples together with fitted waveforms

the light transport. Therefore, the inherent anisotropy of wood was investigated using cubes of 15-mm side length. The oxygen light absorption and the light transmission were measured through a cube of Norway Spruce wood (*Picea abies*) ( $\rho = 387 \text{ g/dm}^3$ ), letting the laser beam enter in the three different principal directions (radially through the annual rings, longitudinally along the annual rings along the stem, and tangentially along the annual ring layers, respectively). The results are presented in Fig. 4. Each principal direction was measured from both sides, and on each side three different averages consisting of 512 individual scans were acquired using a circular detection area with a diameter of 6 mm. The error bars indicate the 95% confidence interval and it can be seen that the spread in, as well as the level of, gas absorption measured increased with decreasing amount of light transmitted.

The same measurements were also performed on a similar cube of Scots Pine (*Pinus sylvestris*) ( $\rho = 668 \text{ g/dm}^3$ ), rendering the same relative difference between the three orientations but with equivalent mean path lengths approximately half the corresponding values for the less dense cube. The lowest gas absorption, and the highest light transmission, was found for the case in which the light was guided along the fibres, that is, when the light path in the wood was shortest.

In the measurements presented in Figs. 3 and 4 it can be seen that the equivalent mean path lengths were about one order of magnitude longer than the geometric distance between the points of light injection and detection. Since wood obviously contains a smaller fraction of oxygen than the ambient air, the distance travelled by the light inside the material is even longer than that. This fact is highlighted in Fig. 5, in which a time dispersion curve recorded for a 6-mm-thick slab of Ash wood (*Fraxinus excelsior*), with annual rings at an inclination of about 45° to the primary impinging laser beam, is displayed.

Dynamic processes related to gas diffusion in wood were also investigated, by measuring the light absorption of oxygen in samples of wood directly after they were brought out into

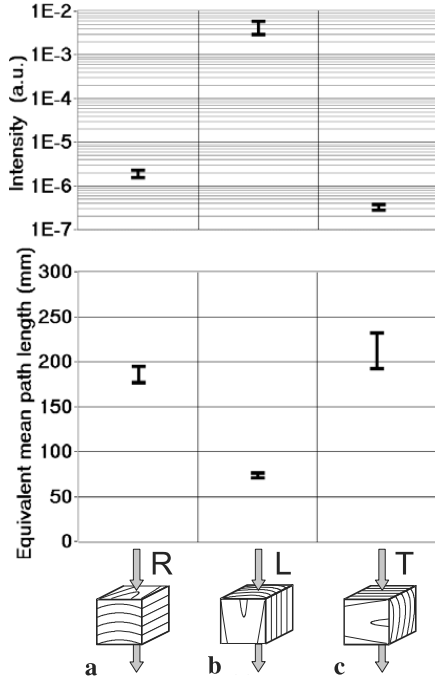


FIGURE 4 Light transmission (upper part) and oxygen absorption (lower part) measurements through a cube (side 15 mm) of Norway Spruce wood **a** radially through the annual rings, **b** longitudinally along the annual rings along the stem, and **c** tangentially along the annual ring layers

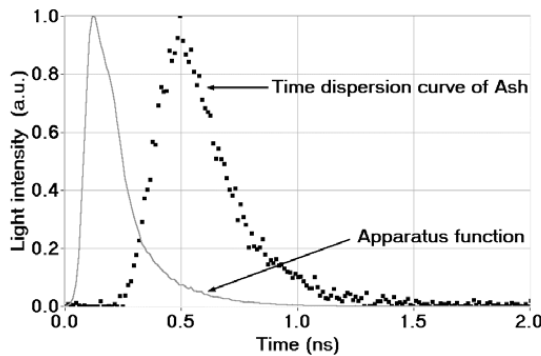


FIGURE 5 Time dispersion curve recorded for a 6-mm-thick sample of Ash wood (*Fraxinus excelsior*). The apparatus function is also included for the pulse only

ambient air from an environment of pure nitrogen. As shown in Fig. 6, the period of previous oxygen-free storage affected the amount of gas exchanged in the sample; the signal started from a lower level for longer periods in the oxygen-free environment. However, the time constant of re-invasion seemed not to be affected by the length of the pre-treatment, and was found to be approximately three hours. The curves presented were measured on the same 10-mm-thick slab of Balsa wood (*Ochroma pyramidale*) ( $\rho = 71 \text{ g/dm}^3$ ) using a circular detection area with a diameter of 25 mm. Each data point was

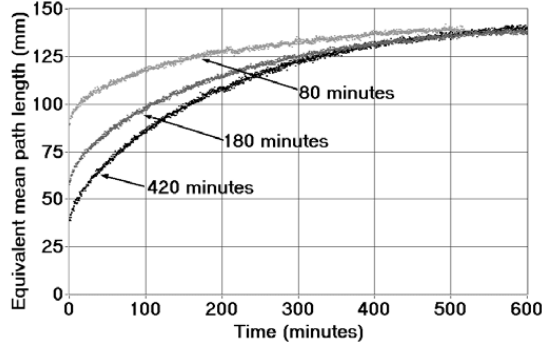


FIGURE 6 Recordings of the diffusion of oxygen into the same 10-mm-thick sample of Balsa wood that had been stored in a pure nitrogen atmosphere for different times, as indicated in the figure

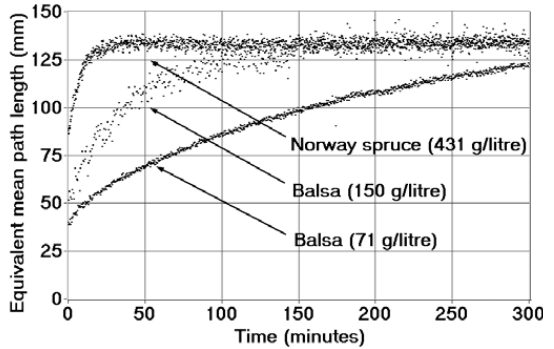


FIGURE 7 Recordings of the diffusion of oxygen into 10-mm-thick samples of Norway Spruce ( $\rho = 431 \text{ g/dm}^3$ ), Balsa ( $\rho = 150 \text{ g/dm}^3$ ), and Balsa ( $\rho = 71 \text{ g/dm}^3$ )

obtained by averaging 64 individual scans on the oscilloscope, an integration time of 16 s.

Further measurements revealed that the time scale of gas re-invasion was different in different samples of wood. In Fig. 7, the diffusion of oxygen into 10-mm-thick slabs of Norway Spruce ( $\rho = 431 \text{ g/dm}^3$ ), Balsa ( $\rho = 150 \text{ g/dm}^3$ ), and Balsa ( $\rho = 71 \text{ g/dm}^3$ ) are presented. Somewhat unexpectedly, the gas penetration was found to be fastest in the densest material. It was observed that both long and short time constants govern the gas transport. It seems that gas spreads quickly through coarser structures, while penetration through the cell walls of the balsa wood was slow. For long times the equivalent mean path length approached an equivalent mean path length that was longer than that in Fig. 3, in which a thickness of 6 mm was used instead of one of 10 mm.

Gas absorption measurements were also performed on marble. However, with the present setup, it was not possible to unambiguously assign the oxygen signal to air inside the sample, due to the very low amount of enclosed gas.

#### 4 Discussion and conclusions

The GASMAS technique provides new opportunities for studying gas enclosures in natural and synthetic

materials. The present study illustrates different aspects of the technique used in the investigation of wood of different kinds. Different species of wood yield widely differing integrated oxygen signals, which are shown to have a relation to the mass density of the wood. The annual ring structure leads to strong signal anisotropy due to differences in light transport. A determination of the gas concentration in materials is possible in principle, as shown in our earlier work [3], but requires a combination of GASMAS data and data obtained in temporally resolved measurements for assessing the mean optical path length. In this way, a generalised Beer–Lambert relation can again be established in the spectroscopy of gas in porous media. However, obtaining accurate values for the index of refraction (i.e. the velocity of light) in the studied materials is particularly difficult. Another aspect that calls for further investigation is the relative distribution of light between the solid phase and the gas phase of the scattering media.

On the other hand, the concentration ratios of gases, and in particular, changes in concentration ratios, can readily be determined if the same approximate wavelength is used for the absorption lines of the two species, so that the same scattering conditions prevail. This scheme can be of particular importance for the study of, for example, physiological processes in plants.

Measurements of the GASMAS type can be an important tool for analysing the gas diffusion properties of porous materials. By monitoring the rate at which atmospheric oxygen re-invades a sample previously exposed to a different ambient atmosphere, such as nitrogen, diffusion coefficients can be evaluated [8]. Gas transport studies using the GASMAS technique are also expected to be useful in studies of gas absorption in, for example, catalysts embedded in zeolites.

Although diffusion in wood was addressed in this paper, we will also mention several related possibilities of considerable practical interest.

Wood, wood-chip, and gypsum boards are important building and construction materials, which are most frequently covered with paints for protection and aesthetic reasons. The varying gas exchange related to different types of paints can be assessed by the present technique. Of particular interest is water vapour and water, with building damage due to moisture being a major consideration. For low levels of moisture, the gaseous water in the pores can be studied (a saturation clearly occurs for higher levels), while for high levels, liquid water replacing the gas in the pores can also be studied in an indirect way, since it will depress the oxygen signal [9]. The related effects due to scattering suppression by the presence of an index-matching fluid have to be elucidated.

Marble and other porous stone materials used in the construction of historical buildings and sculptures suffer damage due to weather exposure, particularly when combined with in-

creasing levels of atmospheric pollutants. Protective surface coatings, which are ideally invisible, are therefore being introduced. Due to the strongly differing properties of the coating and the stone, fluorescence techniques are a powerful tool for detecting such coatings [10]. Recently the Lund group participated with its mobile lidar system in the remote fluorescence imaging of the Parma Cathedral and Baptistery, with spectacular manifestations of facade treatments [11]. GASMAS measurements on untreated and treated surfaces of porous stone might help to elucidate the functioning of the protective coatings in a similar way to that discussed for studies of painted wood. The concentration of oxygen in porous marbles can be expected to be much lower than in wood, but sensitive equipment should be able to pick up the relevant signals.

In the preservation of foodstuffs it is important to keep atmospheric oxygen away, which is frequently accomplished by using plastic films or laminates. This is the case with, for example, meats packaging, where the film also has the additional purpose of preventing drying out and bacterial access. Related techniques are used for beverages, especially milk. It can be anticipated that the GASMAS technique will also find applications in these contexts.

In conclusion, the GASMAS technique opens up many new diagnostic and analytical possibilities, some of which have been experimentally demonstrated in the present paper, while others could be addressed in further investigations.

**ACKNOWLEDGEMENTS** The authors are grateful to Mr. O. Marcillo for assistance in some of the measurements. This work was supported by the Swedish Research Council, the International Programme in the Physical Sciences (Uppsala), the Swedish Institute (Visby Programme), and the Knut and Alice Wallenberg Foundation.

## REFERENCES

- 1 M. Kroll, J.A. McClintok, O. Ollinger: *Appl. Phys. Lett.* **51**, 1465 (1987)
- 2 M. Sjöholm, G. Somesfalean, J. Alnis, S. Andersson-Engels, S. Svanberg: *Opt. Lett.* **26**, 16 (2001)
- 3 G. Somesfalean, M. Sjöholm, J. Alnis, C. Klinteberg, S. Andersson-Engels, S. Svanberg: *Appl. Opt.* **41**, 3538 (2002)
- 4 S.R. Arridge, M. Cope, D.T. Delpy: *Phys. Med. Biol.* **37**, 1531 (1992)
- 5 T.J. Farrell, M.S. Patterson, B. Wilson: *Med. Phys.* **19**, 879 (1992)
- 6 G. Müller, B. Chance, R. Alfano, S. Arridge, J. Beuthan, E. Gratton, M. Kaschke, B. Masters, S. Svanberg, P. van der Zee (Eds.): *Medical Optical Tomography: Functional Imaging and Monitoring* (SPIE, Bellingham 1993)
- 7 D. Gansert, M. Burgdorf, R. Lösch: *Plant Cell Env.* **24**, 1055 (2001)
- 8 M. Sjöholm: 'Determination of Gas Diffusion Coefficients Using the GASMAS Technique', to appear
- 9 S. Svanberg, M. Sjöholm, G. Somesfalean: Method and Device for Investigation of a Surface Layer, Patent application PCT/SE03/00717 (2003)
- 10 G. Ballerini, S. Bracci, L. Pantani, P. Tiano: *Opt. Eng.* **40**, 1579 (2001)
- 11 D. Lognoli, G. Cecchi, I. Mochi, L. Pantani, V. Raimondi, R. Chiari, T. Johansson, P. Weibring, H. Edner, S. Svanberg: *Appl. Phys. B* **76**, 1 (2003)



# PAPER X

## **Diode laser absorption spectroscopy for studies of gas exchange in fruits**

L. Persson, H. Gao, M. Sjöholm, and S. Svanberg.

*Optics and Lasers in Engineering* **44**, 687–698 (2006).





Available online at [www.sciencedirect.com](http://www.sciencedirect.com)

SCIENCE @ DIRECT®

OPTICS and LASERS  
in  
ENGINEERING

Optics and Lasers in Engineering 44 (2006) 687–698

## Diode laser absorption spectroscopy for studies of gas exchange in fruits

L. Persson\*, H. Gao<sup>1</sup>, M. Sjöholm, S. Svanberg

*Department of Physics, Lund Institute of Technology, P.O. Box 118, SE-22100 Lund, Sweden*

Available online 22 August 2005

### Abstract

Gas exchange in fruits, in particular oxygen transport in apples, was studied non-intrusively using wavelength modulation diode laser absorption spectroscopy at about 761 nm, applied to the strongly scattering intact fruit structure. The applicability of the technique was demonstrated by studies of the influence of the skin to regulate the internal oxygen balance and of cling film in modifying it by observing the response of the signal from the internal oxygen gas to a transient change in the ambient gas concentration.

Applications within controlled atmosphere fruit storage and modified atmosphere packaging are discussed. The results suggest that the technique could be applied to studies of a large number of problems concerning gas exchange in foods and in food packaging.

© 2005 Elsevier Ltd. All rights reserved.

*Keywords:* Diode laser spectroscopy; TDLS; Food packaging; Gas exchange; Fruit; Oxygen

### 1. Introduction

Molecular oxygen is a biologically active molecule, and its concentration in fruits is of crucial importance for the ripening process and the quality of the fruits. In particular, the oxygen availability affects the metabolic process of respiration, which releases energy necessary to maintain the life processes by breaking down the organic

\*Corresponding author.

*E-mail address:* [linda.persson@fysik.lth.se](mailto:linda.persson@fysik.lth.se) (L. Persson).

<sup>1</sup>Permanent address: School of Science, Harbin Institute of Technology, Harbin, PR China.

compounds of the fruit. Thus, a decreased respiration rate causes a prolonged lifetime. The rate of the normal aerobic respiration process in which oxygen is consumed and carbon dioxide is produced, decreases with decreasing oxygen concentration and increasing carbon dioxide concentration. However, an oxygen concentration below a certain critical level initiates an anaerobic metabolic pathway for the respiration. This process, known as fermentation, produces off-flavours and causes a loss of quality and a rapid decay of the fruit. Also, a too high carbon dioxide concentration can cause damage to the fruit tissue [1,2]. Thus, there is great interest in optimising gas concentrations during the postharvest time of fruits.

Methods developed to prolong the postharvest lifetime and inhibit physiological deterioration in fruits include controlled atmosphere (CA) storage and modified atmosphere packaging (MAP). The optimum partial pressures of oxygen and carbon dioxide in CA storage and MAP depend on the metabolic behaviours, especially the physiological tolerance to oxygen and carbon dioxide of the particular fruit [3]. In MAP, films with suitable permeability to oxygen and carbon dioxide are used to optimise the concentrations of the gases which the fruits are exposed to. An ideal type of package would be the one resulting in an oxygen concentration low enough to slow down respiration and maturation but higher than the critical concentration for initiation of anaerobic respiration [2,4]. The respiration rate is also highly dependent on the temperature [5,6]. The oxygen uptake increases with temperature while the permeability of the polymeric film frequently used in MAP does not increase to the same extent. Thus, it is very important to design the MAP according to the highest oxygen uptake that will occur due to temperature changes during shipping and handling [7]. To be able to design an optimal package, there is a need for methods to measure and model the internal gas concentrations and the gas exchange in fruits and package systems.

Techniques for assessing the gas content in the air around horticultural produces are readily available, although the implementation might be complicated. A common technique is to use a flush-through system in which the gas exchange can be estimated from the concentration difference between the inlet and outlet gas flow. In order not to make systematic errors, the flow has to be relatively high [8,9]. However, this requires sensitive detection techniques to be able to monitor the small concentration differences, which is often accomplished by a gas chromatographic system combined with unselective detectors, or more selective spectroscopic devices like laser-based photoacoustic trace gas detectors [10]. When it comes to measurements of the internal gas contents and its dynamics, intrusive electrode-based probes or extraction of gas from the fruit interior by syringes are normally used [10–12]. These methods destroy the tissue, which might affect the ongoing physiological processes.

A non-intrusive, compact and easily implemented technique for measuring gas exchange inside fruits would thus be of interest for assessments of internal gas dynamics relevant to, for instance, the optimisation of CA storage and MAP of fruits. The aim of the present work is to introduce a new non-destructive in-situ technique to study gas inside fruits, based on diode laser absorption spectroscopy on highly scattering media, rather than to reveal new knowledge about fruit physiology

in itself. In the present study, we focus on oxygen content and gas exchange measurements in fruits, although other gases such as carbon dioxide and water can be considered. We show the possibility of studying gas exchange in apples through their natural skins. The technique also makes it possible to determine the effect on the gas exchange due to the protective action of cling film, and to study the permeability of different films used in MAP. Although the present study is focused on measurements on fruits, in particular apples, the methodology is general and can be applied to a large number of problems concerning gas exchange in foods and in food packaging.

## 2. Experimental technique

### 2.1. Gas absorption measurements

Gas concentrations can in principle be determined by measuring the gas attenuation of narrow-band light, over a certain distance and employing the well-known Beer–Lambertian law. The level of light unaffected by the gas can readily be assessed by also measuring the intensity at wavelengths close to, but outside the absorption profile.

This simple procedure requires a negligible variation of the absorption properties between the different wavelengths, inside and outside the absorption line profile, caused by other constituents than the gas of interest. This is often true in standard gas measurements in the atmosphere [13], but also in porous materials. A methodology based on the fact that absorption features of free gas are about 10 000 times narrower than the spectral features of liquids and solids was recently proposed and demonstrated. The method is referred to as **gas in scattering media absorption spectroscopy (GASMAS)** [14]. The technique utilises narrow-band tunable lasers, which makes it possible to scan the probing wavelength through the whole pressure broadened absorption profile of the gas. In particular, the wavelength tuning of compact, low-cost diode lasers can easily be achieved by changing the driving current or the temperature of such lasers.

In a porous material the light is scattered, which results in optical path lengths much longer than the distance of a straight line between the point of light injection and the point of light detection in the material. As an example, light travels several metres inside a few centimetre thick slab of polystyrene foam, which gives rise to large differential gas absorption signals even if the geometrical dimensions of the scattering sample are relatively small. Obviously, for absolute gas concentration measurements in materials where scattering dominates over absorption, the actual mean path length travelled by the light has to be measured [15]. However, for assessments of relative gas diffusion dynamics the actual mean path length is not required.

Although the optical path lengths can be long in a porous material, the differential absorption at transition lines of oxygen in the A-band around 760 nm, in a realistic porous sample, is in the best case just a few per cent. This calls for procedures to

increase the detection sensitivity in the presence of noise. A common approach to increase the signal-to-noise ratio is to appropriately modulate the probing light at a specific frequency and to extract the corresponding frequency component, or a harmonic of it, in the detected signal by the use of lock-in techniques. In the present study, wavelength modulation spectroscopy (WMS) as discussed below was employed.

## 2.2. Set-up

A key component in the measurement set-up, see Fig. 1, is the diode laser, Sharp LT031MDO, with a nominal output power of 7 mW, which was used to generate the probing light. The wavelength of the light was scanned, with a repetition rate of 28 Hz, across the R7R7 oxygen line, with the vacuum wavelength 761.003 nm. Additionally, sinusoidal modulation of 55 kHz was superimposed on the diode laser injection current to achieve a modulation of the light that could be used to perform sensitive WMS detection. A Tefzel covered optical fibre with a core diameter of 600  $\mu\text{m}$  was used to guide the light to the sample under study. Before entering the sample, the light was collimated by a collimating lens package, Thorlabs F230SMA-B.

After passage through the sample a photomultiplier tube, Hamamatsu 5070A, masked by a circular aperture with a diameter of 6 mm, detected the light. Ambient light was suppressed by the combination of the sensitivity fall-off towards longer wavelengths for the photomultiplier tube, and a coloured glass filter, RG715, that blocked shorter wavelengths. Additionally, the sample was surrounded by a black box to suppress the ambient light even further. The signal from the photomultiplier tube was split into two parts. One part, referred to as the direct signal, was sent directly to a digital oscilloscope, Tektronix TDS 520B. The other part was filtered by a home-made high-pass filter and phase-sensitive detection at twice the modulation frequency, i.e. 110 kHz, was achieved by the use of a lock-in amplifier, Signal

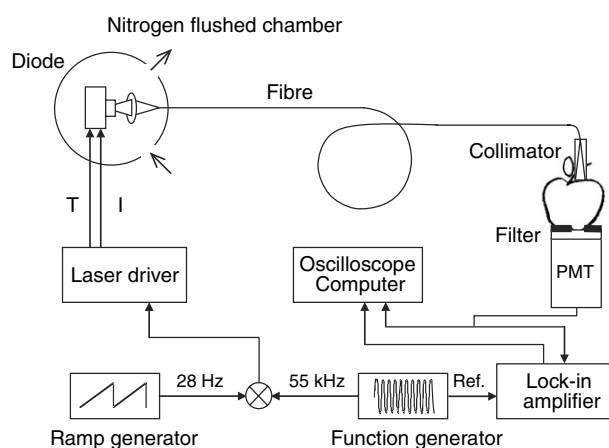


Fig. 1. Schematic layout of the GASMAS set-up used for molecular oxygen detection.

Recovery 7280 DSP. This lock-in signal, referred to as the  $2f$  signal, was sent to the other channel of the oscilloscope, which was computer controlled through GPIB communication by a LabVIEW program.

### 2.3. Evaluation

The oxygen gas content was evaluated from the recorded wavelength scans by calculating the peak-to-peak value of the absorption signature in the  $2f$  signal, as illustrated in Fig. 2 (left). The amplitude of the  $2f$  signal is dependent both on the relative differential absorption due to the gas of interest, and the amount of light reaching the detector, i.e. it depends on the absolute size of the absorption dip. Thus, the peak-to-peak value of the  $2f$  signal was normalised to the amount of light reaching the detector by dividing it with the interpolated direct signal,  $S_{Dir}$ , at the absorption line centre; see Fig. 2 (left). This normalised GASMAS measurement signal, GMS, is thus a measure of the absorption due to the gas of interest. As long

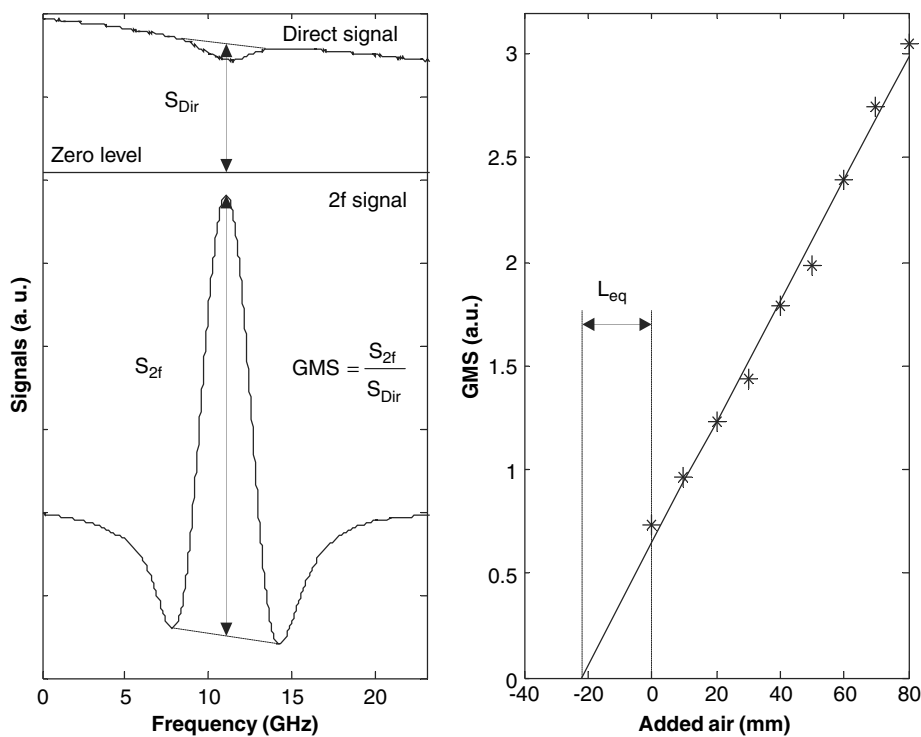


Fig. 2. (Left) Direct absorption and second-harmonic component of the absorption for the R7R7 line in the oxygen A-band measured along an approximately 10 m long path in air. (Right) Standard addition plot for molecular oxygen obtained with the GASMAS set-up showing the extrapolated equivalent mean path length for a 20 mm thick slab of Jonagold apple.

as the absorption is small, the GMS is proportional to the absorbance and thus to the product of the gas concentration and the path length travelled by the light.

One simple procedure to calibrate the arbitrary GMS and transform it into a more meaningful quantity is by using the method of standard addition, in which known amounts of the quantity of interest is added to the unknown quantity, which then can be determined. In the case of oxygen measurements, the light was sent through additional known path lengths of ambient air before entering the sample under investigation. The acquired GMS values were plotted as a function of the added distance of air as can be seen in Fig. 2 (right), where a standard addition measurement on a 20 mm thick slab of Jonagold apple is presented. The data points fall on a straight line as previously discussed and by determining the intercept of this fitted line with the added-distance axis, the equivalent distance in ambient air giving rise to a signal with the same magnitude as the unknown signal from the sample can be determined. In the case presented in Fig. 2 (right), the equivalent mean path length,  $L_{\text{eq}}$ , of molecular oxygen was found to be 22 mm. Since only a small fraction of the apple volume is gas, this means that the light has travelled a substantially longer distance through the apple than the geometrical dimensions of the apple.

### 3. Measurements and results

#### 3.1. Introductory studies

In order to illustrate the general dynamics of gas in fruit samples a study of the equivalent mean path length,  $L_{\text{eq}}$ , of oxygen for fruit slabs of different thickness was performed. Five varieties of apples, Jonagold, Granny Smith, Red Delicious, Golden Delicious, and Royal Gala, bought in a local supermarket, were studied. The different apples were sliced in slabs with well-defined thicknesses ( $\pm 1$  mm) and the equivalent mean path length was immediately measured, in order not to be affected by oxidation processes. Several different positions on each apple slab were sampled, since local variations in the slabs could be anticipated. Each measurement is an average of 500 single wavelength scans and ten such measurements were performed at each position in order to evaluate the influence of noise. The standard deviation of the ten measurements at each position was found to be at most 0.12 mm, and was not proportional to the equivalent mean path length measured, which is in accordance with the fact that optical fringes are limiting the sensitivity. The thicker the apple slab is cut, the more inhomogeneous the sampled tissue volume will be, which could be one reason for the, with increasing thickness, increasing standard deviation of the equivalent mean path length averages for the three different positions. The largest standard deviation was found to be 1 mm, which occurred for the Jonagold 18 mm slab. All these measurements made on the slabs were averaged into one value for each slab as can be seen in Fig. 3. It was observed that the equivalent mean path length for the apples studied follows a quadratic dependence on slab thickness in agreement with theoretical expectations for a medium where scattering dominates over absorption and the light transport can be treated as diffusing photons [15].

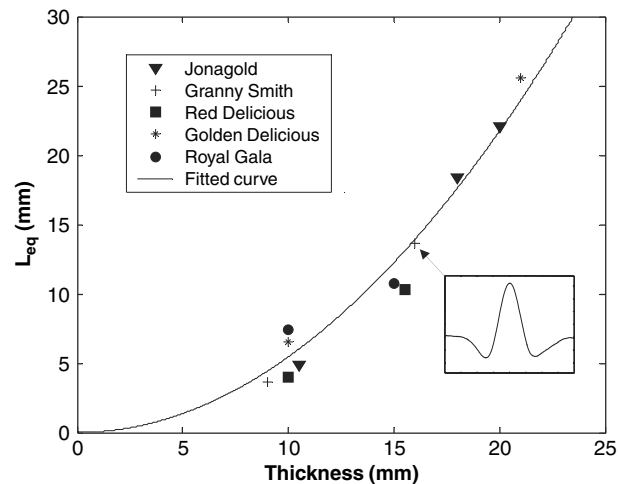


Fig. 3. Equivalent mean path length of oxygen,  $L_{eq}$ , for slabs of different apple varieties with various thickness. Ten measurements, each consisting of 500 single wavelength scans, were performed at three different places on the slab. Each data point is an average of these measurements. The WMS signal from the 16 mm thick Granny Smith slab is shown in the inset.

Since slabs of the same thickness of these different varieties of apples were found to have basically the same  $L_{eq}$ , all data points were fitted to a common quadratic function, with a root mean square error of 1.5 mm, see Fig. 3.

### 3.2. Gas transport studies

To elucidate the feasibility to study gas content inside an intact fruit and to follow diffusion processes in real-time, the influence of the skin on the oxygen content inside a Granny Smith apple was measured in ambient air. Furthermore, measurements were also made on an aubergine to illustrate the possibility of using the technique on produces with substantially lower light transmission.

The equivalent mean path length was measured as a function of time for differently treated apples; see Fig. 4. One untreated apple, with a thickness of 70 mm, was first measured. After that, the apple was immersed in nitrogen gas for about 24 h, by placing it in a plastic bag flushed with nitrogen gas before being sealed. Then it was brought out into ambient air and the re-invasion of oxygen containing ambient air was measured. The same apple was then peeled, immersed in nitrogen gas for 12 h before the measurement procedure was repeated. Finally, a new apple, with a thickness of 74 mm, was exposed to an atmosphere with a higher concentration of oxygen than in ambient air for about 12 h, before it was brought out into ambient air and the measurement procedure was again repeated. The data points that are shown in Fig. 4 are averages from 15000 wavelength scans, corresponding to a sampling time of approximately 15 min.

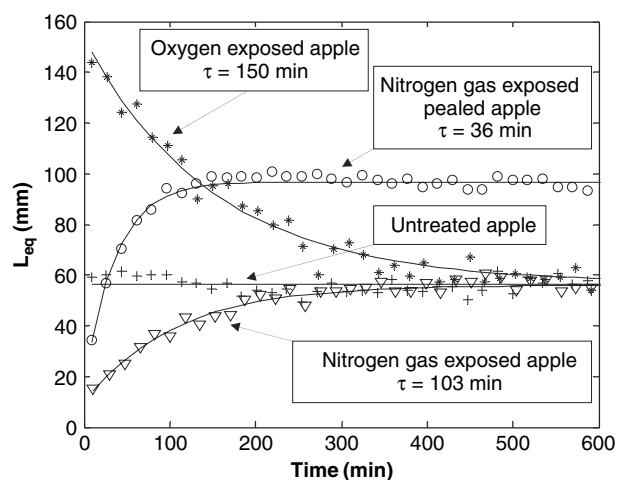


Fig. 4. Measurements of the gas exchange through differently treated Granny Smith apples in ambient air; untreated intact apple (+), intact apple pre-treated by immersion in nitrogen gas for 24 h ( $\nabla$ ), peeled apple immersed in nitrogen gas for 12 h ( $\circ$ ) and another apple pre-exposed to an atmosphere with higher concentration of oxygen than in ambient air for 12 h (\*). Exponential functions fitted to the data together with the estimated time constants are also included.

As was already observed in our first paper [14], the time evolution of the oxygen equivalent mean path length was found to follow a simple exponential curve, which is also expected with the experimental procedures utilized [16]. The time constant—the time the signal takes to change its separation from equilibrium by a factor of  $1/e$  of its value at the starting time—was estimated by a fitting procedure.

As can be seen in Fig. 4, the time constant for the re-invasion of oxygen into the nitrogen-exposed apple with skin is around 100 min. It can also be seen that it takes the apple approximately 5 h to reach the same steady-state oxygen concentration as before the treatment. The figure also shows that in the peeled apple, the concentration equilibrium of oxygen becomes about two times higher than it was before the apple was peeled, and that the gas exchange goes about three times faster than in the presence of the intact skin, which is in accordance with the assumption that the major site of resistance to gas diffusion in fruits is most likely the skin [7]. The time constant for the oxygen-exposed apple was estimated to 150 min, which is slightly different from the time constant estimated for the nitrogen-exposed apple. However, any detailed conclusions about the physiological process should not be drawn from this difference since different apples were used.

These two measurements of re-invasion of ambient air after exposure to oxygen and nitrogen, respectively, were also performed on an aubergine, 57 mm thick, where both the time constants were estimated to approximately 30 min; see Fig. 5. In the figure it can also be seen that the equilibrium value for oxygen is about five times larger in the aubergine than in the Granny Smith apple. It is well known that this type of fruit contains considerable amounts of gas. However, it should be kept in

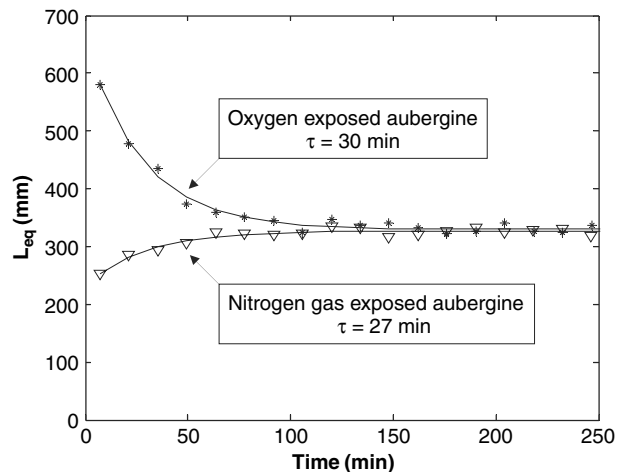


Fig. 5. The rate of gas exchange through an aubergine in ambient air after a previous immersion in nitrogen gas for 24 h ( $\nabla$ ). The same aubergine was after the first measurement exposed to an atmosphere with higher concentration of oxygen than in ambient air for 12 h before being measured again (\*). Exponential functions fitted to the data together with the estimated time constants are also included.

mind that the oxygen equivalent mean path length is sensitive to the gas concentration as well as the scattering properties of the fruit.

### 3.3. Packaging measurements

In MAP different kinds of polymeric films are used with various permeabilities for oxygen and carbon dioxide to delay ripening of the fruit [7,17]. To illustrate the possibility of studying the protective action of cling film with the method presented, the rate of gas exchange in freshly cut fruit was studied. In Fig. 6 diffusion curves for slabs with similar thickness, around 15 mm, of Royal Gala apple are shown. The fruit was cut in slabs and immersed in nitrogen gas, as described above, for 24 h. Before they were released into ambient air and measured, one slab was wrapped in cling film inside the nitrogen environment while the other was not. The data that are shown in the figure are averages of 2500 wavelength scans, corresponding to a sampling time of approximately 3 min. An exponentially decaying function was fitted to the data and the time constant was found to be in the order of a few minutes for the unprotected slab, whereas the slab that was sealed with cling film had an approximately seven times longer time constant. An even more successful sealing was observed with a time constant around 8 h.

An experiment to show the possibility of studying the impact of packaging on the respiration rate was also done. A Granny Smith apple was placed in a sealed plastic bag with limited access to oxygen. In Fig. 7 the diffusion curve is shown, and again each data point is an average based on 15 000 wavelength scans. The time constant for this particular gas exchange was estimated to be around 300 min. However, the

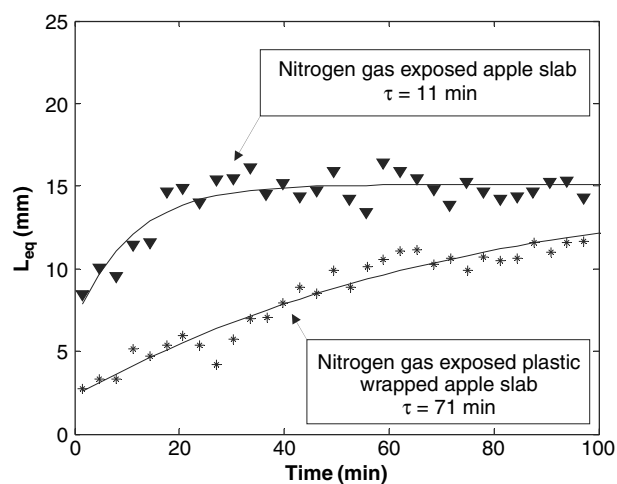


Fig. 6. The rate of gas exchange in freshly cut slices, 15 mm thickness, of Royal Gala apple in ambient air after a pre-immersion of the slices in nitrogen gas for 24 h are shown. One of the two slabs was wrapped in cling film before it was released into ambient air and measured (\*) while the other one was not (▼). Exponential functions fitted to the data together with the estimated time constants are also included.

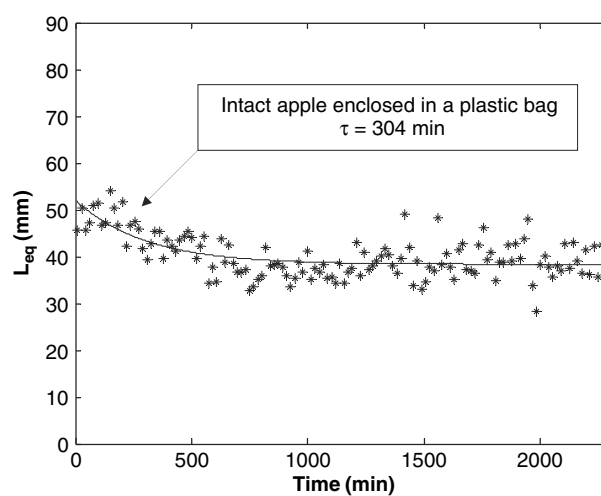


Fig. 7. The figure shows how an apple consumes oxygen in an enclosed atmosphere. A Granny Smith apple was placed in a sealed plastic bag with limited access to oxygen and measurements were performed. An exponential function fitted to the data together with the estimated time constant are also included.

time constant is strongly dependent on the amount of air in the bag when it was sealed, the respiration rate of the apple and the permeability of the plastic bag. The outcome of this experiment is not the time constant in itself, but rather the

illustration of the suitability of the technique to study the time evolution of gas concentrations on their path to equilibrium inside modified atmosphere packaged fruits. This is interesting in assessments of the influence of different polymeric films on the produce inside modified atmosphere packages.

#### 4. Discussion

Non-intrusive measurements of oxygen gas inside intact and sliced apple fruits were demonstrated using the newly introduced GASMAS technique. In contrast to other techniques the gas is measured non-intrusively inside the tissue rather than as gas extracted from the fruits. Gas exchange through the intact skin and through packaging films was demonstrated by observing the response of the oxygen equivalent mean path length to a transient change in the ambient gas concentration. The measurements suggest that the new technique might be developed into a valuable tool for gas studies in plant physiology, CA fruit storage and in MAP processes. Finally, this technique affords the prospect of real-time monitoring of gas exchange for a broad extension range of food storage and packaging.

#### Acknowledgements

This work was supported by the Swedish Research Council, the Asian-Swedish partnership programme of the Swedish International Development Cooperation Agency (SIDA), and the Knut and Alice Wallenberg Foundation.

#### References

- [1] Hertog MLATM, Peppelenbos HW, Evelo RG, Tijskens LMM. A dynamic and generic model of gas exchange of respiring produce: the effects of oxygen, carbon dioxide and temperature. *Postharvest Biol Technol* 1998;14:335–49.
- [2] Jurin V, Karel M. Studies on control of respiration of McIntosh apples by packaging methods. *Food Technol* 1963;17:782–6.
- [3] Beaudry RM. Effect of O<sub>2</sub> and CO<sub>2</sub> partial pressure on selected phenomena affecting fruit and vegetable quality. *Postharvest Biol Technol* 1999;15:293–303.
- [4] Mannapperuma JD, Singh RP. Modeling of gas exchange in polymeric packages of fresh fruits and vegetables. In: Singh RP, editor. *Process optimization and minimal processing of foods*. Boca Raton, FL, USA: CRC Press; 1994. p. 437.
- [5] Fidler JC, North CJ. The effect of conditions of storage on the respiration of apples. I. The effect of temperature and concentrations of carbon dioxide and oxygen on the production of carbon dioxide and uptake of oxygen. *J Hortic Sci* 1967;42:189–206.
- [6] Yearsley CW, Banks NH, Ganesh S. Temperature effect on internal lower oxygen limits of apple fruit. *Postharvest Biol Technol* 1997;11:73–83.
- [7] Cameron AC, Talasila PC, Joles DW. Predicting film permeability needs for modified-atmosphere packaging of lightly processed fruits and vegetables. *Hortic Sci* 1995;30:25–34.
- [8] Varoquaux P, Albagnac G, Gouble B. Physiology of minimally processed fresh vegetables. *Austral Postharvest Hortic Conf* 1995:437–43.

- [9] Andrich G, Zinnai A, Silvestri S, Fiorentini R. Automatic control of aerobic and anaerobic respiration rates of fruits stored in refrigerated and controlled atmospheres. *Automat Control Food Biol Processes* 1994;36:281–7.
- [10] Oomens J, Zuckermann H, Persijn S, Parker DH, Harren FJM. CO-laser-based photoacoustic trace-gas detection: applications in postharvest physiology. *Appl Phys B* 1996;67:459–66.
- [11] Dadzie BD, Banks NH, Cleland DJ, Hewett EW. Changes in respiration and ethylene production of apple in response to internal and external oxygen partial pressures. *Postharvest Biol Technol* 1996;9:297–309.
- [12] Konopacka D, Plochanski WJ. Effect of storage conditions on the relationship between apple firmness and texture acceptability. *Postharvest Biol Technol* 2004;32:205–11.
- [13] Sigrist MW, editor. *Air monitoring by spectroscopic techniques*. New York: Wiley; 1994.
- [14] Sjöholm M, Somesfalean G, Alnis J, Andersson-Engels S, Svanberg S. Analysis of gas dispersed in scattering media. *Opt Lett* 2001;26:16–8.
- [15] Somesfalean G, Sjöholm M, Alnis J, af Klinteberg C, Andersson-Engels S, Svanberg S. Concentration measurement of gas embedded in scattering media by employing absorption and time-resolved laser spectroscopy. *Appl Opt* 2002;41:3538–44.
- [16] Sjöholm M, et al. Determination of gas diffusion coefficients using the GASMAS technique. To appear.
- [17] Renault P, Souty M, Chambroy Y. Gas exchange in modified atmosphere packaging. 1: A new theoretical approach for micro-perforated packs. *Int J Food Sci Technol* 1994;29:365–78.

# PAPER XI

## **Studies of gas exchange in fruits using laser spectroscopic techniques**

L. Persson, B. Anderson, M. Andersson, M. Sjöholm, and S. Svanberg .

543–552, Montpellier (September 2005) *Proceedings of FRUTIC 05, Information and technology for sustainable fruit and vegetable production.*



## Studies of Gas Exchange in Fruits Using Laser Spectroscopic Techniques

Linda Persson, Benjamin Anderson<sup>1</sup>, Mats Andersson,  
Mikael Sjöholm, and Sune Svanberg

Atomic Physics Division, Lund Institute of Technology, P.O. Box 118,  
SE-221 00 Lund, Sweden

<sup>1</sup>Permanent address: LAFOC, University of Cape Coast, Ghana

**Keywords:** Diode laser spectroscopy, GASMAS, food packaging, gas exchange, oxygen, apple, avocado, orange

### Abstract

**Non-intrusive, *in-vivo*, real-time measurements of oxygen contents and oxygen diffusion in fruits using a laser spectroscopic technique are presented, where the narrow absorption features due to the free gas in pores in the fruits are observed. The technique is referred to as gas in scattering media absorption spectroscopy (GASMAS), and is performed using tunable diode lasers. In particular, assessment of oxygen transport in apples and oranges is demonstrated. To illustrate the possibility to use the technique for studies of modified atmosphere packaging processes, measurements on sealed horticultural produces were performed. Furthermore, preliminary studies of avocados concerning the possibility to non-intrusively determine the maturity of fruits are presented. This technique has substantial potential for the development of compact devices providing new types of information in postharvest fruit management.**

### INTRODUCTION

Assessment of free gas in porous materials is of considerable interest in several environmental, biological and medical processes. In the present paper a novel application of a laser spectroscopic technique to the study of gas exchange in porous agricultural products, in particular fruits, is discussed. Although any gas with absorption lines in reach of tunable diode laser sources can be probed by the technique, we here focus on biologically active molecular oxygen, whose concentration is of crucial importance for the ripening process and the quality of fruits. An overview of the influence of oxygen and carbon dioxide partial pressures on selected phenomena affecting fruit and vegetable quality has been given by, e.g., Beaudry (1999).

A common way to analyse gases *in situ* is to use absorption spectroscopy that employs a sufficiently narrow-band light source in combination with the Beer-Lambertian law. However, in porous materials the radiation is heavily scattered, which results in an enhanced average absorption path length compared to the geometrical dimensions of the sample. One approach to measure non-gaseous constituents in scattering media is to use time-resolved spectroscopy employing laser-produced white light; for a recent report, see Abrahamsson et al. (2005). This type of setup was recently used for studies on apples

(Cauchard et al., 2005). The spectral resolution needed in such systems is relatively low since solid materials and liquids have broad absorption features with linewidths normally not sharper than 10 nm, while free gases typically have a linewidth 10000 times sharper (Sigrist, 1994). Thus, the small and narrow absorption imprint in the emerging, multiply scattered diffuse light due to the gas can not be detected with such systems. However, by using single-mode continuous-wave lasers combined with modulation techniques the gas can be detected sensitively, without disturbance from the broader absorption features of the bulk material. In particular, diode lasers are highly suitable for sensitive absorption spectroscopy with high spectral resolution due to their availability in different wavelength ranges, uncomplicated wavelength tunability, and their relatively low cost compared to other laser sources. This methodology to study free gas embedded in scattering materials has been denoted GASMAS (gas in scattering media absorption spectroscopy) (Sjöholm et al., 2001; Somesfalean et al., 2002).

Measurements of molecular oxygen in wood have been performed in order to illustrate the influence of the density and anisotropy of the sample on the GASMAS signal (Alnis et al., 2003). Recently, studies of gas exchange in fruits, in particular apples, have been reported (Persson et al., 2005). The gas contents in the scattering medium gives rise to a signal of a certain strength, which is determined by the gas concentration as well as the average path length travelled by the light in the scattering medium. The latter quantity can be determined by time-resolved measurements allowing the true concentration to be determined (Somesfalean et al., 2002). In particular, transport of gas through the porous medium can be studied. Here, the sample is first exposed to a gas environmental anomaly; it may be placed for a few hours in a sealed plastic bag first flushed with pure nitrogen gas. Then, the sample is placed in the GASMAS setup and the time evolution of the atmospheric oxygen re-invasion is measured spectroscopically. Such gas transport in apples was first studied by Persson et al. (2005) in transillumination geometry, and is further investigated in the present paper in a more practical backscattering geometry. The technique presented may have powerful applications in the study of fruit physiology, controlled atmosphere (CA) storage and modified atmosphere packaging (MAP) performance.

## **EXPERIMENTAL PROCEDURE**

Experimental arrangements for GASMAS measurements are shown in Figs 1 and 2a. The optics and electronics used are similar in the two arrangements and have been described more in detail by Persson et al. (2005). Two measurement geometries have been used; transillumination (Fig. 1) and backscattering (Fig. 2a). The spectroscopic light source used was a diode laser, Sharp LT031MDO, with a nominal output power of 7 mW. The wavelength of the diode laser was scanned by ramping the driving current at a repetition rate of 4 Hz across the R7R7 molecular oxygen line, which is situated at 761.003 nm (vacuum wavelength). Additionally, sinusoidal modulation of about 9 kHz was superimposed on the diode laser injection current to achieve a wavelength modulation of the light allowing sensitive wavelength modulation spectroscopy (WMS) using a lock-in amplifier. The laser radiation was guided to the sample by a 600  $\mu\text{m}$  core diameter optical fibre.

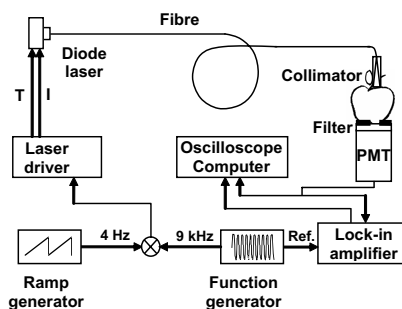


Fig. 1. Schematic layout of the GASMAS setup used for molecular oxygen detection in scattering porous materials such as fruits.

After light transport through the sample, a photomultiplier tube, Hamamatsu 5070A, detected the light. The ambient light was suppressed by a RG715 coloured glass filter used in combination with the sensitivity fall-off towards longer wavelengths for the photomultiplier tube. In the transmission geometry (Fig. 1) a circular aperture with a diameter of 6 mm was used to limit the detection area. The arrangement used in the backscattering geometry was slightly more complicated as can be seen in Fig. 2a. To launch the laser light into the scattering medium, a small right-angle prism providing total internal reflection was positioned in front of the fibre centrally located over the detector. The backscattered light that had travelled through the medium was collected in an annular aperture with an inner and an outer aperture diameter of 10 and 21 mm, respectively.

The DC and AC signals from the photomultiplier tube were detected separately. The DC signal, referred to as the direct signal, was sent to a digital oscilloscope, Tektronix TDS 520B. A high pass filter isolated the AC part and phase sensitive detection was performed with a lock-in amplifier. The component of the signal oscillating at the modulation frequency is similar to the first derivative of the direct signal, and, correspondingly, the component oscillating at twice the modulation frequency is similar to the 2nd derivative, etc. Since the direct signal is sloping, due to the simultaneous change in both wavelength and intensity as a function of injection current, the 1f signal is subject to a disadvantageous offset. This gives an advantage in using higher order components. However, the amplitude normally decreases by increasing the harmonic order. Thus, the component of the signal oscillating at twice the modulation frequency, i.e. 18 kHz, was selected as the output from the lock-in amplifier. This lock-in signal, referred to as the 2f signal, was sent to a second channel of the oscilloscope, which was computer controlled through GPIB communication by a LabVIEW program. An example of an oxygen signal recorded in backscattering geometry for the case of a 67-mm Granny Smith apple is shown in Fig. 2b.

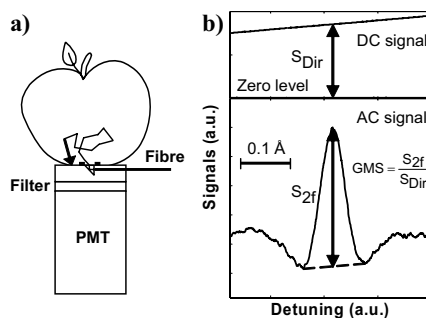


Fig. 2 (a). Modification of the GASMAS setup for backscattering (single-sided) measurements. (b). Direct absorption and second-harmonic component of the absorption for the R7R7 line in the oxygen A-band recorded from an Granny Smith apple in backscattering geometry.

As indicated in the figure the oxygen gas content can be evaluated from the peak-to-peak value of the absorption signature in the  $2f$  signal. Clearly, the amplitude of the  $2f$  signal is determined by the absolute size of the narrow gas absorption feature, i.e., to the fractional absorption due to the gas, and the amount of light reaching the detector. We are interested in the normalised GASMAS measurement signal, GMS, which is proportional to the fractional absorption. Thus, the AC signal (related to the oxygen content and the amount of light detected) was divided by the DC signal (related to the amount of light detected) as indicated in Fig. 2b. For small absorptions the GMS is proportional to the absorbance and thus to the product of the gas concentration and the path length travelled by the light. The standard addition method, just adding a path length of ambient air to be traversed by the laser light in addition to the scattering object under study, was adopted to calibrate a measured GMS and transform it into a more meaningful quantity. The acquired GMS values were plotted as a function of the added distance of air as discussed, e.g. by Persson et al (2005). The data points are expected to fall on a straight line, the zero intercept of which yields the equivalent distance,  $L_{eq}$  in ambient air giving rise to a signal with the same magnitude as signal from the sample.

## RESULTS AND DISCUSSION

Before presenting our new data, recorded mostly using backscattering geometry, we would like, in Fig. 3, to review some pertinent data obtained in our recent study (Persson et al., 2005). The recordings were performed in transillumination on Granny Smith apples using a setup of the type shown in Fig. 1. The gas content inside an intact fruit and the exchange of the gas was followed in real-time.

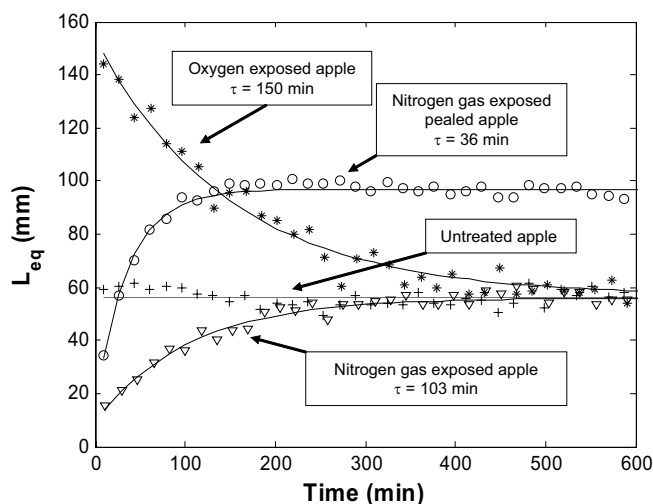


Fig. 3. Measurements of the gas exchange through differently treated Granny Smith apples in ambient air; untreated intact apple (+), intact apple pre-treated by immersion in nitrogen gas for 24 hours ( $\square$ ), peeled apple immersed in nitrogen gas for 12 hours (O) and another apple pre-exposed to an atmosphere with higher concentration of oxygen than in ambient air for 12 hours ( $\cdot$ ). Exponential functions fitted to the data together with the estimated time constants are also included (Persson et al., 2005).

The equivalent mean path length,  $L_{eq}$ , was measured as a function of time for differently treated apples. A "flat" recording for an untreated apple, with a thickness of 70 mm, can be seen in the figure. The apple was then immersed in nitrogen gas for about 24 hours, by placing it in a plastic bag flushed with nitrogen gas before being sealed, as discussed above. Then it was brought out into ambient air and the re-invasion of oxygen containing ambient air was measured. The same apple was then peeled, immersed in nitrogen gas for 12 hours before the measurement procedure was repeated. Finally, a new apple, with a thickness of 74 mm, was exposed to an atmosphere with a higher concentration of oxygen than in ambient air for about 12 hours, before it was brought out into ambient air and the measurement procedure was again repeated. The time evolution of the oxygen equivalent mean path length was found to approximately follow a simple exponential curve, which also could be expected with the experimental procedures utilised (Sjöholm et al., 2005). The time constant for the re-invasion of oxygen into the nitrogen-exposed apple with skin was found to be around 100 min. It takes approximately 5 hours for the apple to reach the same steady-state oxygen concentration as before the treatment. It can also be seen that in the peeled apple, the concentration equilibrium of oxygen becomes twice as high as before the apple was peeled, and that the gas exchange is three times faster than in an intact apple.

Similar recordings obtained with our new more practical backscattering detection geometry (Fig. 2a) are shown for a 67-mm thick Granny Smith apple in Fig. 4. The same apple was also measured in transmission geometry, rendering a slightly slower change in the gas signal with time, which might be explained by the fact that the probed depth of the fruit is different in the two geometries (Sjöholm et al., 2005).

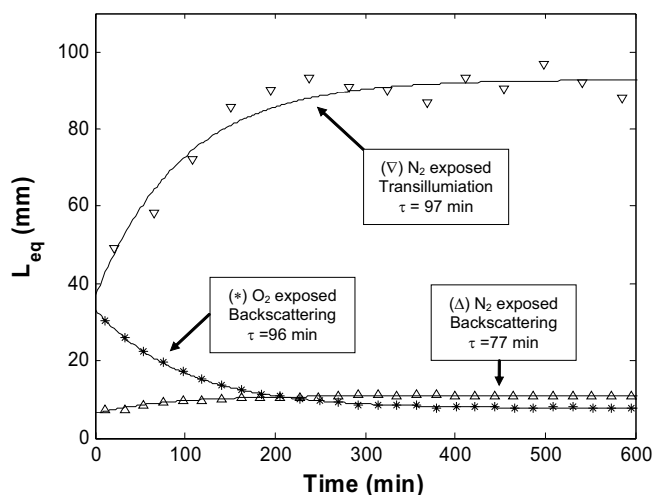


Fig. 4. Measurements of the gas exchange in transillumination and backscattering geometries in ambient air on a Granny Smith apple after different treatments; pre-treated by immersion in nitrogen gas for 24 hours in transillumination ( $\nabla$ ), pre-treated by immersion in nitrogen gas for 24 hours in backscattering geometry ( $\square$ ), and pre-exposed to an atmosphere with higher concentration of oxygen than in ambient air for 12 hours ( $*$ ). Exponential functions fitted to the data together with the estimated time constants are also included.

The same apple was also studied in backscattering geometry after oxygen exposure. As can be seen in the figure, the gas content equilibrium of oxygen becomes slightly lower, which might be due to the extreme levels of oxygen the apple has been exposed to, which might have harmed the apple. However, the reason can also be due to slightly different probed volumes of the apple.

To illustrate the possibility to use the GASMAS technique for modified atmosphere packaging issues, two different horticultural produces, apple and mushroom, with different expected respiration rates, were sealed in plastic bags and the consumption of oxygen was measured inside the produces in backscattering geometry. The results given in Fig. 5 show, as expected, that the change in the oxygen signal is faster for the mushroom than for the apple, which is a result of the faster respiration rate of the former compared to the latter (Gross et al., 2004).

Information and Technology for Sustainable Fruit and Vegetable Production  
 FRUTIC 05, 12-16 September 2005, Montpellier France

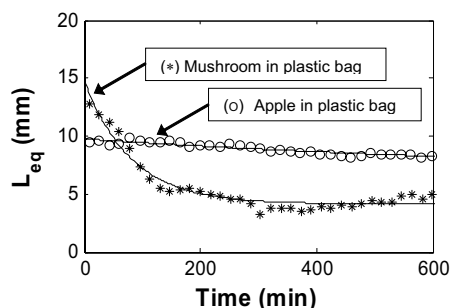


Fig. 5. The time evolution of the oxygen signal for two different horticultural produces with different respiration rates, apple (O) and mushroom (\*), while sealed in plastic bags, measured in backscattering geometry.

Finally, we illustrate some preliminary measurements in backscattering geometry on other types of horticultural produces such as avocado and orange. The GMS values from three avocados with different maturity are shown in Fig. 6. The hardness of the avocados was measured with a Stevens LFRA Texture Analyzer equipped with a circular probe with a diameter of 25 mm. Each avocado was compressed about 2 mm with a probe speed of 0.2 mm/s while the maximum force was measured. With increasing maturity it is noticed that the GMS values are reduced, probably related to both lower gas contents and less scattering. These aspects could be elucidated in time-resolved measurements (Somesfalean et al., 2002).

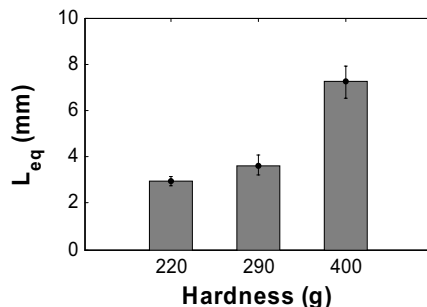


Fig. 6. The equivalent mean path length,  $L_{eq}$ , measured for three avocados with different maturity, in backscattering geometry. Four measurements were performed on each avocado and the averages together with error bars corresponding to one standard deviation are shown.

Gas exchange into an orange, with and without peel, was measured after nitrogen exposure. In Fig. 7 the diffusion curve for the intact orange is shown, where the time constant was estimated to approximately 2.5 hours. No change in the GMS values with time could be observed for the equally treated peeled orange, which could be due to the low signal obtained compared to the background noise. However, the results indicate the possibility to study oxygen dynamics in the peel of an orange.

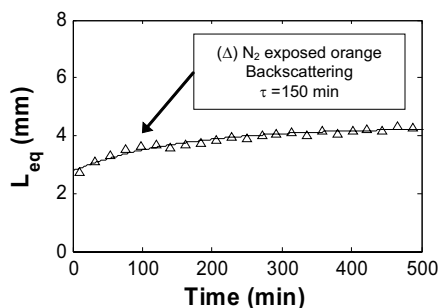


Fig. 7. Measurements of the gas exchange in backscattering geometry on an orange; intact orange pre-treated by immersion in nitrogen gas for 24 hours. Exponential function fitted to the data together with the estimated time constant is also included.

## CONCLUSION

As illustrated by the preliminary work reported in the present paper and by Persson et al. (2005) the GASMAS technique has potential to non-intrusively and in real-time provide information on the conditions of horticultural produces. In contrast to other techniques, the gas is measured non-intrusively inside the tissue rather than as gas extracted from the fruits. Applications regarding basic plant physiology as well as in controlled atmosphere fruit storage and in modified atmosphere packaging processes can be foreseen. Also different stages of processing, including fermentation, could be studied. We presently aim at developing compact and realistic equipment for GASMAS studies also in the field.

## ACKNOWLEDGEMENT

This work was supported by the Swedish Research Council, the Asian-Swedish partnership program of the Swedish International Development Cooperation Agency (SIDA), the International Science Programme (ISP), Uppsala, and the Knut and Alice Wallenberg Foundation. The authors gratefully acknowledge Professor Petr Dejmek at the Department of Food Engineering, Lund University Sweden, for the assistance in the measurements of fruit hardness.

### References

- Abrahamsson, Ch., Svensson, T., Svanberg, S., Andersson-Engels, S., Johansson, J. and Folestad., 2004 Time and wavelength resolved spectroscopy of turbid media using light continuum generated in a crystal fibre. *Optics Express* 12:4103-4112
- Alnis, J., Anderson, Sjöholm, M., Somesfalean, G. and Svanberg, S. 2003. Laser spectroscopy of free molecular oxygen dispersed in wood material. *Applied Physics B* 77:691
- Beaudry, R.M., 1999. Effect of O<sub>2</sub> and CO<sub>2</sub> partial pressure on selected phenomena affecting fruit and vegetable quality. *Postharvest Biology and Technology* 15:293-303.
- Chauchard, F. et al (2005)
- Gross, K.C., Wang, C.Y. Saltveit, M. 2004 *Agriculture Handbook Number 66: The Commercial Storage of Fruits, Vegetables, and Florist and Nursery Stocks,*
- Persson, L., Gao, H., Sjöholm, M. and Svanberg, S. 2005. Diode laser absorption spectroscopy for studies of gas exchange in fruits. *Lasers and Optics in Engineering*, in press.
- Sigrist, M.W., Ed. 1994. *Air Monitoring by Spectroscopic Techniques.* John Wiley and Sons, New York.
- Sjöholm, M., Somesfalean, G., Alnis, J., Andersson-Engels, S. and Svanberg, S. 2001. Analysis of gas dispersed in scattering media. *Optics Letters* 26:16-18.
- Sjöholm, M. *et al.* 2005. Determination of gas diffusion coefficients using the GASMAS technique. To appear.
- Somesfalean, G., Sjöholm, M., Alnis, J., af Klinteberg, C., Andersson-Engels, S. and Svanberg, S. 2002. Concentration measurement of gas embedded in scattering media by employing absorption and time-resolved laser spectroscopy. *Applied Optics* 41:3538-3544.



## PAPER XII

### **Spectroscopic studies of wood-drying processes**

M. Andersson, L. Persson, M. Sjöholm, and S. Svanberg.

*Optics Express* **14**, 3641–3653 (2006).



## Spectroscopic studies of wood-drying processes

Mats Andersson, Linda Persson, Mikael Sjöholm, and Sune Svanberg

Atomic Physics Division, Lund Institute of Technology,  
P.O. Box 118, S-221 00 Lund, Sweden  
[sune.svanberg@fysik.lth.se](mailto:sune.svanberg@fysik.lth.se)

**Abstract:** By the use of wavelength-modulation diode laser spectroscopy, water vapor and oxygen are detected in scattering media nonintrusively, at 980 nm and 760 nm, respectively. The technique demonstrated is based on the fact that free gases have extremely sharp absorption structures in comparison with the broad features of bulk material. Water vapor and oxygen measurements have been performed during the drying process of wood. The results suggest that the demonstrated technique can give information about the drying process of wood to complement that of commercially available moisture meters. In particular, the time when all the free water has evaporated from the wood can be readily identified by a strong falloff in the water vapor signal accompanied by the reaching of a high-level plateau in the molecular oxygen signal. Furthermore, the same point is identified in the differential optical absorption signal for liquid water, with a sharp increase by an order of magnitude in the ratio of the signal intensities at 980 nm and 760 nm.

© 2006 Optical Society of America

**OCIS codes:** (000.2190) Experimental physics; (300.6260) Diode laser spectroscopy; (290.7050) Turbid media

### References and links

1. J. M. Dinwoodie, "*Timber: Its nature and behaviour*," (E & FN, 2000).
2. B. Berglund, B. Brunekreef, H. Knöppel, T. Lindvall, M. Maroni, L. Mølhave, and P. Skov, "Effects of indoor air pollution on human health," *Indoor Air* **2**, 2–25 (1992).
3. S. Joseph Cohen and T. C.S. Yang, "Progress in food dehydration," *Trends in Food Science & Technology* **6**, (1995).
4. D. A. Skoog and M.D. West, "*Fundamentals of Analytical Chemistry*," 7th edition, (Saunders, 1995).
5. G. Müller, B. Chance, R. Alfano, S. Arridge, J. Beuthan, E. Gratton, M. Kaschke, B. Masters, S. Svanberg, and P. van der Zee, eds., "Medical optical tomography, functional imaging and monitoring," in *SPIE Institute Series*, Vol. **11**, (SPIE, 1993).
6. C. Abrahamsson, J. Johansson, S. Andersson-Engels, S. Svanberg, and S. Folestad, "Time-resolved NIR spectroscopy for quantitative analysis of intact pharmaceutical tablets," *Anal. Chem.* **77**, 1055–1059 (2005).
7. T. J. Farrell, M. S. Patterson, and B. Wilson, "A diffusion theory model of spatially resolved, steady-state diffuse reflectance for noninvasive determination of tissue optical properties in vivo," *Med. Phys.* **19**, 879–888 (1992).
8. M. S. Patterson, B. Chance, and B. C. Wilson, "Time-resolved reflectance and transmittance for the noninvasive measurement of tissue optical properties," *Appl. Opt.* **28**, 2331–2336 (1989).
9. C. af Klinteberg, A. Pifferi, S. Andersson-Engels, R. Cubeddu, and S. Svanberg, "In vivo absorption spectroscopy of tumor sensitizers using femtosecond white light," *Appl. Opt.* **44**, 2213–2220 (2005).
10. M. Sjöholm, G. Somesfalean, J. Alnis, S. Andersson-Engels, and S. Svanberg, "Analysis of gas dispersed in scattering media," *Opt. Lett.* **26**, 16–18 (2001).
11. J. Alnis, B. Anderson, M. Sjöholm, G. Somesfalean, and S. Svanberg, "Laser spectroscopy on free molecular oxygen dispersed in wood materials," *Appl. Phys. B* **77**, 691–695 (2003).

12. L. Persson, H. Gao, M. Sjöholm, and S. Svanberg, "Diode laser absorption spectroscopy for studies of gas exchange in fruits," *Opt. Lasers Eng.* **44**, 687–698 (2006).
13. L. Persson, B. Anderson, M. Andersson, M. Sjöholm, and S. Svanberg, "Studies of gas exchange in fruits using laser spectroscopic techniques," in *Proceedings of Fruitic05 Symposium* (Montpellier, France, September 12–16, 2005).
14. G. Somesfalean, M. Sjöholm, J. Alnis, C. af Klinteberg, S. Andersson-Engels, and S. Svanberg, "Concentration measurement of gas imbedded in scattering media employing time and spatially resolved techniques," *Appl. Opt.* **41**, 3538–3544 (2002).
15. L. Persson, K. Svanberg, and S. Svanberg, "On the potential of human sinus cavity diagnostics using diode laser gas spectroscopy," *Appl. Phys. B* **82**, 313–317 (2006).
16. L. Sandra, B. Roderick, and M. L. Roderick, "Plant-water relations and the fibre saturation point," *New Phytol.* **168**, 25–37 (2005).
17. P. Perré, "The role of wood anatomy in the drying of wood: Great Oaks from little acorns grow," 8th Int. IUFRO Wood Drying Conference (Brasov, Rumania, August 24–29, 2003).
18. M. Goyeneche, D. Lasseux, and D. Bruneau, "A film-flow model to describe free water transport during drying of a hydroscopic capillary porous medium," *Transp. Porous Media* **48**, 125–158 (2002).
19. L. James, "Electric moisture meters for wood," Gen. Tech. Rep. FPL-GTR-6. Madison, WI: U.S. Department of Agriculture, Forest Service, Forest Products Laboratory, 1988.
20. H. Forsén and V. Tarvainen, "Accuracy and functionality of hand held wood moisture content meters," VTT Publications 420 (2000).
21. P. J. Wilson, "Accuracy of a capacitance-type and three resistance-type pin meters for measuring wood moisture content," *Forest Products Journal*, **49**, 29–32 (1999).
22. C. Nordling and J. Österman, "*Physics Handbook*," 4th ed. (Studentlitteratur, 1987).
23. S. Matcher, M. Cope, and D. Delpy, "Use of the water absorption spectrum to quantify tissue chromophore concentration changes in near infrared spectroscopy," *Phys. Med. Biol.* **39**, 177–196 (1994).
24. T. Svensson, J. Swartling, P. Taroni, A. Torricelli, P. Lindblom, C. Ingvar, and S. Andersson-Engels, "Characterization of normal breast tissue heterogeneity using time-resolved near-infrared spectroscopy," *Phys. Med. Biol.* **50**, 2559–2571 (2005).

---

## 1. Introduction

Drying processes, i.e., the removal of moisture from materials, are of utmost importance in many industrial contexts and everyday experiences. For instance, wood needs to be dried from its natural moisture before its use as a fuel or as a construction material [1]. An important issue is that moisture in building materials induces mold, especially if the ventilation is insufficient, which is of major concern in the building sector [2]. Grain and cereals need drying for storage and for further processing in the food industry [3]. Paper processing includes important drying steps as is the case also in many further industrial processes.

Many natural materials are porous and hydrophilic. The pores can be filled with air or other gases, but may also be partially or fully filled with water; a frequently undesired situation. Capillary action is an important passive process when porous materials take up water. Materials frequently swell (increase in volume) when wet. In nonporous media the process of osmosis is in action. If the material has some rigid scaffolding structure, such as wood and other building materials, the swelling is minor. Then the pores originally filled with air instead become water filled. By increasing the vapor pressure of water by heating in combination with securing an environment with reduced relative humidity, forced drying can be achieved.

The status of drying materials is often studied by handheld moisture meters that measure the water content by an indirect method relying on the fact that the electrical properties of the material is dependent on the water content. However, these instruments are not able to monitor the whole drying process and are in some cases intrusive. Recent developments in diode-laser-based spectroscopy pose an interesting alternative approach, which would be to monitor the water vapor as well as the liquid water by a more direct, nonintrusive spectroscopic approach.

The present paper deals with the study of drying of wood using high-resolution near-IR laser absorption spectroscopy. A tunable diode laser operating close to 980 nm is used to monitor gaseous water. Liquid water also exhibits a broad absorption peak in the same wavelength

region. For reference, atmospheric oxygen gas in the pores is also monitored in its A band close to 760 nm. This wavelength also provides a convenient off-resonance wavelength in the liquid-water spectrum for assessment of liquid-water contents.

Absorption spectroscopy is a very common method for measuring concentrations of substances utilizing the Beer–Lambert law and a suitable calibration procedure (See, e.g., [4]). However, the application of this method is not straightforward for natural materials such as wood, since the fact that they are inhomogeneous and porous also means that they are highly scattering, making the optical pathlength through the sample undefined. This situation is common in medical optics, where scattering and absorption are intertwined [5], as is also the case in analytical spectroscopy of pharmaceutical preparations [6]. Different techniques for handling multiple scattering of light have been developed for assessing the concentration of liquid and solid absorbing constituents. Spatially separated measurements [7] and time-resolved techniques [8] constitute two main approaches for enabling concentration determinations. A recent example on the determination of tumor sensitizer concentration *in vivo* is given in Ref. [9].

Such techniques have been extended to free gases present in porous media through the introduction of the Gas in Scattering Media Absorption Spectroscopy (GASMAS) technique [10]. Normally a modest resolution is used in solid-state spectroscopy because of the broad absorbing structures. However, if single-mode diode laser spectroscopy using sensitive modulation techniques is employed, then structures appear that are typically 10,000 times narrower due to free gas. So far, the GASMAS technique was applied to the monitoring of free molecular oxygen in materials as diverse as wood, polystyrene foam, and fruits [10–13]. In particular, gas transport through the media could be studied by first subjecting the material to a pure nitrogen atmosphere and then observing the time constant for the reinvasion of normal ambient (oxygen-containing) air. Concentrations could be determined by combining GASMAS measurements with time-resolved measurement, revealing the time history of the photons inside the sample [14]. The GASMAS technique was also very recently applied to the monitoring of human sinus cavities [15].

The present paper focuses on spectroscopic monitoring of the drying of wood, and the GASMAS technique has in this context been extended to water-vapor monitoring. The structure of wood and the basics of wood-drying processes are presented in the next section. Conventional methods for measuring moisture in wood are discussed in Section 3. The experimental arrangements used in the present work are then presented in Section 4. Measurements and results are described in Section 5. A discussion of the results and conclusions from the study are presented in the final section.

## 2. Wood structure and its drying process

### 2.1. Wood structure

Wood has a complicated architecture, described in detailed, e.g., in Ref. [1]. In a tree the wood structure supports the treetop, stores nutritious substances, and transfers minerals and water, which have been absorbed by the root system. Thus, it needs to be strong, hydrophilic, and flexible since a tree grows and lives in a changing environment. Even though there exist hundreds of different types of wood material, they can be divided into two groups, hardwood (deciduous) and softwood (coniferous); see Fig. 1. Hardwood is the most complicated of the two and comprise wood such as balsa, white oak, ash, mahogany, etc. The density of hardwood may vary from about 0.1 to 1.2 g/cm<sup>3</sup>, depending on type of wood. Hardwood is characterized by a combination of complicated cell types orientated both vertically, tangentially, and radially. Softwood, on the other hand, is distinguished by a much simpler combination of cells that runs mostly vertically in a tree. Typical examples of wood that belong to the softwood group are spruce, pine, and larch. The weight of softwood may vary from 0.3 to 0.7 g/cm<sup>3</sup>.

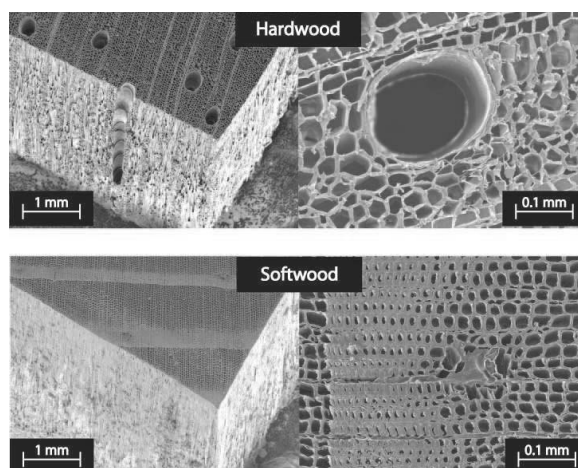


Fig. 1. Microscopic pictures of hardwood (balsa) and softwood (pine).

From a microscopic point of view wood consists of cellular structures that handle tasks carried out in a tree. Water and minerals are stored and transported vertically via cells, forming vessels, and horizontally via cell structures called rays. In total, wood cells can be classified into four different types; parenchyma (storage of nutrients), tracheids (support and conduction), fibers (support), and vessel cells (conduction).

In hardwood all four cell types are present, but tracheids are uncommon. Instead fibers and vessels are responsible for support and conduction of water and minerals. Fibers are usually 1-2 mm long and 10-20  $\mu\text{m}$  wide, and their only function is support. However, vessel cells are about the same length as the fibers but up to 0.5 mm wide. Since the ends of the vessels are situated on top of each other they can make up a long tube. Thus, vessels act as an efficient water tube since the ends of the vessels are more or less dissolved.

In softwood only two cell types are present, namely parenchyma and tracheids. Tracheids are the most common cell type (about 90% of the softwood), and its main function is support and conduction of minerals and water. The size of the cell is about 2-4 mm long and about 30-50  $\mu\text{m}$  wide. It is situated vertically in the tree and conducts water and minerals via small pits located on the cell surface. Parenchyma cells are small, 200 x 30  $\mu\text{m}^2$  in size, taking care of the storage of nutrients.

## 2.2. *Wood drying processes*

All types of wood consist of cellulose, hemicellulose, lignin, and extractives. The density of wood elements is about 1.5  $\text{g}/\text{cm}^3$ , but since wood is based on a cell structure, with size that differs per type of wood, the density of wood may vary from 0.1 to 1.2  $\text{g}/\text{cm}^3$  if the content of water is kept low. However, since the wood cell structure is hydrophilic and full of air, wood is heavily affected by water and moisture.

The moisture content in wood is defined as the ratio between the weight of water in a piece of wood and the weight of the wood when no water is present. This means that the moisture content is higher than 100% in a living tree. During this state water is stored in cells and vessels (free water) but also in cell walls (bound water) that have expanded due to absorbed water.

If a tree is cut into pieces, the moisture content starts to decrease immediately; see Fig. 2.

At first free water is moved to the wood surface by capillary forces where it is evaporated into the atmosphere. Due to the evaporation process the surface temperature is decreased, and heat must be transferred from the environment in order to maintain the drying of the wood.

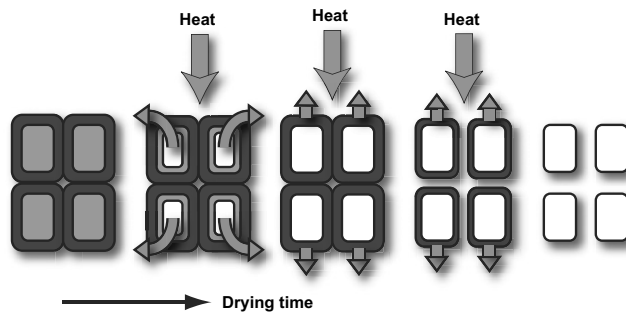


Fig. 2. Wood-drying process. At first the cells are filled with water, but in the end no free water exists, and the absorbed water in cell walls is dried out until an equilibrium state with the surrounding environment is reached.

When all free water has been evaporated the bound water starts to evaporate as well. This state of the wood is known as the fiber saturation point (FSP) and it corresponds to a moisture content of about 25–30%, depending of type of wood. Since bound water is situated inside the cell walls, more energy is needed to evaporate it. Thus, the drying rate decreases and the wood shrinks. In the end of the drying process, the wood reaches an equilibrium state with its environment. The moisture content inside wood depends on temperature and humidity level of the environment. A typical value of the moisture content for dried wood is 12–15% [16–18].

### 3. Commercially available moisture meters

Handheld electric moisture meters are commonly used to measure the moisture content in wood. The measurement technique was developed in the late 1930's, and today there exists a number of manufacturers that develop and sell handheld moisture meters for measuring, e.g., moisture in wood and concrete. Mainly, two different measurement principles exist: resistance and dielectric type moisture meters [19–21].

The resistance type of moisture meter measures the electric resistance in wood between two pins that are connected at the wood surface or inserted into the wood, with typical distances of centimeters between the pins. If the wood is dry it acts as an isolator, and the resistance is in the order of  $10^5$  M $\Omega$ . However, since water in wood contains ions, the resistance in wood decreases down to about 0.5 M $\Omega$  when the moisture content is close to the saturation point.

In order to measure the moisture content using the resistance principal, one has to know the type of wood and from what region it comes. It turns out that all species of wood have different resistance curves even for one type of wood that has grown at two different locations. Today, resistance curves for many species of wood are stored in the device and controlled by a microprocessor.

Although the resistance type of moisture meter is easy to produce and operate, precautions should be considered. At first this measurement method is intrusive. Secondly, the resistance curve for wood is affected by temperature. Thus, a temperature sensor is included in some of the meters. Other disadvantages are the limited measurement range and that the result depends on whether the pins are inserted in parallel or perpendicular to the wood fibers. The upper

limit is set by the fact that above the fiber saturation point (about 25–30% moisture content), the resistance measurement data are not reliable. The lower limit (about 7% moisture content) depends on the difficulties to measure resistance in the order of  $10^5 \text{ M}\Omega$  and above.

The dielectric type of moisture meter uses a nonintrusive measurement technique that measures the dielectric constant of the combined wood and water material. Since the dielectric constant for water is much higher than that of wood (by a factor of 25), the moisture content may be estimated. Anyway, each type of wood has its specific dielectric constant. Specific wood calibration data are stored in the device and controlled by a microprocessor. The dielectric moisture meter is known to have poor performance compared to the resistance type. However, it is commonly used for relative measurements. The surface electrodes are sensitive to other materials close to the surface and density fluctuations of the wood. The measurement range varies from 5% to about 25% moisture content.

#### **4. Setup for diode laser spectroscopy on wood**

We will now describe our spectroscopic setup for moisture studies. While measurements using a light transmission or backscattered geometry can be made with the GASMAS method, the former one was chosen because of its simplicity in terms of the optical arrangement and also regarding the signal interpretation. However, a backscattering geometry is attractive in terms of optical access and is also the only possible one for thick samples. Our setup is based on two almost identical arrangements that are run simultaneously. One setup is used for oxygen measurement while the second is used to measure water vapor (moisture) contents in the same piece of wood. A schematic drawing is shown in Fig. 3. The oxygen measurement setup is explained in more detail in Refs. [12]. However, in the present setup the photo multiplier tube (PMT) sensor is replaced by a silicon detector (Photovoltaic PIN-10DP from UDT) with an active surface of  $100 \text{ mm}^2$ .

The major difference between the oxygen and the water-vapor setup is the wavelength of the diode lasers used. For the oxygen detection a diode laser (Sharp LT031MDO) with a maximum output power of 7 mW, operating at 2 mW at the sample, is used to scan across the R7R7 oxygen line at 761.003 nm (vacuum wavelength). The scan range was typically 20 GHz (0.04 nm). A near-IR Fabry–Pérot diode laser (Specdilas F760) with a maximum output of 200 mW at 980 nm, and efficiently operating at 40 mW at the sample, is used as a spectroscopic light source to detect the water-vapor line (vibration;  $(000) \rightarrow (121)$ , rotation;  $J''=5 \rightarrow J'=4$ ,  $K_a''=0 \rightarrow K_a'=0$ ,  $K_c''=5 \rightarrow K_c'=4$ ) at 978.509 nm (vacuum wavelength). The scan range was typically 35 GHz (0.11 nm).

The basis for the measurement is that the wavelength of the laser light is scanned across the absorption lines by sweeping the operating current of the lasers by the use of a 4 Hz saw tooth ramp. To achieve wavelength modulation spectroscopy (WMS) with lock-in detection, the operating current is also modulated by a sinusoidal wave at 9 kHz with a modulation index of about 1 in both cases. The laser light is focused into a fiber that guides the light to the sample. The water vapor setup uses the same type of silicon detector as the one used for oxygen. The output from each detector is split into two signal branches. One, directly connected to an oscilloscope, is referred to as the direct signal, while the second part goes via the lock-in amplifier before being connected to another channel of the oscilloscope, and is referred to as the WMS signal. The data are stored and analyzed using a computer. Typical readings for oxygen and water vapor are shown in the lower part of Fig. 3. The peak-to-peak value of the WMS signal is measured and normalized by dividing with the direct signal value at the corresponding wavelength in order to determine the fractional absorption during the drying process.

As discussed for instance in [10], a method called standard addition, well known in analytical chemistry, is used in order to calibrate a measured normalized WMS signal and transfer it to a

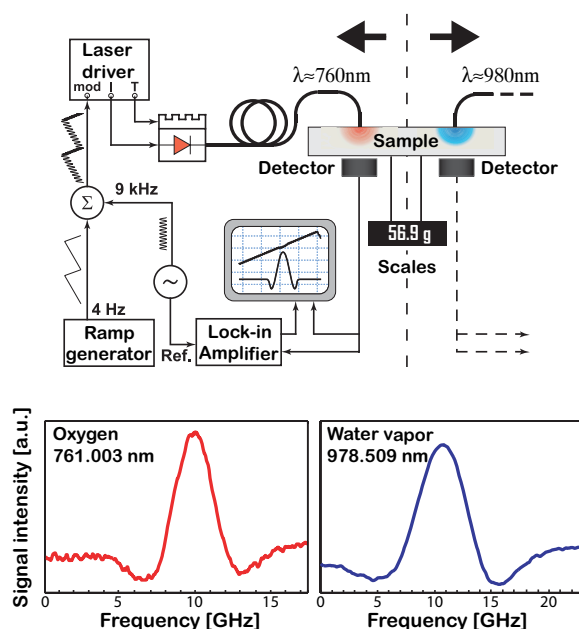


Fig. 3. Schematic drawing of the spectroscopic setup of similar diode laser spectrometers for oxygen (left) and water vapor (right). Typical readings of the WMS signals for oxygen and water vapor in wood are shown in the lower part. The half widths of the signals are of the order of a few GHz in both cases. The half widths at half maximum (HWHM) of the absorption lines are, according to HITRAN, 1.61 GHz for oxygen and 2.72 GHz for water vapor at standard conditions.

more meaningful quantity—a so-called equivalent mean path,  $L_{eq}$ . It is determined by adding free air path lengths in the collimated laser beam before it enters the test sample. The equivalent mean path length corresponds to the distance that the light has to travel in ambient air in order to obtain the same signal as in the sample  $L_{eq} \cdot c_{air} = \langle L_{sample} \rangle \cdot c_{sample}$ , where  $c_{air}$  corresponds to the gas concentration in air,  $\langle L_{sample} \rangle$  to the mean path length in the sample, and  $c_{sample}$  to the gas concentration in the sample. The calibration procedure is carried out by removing the wood sample and placing an optical attenuation filter on top of the detector. A collimator lens was placed at the end of the fiber. The normalized WMS signal was measured for different added air distances between the collimator lens and the filter. A linear function between the normalized WMS signal and added air distance is obtained. This function can then be used to estimate the  $L_{eq}$ . The calibrations are done once for each laser, and these calibration curves are used for all experiments. Precautions were taken when the water-vapor WMS signal was calibrated. The room temperature and relative humidity were measured by a hygrometer (Testo 608-H1) sensor and the partial pressure of the water vapor was estimated.

An analog lab scale (Libror EB-280, Shimadzu) is used to measure the weight of the wood in order to calculate the average moisture content during the drying process. At the end of the drying process a commercial convection oven was used to dry the wood at 110°C in order to determine the truly dry weight.

## 5. Measurements and results

Uniform balsa wood pieces of 10 cm width, 30 cm length, and 0.8 cm thickness derived from the same batch were used in the measurements. The figures of balsa wood shown in Fig. 1 are from the wood samples studied. The wood was kept under water for typically three days and was studied directly after being exposed to the ambient laboratory air. The drying could be followed by reading off the analog scales, onto which the piece of wood was attached.

The results of conventional measurements of the moisture contents during the drying process are shown in Fig. 4, with the instrument applied in a straightforward manner. The weight reading from the scale, expressed as moisture content, is plotted together with data from the resistance and the dielectric moisture meters. It can clearly be seen that the results from the meters poorly describe the real drying process monitored by the scale for moisture content above the FSP. Obviously there is a need for improved measurement techniques for moisture.

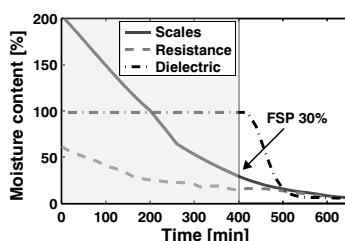


Fig. 4. Measured moisture contents during the drying process of the sample. Curves indicate moisture content (blue curve) when measured by logging the weight of the sample, (red dashed curve) when measured by using a resistance moisture meter (Protimeter Timbermaster), and (black dash-dotted curve) when measured with a dielectric moisture meter (MC-300W, Exotek). The fiber saturation point (FSP) is indicated in the figure (moisture content=30%).

The temperature of the wood surface was also monitored with thermocouples. The measurements were performed on a different sample. In this case the sample had been soaked in water for a longer time than the case when recording the data in Fig. 4. Typical results are shown in Fig. 5(a), where the blue curve shows a weight loss to a stable value of about 33% of the original wet weight, the dry material plateau being reached after about 1200 min. The drying process is, as expected, accompanied by a lowering of the temperature. During the first 600 min the temperature was stable at 9°C below the ambient value (25°C), which was gradually reached after 1200 min. Local possible heating, due to laser beams, was found to be very small. This results in a marginal increase of water vapor pressure.

Since gaseous water (water vapor) is measured in our study it is interesting to consider the vapor pressure of water as a function of the temperature. The corresponding curve is given in Fig. 5(b). It shows the partial pressure of the vapor in a closed volume containing liquid water at the given temperature. We note that the vapor pressure is increasing by a factor 1.8 when the temperature rises from 16°C to 25°C. We also note that water vapor at ambient temperature only accounts for a small percentage of the mass in normal air. Frequently ambient air does not feature the full water vapor pressure corresponding to the ambient temperature. If there is no air movement and large amounts of distributed liquid water the relative humidity would be 100%, like in a sealed-off volume. Due to the exchange of dryer air, the effective humidity becomes less. Readings of 20–40% relative humidity (percentage of the fully saturated value at the given temperature) are common in indoor environments at wintertime in Sweden.

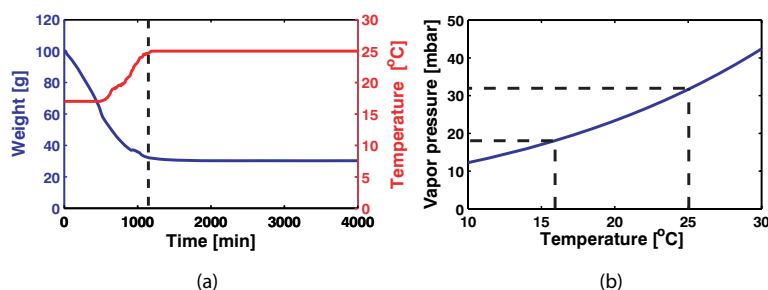


Fig. 5. (a) Measured temperature at the surface of the sample and measured weight during the drying process. (b) Vapor pressure as a function of the temperature [22].

We will now present data from our near-IR laser spectroscopic measurements. We performed simultaneous (molecular) water vapor and molecular oxygen measurements at points separated by about 10 cm on the piece of wood, assuming the material to be laterally uniform. These data were recorded simultaneously as the temperature and weight data in Fig. 5(a). A small air space was left between the sample and the detectors to allow water to homogeneously diffuse out of the sample. The setup is shown in Fig. 3. Oxygen does not have a liquid phase in the temperature range studied (it liquifies at 90K). In contrast, water has a liquid phase as well as a gaseous phase, and the vapor pressure is, as just discussed, temperature dependent.

In understanding the dynamics of wood drying it is useful to first consider the behavior of the molecular oxygen  $L_{eq}$  during the drying, which as mentioned before is proportional to the normalized WMS signal. In Fig. 6(a) the fractional oxygen absorption is plotted in red. The signal is proportional to the oxygen concentration times the effective distance travelled through the gas-filled pores, the latter factor being strongly sensitive to the degree of light scattering in the material. The signal is plotted as an equivalent path length in normal air containing 21% oxygen, as previously discussed. It should be noted that the effective path length through the material, useful in a standard Beer-Lambert law view, can be expected to change during the drying process. One aspect is that while liquid water is an index-matching fluid reducing the scattering when the pores are water filled, the scattering should increase when the air-filled inhomogeneities develop during the drying process. We notice that the oxygen signal increases from a non-zero value (there are air-filled pores even in the very wet wood) by a factor of about 8 to then stay constant at the high value, reached at about 1300 min when all the liquid water is driven out and all the pores are instead gas filled.

The simultaneously measured gaseous water signal is included in blue in Fig. 6(a). Again, the curve starts at a non-zero level (corresponding to the presence of gas-filled pores with saturated water vapor also in the very wet wood). The signal increases to a maximum at about 1200 min, reached slightly before the oxygen signal maximum. At the same time as the oxygen signal stays constant the water vapor signal gradually falls off to a steady value of about 25% of the maximum value. This could be interpreted in the following way: Around 1200 min the pores are almost void of water, as indicated by the dashed line in Fig. 5(a), but there is still a sufficient amount of water to sustain the full saturated water vapor partial pressure. Shortly thereafter, this is no longer the case, and the pores with constant volumes and situated in a material with constant scattering properties gradually lose the saturated vapor pressure and gradually attain the relative humidity value of the laboratory, which for the measurement case with an ambient temperature of 25°C was separately measured to 24% with a hygrometer. This is in good agreement with the measured signal falloff to about 25% of the value with

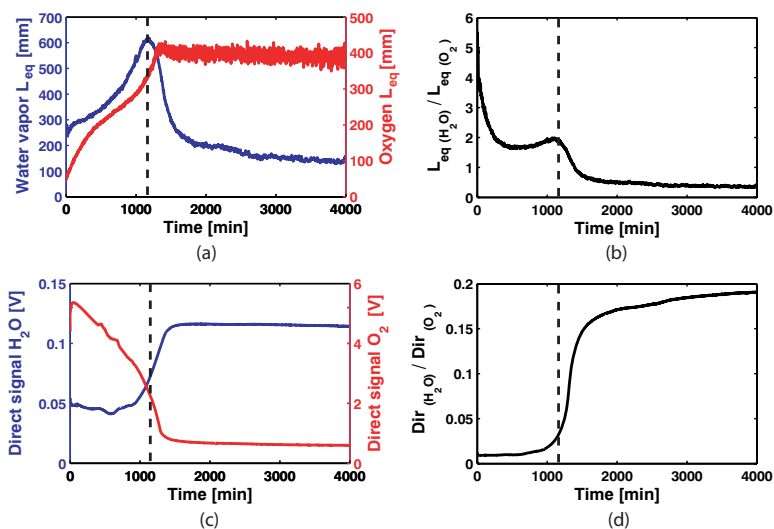


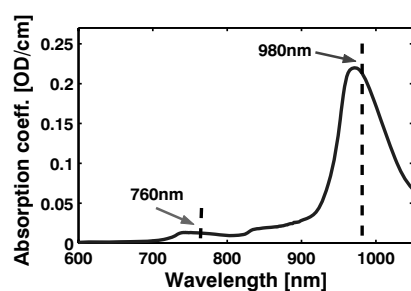
Fig. 6. (a) Equivalent mean path length for water vapor and oxygen during the drying process of balsa. (b) Ratio between detected equivalent mean path length for water vapor and oxygen. (c) Direct signals for water vapor and oxygen during the drying process of balsa. (d) Ratio between detected direct signal for water vapor and oxygen.

full saturation. The displacement of about 100 min between the reaching of the maximum for oxygen and water vapor is compatible with the typical times for air diffusion in balsa wood measured separately [11].

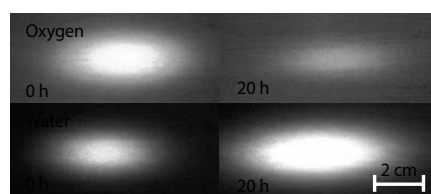
While the above observations are readily interpreted, the detailed behavior of the water vapor signal during the drying is due to many different influences. Let us first state that if two permanent gases such as nitrogen and oxygen had been studied, the same type of behavior (apart from small effects of different diffusivity), i.e., a constant ratio between the signals during the drying phase, would have been expected. This statement has as a prerequisite that the two gases absorb at close-lying wavelengths so that the scattering properties are similar. In contrast to this, the ratio between the water vapor signal and the oxygen signal is strongly varying during the drying process, as can be seen in Fig. 6(b). The temperature increase in the time span 400–1200 min (see Fig. 5, red curve) leads to an acceleration in the water-vapor signal level beyond that for oxygen, for which the concentration is marginally reduced (a few percent) by the temperature increase. This may explain the tendency of increase of the ratio curve toward the end of the drying period. The high initial value in the ratio curve may be related to the time constant for oxygen diffusion through the material also discussed with regard to the different times for the two gases to reach the maximum WMS signal. It should be noted that in the drying up of a pore, the walls of the cavity will be uniformly covered by liquid water due to the surface tension. This may impair the transport of oxygen through the film while the water vapor can freely build up in the central microbubble of the pore, see Fig. 2. Effects of this kind may also influence the balance between the two gases in the cavities during the drying process. As noted, when everything is dry, conditions are static with regard to scattering and the behavior of both curves is clearly understood as discussed above.

So far we have been discussing the fractional absorptive imprint of the gas (intensity on

the absorption line compared to the intensity off the line), which is decisive for concentration measurements based on the Beer–Lambert law. However, it is also interesting to study the dynamics of the total light (off the narrow absorptive features) at the two wavelengths used (980 nm and 760 nm, respectively). Such measurements were performed and the results are shown in Figs. 6(c)–(d) and in Fig. 7. The curves in Fig. 6(c) show a very different behavior with the water signal increasing in the final phase of drying from an almost constant initial level to a final value about 2.5 times higher. On the contrary, the 760 nm signal starts at a high level and, with acceleration, reaches a steady value about 5 times lower when the wood is dry. The ratio of detected direct signal for water and oxygen is shown in Fig. 6(d). In explaining these phenomena it is important to note that liquid water has quite a strong broadband absorption around 980 nm, as detailed in Fig. 7(a) and already noted in the Introduction. We note that this absorption influences the on- and off-resonance frequencies for the narrowband water-vapor signals alike, and does not influence the fractional absorption determining the water-vapor concentration. However, the laser beam is clearly attenuated by the water contents. The initial flat response of the 980 nm curve for the drying wood can be interpreted to mean that the reduction of water during the initial drying is compensated by the increased light path length due to the developing gas-filled pores. Finally, the absorbing liquid water disappears and the detected light settles on a level determined by the attenuation of the light-scattering dry wood.



(a)



(b)

Fig. 7. (a) Absorption spectrum of 1 cm pure water reproduced from the measurements by Matcher *et al.* [23]. (b) Images of the sample on the detection side for oxygen (760 nm) and water vapor (980 nm) during its drying process.

The 760 nm light is off-resonance from the broad liquid water absorption as shown in Fig. 7(a), and bulk absorption due to the water is small, in strong contrast to the case for 980 nm. The high initial light level can be seen owing to the index-matching effect of the water in the pores, which reduces the lateral scattering and allows more light to reach the detector. As the wood dries the scattering increases and less and less light reaches the detector. Steady-state

conditions then prevail in the dry wood. The significant change in the light levels, as well as the normalized WMS signals for both wavelengths when the wood is nearly dry can be interpreted as the final dry-up of the finest compartments long after the tube structure that contained most of the water has dried up. The scattering increases a lot due to the appearance of small pores of size comparable with the wavelength. This reduces the detected 760 nm light level. Also the 980 nm light level changes due to the continued loss of bulk water absorption.

The dynamics of the transmitted light levels at the two wavelengths could also be studied using near-IR imaging of the transmitted light using standard Web cameras (Q-Tec 100). The transmitted light blobs at 980 nm and 760 nm are shown in Fig. 7(b) for fully wet and fully dry (waiting 20 h = 1200 min) conditions. The intensity in the center of the blobs (where the detector is situated) is related to the intensities given in Fig. 6(c); the 760 nm signal is greatly reduced and the 980 nm is increased. The final levels (20 h) correspond to an attenuation by the sample of the incident light of about 80% for the 980 nm signal and 99.95% for the 760 nm signal. These attenuations suggest that the wood sample thicknesses accessible in transmission measurements cannot be considerably larger than 1 cm for most wood types. For thicker samples the backscattering geometry is still applicable. From recordings, such as the ones shown in Fig. 7(b), information of the spatial distribution can also be extracted and compared with theory [7]. However, a detailed analysis of the spatial distribution is outside the scope of the present paper.

## **6. Conclusions and discussion**

Removing moisture from materials is of major importance in fields as diverse as industrial processing, handling of construction materials, and preparation of agricultural products. The origin of excess water is frequently connected to material porosity. Optical measurement techniques are attractive since they are nonintrusive and frequently deliver data in real time. However, quantitative absorption spectroscopy is hampered by the strong scattering in inhomogeneous materials, making the Beer–Lambert law not directly applicable. In the present paper we have demonstrated the application of the GASMAS technique applied in transmission for the monitoring of water vapor in wood, using corresponding molecular oxygen measurements as a reference. The wavelengths used for the free gas monitoring, 980 nm and 760 nm, are also on- and off-resonant for a broad liquid water absorption feature, and thus information of the bulk water is also obtained. The signal intensities observed can mostly be interpreted as the result of the interplay between specific absorption and scattering, both changing during the drying process. In particular, the time when all the free water has evaporated from the wood can be readily identified by a steep falloff in the water vapor signal accompanied by the reaching of a high-level plateau in the molecular oxygen signal. The ratio between these signals, being dimensionless and largely independent of scattering, shows in particular the arrival at a fully dry sample. This situation is also identified in the differential optical absorption signal for liquid water, with a sharp increase of an order of a magnitude in the ratio of the (broadband) signal intensities at 980 nm and 760 nm.

It is thus clear that optical spectroscopy can be a valuable tool for the practical monitoring of drying processes while also yielding additional information on specifics of drying. For the practical application of the method, measurements in back-scattering geometry (as already applied in our sinusitis monitoring [15]) is of great interest. In order to further elucidate the interplay between scattering and absorption, time-resolved measurements of the photon history in the wood for the two wavelengths would provide independent information on the scattering of the material and the liquid water contents. Such measurements can be performed using white light [6,9], capturing the full spectrum, or employing a number of pulsed diode lasers selected at appropriate wavelengths [24].

**Acknowledgement**

The authors thank Rita Wallén from the Department of Cell and Organism Biology of Lund University for her help with the microscope pictures. We also acknowledge useful discussions with Lars-Olof Nilsson from the Division of Building Materials of the Lund Institute of Technology.

This work was supported by the Swedish Research Council and the Knut and Alice Wallenberg Foundation.



# PAPER XIII

**Gas diffusion measurements in porous media by  
the use of a laser spectroscopic technique**

M. Sjöholm, L. Persson, and S. Svanberg.

(2006) *Manuscript in preparation.*



## Gas diffusion measurements in porous media by the use of a laser spectroscopic technique

M. Sjöholm, L. Persson, and S. Svanberg  
Atomic Physics Division LTH, Lund University,  
P.O. Box 118, SE-221 00 Lund, Sweden

Gas diffusion measurements in scattering porous media by tunable laser absorption spectroscopy is presented. The porous sample is exposed to an anomalous ambient gas mixture during a prolonged time period and the transient signal of gas inside the sample is followed spectroscopically by monitoring molecular oxygen. It is shown that the transient gas signal depends on both the spatial distribution of the internal gas and the volume sampled by the diffuse multiply scattered light detected. The light sampling is modeled by Monte Carlo simulations and the gas distribution by the diffusion equation. The concept presented has prospects of becoming a compact tool for non-intrusive, real-time *in situ* measurement of gas transport in porous materials.

### I. INTRODUCTION

Gas contents inside porous materials has for a few years been measured by a diode-laser-based spectroscopic technique entitled GASMAS (gas in scattering media absorption spectroscopy). The technique was first introduced in Ref. [1], and combined with time-resolved measurements the concentration of the gas could be estimated [2]. Already in the initial paper a transient gas signal from a porous sample after exposure to an anomalous ambient gas mixture was recorded and the transient gas signal seemed to follow a simple exponential curve. Similar measurements were also performed on oxygen inside wood [3] and fruits [4, 5]. In occasions of good signal-to-noise ratios it was observed that the transient gas signal could slightly deviate from the simple exponential curve.

The present communication reports on a theoretical description of the time dependence of the transient GASMAS signal from a porous sample after exposure to different ambient gas mixtures. Experimental results are compared with the theoretical description. It is found that the GASMAS signal depends on both the internal gas distribution and the volume sampled by the light detected. We focus on the sample geometry of infinite slabs since it is relevant for several practical applications and has the additional benefit of being relatively easy to model theoretically. However, numerical methods can be used for treating more complex geometries.

In the next Section, gas transport is modeled. Section III describes how the sample is probed by the light and in Section IV it is related to the gas signal detected. In Section V the experimental procedures are outlined and in Section VI the experimental results are compared with theoretical models. Finally, some conclusions are made and directions for future research are outlined.

### II. GAS TRANSPORT MODELING

The most commonly used approach to model gas diffusion is Fick's second law of diffusion, which captures the temporal and spatial evolution of the gas concentration

$C$  in a one-dimensional case along the  $z$ -axis according to

$$\frac{\partial C}{\partial t} = D \frac{\partial^2 C}{\partial z^2}, \quad (1)$$

where  $D$  is the diffusion coefficient. By the method of variable separation, solutions to the diffusion equation in various simple geometries can be obtained [6]. For one-dimensional diffusion in a slab, that initially has a concentration  $C_0$  and is surrounded by a constant concentration  $C_1$ , one solution is

$$\frac{C_1 - C(z,t)}{C_1 - C_0} = \frac{4}{\pi} \sum_{n=1}^{\infty} \frac{(-1)^{(n-1)}}{2n-1} \exp\left\{-Dt \left(\frac{(2n-1)\pi}{L}\right)^2\right\} \cos\left(\frac{(2n-1)\pi z}{L}\right), \quad (2)$$

where  $L$  is the thickness of the slab. In Fig. 1 concentration profiles according to Eq. (2) are displayed for several times after the onset of the dynamic process. This solution is especially convenient at the later stage of the diffusion process, which is well described by only one term in the series. However, at shorter times a series of error-functions provide a more efficient solution [6]. A practical delimiter between the two regimes is provided by the Fourier number,

$$Fo = \frac{Dt}{\left(\frac{L}{2}\right)^2}. \quad (3)$$

For instance, if we try to approximate the full solution by only one term in the series, the deviation from the full solution is the same for both series at a Fourier number of about 0.25. At longer times, the use of only the first term in Eq. (2) provides the best approximation with a maximum deviation from the full solution of only a fraction of a percent.

Although the diffusion equation, in a strict sense, is valid only for free diffusion without the influence of confining walls [7], it is an appropriate model for gas transport in porous media under certain conditions. For instance, the time evolution of spatial gas concentration

profiles in slabs of polyurethane foam has successfully been modeled by Fick's law of diffusion [8]. In that study the spatial concentration profiles were measured by intrusive gas extraction techniques.

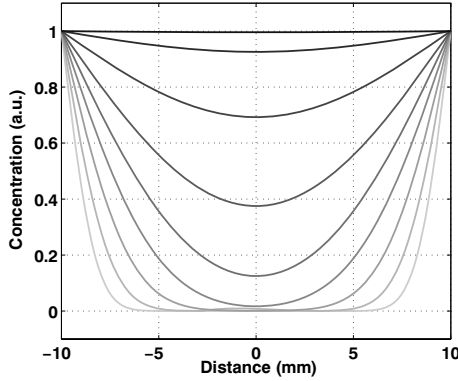


FIG. 1: The change of spatial concentration distribution in a 20 mm thick slab according to Eq. (2) with  $D=1.5 \cdot 10^{-8} \text{ m}^2/\text{s}$ . The curves correspond to time delays of 1, 2, 4, 8, 16, 32, 64, 128 and 256 minutes after initiation. Inside the slab the concentration starts from an initial value of  $C = 0$ , and as time goes on approaches the concentration  $C = 1$  of the gas outside the sample.

### III. LIGHT SAMPLING MODELING

In order to understand the gas imprints detected in the multiply scattered diffuse light, knowledge about the history of the light detected is needed. The quantity of interest is the probability function,  $P(\mathbf{r}; \mathbf{r}_1, \mathbf{r}_2)$ , which defines the probability that light detected in position  $\mathbf{r}_2$  has passed a certain position  $\mathbf{r}$  within the sample while propagating from a light source placed in position  $\mathbf{r}_1$ . Within the framework of photon hitting density [9], this can be formulated as

$$P(\mathbf{r}; \mathbf{r}_1, \mathbf{r}_2) \propto \phi(\mathbf{r}_1, \mathbf{r})E(\mathbf{r}, \mathbf{r}_2). \quad (4)$$

Here, the factor  $\phi(\mathbf{r}_1, \mathbf{r})$  is the photon fluence rate in position  $\mathbf{r}$  due to a light source in  $\mathbf{r}_1$ . The factor  $E(\mathbf{r}, \mathbf{r}_2)$  is called the escape function and is the probability that the light present in  $\mathbf{r}$  will escape to a detector in position  $\mathbf{r}_2$ . This probability can in principle be calculated from analytical solutions of the diffusion approximation to the radiation-transport equation, which is commonly used to describe propagation of light in multiple scattering media [10]. However, such a solution is not valid in the vicinity of a point light source.

A more general approach is provided by simulations based on the Monte Carlo concept, which was used in this study [11]. Multiple light scattering was simulated

in slabs of polystyrene foam and the slab locations passed by the light detected were stored. The material was modeled by the optical parameters provided by Ref. [2], i.e., an absorption coefficient of  $0.2 \text{ m}^{-1}$  and a reduced scattering coefficient of  $4000 \text{ m}^{-1}$ . A transmission geometry of detection with no lateral separation between the injection and detection point was utilized. In Fig. 2 results from simulations on different slabs of thicknesses 10, 20, 30, 40, and 50 mm are shown. The value of a sampling distribution profile in Fig. 2 at a particular  $z$  was obtained by integrating the sampling probability provided by the Monte Carlo simulation over that particular  $xy$ -plane. The distance along the  $z$ -direction has after the calculation been normalized to the thickness of the slab to allow simultaneous presentation of the relative sampling probabilities as a function of the location along the  $z$ -direction. The results indicate that for this particular geometry there is no pronounced thickness dependence of the spatial shape of the sampling probability.

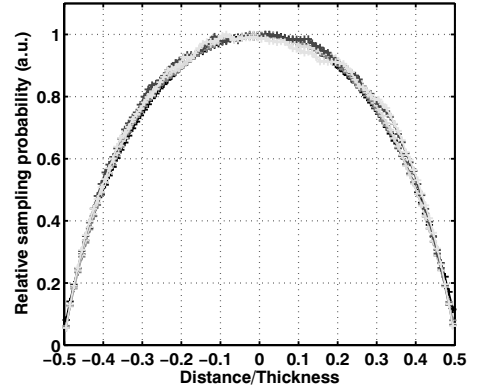


FIG. 2: The relative sampling probability, obtained by Monte Carlo simulations, in slabs of thicknesses 10, 20, 30, 40 and 50 mm.

### IV. LIGHT SAMPLING OF GAS TRANSPORT

The time-dependent gas absorption imprint,  $S(t)$ , detected in the multiply scattered diffuse light is constituted by the spatially integrated contribution of gas present at different locations within the sample multiplied by the local sampling probability. In an infinite slab this can be expressed one-dimensionally as

$$S(t) = k \int_{-\frac{L}{2}}^{\frac{L}{2}} C(z, t) P\left(z; -\frac{L}{2}, \frac{L}{2}\right) dz, \quad (5)$$

where  $C(z, t)$  is the time dependent spatial concentration distribution given by, e.g., Eq. (2) and  $P(z; -\frac{L}{2}, \frac{L}{2})$  is the sampling weight for position  $z$  given that the light enters

at the surface of the slab satisfying  $z = -\frac{L}{2}$  and leaves at  $z = \frac{L}{2}$ , i.e. at the opposite surface of the slab. If Eq. (5) is integrated using the spatial concentration distribution  $C(z, t)$  given by Eq. (2), the gas signal will have a time dependence according to,

$$S(t) = A - \sum_{n=1}^{\infty} B_n \exp\left(-\frac{t}{\tau/n^2}\right) \quad (6)$$

where  $\tau$  is the longest time constant in the series expansion,  $n$  is an odd integer value and the other coefficients can be seen as free parameters in the model.

Within this framework, it is possible to understand why transient gas signals are well described already by only one simple exponential function. The spatial distribution of the term having longest time constant in the series given by Eq. (2) is a cosine function with nodes on the surfaces of the slab and is closely resembling the spatial shape of the sampling weight provided in Fig. 2. Indeed, they have a large overlap meaning that the first term in the series expansion is dominating. However, the spatial weight is relatively somewhat higher nearer the surfaces than the cosine function mentioned, meaning that the distributions corresponding to shorter time constant also contribute to the time dependent gas signal. In addition, we notice that the longest time constant in the series expansion satisfies,

$$\tau = \frac{L^2}{D\pi^2}, \quad (7)$$

which means that the time constant depends quadratically on the slab thickness.

## V. EXPERIMENTAL PROCEDURES

### A. Gas in scattering media absorption spectroscopy

The GASMAS technique relies on the fact that the spectral absorption features of gases are several orders of magnitude sharper than the absorption and scattering structures of solid and liquid materials. Therefore, the gas can be assessed by spectrally narrow-band laser light employed in a differential measurement mode.

### B. The experimental set-up

Although the experimental setup has been described in detail earlier, e.g. in Ref. [5], a short overview is given here. Fig. 3 presents a schematic layout of the experimental setup, in which an absorption line, e.g. the R7R7 line of the molecular oxygen A band around 760 nm, could be spectrally scanned by periodically ramping the injection current of a diode laser at a rate of 4 Hz. Diffusely transmitted multiply scattered light was detected

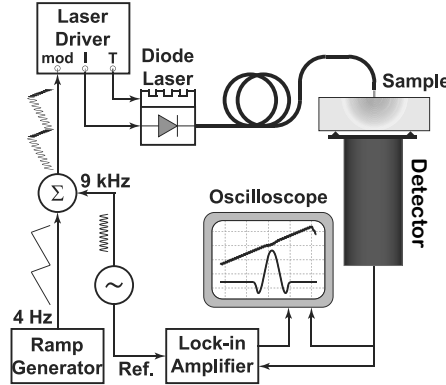


FIG. 3: A schematic layout of the diode-laser-based experimental setup.

by a sensitive photomultiplier tube masked down to a circular detection area of 5 mm diameter. To allow sensitive detection, a wavelength modulation spectroscopy (WMS) scheme was employed. The injection current of the diode laser was modulated in the kHz range and the part of the detected signal oscillating at twice the modulation frequency was picked-up phase-sensitively by a lock-in amplifier and subsequently acquired by a computer controlled oscilloscope. In order to compensate for intensity fluctuations, the WMS signal obtained was normalized against the direct intensity detected. 64 single wavelength scans were averaged giving a new gas signal value about three times per minute.

### C. The porous samples

As a model material, slabs of white expanded polystyrene foam (EPS) was used due to its high gas content and pronounced light scattering. All samples were slowly band sawn from one single large slab of EPS into slabs of lateral dimensions 300x300 mm<sup>2</sup> and thicknesses 10, 20, 30, 40, and 50 mm.

The slabs of polystyrene foam were placed in nitrogen-flushed bags for at least 24 hours. After the storage period in nitrogen gas the samples were brought back out to the ambient normal atmosphere and the transient gas absorption signals were recorded during several hours until equilibrium was reached.

In all the measurements it was made sure that the light injection and detection equipment did not disturb the gas exchange of the sample, i.e., the detector and the injector were positioned at a distance from the surface of the sample. The surrounding of the sample was assumed to be normal air, since the diffusion of gases in the large volume outside the sample was relatively rapid compared to within the sample. However, this could be of influence

if the surrounding volume is limited and mixing is slow, i.e. nitrogen is accumulated and oxygen is depleted in the proximity of the sample.

## VI. MEASUREMENTS AND RESULTS

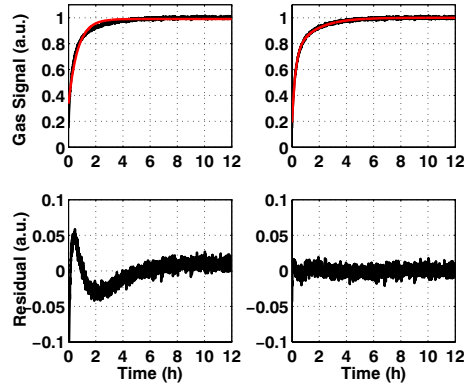


FIG. 4: Experimental transient oxygen signals from a 20 mm thick polystyrene foam slab. Left: fit with one term of Eq. (5). Right: fit with two terms of Eq. (5). The fitting residuals are included in the lower graphs.

The re-invasion of oxygen after the nitrogen treatment previously described was followed spectroscopically. Light diffusely transmitted through the sample was detected with no lateral displacement between the light injection and detection point. Such a recording for a 20 mm thick slab together with a fit of one single exponential term and a sum of two exponential terms, are displayed to the left and to the right, respectively, in, Fig. 4. In the lower part of the figure the residual is provided. In particular, at high level of noise even the influence of the second exponential term would have been obscured.

These results indicate good agreement between the model and the experimentally recorded transient gas signals. However, in order to test the model further, measurements were done on slabs of different thicknesses, as described above. From the light sampling model, we understand that as the thickness increases the relative sampling distribution within the slab will be unchanged. This combined with the gas diffusion model employed means that the longest time constant is anticipated to increase quadratically with the thickness.

The experimentally recorded transient oxygen signals from five slabs of thicknesses 10, 20, 30, 40, and 50 mm are displayed in Fig. 5. Each diffusion process was studied for about 12 hours until it had settled at the steady-state level for some time. The steady-state gas signal values are approximately increasing with the square of

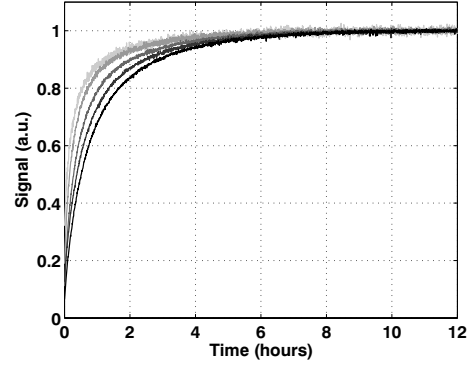


FIG. 5: The normalized transient oxygen signals from polystyrene foam slabs of thicknesses 10, 20, 30, 40 and 50 mm.

the sample thickness, however here the curves are normalized to the steady-state value evaluated during the last hour of measurement to make the time dependence easier to compare between the curves. As expected, it can clearly be seen in Fig. 5 that the transient gas signals reaches the steady state level faster the thinner the sample is. However, the longest time constant does not increase quadratically with the slab thickness as expected from Eq. (7).

## VII. DISCUSSION AND CONCLUSIONS

Gas diffusion measurements in porous materials with the GASMAS technique presented result in transient temporal gas signals. A general modeling approach of these gas signals as a spatially integrated product of the sampling probability, related to the diffuse multiply scattered light detected, and the time-dependent gas distribution inside the porous material is introduced. This modeling approach brings together knowledge from two separate research fields dealing with transport in porous materials and biomedical optics, respectively.

As a first case, gas transport in slabs of expanded polystyrene foam was studied. The sampling probability was obtained from Monte Carlo simulations and the time-dependent gas distribution was modeled by the diffusion equation. In case only a slab of a particular thickness is studied, experimental and theoretical transient gas signal curves show good agreement. For practical purpose, transport parameters of porous materials are often determined for a particular sample size and the behavior of samples of other sizes are inferred from, e.g., the diffusion equation [12]. For instance, the longest time constant is expected to increase quadratically by the slab thickness. However, the presented GASMAS studies of gas transport in expanded polystyrene foam reveal that the time

constant does not show the characteristic quadratic dependence on thickness for this particular material.

This non-Fickian behavior could be due to the presence of open structures between the otherwise closed cells of the foam resulting in faster gas transport to deeper layers of the slab than diffusion through the closed cells could offer. To fully describe this phenomenon, other gas transport models than the gas diffusion equation are required. More research is thus needed to further develop

and evaluate the model to fully agree with experiments. Experiments on slightly more homogenous materials of, for instance, truly closed cell structures are planned as well as other detection geometries providing means of sampling the gas transport at various depths from the surface of the sample. The techniques discussed provide prospects for real-time nondestructive *in situ* gas diffusion studies of porous materials with simple equipment.

- 
- [1] M. Sjöholm, G. Somesfalean, J. Alnis, S. Andersson-Engels, and S. Svanberg, "Analysis of gas dispersed in scattering media," *Opt. Lett.* **26**, 16–18 (2001).
  - [2] G. Somesfalean, M. Sjöholm, J. Alnis, C. Af Klinteberg, S. Andersson-Engels and S. Svanberg, "Concentration measurement of gas embedded in scattering media by employing absorption and time-resolved laser spectroscopy" *Appl. Opt.* **41**, 3538–3544 (2002).
  - [3] J. Alnis, B. Anderson, M. Sjöholm, G. Somesfalean and S. Svanberg, "Laser spectroscopy of free molecular oxygen dispersed in wood materials," *Appl. Phys. B* **77**, 691–695 (2003).
  - [4] L. Persson, H. Gao, M. Sjöholm, and S. Svanberg, "Diode laser absorption spectroscopy for studies of gas exchange in fruits," *Optics and Lasers in Engineering* **44**, 687–698 (2005).
  - [5] L. Persson, B. Anderson, M. Andersson, M. Sjöholm, and S. Svanberg, "Studies of Gas exchange in fruits using laser spectroscopic techniques," *Proceedings of FRUTIC 05, Information and technology for sustainable fruit and vegetable production*, 543–552 (2005).
  - [6] J. Crank, "The Mathematics of Diffusion," (Oxford University Press, New York 1975)
  - [7] R. E. Cunningham, R. J. J. Williams, "Diffusion in Gases and Porous Media," (Plenum Press, New York 1980)
  - [8] C. J. Hoogendoorn, "Thermal ageing," in *Low density cellular plastics - Physical basis of behaviour*, N. C. Hilyard and A. Cunningham (eds), (Chapman & Hall, London 1994).
  - [9] J. C. Schotland, J. C. Haselgrove, and J. S. Leigh, "Photon hitting density," *Appl. Opt.* **32**, 448–453 (1993).
  - [10] M. S. Patterson, S. Andersson-Engels, B. C. Wilson, and E. K. Osei, "Absorption spectroscopy in tissue-simulating materials: a theoretical experimental study of photon paths," *Appl. Opt.* **34**, 22–30 (1995).
  - [11] L. Wang and S. L. Jacques, "Monte Carlo modeling of light transport in multi-layered tissues," standard C, (Laser biology research laboratory, M. D. Anderson cancer center, University of Texas, Houston, Texas 1992).
  - [12] R. Tøgerse at Jackon As, Fredrikstad, Norway (personal communication, 2006).